Helsinki University of Technology Doctoral Theses in Materials and Earth Sciences
Espoo 2007 TKK-ME-DIS-7

CFD PROCEDURE FOR STUDYING DISPERSION FLOWS AND DESIGN OPTIMIZATION OF THE SOLVENT EXTRACTION SETTLER

Doctoral Thesis

Timo Kankaanpää

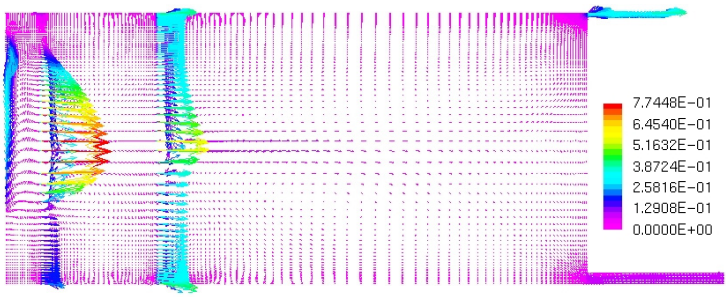

TEKNILLINEN KORKEAKOULU
TEKNISKA HÖGSKOLAN
HELSINKI UNIVERSITY OF TECHNOLOGY
TECHNISCHE UNIVERSITÄT HELSINKI
UNIVERSITE DE TECHNOLOGIE D'HELSINKI

TKK-ME-DIS series
Helsinki University of Technology
Department of Materials Science and Engineering
P.O. Box 6200
FI-02015 TKK
FINLAND

Helsinki University of Technology Doctoral Theses in Materials and Earth Sciences
Espoo 2007 TKK-ME-DIS-7

CFD PROCEDURE FOR STUDYING DISPERSION FLOWS AND DESIGN OPTIMIZATION OF THE SOLVENT EXTRACTION SETTLER

Doctoral Thesis

Timo Kankaanpää

Dissertation for the degree of Doctor of Science in Technology to be presented with due permission of the Department of Materials Science and Engineering, Helsinki University of Technology for public examination and debate in Auditorium V1 at Helsinki University of Technology (Espoo, Finland) on the 23rd of November, 2007, at 12 o'clock noon.

Helsinki University of Technology
Department of Materials Science and Engineering
Laboratory of Materials Processing and Powder Metallurgy

Teknillinen korkeakoulu
Materiaalitekniikan osasto
Materiaalien valmistustekniikan ja jauhemetallurgian laboratorio

Distribution:
Helsinki University of Technology
Laboratory of Materials Processing and Powder Metallurgy
P.O. Box 6200
FI-02015 TKK, Finland

Available in pdf-format at http://lib.tkk.fi/Diss/

Cover: CFD modelled flow pattern (on left) and organic phase volume fraction (on right) in a settler with two picket fences.

ISBN 978-951-22-9038-3
ISBN 978-951-22-9039-0 (electronic)
ISSN 1795-0074

Picaset Oy
Helsinki 2007

ABSTRACT

Computational fluid dynamics (CFD) modelling has been applied to study the behaviour of organic-aqueous dispersion and flow patterns in the copper solvent extraction settler with the aim of developing a complementary method for traditional physical experiments in settler design work. The simulations have been carried out with an Eulerian-Eulerian two-phase model of the commercial CFX-4.4 software in conjunction with the incorporated MUSIG model, which is based on a population balance equation and takes into account the break-up and coalescence models of droplets.

Due to the complicated process phenomena of the phase separation including droplets deformation, variable collision forces, the drop-drop and drop-interface coalescences, film thinning of the continuous phase between droplets or a droplet and its homophase, high-volume fractions of the separated phases and numerical convergence difficulties, a new six-item CFD calculation procedure and the specified boundary conditions were developed. During the developing work, the relative velocity of the phases versus drag force correlations, the dispersed droplet size range, inner iteration of the MUSIG model, the drag force in a dense dispersion, the calibration coefficient of the coalescence model, the discretisation schemes, and steady-state versus transient simulation were tested.

The developed calculation procedure and the temperature-related phase separation correlation coefficient, together with the specified boundary conditions, were applied to the pilot settler with the aim of testing and showing the possibilities of the CFD in the settler design, and gaining new information about dispersion flows and force balances on the droplet level in the settler. The simulation cases took into account the thickness of the dispersion layer versus the specific volume flow rate, temperature and number of picket fences. Furthermore, the pressure drop over the picket fence, the droplet size distribution, the linear velocity of the organic phase, and the hydrodynamic force balances between the viscous, inertia, surface and buoyancy forces were studied.

The developed new calculation procedure proved to be very useful in complicated multiphase modelling. It ensures that all simulation cases can be carried out in the same way, and thus the obtained results are comparable. In addition, use of the procedure improves the overall trust of CFD simulations. The simulated results agree well with experimental data obtained with a pilot settler. The model predicts that the phase separation is achieved more effectively when the picket fences are set into the settler, the temperature is increased or the specific volume flow rate is decreased. These phenomena could also be obtained from the results of the force balances. The inertia forces decrease and, respectively, the buoyancy and surface forces increase when the picket fences are set, and when the dispersion disengages and flows from the front end of the settler towards the rear end. Furthermore, an effective separation requires that the buoyancy forces become stronger than the surface forces. It can be concluded that settler operations with picket fences can be optimized with the aid of CFD modelling.

KEYWORDS: Solvent Extraction, Settler, Picket Fence, CFD, Two-phase, Break-up, Coalescence, Dispersion, Phase Separation.

PREFACE

The research work of this thesis was carried out in the Laboratory of Materials Processing and Powder Metallurgy, Helsinki University of Technology, and revised at Outotec Research Oy, during the years 2000-2007.

I would like to express my sincere gratitude to my Professor Michael Gasik and my supervisor, Docent Ari Jokilaakso for the opportunity of studying this interesting and challenging research work and for their comments and interest in my work. I am also most indebted to Docent Pekka Taskinen and Dr. Kari Koskinen for their interest in my work, and for their valuable comments and advice concerning the whole research work and the early manuscript.

I would also like to thank Mr. Eero Ekman, Mr. Mika Haapalainen, Dr. Jiliang Xia, Mr. Michael Friman and Dr. Jussi Vaarno for their kind co-operation and supporting discussions. Furthermore, I wish to thank my colleagues and the staff of the Laboratory of Materials Processing and Powder Metallurgy and Outotec Research Oy for pleasant working atmosphere.

I am grateful to Outokumpu Research Oy, Outokumpu Oyj Foundation and Tekniikan Edistämissäätiö for financing and the CSC for calculation resources.

I am also extremely grateful to Dr. Kalle Härkki, Dr. Jarkko Partinen and Mr. Henri Virtanen for the possibility to finalise this study while working at Outotec Research Oy.

Many thanks to all my friends, who have shared many relaxing moments on football pitches, badminton and tennis courts.

Finally, the warmest thanks to my parents, sister and brother, and the special thanks to my godson Otto for their patience, trust and support during these years.

Pori, October 2007

Timo Kankaanpää

CONTENTS

LIST OF SYMBOLS

LATIN

A_p	projected area of the droplet in the direction of flow	[m^2]
A_{hs}	horizontal surface area of the settler	[m^2]
$\boldsymbol{A'}$	vector area, which is available to flow	[m^2]
$\boldsymbol{A}$	vector surface area	[m^2]
a	height of the organic phase layer	[m]
B_B	droplet birth rate due to break-up	[$1/(m^3 \cdot s)$]
B_C	droplet birth rate due to coalescence	[$1/(m^3 \cdot s)$]
b	width of the settler	[m]
C_D	drag coefficient	[-]
C_L	lift coefficient	[-]
C_{TD}	turbulence dispersion coefficient	[-]
C_μ	constant in k-ε turbulence model	[-]
$C_{1\varepsilon}$	constant in k-ε turbulence model	[-]
$C_{2\varepsilon}$	constant in k-ε turbulence model	[-]
C_{out}	outflow coefficient	[-]
c	height of the overflow	[m]
D_B	death rate due to break-up	[$1/(m^3 \cdot s)$]
D_C	death rate due to coalescence	[$1/(m^3 \cdot s)$]
d_i	diameter of a droplet	[m]
d_s	Sauter mean diameter	[m]
$d_{d,s}$	diameter of single droplet or Sauter mean diameter	[m]
d_d	average droplet diameter	[m]
Eo	Eotvos number ($E_o = \Delta\rho g d_i^2/\sigma$)	[-]
E_{ij}	mean rate of strain tensor	[1/s]
$\underline{e}_i(d)$	increase in surface energy due to binary break-up	[J]
$\overline{e}(\lambda)$	mean kinetic energy of an eddy with size λ	[J]
$\boldsymbol{F^{buo}}$	buoyancy force	[N/m^3]
$\boldsymbol{F^{drag}}$	drag force	[N/m^3]
$\boldsymbol{F^{lift}}$	lift force	[N/m^3]
$\boldsymbol{F^{td}}$	turbulent dispersion force	[N/m^3]
Fr	Froude number	[-]
f_{BV}	breakage volume fraction	[-]
f_B	calibration coefficient of the breakage model of MUSIG	[-]
f_C	calibration coefficient of the coalescence model of MUSIG	[-]
f_i	fraction of the dispersed phase volume fraction in MUSIG-size group-i	[-] or [$1/m^3$]
g	specific droplet break-up rate	[1/s]
$\boldsymbol{g}$	acceleration due to gravity	[m/s^2]
h_0	initial film thickness	[m]
h_f	critical film thickness	[m]
h_{disp}	height of the dispersion layer	[m]
h_c	height of the coalescing interface	[m]
h_s	height of the sedimenting interface	[m]
h_p	height of the boundary between the sedimentation and	

	the dense-packed zones	[m]
K	experimental constant	[-]
K^{ij}	area porosity tensor	[-]
k	turbulent kinetic energy	[m^2/s^2]
L	characteristic length	[m]
Mo	Morton number ($Mo = g\mu_c^4 \Delta\rho/\rho_c^2\sigma^3$)	[-]
m_{org}	mass of the organic phase	[kg]
m_{water}	mass of the water phase	[kg]
N	total number of MUSIG-size groups	[-]
n_i	droplet number density of MUSIG-size group-i (number of MUSIG-size group-i droplets per unit volume)	[$1/m^3$]
$P_B(v_j{:}v_i, \lambda)$	breakage probability of a droplet of volume v_j (size d_j)	[-]
p	pressure	[Pa]
Q	specific droplet coalescence rate	[m^3/s]
$\boldsymbol{R}$	vectorial velocity through external coordinate space	[m/s]
Re	Reynolds number	[-]
r_{ij}	equivalent radius	[m]
r	droplet radius	[m]
S	net rate of generation of droplets	[$1/(m^3 \cdot s)$]
$\boldsymbol{S_M}$	vectorial source term of body forces	[-]
S_i	source term of the rate of mass transfer into the MUSIG-size group due to break-up and coalescence processes	[$kg/(m^3 \cdot s)$]
S_i'	source term of the rate of mass transfer into the MUSIG-size group due to break-up and coalescence processes	[$1/(m^3 \cdot s)$]
T	temperature	[°C]
t	time	[s]
t_{ij}	coalescence time	[s]
t_f	time for complete phase separation	[s]
t_i	end of sedimentation time	[s]
$\boldsymbol{U}_c$	control volume averaged vectorial velocity of the continuous phase	[m/s]
$\boldsymbol{U}_d$	control volume averaged vectorial velocity of the dispersed phase	[m/s]
$\boldsymbol{U}_{rel}$	relative (or slip) velocity between phases	[m/s]
u	velocity vector component of x-direction	[m/s]
V	volume of the grid cell	[m^3]
V'	volume that is available to flow	[m^3]
V_{fr}	volume flow rate	[m^3/s]
V_{spec}	specific volume flow rate	[$m^3/(m^2 \cdot h)$]
V_o	fluid velocity	[m/s]
v	velocity vector component of y-direction	[m/s]
v_i	droplet volume of MUSIG-size group-i	[m^3]
We	Weber number	[-]
$\boldsymbol{X}$	vectorial velocity through internal coordinate space	[m/s]
y	experimental constant	[-]

GREEK

α_c	volume fraction of the continuous phase	[-]
α_d	volume fraction of the dispersed phase	[-]
$\alpha_{d,i}$	volume fraction of the MUSIG-group-i in the dispersed phase	[-]
α_{dm}	maximum attainable value for the volume fraction of the dispersed phase	[-]
β	constant parameter	[-]
χ_c	critical dimensionless energy for droplet break-up	[-]
δ_k	constant in k-ε turbulence model	[-]
δ_ε	constant in k-ε turbulence model	[-]
δ^{ij}	delta function	[-]
ε	turbulent dissipation rate	[m^2/s^3]
Γ_{ij}	coalescence rate	[$1/(m^3 \cdot s)$]
γ	porosity	[-]
η	Kolmogorov length scale	[m]
λ_{ij}	coalescence efficiency	[-]
λ	eddy size	[m]
λ_{min}	minimum eddy size	[m]
μ	dynamic viscosity	[Pa·s]
μ_t	turbulent viscosity	[Pa·s]
μ_m	mixture viscosity	[Pa·s]
θ_{ij}^T	collision rate due to turbulence	[$1/(m^3 \cdot s)$]
ρ_c	density of the continuous phase	[kg/m^3]
ρ_d	density of the dispersed phase	[kg/m^3]
ρ_0	reference density	[kg/m^3]
σ	interfacial tension	[N/m]
τ_{ij}	contact time	[s]
Ω_B	break-up rate	[$1/m^3 \cdot s$]
$\omega_{B,\lambda}$	collision density or frequency of eddies of size between λ and λ+dλ with droplets d	[$1/(m^4 \cdot s)$]
ξ	eddy/droplet size ratio (=λ/d)	[-]

SUBSCRIPTS

c	continuous phase
d	dispersed phase
$disp$	dispersion
h	droplet size group
i	iteration number
i	MUSIG-size group of a droplet
j	MUSIG-size group of a droplet
k	MUSIG-size group of a droplet

1 INTRODUCTION

Liquid-liquid extraction, or also called *solvent extraction*, is a process for separating components in solution by their distribution between two immiscible liquids (Robbins, 1984; Skelland and Tedder, 1987). This unit process has a lot of applications in the organic chemical industry, for example, the petrochemical and pharmaceutical industries, and during the last few decades it has been used more widely in hydrometallurgy (copper, cobalt, nickel and zinc). Hydrometallurgical process methods, which include leaching, solvent extraction and electrowinning, are used, for example, for copper production when copper presents in the earth's crust as oxidized minerals, such as carbonates, oxides, hydroxyl-silicates, sulfates, and sometimes as chalcocite (Cu_2S). About 20 % of the world's copper production, of which 90 % comes from North and South America (Jenkins et al., 1999), is produced by hydrometallurgical methods; such production is expected to increase. In copper production, the most applied solvent extraction process method is a mixer-settler process, which belongs to the group of stagewise equipment (Goldberger et al., 1984; Ritcey and Ashbrook, 1979). In this study, the focus is on copper production by solvent extraction, and especially on the settler process involved.

1.1 Solvent extraction

The solvent extraction (SX) is an equilibrium process used to concentrate and purify dilute leach solution so that it can be used in, for example, the electrowinning process. Dilute leach solution may contain only approximately 10 g/l copper, but after extraction its copper content rises to approximately 45 g/l, at which point cathode copper can be produced (Kongas and Hughes, 2003). In the extraction stage, the metal ion is transferred from an aqueous phase to an organic phase as a complex compound, which is soluble in the organic phase. The complex compound is formed when the metal ion is combined with extractant, which is insoluble in water. In the stripping stage, the extracted metal ion is transferred from the organic phase to the aqueous phase. Other main unit processes are regeneration and washing. The regeneration stage, in which the extractant is restored to its original effectiveness, is used only occasionally. The regeneration is usually achieved by clay treatment and filtration (Jenkins et al., 1999). In proportion, the washing stage is used to remove impurities of the pregnant leach solution in the loaded organic extractant. Impurities of solid particles due to crystallization are possible in the process streams, for example, at high altitudes in mountains, where winter temperature may fall to below zero (Kongas and Hughes, 2003). This is important to notice and take into account in process design because, according to Tadros and Vincent (1983a) and Friberg and Yang (1996), the solid particles may stabilize dispersion and thus disturb a phase separation in a settler. The SX process is continuous and usually takes place in cascades of two to three extraction mixer-settlers and one to two strip mixer-settlers. The whole SX plant consists of one to four (or six) cascades, with an extraction efficiency per cascade of about 90 % (Jenkins et al., 1999).

1.1.1 Solvent extraction circuit

A single copper solvent extraction circuit takes place in the following way (Figure 1). Firstly, pregnant leach solution from a leaching process and a stripped organic phase from a stripping stage are fed into a mixer of the extraction stage. After mixing, the phases are separated in a settler, and then Cu-depleted aqueous leach solution is sent back to the leaching process and Cu-loaded organic extractant is fed into the mixing unit of the stripping stage. There, copper ion is stripped into copper-depleted electrolyte from electrowinning. After mixing and separation, Cu-enriched aqueous electrolyte and stripped organic extractant are obtained. The enriched electrolyte is sent back to the electrowinning, where its copper is electrodeposited as pure metallic copper. The stripped organic extractant is returned back to the extraction stage, where it starts a new circle. The copper extraction equilibrium depends on pH. In the extraction stage, the extractant can be loaded with copper ions, when the sulphuric acid (H^+) concentration in the pregnant aqueous leach solution is lowered so that the pH is typically between 1.8 and 2.5. In the stripping stage, high sulphuric acid concentration (about 180 g/L) is needed to shift the equilibrium. (Ritcey and Ashbrook, 1984; Chapman, 1987; Cox, 1992; Biswas and Davenport, 1994; Davenport et al., 2002)

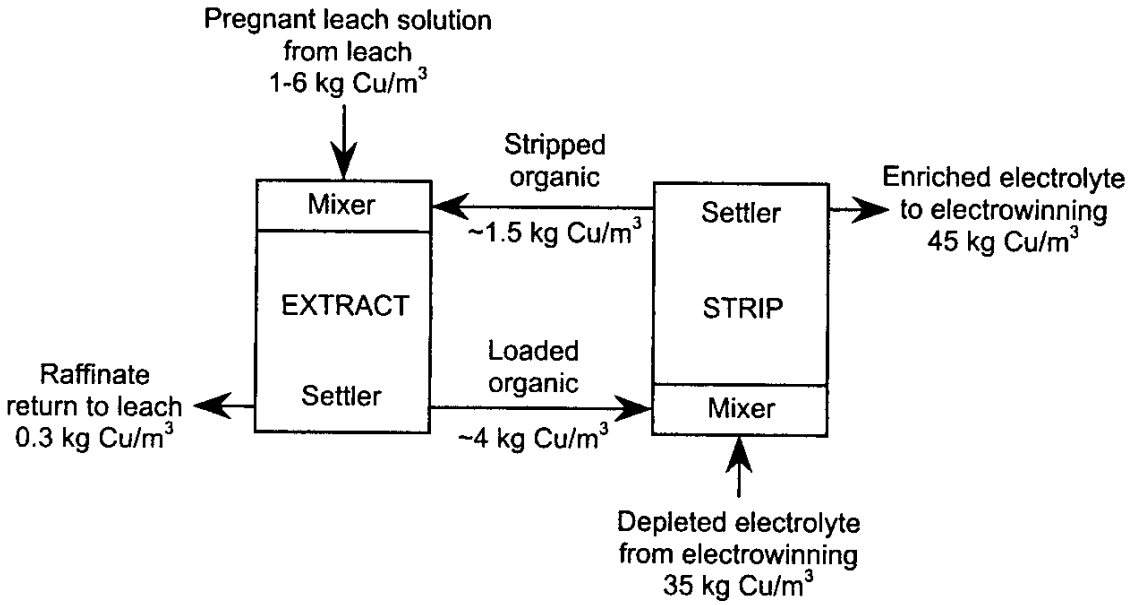

Figure 1. Schematic plan view of copper solvent extraction circuit (Davenport et al., 2002).

1.1.2 Mixer-settler

In the first step of a typical mixer-settler process-unit (Figure 2), the aqueous and organic phases are pumped into a mixer or mixers in order to achieve a homogeneous dispersion[1] and quite a small droplet size because the mass transfer is then high. However, overmixing should be avoided, because it can cause droplets that are too small; these may form stable emulsion[2], which does not separate into two clear liquid phases. Furthermore, incoming air should be also avoided, because it can increase crud

formation and cause oxidation of the extractant. Crud is the name for a solid stabilized emulsion, which is formed when small and fine solid particles, for example, clay and silica from pregnant leach solution, are accumulated at the interface between the aqueous and organic phases (Virnig et al., 1999). On the other hand, pregnant leach solution may also contain impurities like chloride, iron, manganese or nitrate, which cause operational problems (Menacho et al., 2003). All these difficulties or problems have to be taken into account when impeller type, number of mixing units and tip speeds of impeller are selected. According to Jenkins et al. (1999), residence times to produce the desired dispersion in mixers vary between 1 and 3 minutes.

After mixing, the dispersion is fed into a settler, where the aqueous and organic phases are separated by gravity. Settlers are square in plan and typically their square area is about several hundreds square meters. Dispersion moves towards the settler back wall and, at the same time, the phases separate into own layers. In the rear end of the settler, an adjustable weir and launders (weir boxes) are used to control the vertical position of the phase interface and to collect both the phases, respectively. Typically, the height of the denser aqueous phase is about 0.5 m and of the lighter organic phase about 0.3 m. Retention times of the dispersion in the settlers are about 10 to 20 minutes, respectively (Jenkins et al., 1999).

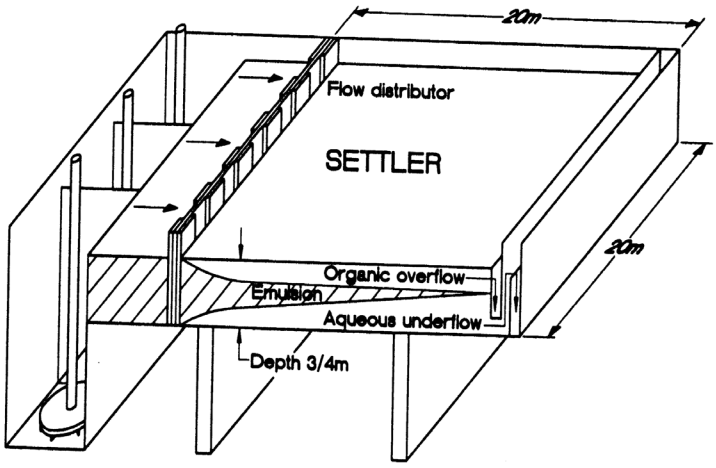

Figure 2. Mixer-settler unit process (Biswas and Davenport, 1994).

[1]Dispersion is a name for a system that contains one phase in a finely divided form in another phase. In solvent extraction this means liquid-liquid dispersion, or, actually, "coarse" dispersion, in which a droplet size ranges from hundreds of micrometers to a couple of millimetres. (Stein, 1996)

[2]When the droplet size is less than 50 μm, the dispersion is called emulsion, which is stable and the phases cannot separate from each other, or if they can separate, they can do so only very slowly (Kralchevsky et al., 1997; Stein, 1996).

The mixer-settler operation can be a batch process or continuous, and, what is more, any mixer can be coupled with any settler to provide the complete stage. If the process is operated in batch mode, both the mixing and the settling are carried out in the same vessel, whereas separate vessels are usually used in the continuous process. In general, modern settlers are square in plan and the phase separation takes place so that the dispersion is separated into the aqueous and organic layers. The most common method to make the phase separation more effective is to use picket fences, which are installed in different locations of the settler. The idea of the picket fences is to retain a deep and dense dispersion layer in the first part of the settler, as shown in Figure 3 (Nyman et al., 1996). This thick and dense dispersion (dense-packed layer) acts like a filtration medium, catching the smallest drops into bigger ones due to drop-drop coalescence. The picket fence also ensures a smooth flow, which enhances controlled drop-interface coalescence. It is very important that the flow rate is not too high, because, otherwise, there would be a possibility of entrainment levels, either organic droplets in the aqueous phase or water droplets in the organic phase, in the separated phases increasing in the rear end of the settler (Miller, 2002).

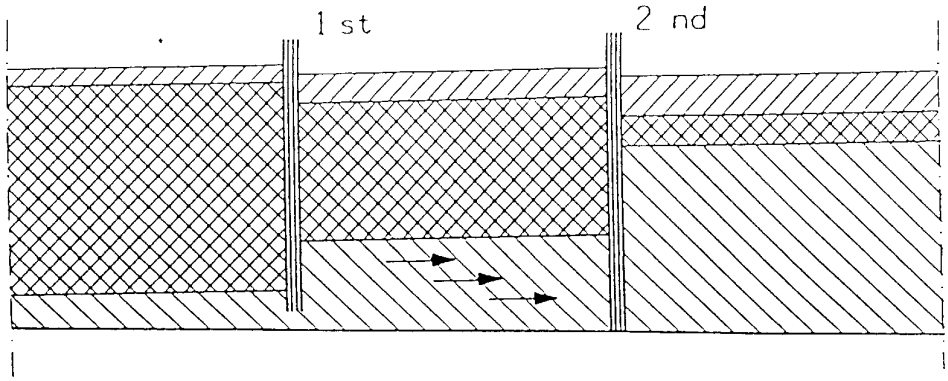

Figure 3. Formation of deep and dense dispersion layer due to picket fences in a settler (Nyman et al., 1996).

There are many types of mixer-settlers, for example, VSF units (Pekkala et al., 1999; Lindell et al., 1998) and Compact Mixer-Settlers (Nyman et al., 2003a; Nyman et al., 2003b), which all have a similar physical process idea for dispersion formation and disengagement of the dispersion. The main difference between these contactors is the flow arrangement incorporated in the system, for example, connection pipes between mixers and settlers, hydraulic horizontal levels and vertical divider plates (picket fences) in a settler.

1.2 Phase separation and droplet coalescence

Barnea and Mizrahi (1975a,b,c,d) were among the first researchers who defined experimentally the structure of the dispersion band and the flow patterns of the dispersed and continuous phases in a settler. According to Barnea and Mizrahi (1975a), the dispersion band in the settler consists of two main sub-layers: The “dense” sub-layer near the coalescence front or active interface, and the “even concentration” sub-layer near the settling front filling the remaining volume. The active interface is the limit

between the dispersion band and the separated layer of the dispersed phase. Respectively, the settling front or passive interface is the limit between the dispersion band and the separated layer of the continuous phase. Their results showed that the flow pattern of the dispersion with simultaneous phase separation due to the density difference of the phases is a very complicated phenomenon. One of the reasons for this is the occurrence of a constantly altering force balance at the interface layer between the dispersed and continuous phases in organic-aqueous (O/A) or aqueous-organic (A/O) dispersion. The forces, either semi-macro forces[3] at the droplet level or short-range and long-range forces[4] at the molecular level, affect the deformability and mobility of the interface; these forces control the drainage of a thin continuous phase film between the droplets or the droplet and its homophase.

The coalescence process involves collision of two droplets or a droplet and its homophase followed by the thin film drainage between the droplets or the droplet and its homophase. The drainage of the thin film depends on the magnitude and duration of the force acting on the droplets. According to Leng and Calabrese (2004), the force can be hydrodynamic (flow-driven collision), hydrostatic (gravity-driven collision) or physicochemical. The hydrodynamic phenomenon can be divided into the internal flow field and the external flow field (Chesters, 1991). The internal flow field means the flow phenomenon, which occurs inside the thin film, and the external flow means the continuous phase flow, which affects and defines the frequency and magnitude of the force (laminar or turbulent shear force) and the duration of droplet collisions. Hydrostatic force is due to the buoyancy force induced by the density difference of the dispersed and the continuous phase and the difference in rise- or fall-velocities of droplets of different sizes (Chesters, 1991; Rother et al., 1997). Physicochemical force depends on the physical properties of the continuous and the dispersed phase, and thus it affects both the flow-driven collision and the gravity-driven collision. In the settler, the coalescence process is dominated mostly by the gravity-driven collision, but there is also the flow-driven collision, especially in the front end of the settler.

1.2.1 Liquid film thinning

The liquid film around the droplet must drain to a critical thickness before the coalescence can take place. This means that the contact time of the droplets has to be longer than the critical drainage time needed to take for the film to thin sufficiently for rupture to occur. If the contact time is too short, the critical film thickness is not reached, and thus the film does not rupture and the droplets only rotate around each other. The formation of the thin film between two approaching droplets (Figure 4) is a multi-stage and complex process. Burrill and Woods (1973) have proposed that the film formation can be assumed to begin when a distance between the droplets is from about 3 μm to 1 mm.

[3]Semi-macro forces on the droplet level consist of body and surface forces.
[4]Short-range and long-range forces include steric interaction forces, van der Waals forces and electrostatic forces, respectively (Erbil, 1997; Birdi, 1997; Nir and Vassilieff, 1988; Tadros, 1988; Tadros and Vincent, 1983b).

According to the description of Kralchevsky et al. (1997) and Ivanov and Dimitrov (1988), the film thinning process takes places as follows: Firstly, the surfaces of two approaching droplets deform only slightly (Figure 4a). In the next stage, hydrodynamic or hydrostatic force presses the droplets closer to each other and, at a distance of about 100 nm, the curvature at the centre inverts its sign and a concave lens-shaped formation called a "dimple" is formed (Figure 4b). The dimple formation and its stability depend on the relation of the attractive London-van der Waals and the repulsive electric double layer forces (Chen, 1984). It is possible that the dimple does not form and then a reverse bell-shaped deformation appears (Figure 4d). The dimple formation demands that the driving force is able to overcome the energy barrier created by the electrostatic repulsion force and/or the increase of the surface area during the droplet deformation. However, if the dimple appears, it exists usually for only a short period of time. Firstly, it grows, but, as a result of a fast outflow of liquid, it decreases and finally disappears. The resulting plane-parallel film forms and it thins almost by constant radius (Figure 4c) that depends on the electrostatic repulsion forces. This film is also called the primary or common black film. Before the formation of very thin film (Figure 4e), the bell-shaped deformation, which may rupture quickly due to thermal fluctuations or other disturbances, appears (Figure 4d), or otherwise it transforms into a thinner Newton black film (also called a secondary film), (Figure 4e). This Newton black film ruptures or expands until reaching the final equilibrium state (Figure 4f). The characteristic thickness of the Newton black film is about 5 to 10 nm. Its stability depends on the short-range steric repulsion force, which is effective when the distance between droplets is less than 10 nm (Chen, 1985).

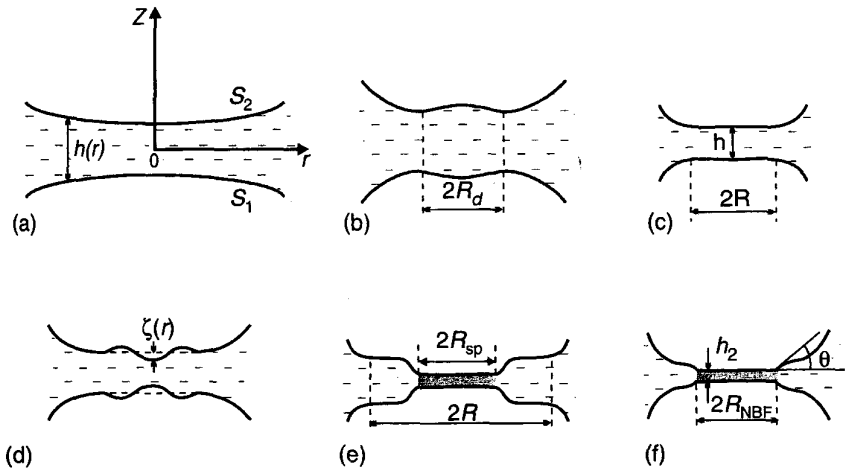

Figure 4. Main stages of formation and evolution of a thin film between two droplets (The following notations are only valid in this figure: S_1 and S_2 are the phase boundaries, $h(r)$ is the film thickness, R_d is the radius of the dimple, R is the film radius, $\zeta(r)$ is the amplitude of the fluctuation, R_{sp} is the radius of the Newton black film, R_{NBF} is the radius of the Newton black film when the equilibrium value is reached, h_2 is the characteristic thickness of the Newton black film, θ is the equilibrium contact angle.) (Kralchevsky et al., 1997).

1.2.2 Critical film thickness and film rupturing

Although the film thinning process seems to take place in a quite organized way, it is not always so. This phenomenon has been studied widely and many liquids have been used to help carry out difficult measurements and achieve reliable results. Gillespie and Rideal (1956) and Charles and Mason (1960a) found in their study that the film does not drain regularly and it may rupture before drainage is complete. In addition, the film thickness is not necessarily uniform and the larger droplet is more stable than the smaller droplet, and thus the film drainage decreases. Radoev et al. (1983) reported also the non-homogeneity of the film thickness. The non-homogeneity was increased with a radius of the film. In general, the thickness of the bell-shaped film (Figure 4d) means the critical film thickness. MacKay and Mason (1963) and Burrill and Woods (1973) have reported that the critical thickness for the rupturing of the thin film is less than 50 nm and it is independent of temperature (MacKay and Mason, 1963). Although, they have carried out their measurements with different liquids and sometimes with surfactants, the order of magnitude of the critical film thickness can be applied to liquids used in the solvent extraction process.

1.2.3 Factors affecting coalescence

Factors affecting the coalescence rate can be divided into four main groups: droplet size, external force, physical properties and solid matters at the interface. These aspects apply to droplet coalescence in general and coalescence in settler conditions in particular.

Droplet size

- Probably the most important factor is the droplet size and its distribution (Nienow, 2004). Magiera and Blass (1997) have reported that droplet sizes should be larger than 100 μm before the phases can separate quickly by gravity. Thus the droplet size has to be suitably large for coalescence, but also it has to be small enough for an effective mass transfer rate in the mixer. When the droplet size increases at the interface of the continuous phase, the coalescence rate decreases. At the interface, the droplet stability increases with diameter, because a large droplet flattens and deforms easier than a small droplet, and thus its stability increases. On the other hand, the collision frequency, collision force and contact times between droplets increase when the droplet size increases. So the coalescence process takes place in some kind of droplet-size range, droplets smaller than d_{min} will coalesce and those larger than d_{max} will break-up (Liu and Li, 1999).

- At the phase interface, secondary droplets may occur and disturb the coalescence process, because these secondary droplets coalesce very slowly. The secondary droplet formation depends on the viscosity ratio of the dispersed and continuous phase. Charles and Mason (1960b) reported that, when the viscosity ratio (μ_d/μ_c) was less than 0.02 or greater than 11, no secondary droplets formed. Furthermore, the formation of the secondary droplets could be avoided when a high concentration of surfactant was added or an electrostatic field was applied.

External force related to droplets

- The coalescence rate increases with external force when droplets, or a droplet and its homophase, are not too close to each other, because then the collision events are more frequent. However, when the distance between two droplets or a droplet and its homophase is very small, the droplets deform and flatten, and thus the surface area of the contact and the film drainage time increase. This means that, at the front end of the settler, the external forces can be very high, but their magnitude should decrease when the dispersion flows towards the settler back wall. (Leng and Calabrese, 2004)

- The coalescence rate or the phase separation rate increases when the density difference between the phases increases. However, this is not so obvious, because when the viscosity and the density differences increase, the coalescence rate decreases. A droplet-interface coalescence rate decreases due to a flattening of the droplet when the density difference increases. (Ritcey and Ashbrook, 1984; Hartland and Jeelani, 1994)

- Some kinds of vibration can also promote coalescence. Oscillation of droplets during droplet collisions may decrease the force pressing on the thin film between the droplets (flattening of the droplets) and hence the film area decreases, which further enhances the coalescence rate (Jeelani and Hartland, 1991).

- The external force affects the geometry of the interface of the phases and thus the concavity and convexity of the interface have also an effect on the coalescence process. Coalescence increases when the interface curvature is convex to the drop and, on the contrary, when the interface curvature is concave. (Ritcey and Ashbrook, 1984; Hartland and Jeelani, 1994)

- Electrostatic effects and an applied electric field may also promote coalescence (Charles and Mason, 1960a; Allan and Mason, 1961). However, it is also possible that electrical charges create a force of repulsion between droplets and thus coalescence becomes more difficult (Leng and Calabrese, 2004).

- When pH is increased, the coalescence rate decreases, because adsorbed OH^- ions at the interface cause stronger repulsive forces between oil droplets (Leng and Calabrese, 2004).

Physical properties

- A high droplet viscosity inhibits coalescence by making film drainage more difficult, but it may also promote coalescence by increasing resistance to leading surface deformation during impact (Leng and Calabrese, 2004). The coalescence rate decreases when the viscosity of the continuous phase increases (Charles and Mason, 1960a). This means also that the elasticity of the continuous phase increases; the effect of this on the coalescence time becomes significant when the droplet size decreases (Dreher et al., 1999).

- A high interfacial tension between the phases can increase the coalescence rate, because it decreases the drainage film area of the continuous phase. On the other hand, the high interfacial tension also hinders the flow of the continuous phase film, resulting in a decrease of the coalescence rate. Thus the interfacial tension has two opposing effects on the coalescence process and, furthermore, there are also Marangoni[5] phenomena, which have an influence on the coalescence rate. (Ritcey and Ashbrook, 1984; Hartland and Jeelani, 1994; Leng and Calabrese, 2004)

- Temperature has a very strong influence on the coalescence rate, because it controls the physical properties of the dispersed and continuous phases. In general, the coalescence rate increases when temperature increases (Charles and Mason, 1960a). Since temperature defines the physical properties, it also affects the mobility of the interface. Increased mobility decreases the resistance between the droplet and the film, and thus the film drainage rate increases. In general, clean and mobile interfaces promote efficient film drainage and lead to a higher coalescence probability. (Leng and Calabrese, 2004)

Solid matter

- Different kinds of impurities reduce the coalescence rate by immobilizing the droplet-film interface and increasing the surface area of contact, due to lower interfacial tension (Charles and Mason, 1960a), or by increasing electrostatic repulsive forces (Leng and Calabrese, 2004). Furthermore, the coalescence rate depends on the wetting properties of solid impurities. When a solid impurity is wetted by the dispersed phase, the coalescence rate increases and conversely, if one is wetted by the continuous phase, the coalescence rate decreases (Friberg and Yang, 1996).

[5]Marangoni phenomena mean spontaneous interfacial flows, either ordered or disordered type, driven by interfacial tension gradients, which are due to solute concentration, temperature or interfacial electrical potential changes (Perez de Ortiz, 1992; Sawistowski, 1971).

As discussed in the previous chapters, the film thinning and the droplet coalescence are very complicated processes. In general, the coalescence time and the film-thinning rate are the most important parameters for studying the phase separation. However, estimation is very difficult, because the parameters depend on many factors, such as the angle and the velocity of approaching droplets, the collision force (flow-driven or gravity-driven force, attractive van der Waals and repulsive electrostatic forces) pressing on the film, the droplet size, the physical properties of the both phases, interfacial tension gradients, the mobility of the interface and the form of the interface (dimpled, spherical or planar) (Jeelani and Hartland, 1993b; Murdoch and Leng, 1971). Therefore, the coalescence time and the film-thinning rate have been estimated by different approximated expressions and analytical equations in special cases that take into account the previous factors, either separately or partly together (Gillespie and Rideal, 1956; Charles and Mason, 1960a; Chappelear, 1961; Princen, 1963; Tsekov and Ruckenstein, 1994; Murdoch and Leng 1971; Chesters, 1991; Tobin and Ramkrishna, 1999; Jeelani and Hartland, 1993b; Jeelani and Hartland, 1994; Liu and Li, 1999). The most widely used approximation has been the parallel boundaries, which exist on both sides of the thin film. The advantage of this approximation is that equations can be written analytically very easily. However, none of these approximations can take into account droplet interactions due to the dispersion flow patterns.

1.3 Coalescence and sedimentation profiles

When the dispersion is continuously fed into the settler, the thickness of the dispersion band increases with time until the constant steady-state value is reached. On the other hand, this steady-state dispersion thickness (h_{disp}) increases with the specific volume flow rate of the dispersion ($V_{spec} = V_{fr,disp}/A_{hs}$) and it can be usually given by

$$h_{disp} = K\left(\frac{V_{fr,disp}}{A_{hs}}\right)^{y} \tag{1}$$

where K and y are experimentally defined constants, which depend on the dispersion characteristics, liquid system, temperature, phase ratio and mixing conditions (Mizrahi and Barnea, 1973), and $V_{fr,disp}$ is the volume flow rate of the dispersion and A_{hs} is the horizontal surface area of the settler. (Barnea and Mizrahi, 1975d; Jeelani and Hartland, 1985; Jeelani and Hartland, 1993a)

The dispersion disengagement can occur either by the drop-interface coalescence or by the drop-drop coalescence. The former can be further divided into two stages: A primary break and a secondary break. The primary break time is the time required for the two phases to meet at a sharply defined interface. The secondary break time is the time required when the very small droplets of one phase in the other are separated. Generally, the primary break occurs when the mean droplet size is greater than about 150 μm and the secondary break occurs when the mean droplet size is less than 100 μm. (Ritcey and Ashbrook, 1984; Hartland and Jeelani, 1994)

In steady state, droplets undergo the drop-drop coalescence while moving both vertically and horizontally due to sedimentation and bulk flow, and finally coalesce with the bulk homophase at the coalescence front. When the dispersion flows towards the

settler back wall, the thickness of the dispersion band decreases with the length of the settler and it becomes zero or finite in the rear end of the settler. For the stable process operation, the volume rate of the interfacial coalescence has to be equal to the volume flow rate of the dispersed phase to the settler so flooding can be avoided. (Hartland and Jeelani, 1994; Jeelani and Hartland, 1993a)

Figure 5a shows the drop-interface coalescence in which the buoyancy (gravity) holds the droplet at the interface of the continuous and the dispersed phase until the separating continuous phase film drains and finally ruptures, and thus the droplet coalesces with its homophase. The drop-drop coalescence (Figure 5b) is not so well defined because the effect of gravity during sedimentation is smaller than at the active interface, but it depends on the flow-driven collision forces, the droplet size and the volume fraction of the dispersed phase (Jeelani and Hartland, 1986). The picket fences divide the settler into distinct process sections as a point of view of the phase separation. The drop-drop coalescence occurs in the feed end of the settler and between the picket fences; the drop-interface coalescence occurs in the rear end of the settler. Furthermore, droplets coalesce at the solid surfaces of the picket fences.

(a) Drop-interface coalescence

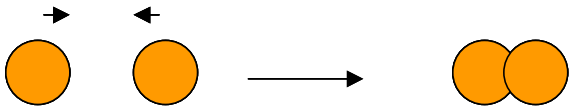

(b) Drop-drop coalescence

Figure 5. Disengagement of organic-water dispersion.

When the phase separation occurs in the settler, the drop-drop coalescence and the drop-interface coalescence take place vertically and horizontally in different locations that depend on the initial type of dispersion (O/A- or A/O-dispersion, the volume fraction of the dispersed phase), the droplet size, the geometry of the settler, the arrangement of the picket fences and the collision force (gravity-driven and/or flow-driven). The places in which the drop-drop and the drop-interface coalescence take place create the dispersion disengagement profile, which can be described by the coalescence and sedimentation profiles, and the dispersion overall flow pattern.

Figure 6a shows the situation where the dispersed oil droplets in water move upwards and form the dense-packed layer. The thickness of this layer increases with time until the steady state is achieved, as shown in Figure 6b. The drop-interface coalescence takes place in the upper part of the settler, and thus the height of the coalescing interface h_c decreases with time. When the droplets are moving upwards (upward sedimentation), the height of the sedimenting interface at the bottom of the

dispersion increases with time. This means that the thickness of the continuous water phase increases. The volume fraction of the dispersed organic phase in the sedimentation zone increases with time. At the same time, the thickness of the sedimentation zone decreases and becomes zero when the bottom of the dense-packed layer meets the sedimenting interface. As the drop-interface coalescence proceeds at the active interface, the thickness of the dense-packed layer decreases and finally disappears or achieves a finite thickness at a time t_f when "complete" phase separation occurs. At time t_i, which marks the end of sedimentation, the thickness of the dense-packed layer reaches a maximum value. The total dispersion thickness is the sum of the thicknesses of the sedimentation and the dense-packed layers. In this case, when the dense-packed and the sedimentation layers occur, the dispersion decay profile is sigmoidal.

However, the dense-packed layer does not form if the sedimentation rate is less than the interfacial coalescence rate. This may occur when droplet sizes are not large enough due to the ineffective drop-drop coalescence (binary coalescence) during the sedimentation and thus the droplets do not have enough time to accumulate to the boundary between the sedimenting and the coalescing interface. In this case, there is no inflection point on the coalescence profile and thus the dispersion decay profile is exponential. A strong turbulence at the feed end of the settler due to the flow of the inlet dispersion may reduce the rate of the sedimentation because droplets flow both vertically and horizontally; this may reduce the thickness of the dense-packed dispersion and the rate of the interfacial coalescence. On the other hand, the turbulence also increases the drop-drop coalescence, and thus the droplet sizes increase and the sedimentation rate increases. (Jeelani and Hartland, 1998; Jeelani et al., 1999; Hartland and Jeelani, 1987)

The volume flow rate of the droplet sedimentation is a function of the droplet size, the volume fraction of the dispersed phase and the flow pattern of the phases. Respectively, the formed flow pattern depends on the kinetic energy of the feed dispersion, the geometry of the inlet port and the arrangement of the picket fences. The volume rate of the interfacial coalescence depends on the droplet size at the coalescing interface and the thickness of the dense-packed zone, which affects the buoyancy (gravitational) force pressing on the draining film above (beneath) the droplets at the coalescing interface. On the other hand, the thickness of the sedimentation zone depends on the volume flow rate of the dispersion, the droplet size, the volume fraction of the dispersed phase and the effectiveness of the binary coalescence. Respectively, the thickness of the dense-packed zone depends on the volume flow rate of the dispersed phase and the droplet size at the coalescing interface. (Hartland and Jeelani, 1994)

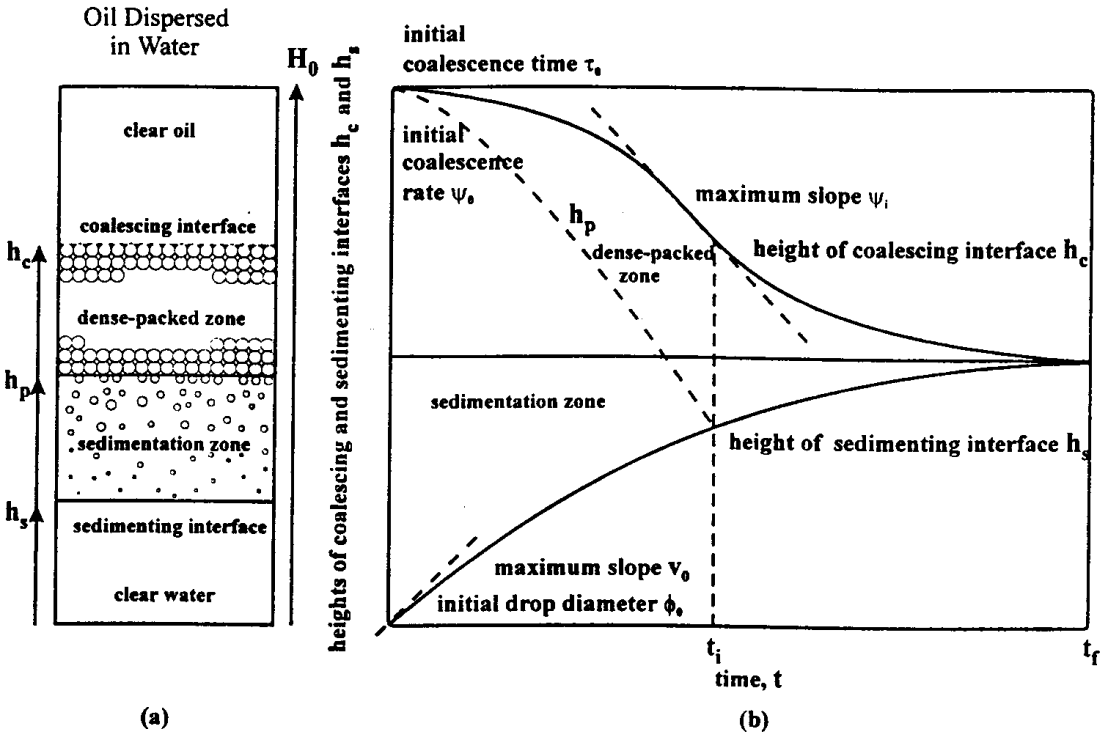

Figure 6. (a) Heights of the sedimenting (h_s) and the coalescing (h_c) interfaces and the dense-packed zone formed at the top of the dispersion due to upward sedimentation of the dispersed lighter oil drops in heavier water. (b) Schematic variation in the heights of sedimenting and coalescing interfaces with time (t) for the dispersion shown in part (a). The variation in the height of the boundary between the sedimentation and the dense-packed zones (h_p) is also shown. All the heights are measured from the bottom. Figures (a) and (b) are from Jeelani and Hartland (1998).

In the continuous process, the profiles do not change so much or not at all with time, but the profiles are different in different locations of the settler. During the start-up, before the process has achieved steady state, the dispersed droplets sediment, break-up and coalesce with time, and thus the continuous phase, the dispersed phase, the sedimentation and the dense-packed layers form. The thicknesses of these layers differ from each other with the length of the settler. Actually, at steady state when the sediment, break-up and coalescence (the drop-drop and the drop-interface coalescence) processes are in balance, the coalescence and the sedimentation profiles are similar to those shown in Figure 6 when these profiles are plotted as a function of the settler length.

1.4 Designing the settler process

The main ideas in the development of the solvent extraction settler processes are to achieve clean phase separation (high interfacial coalescence rate), minimize the loss of the reagents (no entrainments) and decrease the surface area (footprint) of the settlers (Vancas, 1996; Warwick et al., 1970; Pekkala et al., 1999; Lewis, 1979; Mizrahi and Barnea, 1973). All these factors are also important economically, because an ineffective too-large process unit ties up capital, for example, in large reagents inventories or in

construction zones with long pipelines (Warwick and Scuffham, 1972; Hopkins and Lewis, 1990). The common design parameters for the settler are the specific volume flow rate of the dispersion, linear velocities of the aqueous and organic phases, which depend on the thickness of the phase layers, and length-to-width ratios of the settler (Vancas, 2003). On the other hand, there are also other parameters, such as picket fences, discharge launders of the separated phases, roof construction avoiding airborne dust, phase continuity, phase ratio in the feed, temperature and geometry and location of the dispersion feed inlet, affecting the flow pattern in the settler. This affects the sedimentation and coalescence rates, which, in turn, have to be taken into account in designing work (Vancas, 2003). The picket fence geometry, location and arrangement have significant effects on the separation process. The geometry of the picket fence can be appropriate for the separation of the phases, but it also restricts the flow capacity. The fence should not be made too tight due to a possibility of overflow in the first part of the settler when the specific volume flow rate is increased and the pressure drop over the picket fence is too high. All these parameters, together with their mutual interactions, present challenging tasks for engineers when new or existing settler units are designed or modernized and optimized.

In the settler design, the coalescence and the sedimentation profiles describing dispersion behaviour are important, and usually the designing procedure has been based on data obtained from pilot-plant mixer-settlers (Fisher and Notebaart, 1983; Pekkala et al., 1999; Lewis, 1979; Orjans et al., 1979) or from laboratory-scale mixer-settlers (Jeffreys et al., 1967; Jeffreys et al., 1970; Padilla et al., 1996) or from empirically defined mathematical models (Ruiz and Padilla, 1996). However, since the pilot-scale experiments involve a high capital cost and large solvent inventories, and are also time-consuming, the possibility of designing large continuous settlers on the basis of small-scale batch settling tests has been considered. Although, the coalescence and the sedimentation profiles occur in batch and in continuous settlers, the profile data are not directly congruent between the process types. Therefore, different kinds of correlation functions and models have been developed for prediction of the steady-state dispersion thickness either in settlers or in columns (Jeelani and Hartland, 1985; Dalingaros and Hartland, 1986; Jeelani and Hartland, 1986; Hartland and Jeelani, 1987; Dalingaros et al., 1987) and for predicting the shape of the sedimentation and the coalescing profiles with time in a batch settler (Hartland and Jeelani, 1988; Jeelani et al., 1990; Jeelani and Hartland, 1993a; Jeelani and Hartland, 1998; Jeelani et al., 1999). Experimentally defined correlation parameters from unsteady-state batch experiments can be used in equations of the steady-state continuous settler, if the physical properties of the liquid systems, the operating conditions, the specific volume flow rate, the droplet size, the volume fraction of the dispersed phase, the degree of turbulence and the degree of contamination are similar in the batch experiments and the continuous process. Correlation parameters linked to equations of the continuous steady-state settler can be usually solved by, for example, the least squares fit method. When dynamic similarity (geometric and kinematic) exists, it is possible to predict the steady-state dispersion thickness as a function of throughput from unsteady-state dispersion decay data.

Recently, Henschke et al. (2002) have developed a model, which considers droplet sedimentation, balances of the amount of droplets, droplet deformation in the dense-packed zone and drop-drop and drop-interface coalescences. The model includes a coalescence parameter, which takes into account asymmetrical film drainage due to droplet deformation. This model's only parameter has to be adjusted using single

experimental results of a single experiment. Frising et al. (2006) have mentioned that the required experimental setup is not so sensitive for parameter defining than the previous models. In general, the physical experiments have to be carried out carefully, because there may be a possibility of formation of two types of dispersion in the same settler; this has been reported by Nadiv and Semiat (1995).

The problem, which has been encountered in previous models, is that they need physical experiments for defining unknown parameters of the models. In addition, these models cannot take into account detailed velocity profiles of the dispersed and continuous phase, which are due to the settler geometry and phase interactions. The flow patterns are important, because they affect the sedimenting and coalescing profiles, by, for example, decreasing or increasing turbulence and collision forces, and thus increasing or decreasing the coalescence and sedimentation rates. Nowadays, Computational Fluid Dynamics (CFD) modelling can produce a very detailed velocity profile from studied processes.

1.5 Complementary designing and optimizing - CFD

Computational Fluid Dynamics (CFD) modelling has grown rapidly in the last ten years and there have been many articles in chemical engineering journals describing how CFD has become closer to everyday engineering work (Shanley, 2000; Bakker et al., 2001a; Bailey et al., 2001; Bakker et al., 2001b and Shelley, 2004). The reasons for this success are many, but perhaps the most important reason according to Mukhopadhyay et al. (2004) is that the time and cost associated with new product and process development can be decreased when CFD is used to test new design options and reduce the number of physical experiments with pilot equipment.

Although a large literature review with different databases from the field of solvent extraction and CFD was carried out, only two articles (Gigas and Giralico, 2002; Giralico et al., 2003) were found in which CFD was applied to the settler process of solvent extraction. The reasons for the small number of articles are, for example, the mixer-settler process is very complex, especially from the point of view of dispersion hydrodynamics, and commercial CFD software cannot take into account all physical phenomena that occur at the phase interface and affect the phase separation. Furthermore, the geometry of the settler may be very simple, but when that of the picket fence is taken into account, the modelled geometry becomes much more complicated. Also there are two outlets that are used for the organic and aqueous phases. The outlet boundaries of the CFD software are not so well defined in the multiphase modelling.

Nowadays, a single-phase modelling is well known and can be applied very easily to almost any chemical engineering processes. The single-phase calculations are useful when the flow patterns of unit processes are of interest. Gigas and Giralico (2002), Giralico et al. (2003), Kankaanpää (1999), Kankaanpää et al. (2001) and Hirsi (2004) have applied the single-phase calculations to study the geometry of settlers and picket fences. Kankaanpää (1999) studied the possibilities of modelling fluid flow patterns in the settler. The simulated results varied to some extent from those of the water model at the inlet end of the settler, but, at the outlet end, the flow patterns agreed well. The results proved that CFD is quite a reliable tool to model the flow patterns of settlers when a fine grid is used. Hirsi (2004) also reported similar good results when he

optimized the vertical locations of the picket fence pairs in the Compact Mixer-Settler. That work was carried out as a part of the research for this thesis and supervised by the author. Kankaanpää et al. (2001) reported that the pressure drop over the picket fence could be defined by using the CFD, when a maximum of 5 % inaccuracy was allowed. They also mentioned that a CFD-method working with this accuracy was preferable when compared with experimental methods in optimizing the geometry of the picket fence.

When computing resources have increased, multiphase modelling has been applied more and more to industrial applications. Multiphase modelling is needed when different kinds of process equipment concepts with real fluids are studied in the real atmosphere. In general, this modelling is performed with two phases, one of which is the continuous phase and the other is the dispersed. The most common two-phase methods are the Eulerian-Eulerian and Lagrangian methods. In the Eulerian-Eulerian model, one solution field is defined for each phase separately and transport equations interact via inter-phase transfer terms (Oliveira and Issa, 2003). Respectively, in the Lagrangian model, the solution field is only defined for the continuous phase in which a number of droplet trajectories are simulated and the mean values obtained from statistical calculations characterize the droplet performance (Xia et al., 2004; Xia et al., 2005). In the real situation, the dispersion does not only contain one droplet size. A droplet size distribution would be possible to take into account whether the droplet sizes were divided into several size groups and whether each of these groups was treated as a separate phase in a multiphase flow calculation. However, in this case, the calculation times would be very high due to the large number of equations. On the other hand, population balance modelling gives a very good opportunity to handle the dispersed phase and its droplet size distribution (Ramkrishna and Mahoney, 2002). Furthermore, during the last few years, the population balance method has been also incorporated into CFD simulation techniques.

Leng and Calabrese (2004) have described population balances as a set of mathematical tools that enable one either to predict the time evolution of the droplet size distribution or to determine specific information, such as breakage frequency and daughter droplets size distribution, or collision frequency and coalescence efficiency, from an analysis of time-variant droplet size. Actually, there is the question of "counting the number of droplets". The counting can be carried out either by the Eulerian or Lagrangian method. The former assumes that the dispersion properties are uniform throughout the calculation domain, so all droplets are assumed to have similar properties or these properties are assumed to change in same way. The latter assumes that the calculation domain is non-homogeneous regarding the dispersion properties. Droplets are studied in internal and/or external coordinates. The internal coordinates define characteristics of the droplets, such as diameter. The external coordinates denote the location of the droplets in physical space. The general population balance equation can be given by

$$\frac{\partial}{\partial t}\left(n_i\right) = \nabla_r\left(\boldsymbol{R}n_i\right) + \nabla_x\left(\boldsymbol{X}n_i\right) + S \qquad (2)$$

where n_i is the droplet number density, $\boldsymbol{X}n_i$ is the droplet flux through internal coordinate space and it represents the convection term for properties of the droplet, $\boldsymbol{R}n_i$

is the droplet flux through external coordinate space and S is the net rate of generation of droplets.

The left side term represents the accumulation rate of droplets in a volume, the first term on the right side represents change in the convective motion of droplets (input - output flow) relative to the external coordinate of the volume; the last two terms represent the net generation rate of particles. The term S takes into account the coalescence of smaller droplets to larger ones and, respectively, the break-up of larger droplets to smaller ones. These are obtained by special death- and birth-rate functions, which both are connected to coalescence and break-up processes in the following way:

$$S = B_B - D_B + B_C - D_C \tag{3}$$

where B_B is the birth rate due to break-up, B_C is the birth rate due to coalescence, D_B is the death rate due to break-up and D_C is the death rate due to coalescence. (Coulaloglou and Tavlarides, 1977; Ramkrishna, 2000; Herbst, 1979)

These days, commercial CFD software includes many physical models, which cover the most important chemical engineering processes. However, the use of these models is not so simple in every application. Jakobsen et al. (2005) have proposed that multiphase flow simulations need more studies, especially in the high volume fraction of dispersed phases, because the current models have many limitations that restrict their reliable application in engineering cases. They have mentioned that the multiphase flow simulations are numerically unstable considering both 2D and 3D models because of the applications of low-accuracy discretizations, “large” density differences between the phases, ill-conditioned implementations of interfacial closures in the limit of zero volume fractions, and large gradients or discontinuities in the flow fields that can occur in these flow systems. Due to these difficulties, they have further proposed that proper convergence criteria and improved boundary conditions should be formulated.

1.6 Scope of the thesis

The aim of this thesis was to develop a CFD procedure, which can be used as an additional or complementary method for traditional physical experiments in studying dispersion behaviour and flow patterns, and designing/selecting picket fence arrangements in the solvent extraction settler process. These requirements meant that it was necessary to develop a new CFD calculation procedure due to complicated process phenomenon, high volume fractions of the separated phases and numerical convergence difficulties, which were reported by Giralico et al. (2003). Furthermore, according to QNET-CFD seminar that was held in Brussels in 2004, different kinds of instability or convergence difficulties are quite a common in multiphase calculations and they need special methods that can be used to improve the quality of industrial applications of CFD and raise the level of trust that can be placed in industrial CFD simulations (QNET, 2004).

The CFD procedure was applied to organic-aqueous dispersion in the copper solvent extraction settler. The copper process fluids and the formed dispersion are so dark that the flow patterns and the dispersion disengagement phenomenon are almost impossible

to see. If these are known better with the aid of CFD, settlers can be designed more easily, cheaply and quickly, and thus some physical experiments in a laboratory or pilot scale can be avoided. In the metallurgical solvent extraction industry, the main targets are to decrease the size of settlers and the solvent inventories without decreasing process capacity. Similar trends and targets are also met in the petroleum industry, especially on offshore platforms, where gravity separators have been studied experimentally and numerically (Arntzen and Andresen, 2001; Simmons et al., 2004; Simmons et al. 2002; Wilkinson and Waldie 1994).

2 GOVERNING EQUATIONS

The Eulerian-Eulerian multiphase model was selected for use because it gives better opportunities to study phase interactions and phase separation than the Lagrangian method. The reason is that the Eulerian-Eulerian model is appropriate to cases where the volume fraction of the dispersed phase is high and varies widely, which is actually the situation in the settler. The Lagrangian model can be used when the range of the volume fraction of the dispersed phase is narrow and low. Furthermore, the droplet coalescence and the break-up models have been implemented in the Eulerian-Eulerian model of the commercial CFX-4.4 software. The continuity and momentum equations are written for the continuous phase *c* and the dispersed phase *d*. The continuity equation expresses the idea of mass conservation within the control volume of interest. The momentum equation is an expression of momentum conservation. The energy equation is not shown here because heat transfer does not take place in the settler. The other flow assumptions are isothermal, incompressible and turbulent, and the values of density and viscosity of the phases are assumed constant.

2.1 Continuity equation

The continuity equation for an incompressible continuous phase, when density is a constant value can be written as Versteeg and Malalasekera (1995), Fox and McDonald (1985) and White (1991):

$$\rho_c \left[\frac{\partial \alpha_c}{\partial t} + \nabla \cdot \left(\alpha_c \boldsymbol{U}_c \right) \right] = 0 \tag{4}$$

where ρ_c is the density of the continuous phase, α_c is the volume fraction of the continuous phase, t is time and $\boldsymbol{U}$ is the velocity vector. The velocity vector is only given in two directions because the settler model is two dimensional, $\boldsymbol{U} = \bar{u} + \bar{v}$. $\bar{u}$ is the horizontal (x-direction) velocity component and $\bar{v}$ is the vertical (y-direction) velocity component. The sum of the volume fraction of the phases is equal to one, ($\alpha_c + \alpha_d = 1$).

Respectively, the continuity equation for the dispersed phase can be given by

$$\rho_d \left[\frac{\partial \alpha_d}{\partial t} + \nabla \cdot \left(\alpha_d \boldsymbol{U}_d \right) \right] = 0 \tag{5}$$

2.2 Momentum equation

There are two different types of forces that affect fluid parcels; namely surface forces and body forces. Since the momentum equation is only written on the droplet level, the short-range and long-range forces are ignored from the body forces. The surface forces include pressure forces and viscous forces due to surface stresses and fluid motion. The surface forces are accounted explicitly in the momentum equation and

the body forces are taken into account with source term ($\boldsymbol{S_M}$). The momentum equation for the continuous phase can be written as Versteeg and Malalasekera (1995), Fox and McDonald (1985), White (1991) and Soo (1990):

$$\rho_c\left[\frac{\partial(\alpha_c \boldsymbol{U}_c)}{\partial t}+\nabla\cdot(\alpha_c \boldsymbol{U}_c \boldsymbol{U}_c)\right]=-\alpha_c\nabla p+\mu_c\nabla^2(\alpha_c \boldsymbol{U}_c)+\boldsymbol{S}_{M,c} \tag{6}$$

and for the dispersed phase:

$$\rho_d\left[\frac{\partial(\alpha_d \boldsymbol{U}_d)}{\partial t}+\nabla\cdot(\alpha_d \boldsymbol{U}_d \boldsymbol{U}_d)\right]=-\alpha_d\nabla p+\mu_d\nabla^2(\alpha_d \boldsymbol{U}_d)+\boldsymbol{S}_{M,d} \tag{7}$$

where μ is the dynamic viscosity and p is the pressure. The term on the left side is a convection term and the first term on the right side is a pressure term, the second is a viscous term and the last is the source term.

2.3 Body forces

In the solvent extraction settler, the body forces due to the buoyancy force, the inter-phase drag force, the turbulent dispersion force and the lift force are taken into account. The body forces are readily available when having solved the volume fractions of the continuous and dispersed phase, for example, as described in Chapter 2.5.

2.3.1 Buoyancy force

The buoyancy force ($\boldsymbol{F}^{buo}$) due to the density difference of the continuous and dispersed phase can be presented in following way (CFX-4.4 Solver Manual):

$$\boldsymbol{F}^{buo}=(\rho-\rho_0)\boldsymbol{g} \tag{8}$$

where ρ_0 is a reference density and $\boldsymbol{g}$ is the acceleration of gravity vector. The buoyancy force for the continuous phase is zero ($\boldsymbol{F}_c^{buo}$ = 0) because the density of the continuous phase is the buoyancy reference density. But, for the dispersed phase, the buoyancy force is given by

$$\boldsymbol{F}_d^{buo}=\alpha_d(\rho_d-\rho_c)\boldsymbol{g} \tag{9}$$

2.3.2 Drag force

The drag force ($\boldsymbol{F}^{drag}$) exerted on a dispersed droplet by the moving continuous phase arises from two mechanisms. Skin friction due to the viscous surface shear stress and form drag due to the pressure distribution around the droplet. The drag force between the continuous phase and the dispersed phase can be written as Soo (1990):

$$\boldsymbol{F}^{drag} = \frac{1}{2}\rho|\boldsymbol{U}_{rel}|\boldsymbol{U}_{rel}A_pC_D \tag{10}$$

where $\boldsymbol{U}_{rel}$ is the relative velocity between the phases, A_p is the projected area of the droplet in the direction of fluid flow and C_D is a drag coefficient that, in general, is defined by experimental measurements of special phenomenon. The drag coefficient depends on the droplet diameter, the flow regime and the Reynolds number, which is given by

$$Re = \frac{\rho_c \boldsymbol{U}_{rel} d_{d,s}}{\mu_c} \tag{11}$$

where $d_{d,s}$ is the single droplet diameter or the Sauter mean diameter. The selection of the proper drag coefficient is discussed and given later in two-phase calculations. When all droplets in a unit volume are taken into account, and droplets are assumed to be of a spherical shape, the total drag per unit volume on the dispersed phase is (CFX-4.4 Solver Manual):

$$\boldsymbol{F}_d^{drag} = \frac{3}{4}\frac{C_D}{d_{d,s}}\alpha_d\rho_c|\boldsymbol{U}_c - \boldsymbol{U}_d|(\boldsymbol{U}_c - \boldsymbol{U}_d) \tag{12}$$

Respectively, the total drag per unit volume on the continuous phase is

$$\boldsymbol{F}_c^{drag} = -\boldsymbol{F}_d^{drag} \tag{13}$$

2.3.3 Lift force

In the dispersion flow, the pressure distribution on the upper and lower surfaces of the droplets fluctuates and affects the flow pattern of the moving and the circulating droplets. This pressure alternation is due to the presence of a mean velocity gradient in the fluid. The force, which comes into being during this phenomenon, is called the lift force ($\boldsymbol{F}^{lift}$). Depending on the pressure gradient and the flow situation (the droplet can move against the flow of the continuous phase, or the droplet can move in the same direction as the continuous phase, or the droplet can be stagnant), the lift force can act up or down.

The lift force, which depends on the relative velocity and the curl of the continuous phase, is given as the force per unit volume of the phase. It can be written for the dispersed phase in the following way (Drew and Lahey, 1987; CFX-4.4 Solver Manual):

$$\boldsymbol{F}_d^{lift} = \alpha_d\rho_c C_L(\boldsymbol{U}_c - \boldsymbol{U}_d)\times\nabla\boldsymbol{U}_c \tag{14}$$

where C_L is the lift coefficient. The lift force on the continuous phase is equal but opposite in sign.

$$\boldsymbol{F}_c^{lift} = -\boldsymbol{F}_d^{lift} \tag{15}$$

2.3.4 Turbulent dispersion force

The droplets are dispersed due to turbulent flow. This interaction can be taken into account by the turbulent dispersion force ($\boldsymbol{F}^{td}$), which depends on the amount of momentum in turbulent fluctuations in the continuous phase and the gradient of the volume fraction of the continuous phase. The turbulent dispersion force can be written for the continuous phase in the following way (CFX-4.4 Solver Manual):

$$\boldsymbol{F}_c^{td} = -C_{TD}\rho_c k_c \nabla \alpha_c \tag{16}$$

where C_{TD} is the turbulent dispersion coefficient and k_c is the turbulent kinetic energy of the continuous phase. For the dispersed phase, this force is equal but opposite in sign.

$$\boldsymbol{F}_d^{td} = -\boldsymbol{F}_c^{td} \tag{17}$$

2.4 Turbulence model

Because turbulence was not the research target, it was decided to use the standard k-ε turbulence model (Launder and Spalding, 1974), which is the most used model in engineering applications (Pope, 2003; Versteeg and Malalasekera, 1995). When effective viscosity is considered as the sum of molecular and turbulent (Equation (20)) viscosities and substituted into Equations (6) and (7), the total Navier-Stokes equations for the continuous and the dispersed phases are obtained:

$$\rho_c\left[\frac{\partial(\alpha_c \boldsymbol{U}_c)}{\partial t} + \nabla\cdot(\alpha_c \boldsymbol{U}_c \boldsymbol{U}_c)\right] = -\alpha_c \nabla p + (\mu_c + \mu_t)\nabla^2(\alpha_c \boldsymbol{U}_c) + \boldsymbol{F}_c^{buo} + \boldsymbol{F}_c^{drag} + \boldsymbol{F}_c^{lift} + \boldsymbol{F}_c^{td} \tag{18}$$

$$\rho_d\left[\frac{\partial(\alpha_d \boldsymbol{U}_d)}{\partial t} + \nabla\cdot(\alpha_d \boldsymbol{U}_d \boldsymbol{U}_d)\right] = -\alpha_d \nabla p + (\mu_d + \mu_t)\nabla^2(\alpha_d \boldsymbol{U}_d) + \boldsymbol{F}_d^{buo} + \boldsymbol{F}_d^{drag} + \boldsymbol{F}_d^{lift} + \boldsymbol{F}_d^{td} \tag{19}$$

where $\boldsymbol{U}_c$ and $\boldsymbol{U}_d$ are the control volume averaged vectorial velocities when turbulence is taken into account. In the k-ε turbulence model, the turbulent viscosity (μ_t) depends on the turbulent kinetic energy (k) and the turbulent dissipation rate (ε).

The turbulent viscosity can be given by:

$$\mu_t = \rho C_\mu \frac{k^2}{\varepsilon} \tag{20}$$

The transport equations for k and ε can be written for both phases as follows (Versteeg and Malalasekera, 1995):

$$\rho\left[\frac{\partial(\alpha k)}{\partial t}+u\frac{\partial(\alpha k)}{\partial x}+v\frac{\partial(\alpha k)}{\partial y}\right]$$

$$=\nabla\left[\alpha\left(\mu+\frac{\mu_t}{\delta_k}\right)\nabla k\right]+2\alpha\mu_t E_{ij}E_{ij}-\alpha\rho\varepsilon \tag{21}$$

$$\rho\left[\frac{\partial(\alpha\varepsilon)}{\partial t}+u\frac{\partial(\alpha\varepsilon)}{\partial x}+v\frac{\partial(\alpha\varepsilon)}{\partial y}\right]$$

$$=\nabla\left[\alpha\left(\mu+\frac{\mu_t}{\delta_\varepsilon}\right)\nabla\varepsilon\right]+C_{1\varepsilon}\frac{\varepsilon}{k}2\alpha\mu_t E_{ij}E_{ij}-C_{2\varepsilon}\alpha\rho\frac{\varepsilon^2}{k} \tag{22}$$

The mean rate of strain tensor E_{ij} is

$$E_{ij}=\frac{1}{2}\left(\frac{\partial u_i}{\partial x_j}+\frac{\partial u_j}{\partial x_i}\right) \tag{23}$$

The model coefficients used were the default values of the CFX-4.4, which are as follows: $C_\mu = 0.090$; $C_{1\varepsilon} = 1.440$; $C_{2\varepsilon} = 1.920$; $\delta_k = 1.0$ and $\delta_\varepsilon = 1.22$ (CFX-4.4 Solver Manual). The buoyancy effect was not taken into account in the turbulence model, because the flow in the settler is mostly horizontal and, especially in the front end of the settler, where is the strongest turbulence.

2.5 Multiple-Size-Group Model (MUSIG)

In this work, MUSIG, developed by Lo (1996), was used. The model has been incorporated into CFX 4.4 software and can handle dispersed multiphase flows in which the dispersed phase has a large variation in size. MUSIG provides a framework in which the population balance method together with the break-up (Luo and Svendsen, 1996) and coalescence (Prince and Blanch, 1990) models are incorporated into three-dimensional CFD calculations. Although the break-up and the coalescence models are developed basically for bubbles, these can also be applied to droplets, therefore the name “droplet” is used in the following definitions. MUSIG assumes that all droplets move at the same velocity, and these velocities are related to the average value algebraically, thus only one set of momentum equations for all the droplets has to be solved. The advantage of MUSIG is that it offers an opportunity to consider a larger number of droplet size groups to give a better representation of the size distribution, and only one velocity field for the continuous phase and one for the dispersed phase have to

be solved. In the following, the MUSIG calculation procedure is described as it is defined in the CFX-4.4 Solver manual.

The MUSIG model is carried out with an Eulerian-Eulerian two-phase model and assumes similar properties for all droplets. When the internal coordinates of the general population balance Equation (2) are ignored, droplet number density is related to the volume fraction of droplet MUSIG-size group-*i* and the droplet sizes change only by the break-up and coalescence process; the continuity equation for one MUSIG-size group-*i* can be written as

$$\rho_d \left[\frac{\partial \alpha_{d,i}}{\partial t} + \nabla \cdot \left(\alpha_{d,i} \boldsymbol{U}_d \right) \right] = S_i \tag{24}$$

where S_i is the source term of the rate of mass transfer into the MUSIG-size group due to the break-up and coalescence process. Equation (24) can be applied to all MUSIG-size groups because the sum of all droplet volume fractions equals the volume fraction of the dispersed phase.

$$\sum_i \alpha_{d,i} = \alpha_d \tag{25}$$

The individual volume fraction of MUSIG-size-group-*i* can be written as

$$\alpha_{d,i} = \alpha_d f_i \tag{26}$$

where f_i is the fraction of the dispersed phase volume fraction in MUSIG-size group-*i*.

Now, when Equation (26) is substituted into Equation (24), the continuity equation for the MUSIG-size group-*i* is yielded:

$$\rho_d \left[\frac{\partial \left(\alpha_d f_i \right)}{\partial t} + \nabla \cdot \left(\alpha_d f_i \boldsymbol{U}_d \right) \right] = S_i \tag{27}$$

The source term S_i can be calculated from the population balance Equation (29) when the product of the droplet number density of MUSIG-size group-*i* (n_i) and the droplet volume of MUSIG-size group-*i* (v_i) are related to the volume fraction of MUSIG-size group-*i* by:

$$n_i v_i = \alpha_d f_i \tag{28}$$

In this way, the normal population balance equation can be related to the continuity equation of the dispersed phase. Equation (29) becomes identical to Equation (27) when the dispersed phase density multiplies both sides.

$$\frac{\partial}{\partial t}\left(n_i \right) + \nabla \cdot \left(\boldsymbol{U}_d n_i \right) = \frac{\partial}{\partial t}\left(\alpha_d f_i \right) + \nabla \cdot \left(\boldsymbol{U}_d \alpha_d f_i \right) = S_i^{'} = B_B - D_B + B_C - D_C \tag{29}$$

The birth rate of the MUSIG-size group-*i* droplets due to break-up of larger droplets can be given by:

$$B_B = \sum_{j=i+1}^{N} g\left(v_j : v_i\right) n_j \tag{30}$$

where N is the total number of MUSIG-size groups and the function of g is the specific droplet break-up rate. The death rate of the MUSIG-size group-*i* droplets due to break-up to smaller droplets can be given by:

$$D_B = g_i n_i \tag{31}$$

The birth rate of the MUSIG-size group-*i* droplets due to coalescence of group-*j* and group-*k* droplets can be given by

$$B_C = \frac{1}{2} \sum_{j=1}^{i} \sum_{k=1}^{i} Q_{jk} n_j n_k \tag{32}$$

where the function of Q is the specific droplet coalescence rate. The death rate of the MUSIG-size group-*i* droplets due to coalescence with other droplets can be given by

$$D_C = n_i \sum_{j=1}^{N} Q_{ij} n_j \tag{33}$$

During the normal iteration, additional transport Equations (27) are solved for the scalar variable f_i. After that, the size distribution of the dispersed phase can be defined from the solution of f_i and the Sauter mean diameter (d_s), which is used in computing the drag force between the continuous phase and dispersed phase and also momentum equations, can be calculated from:

$$d_s = \frac{1}{\sum_i \frac{f_i}{d_i}} \tag{34}$$

where d_i is the droplet diameter of the MUSIG-size group-*i*.

2.5.1 Droplet break-up model (Luo and Svendsen, 1996)

Luo and Svendsen (1996) assumed in their break-up model based on turbulence that turbulence is isotropic and took into consideration the binary breakage of the droplet. Thus, droplets break into two different sized droplets, although Chatzi and Lee (1987) have proposed that it is more realistic to assume that the average number of the daughter droplets is larger than two. The droplet breakage is caused by turbulent eddies, which bombard the surface of the droplet. The break-up is determined by the probability function, which is based on the energy level of the arriving eddy. The droplet break-up

is only possible when the length scale of eddies is equal to, or smaller than, the diameter of the droplet. The eddies that fulfil this criterion also have to have the kinetic energy that exceeds the increase in surface energy required for breakage. The surface energy of the droplet increases because the surface area of the droplet increases due to deformation. If eddies are too large, they merely convect droplets without breakage. It is also possible that smaller eddies do not have sufficient energy to break-up droplets, and thus they may only deform the shape of the droplets. This occurs typically in more settled conditions where eddies of ever-increasing size have lost their kinetic energy and have become dominated by viscous forces. The break-up rate of droplets of volume v_j (size d_j) into droplets of volume v_i (size d_i) can be given by

$$\Omega_B(v_j : v_i) = \int_{\lambda_{\min}}^{d} P_B(v_j : v_i, \lambda)\omega_{B,\lambda}(v_j)d\lambda \tag{35}$$

where $\omega_{B,\lambda}$ is the arrival frequency of eddies (collision density of eddies) of size between λ and $\lambda+d\lambda$ onto droplets of volume v_j (size d_j), $P_B(v_j:v_i, \lambda)$ is the probability for a droplet of volume v_j (size d_j) to break into two droplets, one with volume $v_i = v_j f_{BV}$. When the droplet is hit by an arriving eddy of size λ, λ_{min} is the minimum eddy size, which has the energy required for droplet break-up. f_{BV} is the breakage volume fraction and is a stochastic variable. In the binary break-up, it can be defined as

$$f_{BV} = \frac{v_i}{v_j} = \frac{d_i^3}{d_j^3} = \frac{d_i^3}{d_i^3 + d_h^3} \tag{36}$$

where v_i and v_j are volumes of the daughter droplet and the parent droplet in the binary break-up, respectively. d_i and d_h are diameters of the daughter droplets of the parent droplet with diameter d_j. The specific droplet break-up rate is obtained when the break-up model is calibrated by coefficient f_B and when Equation (35) is rewritten per the number of droplets (n):

$$g(v_j : v_i) = f_B\Omega_B(v_j : v_i)\frac{1}{n} \tag{37}$$

Luo and Svendsen (1996) defined the collision frequency of eddies of a size between λ and $\lambda+d\lambda$ with droplets of size d in the inertial sub-range of isotropic turbulence. It can be written for the droplet d_j by

$$\omega_{B,\lambda}(d_j) = \omega_{B,\xi}(\xi) = 0.923 \cdot n(1-\alpha_d)(\varepsilon d_j)^{1/3}\frac{(1+\xi)^2}{d_j^2\xi^{11/3}} \tag{38}$$

where ξ is the dimensionless size ratio of an eddy and droplet ($\xi = \lambda/d_j$).

The breakage probability of the droplet, which is equal to the probability of the arriving eddy of size λ having a kinetic energy greater than, or equal to, the minimum energy required for the break-up, can be given by

$$P_B(v_j : v_i, \lambda) = e^{-X_c} = \exp\left(\frac{\bar{e}_i(d_j)}{\bar{e}(\lambda)}\right) = \exp\left(-\frac{12\left(f_{BV}^{2/3} + (1-f_{BV})^{2/3} - 1\right)\sigma}{\beta\rho_c\varepsilon^{2/3}d_j^{5/3}\xi^{11/3}}\right) \tag{39}$$

where χ_c is the critical dimensionless energy for break-up, $\bar{e}_i(d_j)$ is the increase in surface energy, when a droplet of size d_j breaks into two droplets, $\bar{e}(\lambda)$ is the mean kinetic energy of an eddy with size λ and β is the empirical parameter from turbulence theory and, in this model, it is the constant parameter of value 2.0. Now Equation (37) can be rewritten when Equations (35), (38) and (39) are substituted.

$$g\left(v_j : v_i\right) = f_B \cdot 0.923\left(1-\alpha_d\right)\left(\frac{\varepsilon}{d_j^2}\right)^{\frac{1}{3}} \int_{\xi_{\min}}^{1} \frac{(1+\xi)^2}{\xi^{\frac{11}{3}}} e^{-\chi_c} d\xi \tag{40}$$

ξ_{min} is the dimensionless minimum size of eddies in the inertial sub-range of isotropic turbulence and is defined by $\xi_{min} = \lambda_{min}/d_j$. In the MUSIG model, the selected minimum size of eddy λ_{min} is 11.4η, which has been given by Tennekes and Lumley (1974). Thus, $\xi_{min} = \lambda_{min}/d_j = 11.4\eta/d_j$, in which η is the Kolmogorov length scale (i.e. the smallest eddy size that turbulence can sustain before all fluctuations are dumped by viscosity), which can be given by (Pope, 2003)

$$\eta = \left(\frac{\mu_c^3}{\rho_c^3 \cdot \varepsilon}\right)^{1/4} \tag{41}$$

2.5.2 Droplet coalescence model (Prince and Blanch, 1990)

The implemented coalescence model only includes the turbulence collision mechanism between two droplets; the turbulence is assumed to be isotropic and droplet sizes lie in the inertial sub-range. Buoyancy-driven collision and laminar shear collision rates are ignored. Actually, ignoring the buoyancy-driven collision due to the difference in rise velocities of droplets of different size is acceptable, because the MUSIG model assumes that all the droplets have the same velocity (Prince and Blanch, 1990; Jakobsen et al., 2005). However, the buoyancy force is taken into account when it controls the phase separation by density difference of the dispersed and continuous phase via the body forces. Prince and Blanch (1990) considered that the coalescence of two droplets takes place in three steps: firstly, droplets collide, trapping a small amount of continuous phase between them (compare Figure 4). Secondly, this liquid film drains until it reaches a critical thickness. And finally, at this point, the film ruptures and droplets coalesce.

The coalescence rate (Γ_{ij}) due to the turbulence collision mechanism can be given by

$$\Gamma_{ij} = \theta_{ij}^T \lambda_{ij} \tag{42}$$

where θ_{ij}^{T} is the collision rate due to turbulent velocity fluctuation of the continuous phase and λ_{ij} is the coalescence efficiency. Prince and Blanch (1990) assumed that the fluctuating turbulent velocity, which causes the droplet collisions, is in the inertial sub-range of isotropic turbulence. Thus they presented the collision rate, which can be written by

$$\theta_{ij}^{T} = \frac{1.4\pi}{16}\left(d_i + d_j\right)^2 \varepsilon_c^{1/3}\left(d_i^{2/3} + d_j^{2/3}\right)^{1/2} n_i n_j \tag{43}$$

where ε_c is the energy dissipation rate of the continuous phase. This turbulent collision rate equation is quite similar to the equation for liquid-liquid systems developed by Coulaloglou and Tavalarides (1977). Both of these are based on the turbulent energy dissipation rate of the continuous phase.

After the modelling cases, an error in the CFX Fortran code of Equation (43) was noticed. The code calculates the collision cross-sectional area of the droplet with the diameter instead of the radius. Therefore, the collision rate is four times higher than in reality and Equation (43) is in the CFX Fortran code:

$$\theta_{ij}^{T} = \frac{1.4\pi}{4}\left(d_i + d_j\right)^2 \varepsilon_c^{1/3}\left(d_i^{2/3} + d_j^{2/3}\right)^{1/2} n_i n_j \tag{44}$$

However, this is not so serious, because the coalescence model includes the coalescence calibration coefficient, which is used to optimize the coalescence rate.

The probability that the drainage of the continuous phase film will occur is called the coalescence efficiency (λ_{ij}), and is defined as the probability of coalescence per collision. Coulaloglou and Tavalarides (1977) proposed that the coalescence efficiency can be calculated by Equation (45), which compares the time to reach the critical film thickness (the coalescence time, t_{ij}) with the available contact time (τ_{ij}) determined by the external turbulent flow field.

$$\lambda_{ij} = e^{-\frac{t_{ij}}{\tau_{ij}}} \tag{45}$$

Prince and Blanch (1990) presented the coalescence time:

$$t_{ij} = \left(\frac{r_{ij}^3 \rho_c}{16\sigma}\right)^{1/2} \ln\frac{h_0}{h_f} \tag{46}$$

where h_0 and h_f are the initial film thickness and the critical film thickness, respectively. r_{ij} is the equivalent radius of the droplet and is given by Chesters and Hofman (1982) as:

$$r_{ij} = 2 \cdot \left(\frac{1}{r_i} + \frac{1}{r_j}\right)^{-1} = \frac{d_i d_j}{\left(d_j + d_i\right)} \tag{47}$$

Equation (46) shows that the coalescence time decreases when the interfacial tension increases.

After modelling cases, another error was noticed in CFX. The equivalent radius, which was presented in the paper of Prince and Blanch (1990), was written incorrectly. Therefore, the same error was also in the CFX Fortran code. The code calculates the equivalent radius with Equation (48), which means that the equivalent radius is four times smaller than it is in Equation (47). Fortunately, this error does not affect the final results, because the coalescence rate is optimized by the coalescence calibration coefficient.

$$r_{ij} = \frac{1}{2}\left(\frac{1}{r_i} + \frac{1}{r_j}\right)^{-1} = \frac{1}{4}\left(\frac{d_i d_j}{(d_j + d_i)}\right) \tag{48}$$

The contact time of two droplets can be estimated from the turbulence intensity, when the contact time is assumed to be proportional to the characteristic period of velocity fluctuation of an eddy in the inertial sub-range region (Levich, 1962; Coulaloglou and Tavalarides, 1977; Prince and Blanch, 1990; Pope, 2003). Thus, the contact time can be presented by

$$\tau_{ij} = \frac{r_{ij}^{2/3}}{\varepsilon^{1/3}} \tag{49}$$

Since the MUSIG model has the calibration coefficient f_C for the coalescence process, the specific coalescence rate per number of droplets n_i and n_j can be given by

$$Q_{ij} = f_C \Gamma_{ij} \frac{1}{n_i}\frac{1}{n_j} = f_C \theta_{ij}^T \lambda_{ij} \frac{1}{n_i}\frac{1}{n_j} \tag{50}$$

2.6 Porous media

Because calculation resources were not sufficient to model the settler and the picket fence or fences together, an equivalent porous media was invented, and used to replace the geometry of the picket fence. This new idea gave an opportunity to model both units at the same time. The porous media model of CFX-4.4 (CFX-4.4 Solver manual) is defined by Darcy's law, which is explained by, for example, Greenkorn (1983). However, the model implemented in CFX has been simplified. It does not take into account the pore structure, which depends on permeability, tortuosity and connectivity. In the porous media model, porosity γ is the ratio of the volume V' available to flow in an infinitesimal control cell surrounding the point, and the physical volume V of the cell.

$$V' = \gamma V \tag{51}$$

The vector area available to flow ***A'*** through an infinitesimal plane control surface of vector area ***A*** is given by:

$$\boldsymbol{A'} = \boldsymbol{KA} \tag{52}$$

where $\boldsymbol{K} = (K^{ij})$ is the symmetric second rank tensor, called the area porosity tensor. K^{ij} is assumed to be isotropic and it can be written by

$$K^{ij} = \gamma \delta^{ij} \tag{53}$$

where δ^{ij} is the delta function and is equal to one in the porous media and zero elsewhere. In those grid cells where this porous media is taken into account, the continuity and the momentum equations for the continuous and the dispersed phase have to be rewritten to take the reduced cross-sectional area experienced by the flow into account. The transport equations of k and ε do not change and they are similar to cases without the porous media.

The continuity equation for the continuous phase in the porous media:

$$\rho_c \left[\gamma \frac{\partial \alpha_c}{\partial t} + \nabla \cdot \left(\alpha_c \boldsymbol{K} \boldsymbol{U}_c \right) \right] = 0 \tag{54}$$

The momentum equation for the continuous phase in the porous media:

$$\rho_c \left[\gamma \frac{\partial \left(\alpha_c \boldsymbol{U}_c \right)}{\partial t} + \nabla \cdot \left(\alpha_c \boldsymbol{K} \boldsymbol{U}_c \boldsymbol{U}_c \right) \right]$$

$$= -\alpha_c \gamma \nabla p + \left(\mu_c + \mu_t \right) \nabla^2 \left(\alpha_c \boldsymbol{K} \boldsymbol{U}_c \right) + \boldsymbol{F}_c^{buo} + \boldsymbol{F}_c^{drag} + \boldsymbol{F}_c^{lift} + \boldsymbol{F}_c^{td} \tag{55}$$

The continuity equation for the dispersed phase in the porous media:

$$\rho_d \left[\gamma \frac{\partial \left(\alpha_d f_i \right)}{\partial t} + \nabla \cdot \left(\alpha_d f_i \boldsymbol{K} \boldsymbol{U}_d \right) \right] = S_i \tag{56}$$

The momentum equation for the dispersed phase in the porous media:

$$\rho_d \left[\gamma \frac{\partial \left(\alpha_d \boldsymbol{U}_d \right)}{\partial t} + \nabla \cdot \left(\alpha_d \boldsymbol{K} \boldsymbol{U}_d \boldsymbol{U}_d \right) \right]$$

$$= -\alpha_d \gamma \nabla p + \left(\mu_d + \mu_t \right) \nabla^2 \left(\alpha_d \boldsymbol{K} \boldsymbol{U}_d \right) + \boldsymbol{F}_d^{buo} + \boldsymbol{F}_d^{drag} + \boldsymbol{F}_d^{lift} + \boldsymbol{F}_d^{td} \tag{57}$$

3 CALCULATION PROCEDURES

The settler process was studied in steady state, but one simulation was carried out in transient state. The reason for the steady-state calculations was that we were not interested in how fast the phases can separate from each other but in the final situation of the phase layers and actually the thickness of the dispersion layer. This method was acceptable since, after the phase separation when the phases have reached the exact heights, the steady state can be assumed. However, because the upper assumption was not so unambiguous and there was a possibility of fluctuation of the dispersion layer, the transient calculation was carried out. The aim of the transient calculation was to study the physical stability of the separated phase layers. In addition, the calculations were carried out for two-dimensional, turbulent, isothermal and incompressible, without mass transfer, Marangoni phenomena, droplet deformations and phase inversion.

3.1 Software and hardware used

The governing mass and momentum equations were solved using the commercial CFX-4.4 software package (CFX-4.4 Solver manual). The CFX software is based on the finite-volume method in which partial differential equations are integrated over each control volume to obtain discrete equations, which connect the variables at the centre of the control volume with its neighbours. Furthermore, the simulations were carried out with Unix meta-computer of CSC (SGI Origin 2000 hardware) and with a personal computer with a Windows 2000 operating system (Pentium IV 3.2 GHz, 2 Gb memory).

3.2 Discretisation methods and solution algorithms

In the two-phase test simulations, the CENTRAL differencing scheme was employed for pressure, the UPWIND (first-order) differencing scheme for the volume fraction and the HYBRID scheme for the other terms. In the final two-phase simulations, the discretisation processes were carried out with the improved RHIE-CHOW (Rhie and Chow, 1983) interpolation method and with the following schemes: The UPWIND scheme, which was employed for the volume fraction, the CENTRAL differencing scheme, employed for pressure, the linear fully implicit backward differencing scheme, for the transient terms and the QUICK (Leonard, 1979) scheme for the other terms. It was impossible to use the second-order or higher scheme for the volume fraction due to convergence problems. The difference between the HYBRID and the QUICK methods was not so large; this comparison is shown later.

The SIMPLE-C algorithm (Van Doormal and Raithby, 1984) was used to solve the pressure-velocity coupling. The Inter-Phase Slip algorithm (IPSA) (Spalding, 1977; Spalding, 1983) was used to solve the interaction of turbulent energy and volume fraction between the continuous and the dispersed phase, and a modified IPSA-C (CFX-4.4 Solver manual) algorithm was used for momentum.

4 MODELLING WITH ONE CONSTANT DROPLET SIZE

Two-phase modelling of the settler was started with a constant droplet size, although one droplet size could not predict the dispersion flow accurately enough. The main target was to figure out accurate functional boundary conditions that did not over-estimate the phase separation. The modelling becomes very difficult due to two outlets, which have to assure the correct mass flow rates of both phases between the inlet and the outlets. Table A in Appendix 1 presents the 16 different variations for outlet boundary conditions that were tested. The main idea was to use the boundary conditions, which were very close to a real physical phenomenon. At the outlets, the volume fraction information was avoided if possible, because the effectiveness of the phase separation with the used droplet size could not be known. The main problems were back flows, which took place in another outlet, usually in a pressure boundary, an inconsistent mass flow rate balance between the phases, and the disappearance of the continuous phase from the calculation domain.

As a conclusion from these test cases, it can be said that the difficulties were a consequence of the separated phase layers in which the volume fraction of the other phase is very close to zero. In these grid cells, the numerical code has problems in handling the numbers, which are almost zero. The boundary conditions of test number 10 in Table A in Appendix 1 were selected. The only method was to use mass flow rate boundaries at the outlets in order that the back flowing and the disappearance of the continuous phase could be avoided. In this method, it was assumed that all water flowed via the lower outlet and all organic flowed via the upper outlet. The rising pipe was not taken into account because it predicted results similar to those without the pipe; moreover, extra grid cells could thus be avoided and the calculation time was shorter. However, the forced mass flow rates caused the small volume fraction errors of the phases at the outlets. At the upper outlet, there was some amount of the water phase and, at the lower outlet, there was some amount of the organic phase. This inconsistency was not considered so serious for the total phase separation, so it was accepted at that moment.

4.1 Phase separation with constant droplet size

4.1.1 Geometry and boundary conditions

The modelled pilot-settler and a picket fence are presented in Figures 7 and 8, respectively. The effective length of the settler was 2600 mm, the overall height was 1385 mm, the width was 200 mm and the liquid height was about 1200 mm, depending on the specific volume flow rate. The picket fence geometry consisted of three plates, which had one slot in the middle of the first and the last plate. The second plate had two slots in both edges. Because the geometry of the picket fence was complicated with respect to other details in the settler geometry, it could not be used in the settler model as in a real form, and therefore the flow resistance of the fence was added to the settler model by using homogeneous porous media (Kankaanpää, 2000). The porosity (γ) value 0.02 was calculated from the real picket fence geometry.

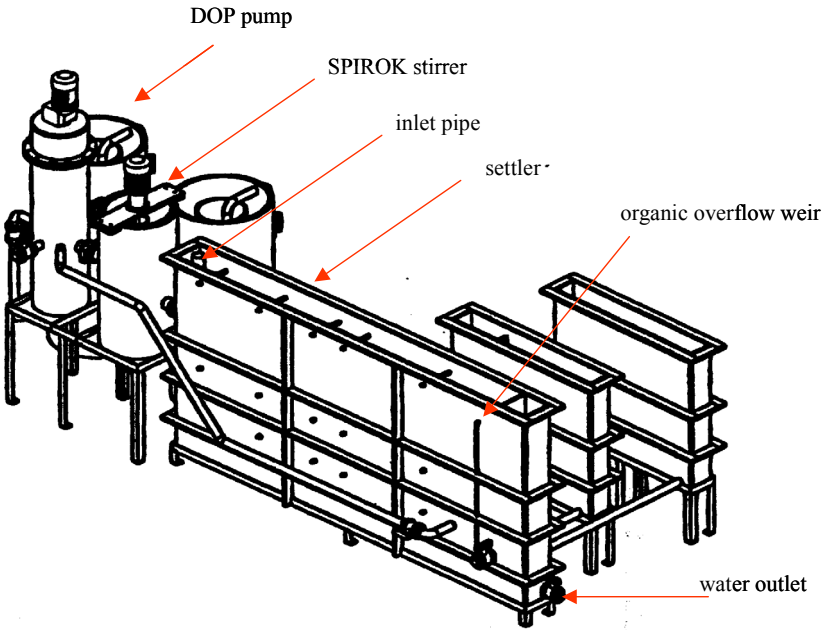

Figure 7. Pilot-settler equipment (Ekman, 1999).

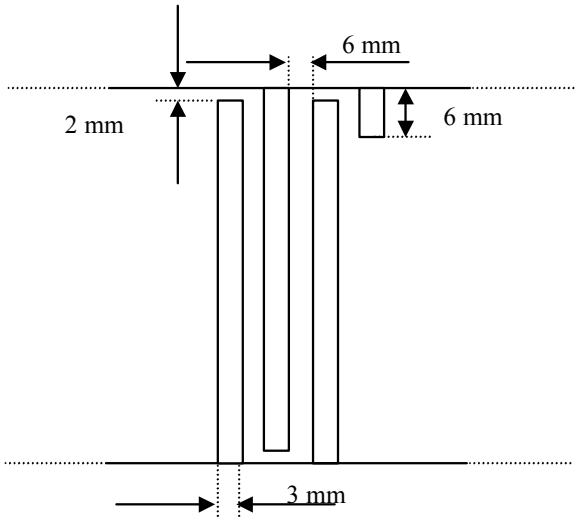

Figure 8. Top view of a schematic diagram of the half picket fence. The centreline runs along the upper edge of the figure.

The geometry of the settler model was two-dimensional and the inflow was approximated from the real inlet geometry. In the pilot settler (Fig. 7), the dispersion was fed via the inlet pipe, which turned the dispersion flow towards the front wall of the settler from which it turned again towards the settler back wall. In the numerical model, the dispersion was fed from the front wall of the settler as an equally divided layer. The height of the "inflow layer" was equal to the height of the real inlet. In other words, the

dispersion was fed directly from the feed end of the settler, that is, not as circulating flow like it was in the pilot equipment. At the inlet, the organic-aqueous (O/A) ratio was 1 and the inlet velocity 0.108 m/s was calculated from the specific volume flow rate 12 m^3/m^2h. The free surface (organic-air interface) was treated as a flat and frictionless wall. The sidewalls of the settler were treated as the symmetry planes. A droplet size was constant in each case and different droplet sizes 400, 500, 600, 700 and 800 μm were examined. These droplet sizes described sufficiently well the organic droplet size distribution, which was measured by Ruiz et al. (2001) in a continuous mixing vessel. Their droplet sizes varied between about 200 and 1200 μm. Furthermore, the phase separation with one and two picket fences was simulated with the droplet sizes 500 and 700 μm. The continuous phase was water. Since the correct values of the physical properties of the phases were not available, the values had to be approximated at temperatures of 20 °C and 24 °C. The physical properties of the pure water used in simulations were density (at 24 °C) ρ_c = 997.329 kg/m^3 (Keskinen, 1989), dynamic viscosity (at 24 °C) μ_c = 0.9142 mPa·s (Keskinen, 1989) and for organic ρ_d = 815.0 kg/m^3 (at 24 °C) (Ekman, 2003) and μ_d = 1.916 mPa·s (at 24 °C) (Ekman, 2003). The value of interfacial tension 35.0 mN/m was selected from the benzene-water system at a temperature of 20 °C (Fox and McDonald, 1985). It was acceptable to use the physical properties of the pure liquids during the model development; the model validation, however, was carried out with real liquids.

The flow phenomenon was assumed as turbulent, although the flow Reynolds number was not in a turbulent region everywhere. However, a similar assumption has also been used by Wilkinson et al. (2000) when local velocities (for example, at the inlet) are much higher than a superficial velocity based on the hydraulic diameter of the settler. In our case, the calculated Reynolds numbers at the approximated inlet were about 5 300 and 13 500 for the organic phase and for the water phase, respectively. The calculations were carried out for two-dimensional, turbulent, isothermal, incompressible, and steady-state flows with and without picket fences. The automatic drag force selection of the CFX-4.4 (CFX-4.4 Solver Manual) was used because the right drag correlation was not our target in this case; rather, our aim was to study the phase separation with the different droplet sizes and used outlet boundary conditions. The accurate value of the lift force and the turbulent dispersion force coefficients were not available for the studied liquid-liquid system, since the values depend on the volume fraction of the dispersed phase and the flow conditions. For example, Behzadi et al. (2004) have reported that the lift force coefficient decreases exponentially when the volume fraction of the gas phase increases, and it varies from 0.02 to 0.4. As a consequence of defining difficulties, these values were approximated from literature and used as constant. The lift force coefficient C_L was set at 0.1 (Behzadi et al., 2004; Thakre and Joshi, 1999) and the turbulent dispersion coefficient C_{TD} was also set at 0.1 (Olmos et al., 2001). Three different two-dimensional meshes, which contained 2 800, 10 686 and 34 524 cells, respectively, were tested to check grid independency, which means that the simulated solution (velocity profile, pressure profile, volume fraction profile…) does not change anymore. It was found that 10 686 nodes were needed to produce the grid-independent solution. The grid is shown in Figure 9.

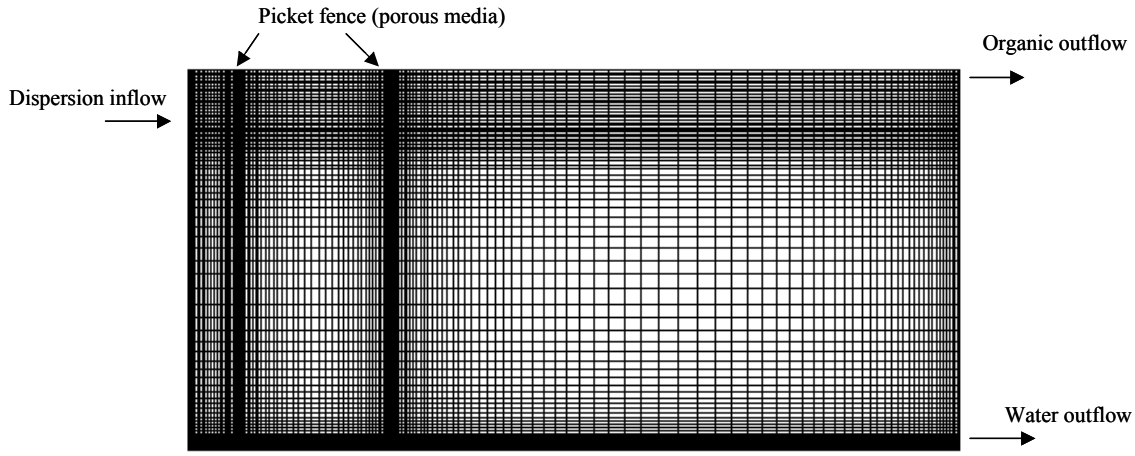

Figure 9. Side view of the mesh of the grid-independent settler geometry.

4.1.2 Results

The simulated results (Kankaanpää, 2005) of the dispersion disengagement showed that organic droplets coalesced better and better and then the dispersion layer became thinner when the droplet size increased. The simulated results of the droplet sizes 500, 600 and 700 μm in Figure 10 show that the separation of the organic and the water phase is very difficult when the droplet size is too small, approximately less than 600 μm. When the droplet is larger than 600 μm, the separation becomes much more effective. Furthermore, the effect of the picket fence can be seen from Figure 11. It causes a dense and quite deep dispersion layer in the front end of the settler and the phases separate better than without the picket fence (Figure 10c). At the larger droplet diameters, it was also noticed that the active surface of the dispersion moved upwards, which is right in the water continuous system. This means that the organic layer becomes thicker when the coalescence rate increases.

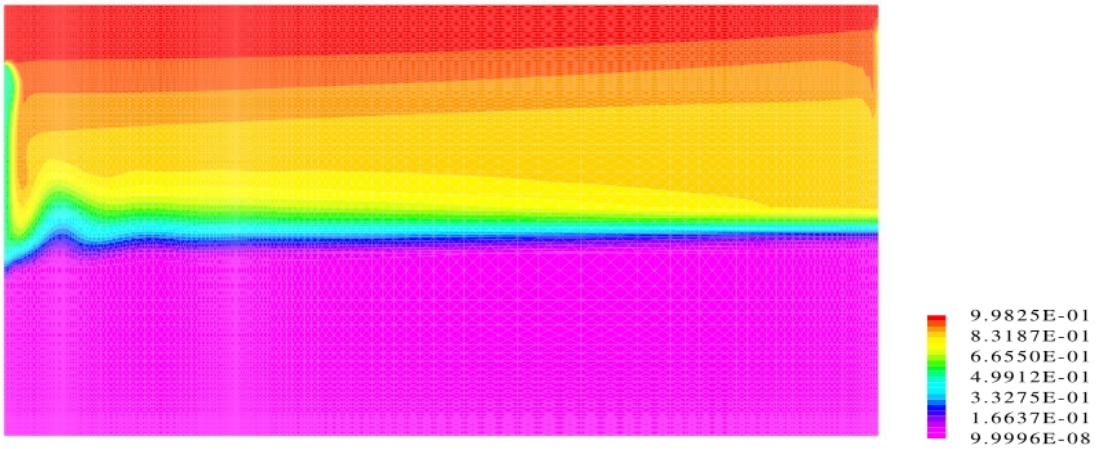

a)

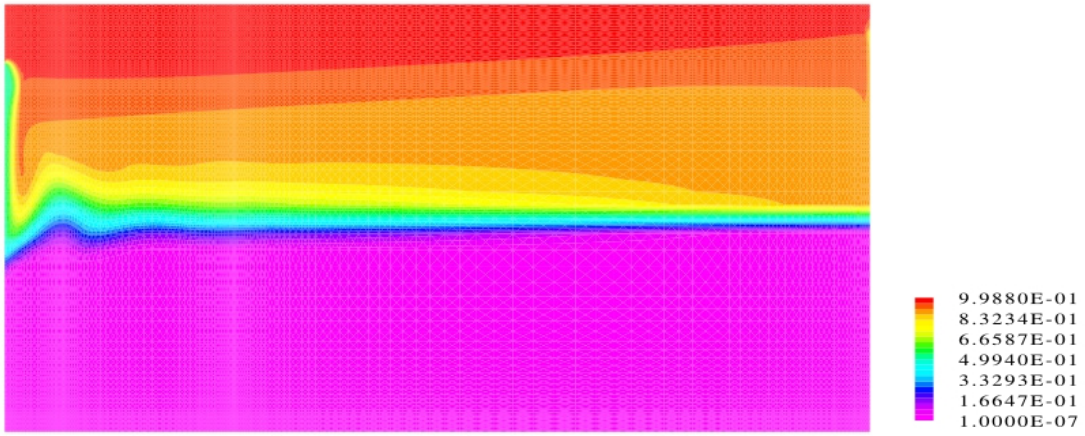

b)

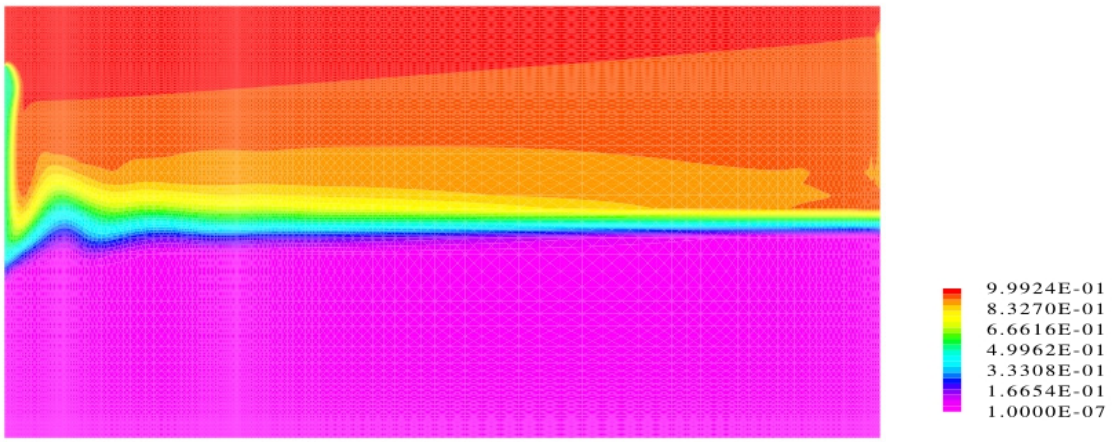

c)

Figure 10. The volume fraction of the organic phase with droplet sizes: a) 500 µm, b) 600 µm and c) 700 µm. Dark red indicates the totally separated organic phase and violet indicates the aqueous phase.

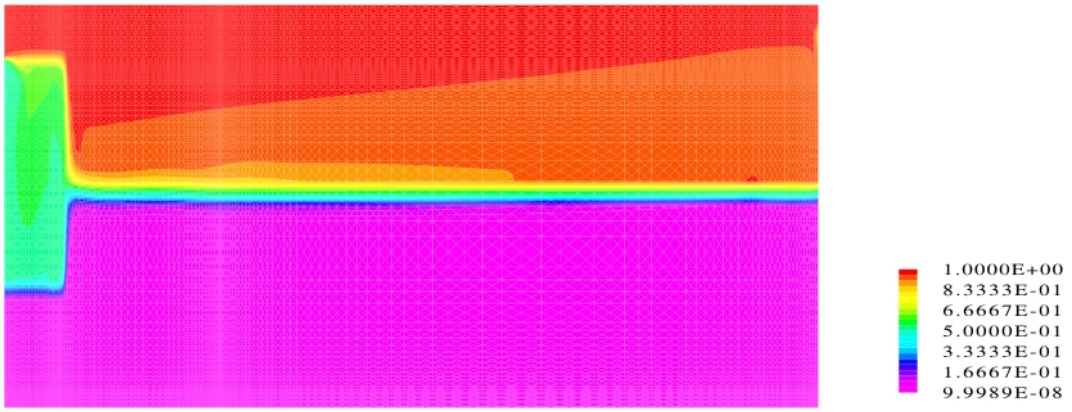

Figure 11. The volume fraction of the organic phase with droplet size 700 μm when there is one picket fence. Dark red indicates the totally separated organic phase and violet indicates the aqueous phase.

The pressure drop over the picket fences was about 86.5 Pa, which meant that the fence dammed the dispersion or the organic phase about 9.7 mm in the front of the fence. The average pressure drop value over the picket fence was defined by a difference of pressure values (200 data points), which were situated 1.0 mm before and after the fence. When the simulated value was compared with the value 10 mm, which was defined from the physical experiments of Ekman (1999), it was noticed that it did not differ at all. The simulated thicknesses of the dispersion were in the right area. The thickness of the dispersion with the droplet size 500 μm without the picket fence and with one and two picket fences was 590 mm, 481 mm and 475 mm, respectively. In the case of 700 μm, the thicknesses were 511 mm, 377 mm and 107 mm. Respective values of the physical experiments, which were carried out by Ekman (1999) at 20 °C were about 357 mm without picket fences and about 180 mm with one picket fence. However, the comparison of the pressure drop and the simulated dispersion thicknesses with the physical measurements was quite difficult, because the physical properties (density, dynamic viscosity and interfacial tension) of the real liquids used in pilot experiments were not known. However, it was known that these values were not exactly the same, because the liquids in the physical experiments were not pure and the reagent concentration and copper loading degree affected the physical properties. Furthermore, the defined thickness of the dispersion layer depends on the amount of the entrainments that can be taken into account with the allowed volume fraction limit of the other phase. This determines the volume percent of the other phase that the separated phases can contain. In the previous simulations, this limit was 5 vol-% (50 000 ppm).

Although these constant droplet size calculations showed that CFD could be used to study the solvent extraction settler process, it was decided to develop the CFD model closer to reality, which meant that droplets break-up and coalescence phenomena have to be taken into account. However, before these extra source terms, the drag force correlation, the physical properties of the phases and more realistic outlet boundary conditions were defined. The used mass flow boundaries, which assumed that all

aqueous phase flowed through the lower outlet and all organic flowed via the upper outlet, were not necessarily correct, because the phase separation depends on the droplet size of the dispersion. Specifically, when the dispersion contains droplets that are too small, it is wrong to assume that both phases separate totally, and only the organic phase flows via the upper outlet and the water phase flows via the lower. Furthermore, Figures 10 and 11 show that the thickness of the organic phase decreases when the dispersion flows towards the back wall of the settler. In reality, the thickness of the organic layer should increase. This inconsistency depends on the mass flow rate boundary at the upper outlet when it forces the organic phase through the outlet.

4.2 Selection of the drag force coefficient correlation

When the outlet boundary conditions were adjusted to perform quite well, the selection of an appropriate drag force correlation was focused on. As was mentioned earlier, the drag force and drag force coefficient depend on droplet diameter, the flow regime defined by droplet Reynolds number, and also the volume fraction of the dispersed phase. Equation (10) points out that the shape and the size of the droplet are very important and they have to be taken into account when the drag coefficients are studied and selected. In the dispersion flow, the droplets may deform and oscillate, if they are not very small. During the oscillation and deformation, the circulation flow patterns occur inside the droplets, which decrease the drag force due to the reduced velocity gradients (Kumar et al., 1980). However, small amounts of surface-active impurities, which usually cause Marangoni phenomena, may eliminate these circulation patterns and thus increase the drag force between the continuous and the dispersed phase (Clift et al., 1978). This proves that the drag force phenomenon is quite complex, since it varies between pure and contaminated substances.

In the CFX-4.4 (CFX-4.4 Solver Manual), the drag force coefficient correlations are divided into distinct regions according to the Reynolds number of the droplets. These regions are very slow flow Stokes region ($0 \leq Re \leq 0.2$) where inertial effects can be omitted, viscous region ($0 \leq Re \leq 1000$) where inertial effects play a role, but where viscous effects dominate, and turbulent region ($1000 \leq Re \leq 2 \cdot 10^5$). For the selection of the right drag correlation, the relative velocity between the phases has to be known because it is used to calculate the Reynolds number of the droplets. The defining of the relative velocity between phases in multiphase processes is a very challenging task and, actually, it is only possible to define it by making physical measurements. In general, these measurements are carried out with simplified experimental arrangements in which, for example, the Particle Image Velocimetry (PIV) technique (Augier et al., 2003) can be used to measure the relative velocities.

CFD modelling with the Eulerian-Eulerian model gives an opportunity to define the relative velocity between the interacted phases. The relative velocity can be calculated by using the resultant velocities of the velocity vector components in the following way:

$$\boldsymbol{U}_{rel} = \left| \boldsymbol{U}_c - \boldsymbol{U}_d \right| \tag{58}$$

Although, the relative velocity is easy to define from the software, the right Reynolds number region of the dispersed droplets is not. The main reason for this is that

the software always uses some drag force model when the Eulerian-Eulerian model is used. Thus, the calculated relative velocity value depends on the used drag model. A problem arises because there can be no certainty that the flow situation really is in this Reynolds region in which the drag model is used. In this study, the problem was solved so that different drag force coefficient correlations of the droplets recommended by the CFX-4.4 Solver Manual were compared with each other in the middle of the settler. The tested correlations were: Automatic (drag is the viscous regime correlation when this is greater than the distorted regime correlation; otherwise it is the minimum of the distorted regime correlation and the spherical cap regime correlation), Ishii-Zuber (1979) for the viscous region and Grace et al. (1976) for the turbulent region (distorted regime). The test calculations were carried out with the same geometry and boundary conditions as the previous cases at 24 °C, but only the droplet size 700 μm was used. Furthermore, some cases were also calculated with slightly higher density, dynamic viscosity and interfacial tension values, which approximated to the situation when the temperature is lower, about 10 °C (Table I). The modelled relative velocities (Figure 12) and Reynolds numbers (Figure 13) were compared with the theoretical terminal velocities (Table I), which were calculated from the *Re-Eo-Mo* figure of Grace et al. (1976).

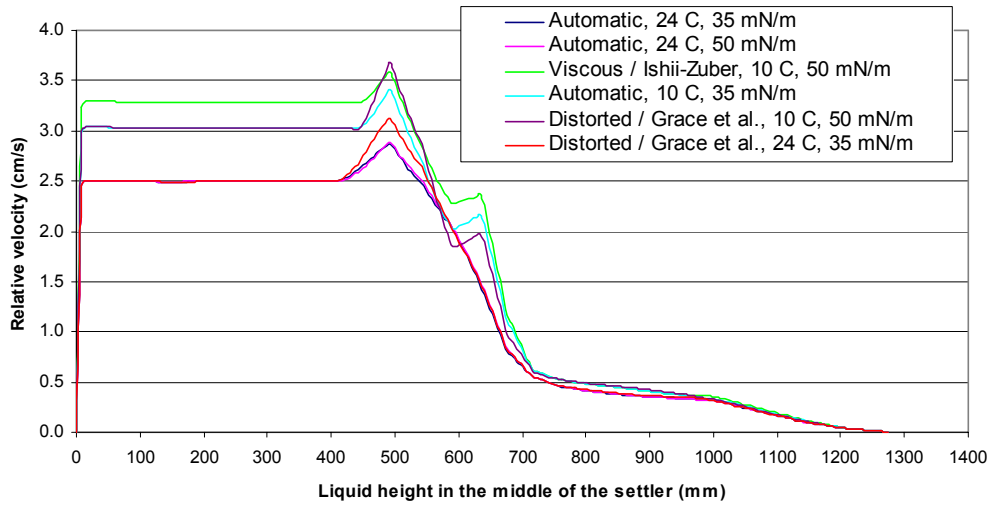

Figure 12. Simulated relative velocities as a function of the liquid height in the middle of the settler (x = 1.292 m). The constant droplet size is 700 μm.

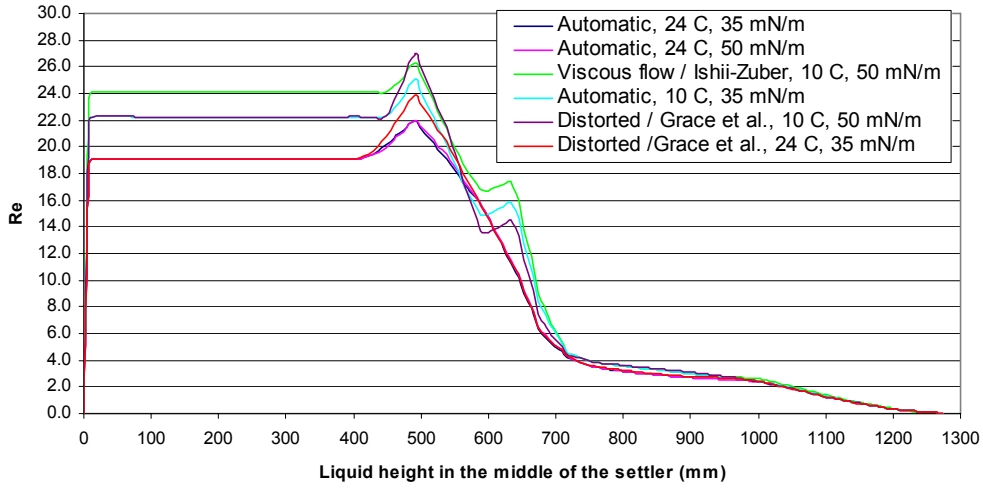

Figure 13. Droplet Reynolds numbers calculated from the simulated relative velocities as a function of the liquid height in the middle of the settler (x = 1.292 m). The constant droplet size is 700 µm.

Table I. Theoretical Reynolds numbers and terminal velocities of the droplet size 700 µm.

Temperature (°C)	24		10	
	Continuous phase	Dispersed phase	Continuous phase	Dispersed phase
Density (kg/m^3)	997.329	815.0	1100.0	830.0
Dynamic viscosity (mPas)	0.9142	1.916	1.05	2.70
Interfacial tension (mN/m)	35	50	35	50
Eotvos (*Eo*)	0.025	0.018	0.037	0.026
Morton (*Mo*)	2.93E-11	1.00E-11	6.21E-11	2.13E-11
Log (*Mo*)	-10.5	-11.0	-10.2	-10.7
Re from Grace et al. (1976)	20	20	25	25
Terminal velocity (cm/s)	2.6	2.6	3.4	3.4

Figure 13 shows that the simulated *Re*-number values are in the viscous region. Furthermore, when the maximum values of the simulated relative velocity (Figure 12) calculated by the Ishii-Zuber correlation (Eq. 59) are compared with the theoretically calculated terminal velocity values (Table I), it can be noticed that they are quite close to each other. Therefore, the drag coefficient correlation of Ishii-Zuber (1979) was selected:

$$C_D = \frac{24}{Re}\left(1 + 0.1Re^{0.75}\right) \tag{59}$$

Although this comparison was quite crude, it was better than a simple guess. Thus this method was acceptable when physically measured relative velocity values were not available.

5 VALIDATION DATA

5.1 Physical experiments of the pilot settler

The simulated results were validated by means of the physical experiments, which had been carried out by Ekman in the pilot unit (Figure 7) at Outokumpu Research Center in Pori, Finland. One or two plastic picket fences were used. Ekman (1999) studied how organic and water phases separated in the settler with one or two picket fences when the specific volume flow rate (V_{spec}) was increased. All experiments had been carried out with the continuous water phase and O/A ratio was about 1. The fluids were as follows: Aqueous 1 g/l Cu, pH 1.7, 70 g/l SO_4; Organic: 10 % LIX984N (5 g/l Cu). The temperature was about 10 °C and/or 20 °C. After separation, the thickness of the phase layers (organic, dispersion and water) had been measured. The results are shown in Table II.

Table II. The thickness of the organic, water and dispersion layers in the pilot settler. The continuous phase is water and O/A is about 1. Experimental data from Ekman (1999).

		No. of	Approximately heights (mm) in different locations of the settler								
V_{spec}		picket	(186 - 669 mm)			(1162 - 1389 mm)			(2115 - 2584 mm)		
(m^3/m^2 h)	T (°C)	fences	organic	dispersion	water	organic	dispersion	water	organic	dispersion	water
4.09	19.9	0	693	50	450	695	50	450	665	90	440
6.24	19.9	0	615	140	440	631	135	430	613	155	430
9.02	19.9	0	570	160	470	560	165	475	551	175	475
9.71	19.9	0	506	215	480	511	215	475	518	210	475
11.16	19.8	0	412	290	500	443	270	490	444	270	490
13.02	19.8	0	339	365	500	364	360	480	360	365	480
15.04	19.9	0	65	880	260	65	875	265	61	885	260
av. temp.	20										
(m^3/m^2 h)	T (°C)	No.	organic	dispersion	water	organic	dispersion	water	organic	dispersion	water
6.09	20.4	1	696	40	460	691	45	460	687	50	460
8.88	20.4	1	625	115	460	610	100	490	606	115	480
9.52	19.7	1	561	170	470	571	135	495	682	40	480
9.88	20.5	1	541	210	450	567	145	490	562	170	470
14.68	20.2	1	295	390	520	385	310	510	395	300	510
16.59	20.1	1	236	450	520	297	410	500	297	420	490
17.94	20.0	1	206	480	520	202	515	490	127	620	460
av. temp.	20										
(m^3/m^2 h)	T (°C)	No.	organic	dispersion	water	organic	dispersion	water	organic	dispersion	water
5.92	9.9	1	688	80	430	696	70	430	717	40	440
8.05	10.0	1	683	75	440	689	70	440	684	60	455
9.33	10.5	1	530	340	330	516	350	335	526	345	330
9.59	10.3 / 13.5	1	487	335	380	492	325	385	498	320	385
9.59	9.8 / 10.8	1	451	410	340	446	405	350	448	405	350
10.33	9.5	1	401	555	245	422	520	260	427	490	285
11.08	10.5	1	366	605	230	362	595	245	373	580	250
11.94	10.0	1	308	595	300	303	595	305	298	595	310
12.41	10 / 11	1	174	840	190	174	840	190	175	840	190
13.58	10.0	1	113	935	155	94	970	140	105	950	150
13.69	8.5	1	78	1020	105	58	1050	95	54	1050	100
av. temp.	10										
(m^3/m^2 h)	T (°C)	No.	organic	dispersion	water	organic	dispersion	water	organic	dispersion	water
12	10	2	n.d.*	987	n.d.*	n.d.*	274	n.d.*	n.d.*	274	n.d.*

* not determined

5.2 Physical properties of the liquid phases

Because the validation data had been carried out with certain liquids, the physical properties of the same liquids were needed for the numerical model. The interfacial tension between the organic extractant (LIX 984N dissolved in the diluent SHELLSOL D70) and the aqueous phase was carried out by the KSV Sigma 70 surface tension analyzer, which was based on the Du Nouy platinum ring method. The measurements were carried out at a room temperature of 25 °C and at 10 °C. However, at the lower temperature, grey sediments deposited at the bottom of the vessel and thus its value was not reliable. At 25 °C, the interfacial tension was 23 mN/m. According to Stein (1996),

the interfacial tension usually increases when temperature decreases. Nowadays, all solvent extraction plants use hydroxyoxime-based extractants when copper is extracted from sulfate solutions. Therefore, the interfacial tension values at temperatures of 10 °C and 20 °C could have been approximated with the aid of the data of Ruiz et al. (2001) (Table III) by assuming that the measured interfacial tension value 23 mN/m increased with the same slope as the values of Ruiz et al. (2001) when temperature decreased. The approximation was made with the least squares method and is shown in Figure 14.

Table III. The interfacial tension between the aqueous and the organic phases (Ruiz et al., 2001).

Aqueous phase Cu (g/l)	pH	Organic phase, reagent concentration (%)	T (°C)	σ (mN/m)
12	2	10	23	27.08
12	2	10	25	25.31
12	2	10	30	21.07
12	2.5	10	23	27.12
12	1.5	10	23	26.93
9	2	10	23	27.35
6	2	10	23	27.43
12	2	20	23	21.73

Organic phase: LIX 860-IC + LIX 84-IC

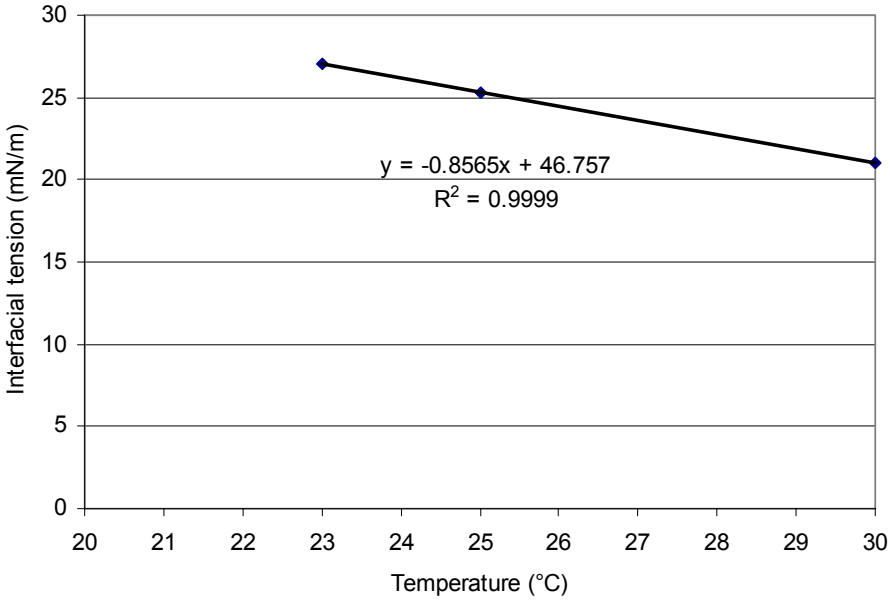

Figure 14. Temperature dependency of interfacial tension according to experimental data by Ruiz et al., (2001). Aqueous phase 12 g/l Cu, pH 2, and organic phase LIX 860-IC + LIX 84-IC.

Approximated interfacial tension values and the dynamic viscosity and the density values measured by Peuha and Paatero (2004) for the organic extractant and the aqueous phase are given in Table IV.

Table IV. Physical properties of the aqueous (1 g/l Cu and 70 g/l SO_4) phase and organic (10 % LIX 984N) phase.

Phase	T / °C	Density* (kg/m^3)	Dynamic viscosity* (mPa·s)	Interfacial tension (mN/m)
water	20	1085.0	1.381	27
organic	20	797.7	1.827	
water	10	1088.0	1.755	36
organic	10	804.6	2.103	

* Peuha and Paatero (2004)

6 MODELLING WITH COALESCENCE AND BREAK-UP PROCESSES OF DROPLETS

The settler model described in Chapter 4.1 was modified in order to simulate more accurate and more realistic outlet boundary conditions. In the two-phase modelling, the pressure boundaries should be used, since only then can the mass flow rate be checked. However, in the previous test calculations, the pressure boundary condition caused the back flow phenomenon to enter another outlet. The new outlet geometries were developed, which restored that problem. Both outlets were extended as Xia et al. (1997) have proposed and, what is more, the lower outlet was two times longer than the upper outlet. Furthermore, the height of the upper outlet was defined by the weir Equation (60) and Figure (15), which depend on the overflow volume flow rate (Hietala, 1981). This new geometry (Figure 16) made it possible to use the pressure boundary in the upper outlet, in which there was normal atmospheric pressure. In the lower outlet, the mass flow boundary was used, but only the velocity value, which was equal to the velocity of the aqueous phase, was given. This assumed that all water flowed through the lower outlet that is predictable when water is the continuous phase. The advantage of these boundary conditions is that the user does not need to know whether the phases can separate from each other with the used droplet size of the dispersion.

The height of the organic overflow (c) in the end of the settler was calculated by Equation (60) given by Hietala (1981):

$$V_{fr,org} = \frac{2}{3}\sqrt{2 \cdot g} \cdot C_{out} \cdot b \cdot c^{3/2} \tag{60}$$

where

$$C_{out} = 0.605 + \frac{0.001}{c} + 0.08 \cdot \frac{c}{a} \tag{61}$$

where $V_{fr,org}$ is the volume flow rate of the organic phase, g is the acceleration of gravity, C_{out} is the outflow coefficient, b is the width of the settler, c is the height of the overflow and a is the height of the organic layer. It was assumed that a was half of the height of the settler back wall (O/A was 1).

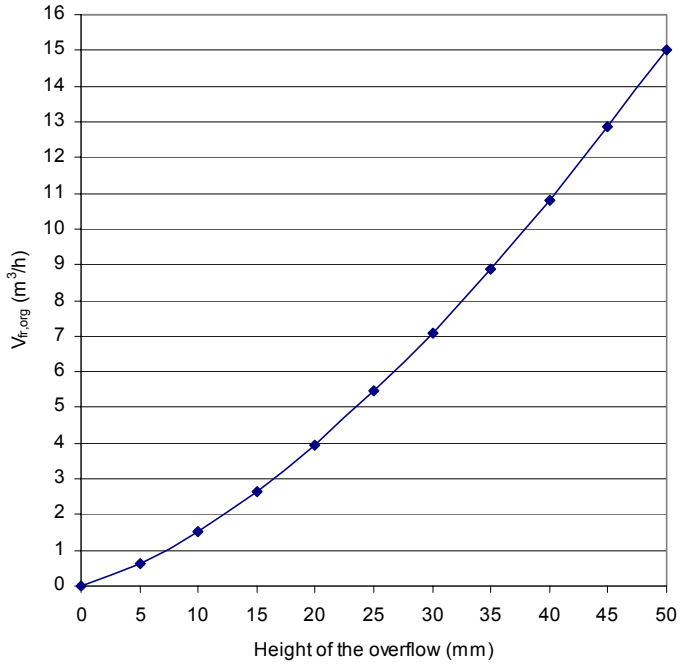

Figure 15. Volume flow rate of the organic phase as a function of the height of the overflow.

The height of the upper outlet was 10 mm, and 17 mm in the cases where the specific volume flow rates (V_{spec}) were 6 m^3/m^2h and 12 m^3/m^2h, respectively.

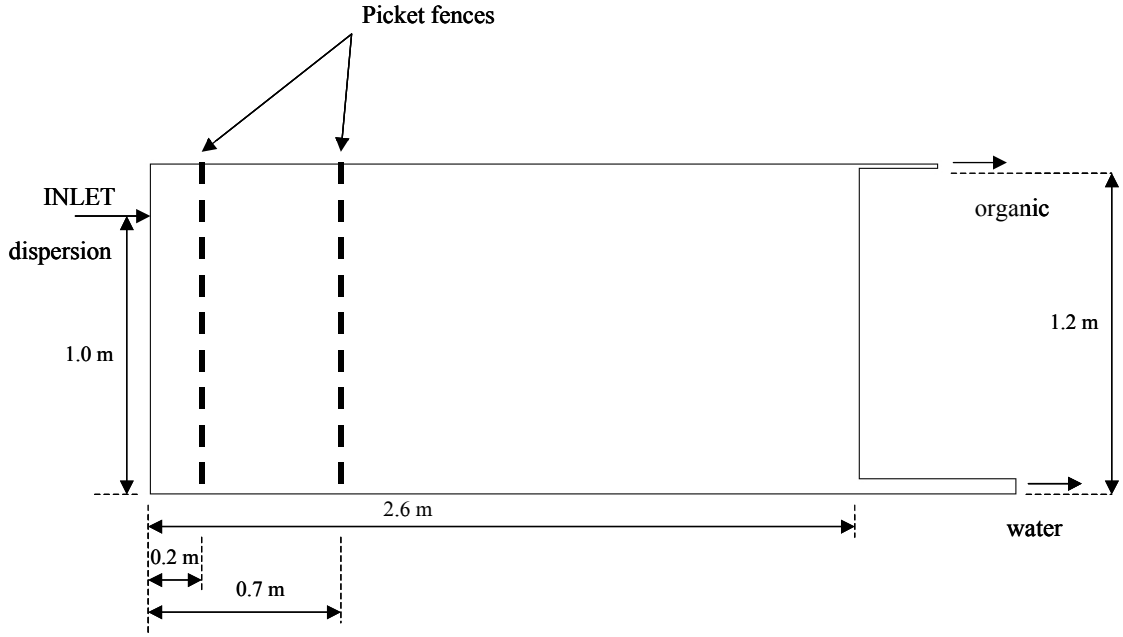

Figure 16. Schematic side view of computational 2D domain of the settler. Dimensions are approximate values. Vertical direction is y-direction and longitudinal direction is x-direction.

6.1 Test calculations of MUSIG model parameters

The MUSIG model has nine parameters, which have to be selected before calculation. These are the number of the droplet size groups, the minimum, the maximum and the mean droplet diameters, the coalescence and break-up calibration coefficients, the initial and critical film thicknesses of the continuous phase and the inner iterations between MUSIG updates.

The parameter test calculations were carried out for two-dimensional, turbulent, isothermal, incompressible, and steady-state flows without picket fences. At the inlet, the organic-aqueous (O/A) ratio was 1 and the inlet velocity (0.108 m/s) was calculated from the specific volume flow rate 12 m^3/m^2h, which meant that the height of the upper outlet was 17 mm. The free surface (organic-air interface) was treated as a flat and frictionless wall. The sidewalls of the settler were treated as the symmetry planes. The lift force coefficient C_L was set at 0.1 (Behzadi et al., 2004; Thakre and Joshi, 1999) and the turbulent dispersion coefficient C_{TD} was also set at 0.1 (Olmos et al., 2001).

6.1.1 Grid independency test

The grid independency test was carried out with three different two-dimensional meshes, which contained 4 470, 12 582 and 48 520 cells, respectively, with a constant droplet size of 500 μm. The physical properties were selected from Table IV at a temperature of 20 °C, but the interfacial tension was 35 mN/m, because the accurate value was not yet available. Automatic drag force selection of the CFX-4.4 was used. Comparison between the meshes was made with 10 different checking lines and it was found that 12 582 nodes were needed to produce the grid-independent solution (Figure 17).

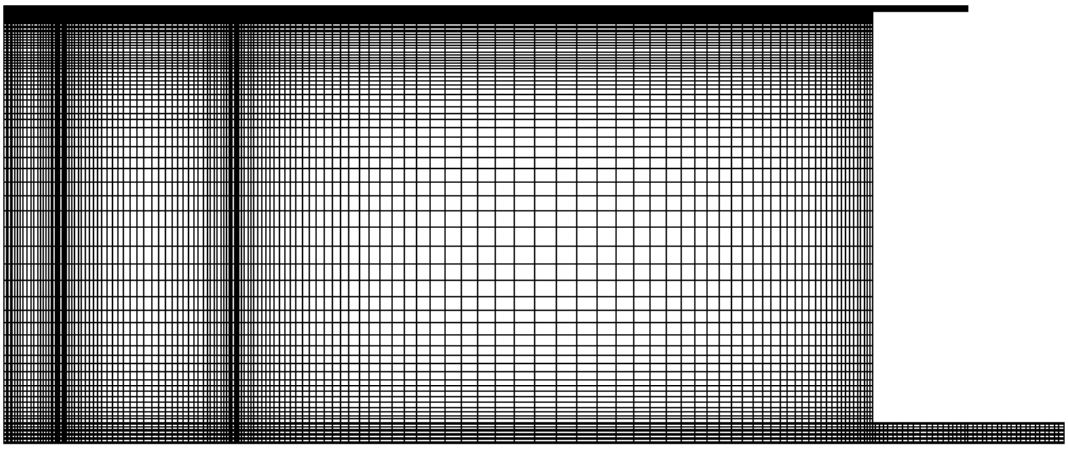

Figure 17. Side view of the mesh of the grid-independent new settler geometry.

6.1.2 Droplet size range

Droplet size range was tested with the coarsest grid (4 470 grid cells) and with the constant droplet sizes 100, 200, 300, 400, 500 and 800 µm. The aim of this part of the study was to find an approximation of the droplet size range, which could be used in the MUSIG model. Figure 18 shows the volume fraction of the continuous phase as a function of the liquid height in the middle of the settler (x = 1.577 m).

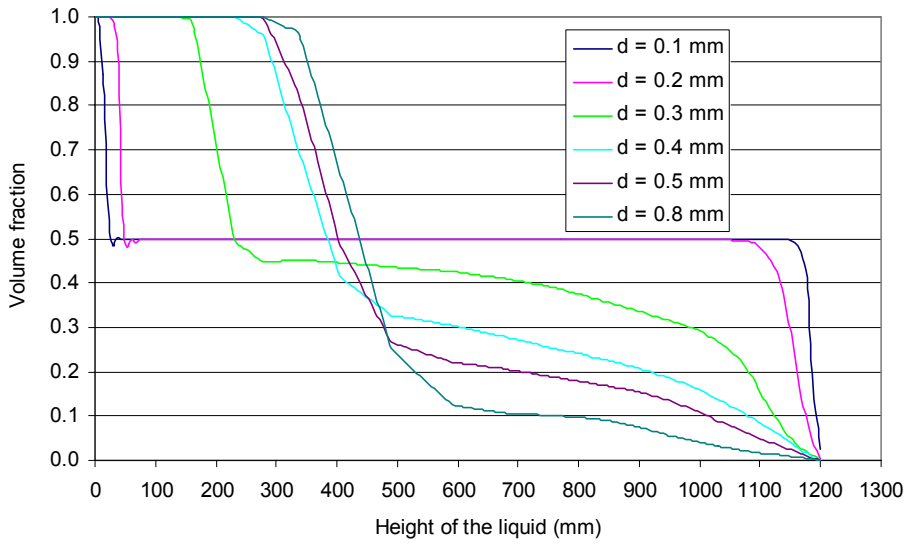

Figure 18. The volume fraction of the continuous phase versus the liquid height in the middle of the settler (x = 1.577 m) with different droplet sizes.

The simulated results in Figure 18 show that the sedimenting interface moves upwards when droplet size increases. It can be seen that the water and the organic phase do not separate at the droplet sizes of 100 and 200 µm, but when the droplet size becomes larger than 300 - 400 µm, the dispersion disengagement becomes more effective. These results agree well with Magiera and Blass (1997) who reported that droplet size should be larger than 100 µm before the phases can separate.

6.1.3 Inner iterations of the MUSIG model

Inner iterations of the MUSIG model mean the calculation of the transport equations (27) for the scalar variable f_i. The number of inner iterations of the population balance equations was tested with the same boundary conditions as the grid independency and the droplet size range tests, but the automatic drag force was replaced by the drag force correlation of Ishii-Zuber (1979) and an accurate value of the interfacial tension (27 mN/m) used. The number of the droplet size groups was 5, which were equally divided according to their diameter (Table V). The minimum diameter of the droplet was 100 µm, the maximum was 700 µm and the mean 350 µm. At the inlet, turbulence intensity was 5 %, dissipation length scale 0.114 m, and the mean diameter of the droplet was 292.3 µm. The default values of initial (10^{-4} m) and critical film thicknesses (10^{-8} m) of the continuous phase were used because exact values could not be measured. However,

these values were in the range that was reported by McKay and Mason (1963) and Burrill and Woods (1973).

Table V. MUSIG model group discretisation when the droplet sizes are equally divided.

Musig group number	Min. droplet diameter (μm)	Max. droplet diameter (μm)	Mean droplet diameter (μm)
1	100	220	180
2	220	340	292
3	340	460	409
4	460	580	527
5	580	700	646

The default values of the calibration coefficients of the breakage model (f_B = 1) and coalescence model (f_C = 0.05) were used. The test cases were carried out with 100, 200 and 400 inner iterations. The comparison was made visually in two locations of the settler; the results showed that 200 iterations were enough to produce an iteration-number-independent solution. Figure 19 shows, as an example, the volume fraction of the mean droplet size 292.3 μm (MUSIG size group 2) as a function of the liquid height in the middle of the settler. It can be noticed that 200 and 400 iteration cases agree very well when these three cases are compared.

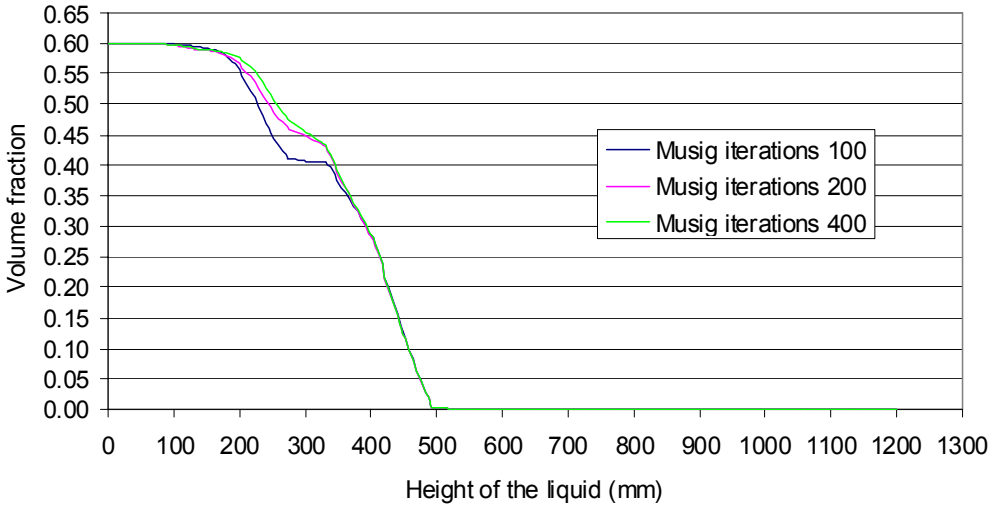

Figure 19. The volume fraction of the mean droplet size 292.3 μm versus the liquid height in the middle of the settler (x = 1.8 m).

6.1.4 Drag force in dense dispersions

Although, the selected drag force correlation of Ishii-Zuber (1979) performed well, its disadvantage is that it has been developed for a single droplet that moves through the continuous phase. In the dispersion flow, the interaction of droplets has to be taken into account because it decreases the relative velocity between the dispersed and the

continuous phase. Thus, the Reynolds number will decrease and the drag coefficient will increase. The drag force correlation of Ishii-Zuber (1979) contains an option for dense dispersions. The effect of the presence of other droplets is taken into account by mixture viscosity (μ_m) (Equation (62)), which describes the increased resistance to the motion of a single droplet.

$$\frac{\mu_m}{\mu_c} = \left(1 - \frac{\alpha_d}{\alpha_{dm}}\right)^{-2.5\alpha_{dm}\left(\frac{\mu_d + 0.4\mu_c}{\mu_d + \mu_c}\right)} \tag{62}$$

where α_{dm} is the maximum attainable value for the volume fraction of the dispersed phase; it is set at 1.0 for droplets.

Ishii and Zuber (1979) has mentioned that this mixture viscosity correlation can be applied to dispersion systems in which the volume fraction of the dispersed phase can be as high as 0.95 when turbulent motions and droplet coalescences are absent.

The mixture viscosity correlation was compared with the normal dilute drag force correlation. Calculations were carried out with the same droplet size range and boundary conditions as the inner iteration tests of the MUSIG model, but only 100 inner iterations were used. Figure 20 shows that the droplet Reynolds number of the case of the mixture viscosity differs quite a lot from the droplet Reynolds number of the case of the dilute concentration in the upper part of the settler. Furthermore, the mixture viscosity caused convergence problems, which was noticed as an error of mass flow rates. The error was about 10 times larger than in the case of the dilute concentration. These problems were due to the volume fraction of the dispersed phase, which was higher than 0.95. As a consequence of this, the expression in parenthesis of Equation (62) approached zero. Therefore, it could be concluded that the dense particle effect of the Ishii-Zuber (1979) correlation was not useful in the separation process when the volume fraction of the dispersed phase was very close to unity.

The relative velocity (and *Re*-number) is lower in the lower part of the settler than at mid-height because the Sauter mean diameter of the droplet is smaller at the bottom than in the dispersion layer. When the droplet moves upwards, its diameter increases, but at the same time the volume fraction of the dispersed phase increases also. Therefore, the relative velocity (and *Re*-number) decreases. The shape of the curve of the dilute concentration is correct.

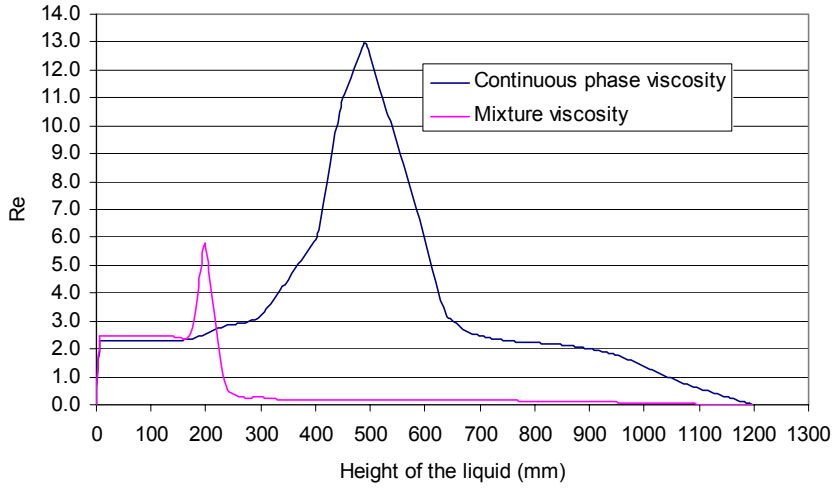

Figure 20. Droplet Reynolds number as a function of the height of the liquid with the cases of the mixture viscosity correlation and the continuous phase viscosity. The curves are plotted in the middle of the settler (x = 1.577 m).

Since it was necessary to be sure that the drag force correlation of Ishii-Zuber (1979) was applicable to use in the settler process, the Reynolds number of droplets based on relative velocity values calculated by Equation (58) with the drag force correlation of Ishii-Zuber (1979) was compared with the Reynolds numbers calculated by the relative velocity correlations of Kumar et al. (1980) and Kumar and Hartland (1985). Hartland and Jeelani (1994) have mentioned that these correlations cannot be applied in dispersions, which flow horizontally, because the correlations have been developed for a sedimentation process in which dispersion flows mostly vertically. However, because the dispersion flows both vertically and horizontally in the settler, it was decided to test these correlations.

Kumar et al. (1980) have developed Equation (63) for the spray columns in which the continuous phase moves counter-current to the dispersed phase.

$$\frac{U_{rel}^2}{d_d g} = 2.725 \frac{\Delta\rho}{\rho_c}\left(\frac{1-\alpha_d}{1+\alpha_d^{1/3}}\right)^{1.834} \tag{63}$$

Equation (63) is allowed to be used in the range of the volume fraction of the dispersed phase from 0.01 to 0.75 and Reynolds number of a droplet from 7 to 2450.

Kumar and Hartland (1985) have developed the empirical correlation for the prediction of the volume fraction of the dispersed phase and relative velocity in liquid-liquid dispersions settling process under gravity. This equation can be given by

$$\frac{4 d_d g \Delta\rho (1-\alpha_d)}{\left[3\rho_c U_{rel}^2 \left(1+4.56\alpha_d^{0.73}\right)\right]} = 0.53 + \frac{24\mu_c}{d_d U_{rel} \rho_c} \tag{64}$$

Equation (64) is allowed to be used in the range of the volume fraction of the dispersed phase from 0.01 to 0.76 and Reynolds number of a droplet from 0.16 to 3169.

When the above equations were compared, the average droplet diameter (d_d) in Equations (63) and (64) was replaced by the Sauter mean diameter, which was obtained from CFD solution. Figure 21 shows the Reynolds number of the droplets as a function of the liquid height. It can be seen that the correlation of Kumar and Hartland (1985) agrees quite a well with the CFD simulation, but the correlation of Kumar et al. (1980) differs very much from the CFD simulation. This proves that the drag force correlation of Ishii-Zuber (1979) performs quite well in the settler process.

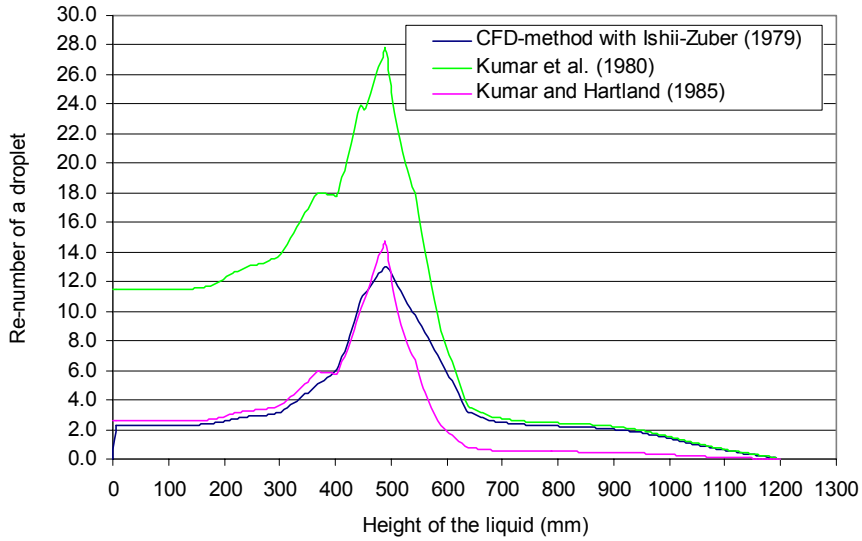

Figure 21. Reynolds number of a droplet as a function of the height of the liquid in the middle of the settler (x = 1.577 m).

6.1.5 Calibration coefficient of the coalescence model

The default values of the calibration coefficients f_B = 1 and f_C = 0.05 predicted the phase separation phenomenon correctly. The active surface of the dispersion moved upwards, which is right in the water continuous system. This means that the organic layer becomes thicker when the coalescence rate increases with increased droplet size. Figure 22 shows the Sauter mean diameter of the organic phase when the calculation has not yet converged. It can be easily seen that the coalescing interface moves downwards and the sedimenting interface moves upwards. Furthermore, the drop-drop coalescence takes place in the front end of the settler, because there is the strongest turbulence. When dispersion moves towards the settler back wall, where water flows via the lower outlet and the organic phase via the upper outlet, the interfacial coalescence will start to control the separation process.

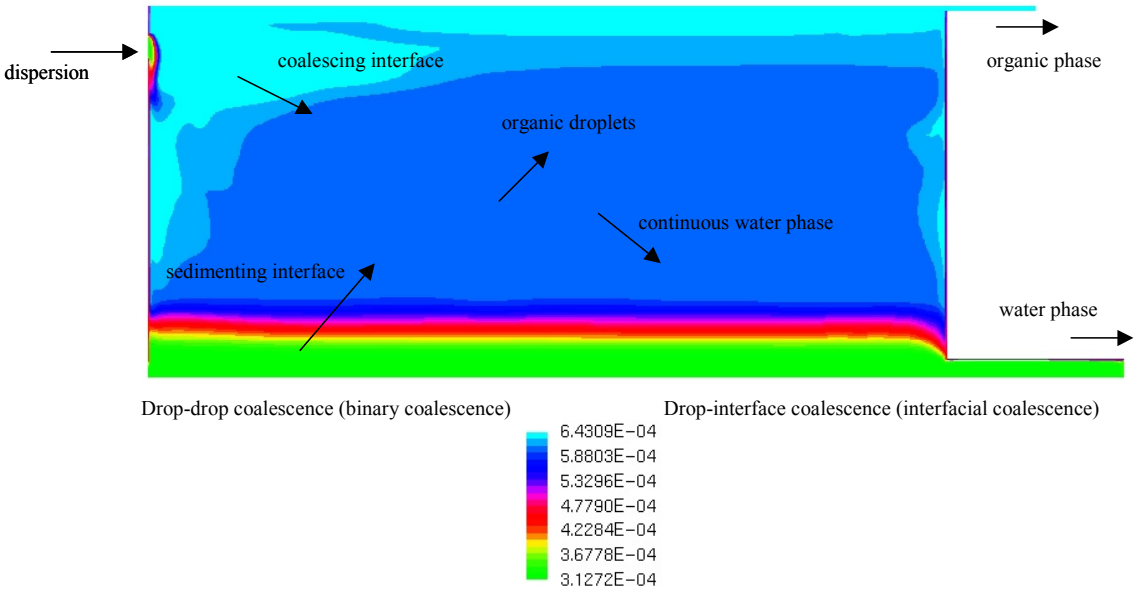

Figure 22. Sauter mean diameter of the organic droplets. Result has not yet converged. There are five MUSIG groups; f_C is 0.05. The minimum droplet diameter is 100 µm and the maximum is 700 µm. The mean droplet diameter is 350 µm.

However, it was noticed that the default value of the coalescence calibration coefficient was too large, because it predicted a too effective coalescence of the droplets with the droplet size range of 100-700 µm. The separated organic phase contained only the largest droplet sizes (mean diameters 645 µm). This phenomenon was regarded as unrealistic when the situation was compared with the theory of the phase separation. Therefore, three test cases were carried out in which the coalescence calibration coefficient and the droplet size range were varied. The break-up calibration coefficient was not changed, because the settler process is mainly controlled by the coalescence phenomenon.

In the first case, the droplet size group number was 10; the groups were equally divided according to droplet diameter and the default value of the coalescence calibration coefficient (f_C = 0.05) was used. The droplet size range was changed so that the minimum diameter of the droplet was 80 µm, the maximum was 1200 µm and the mean 700 µm. The other boundary conditions were similar to those in the previous cases, but at the inlet, the mean droplet size was 260.1 µm. Figures 23 and 24 show the volume fraction of the organic phase and the Sauter mean diameter of the dispersed droplets, respectively.

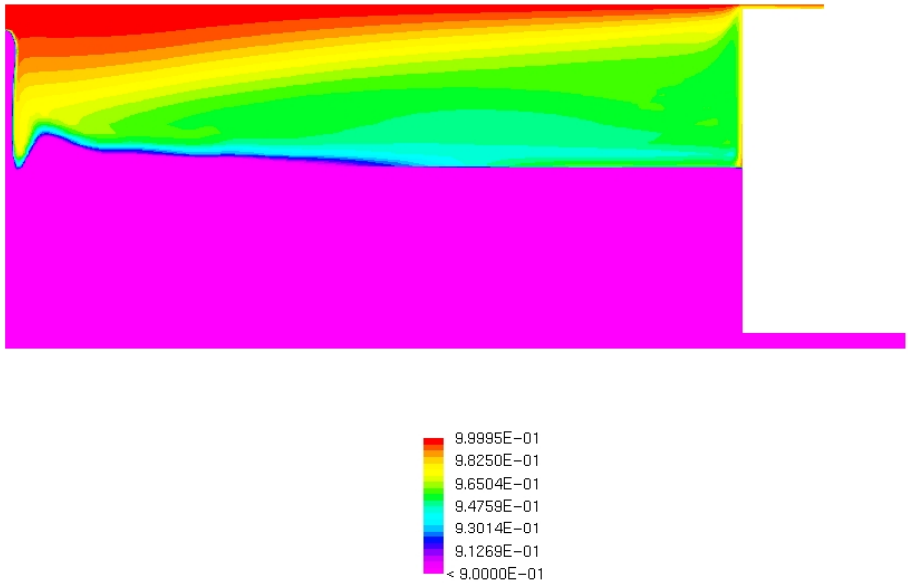

Figure 23. The volume fraction of the organic phase when $f_c = 0.05$.

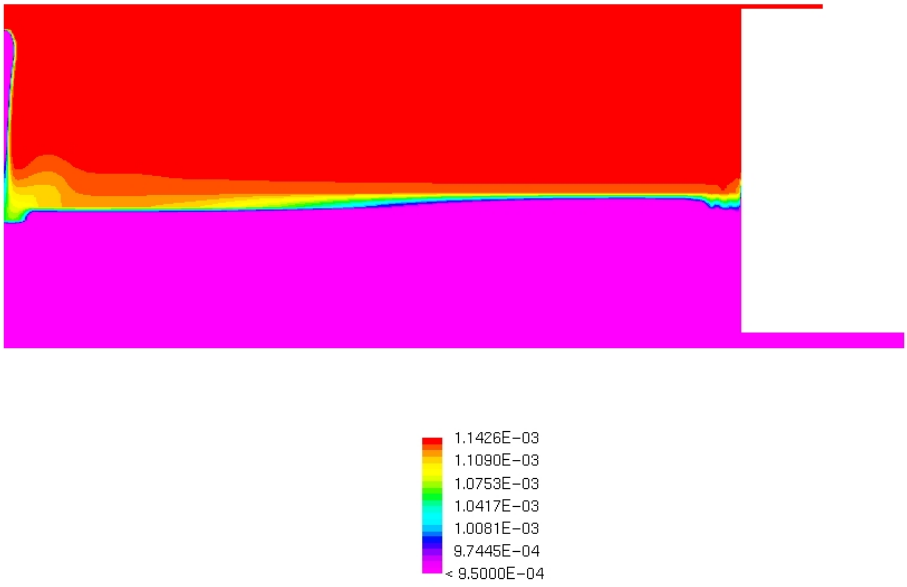

Figure 24. The Sauter mean diameter of the dispersed droplets when $f_c = 0.05$.

In the second case, all other boundary conditions were similar to those in the first case, but now the value of the coalescence calibration coefficient was decreased and set at 0.005. The volume fraction of the organic phase and the Sauter mean diameter of the droplets are shown in Figures 25 and 26, respectively. In the third case, the coalescence calibration coefficient was set at 0.01; the simulated results are shown in Figures 27 and 28.

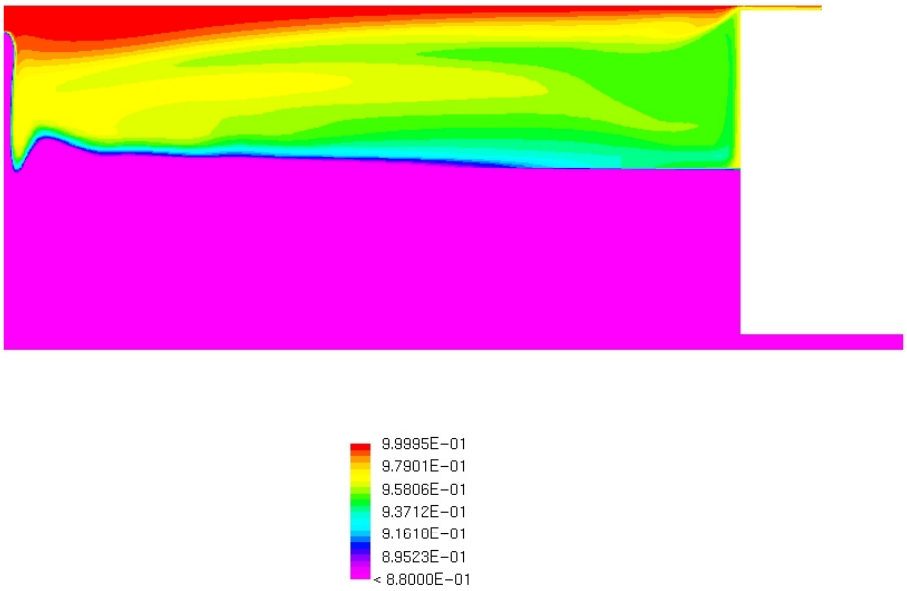

Figure 25. The volume fraction of the organic phase when f_c = 0.005.

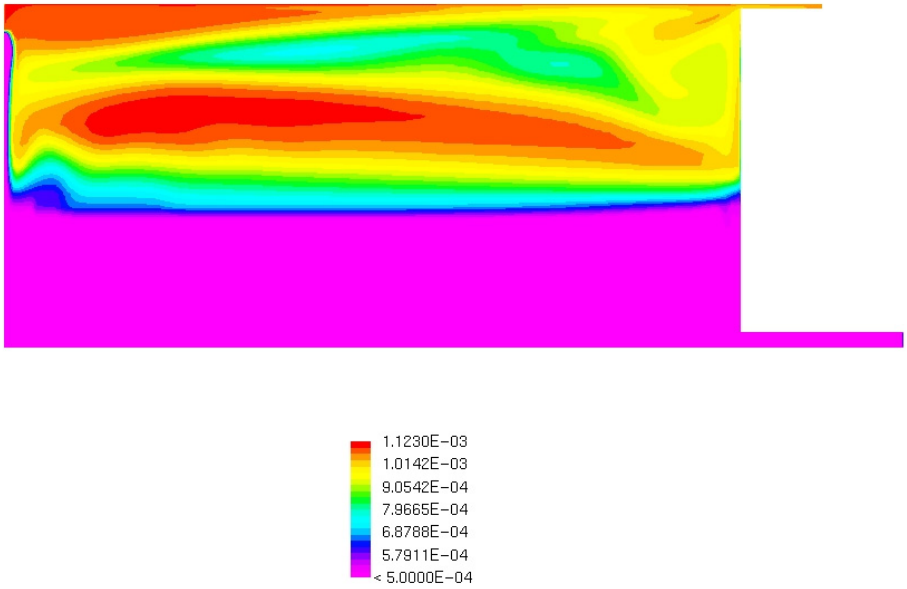

Figure 26. The Sauter mean diameter of the dispersed droplets when f_c = 0.005.

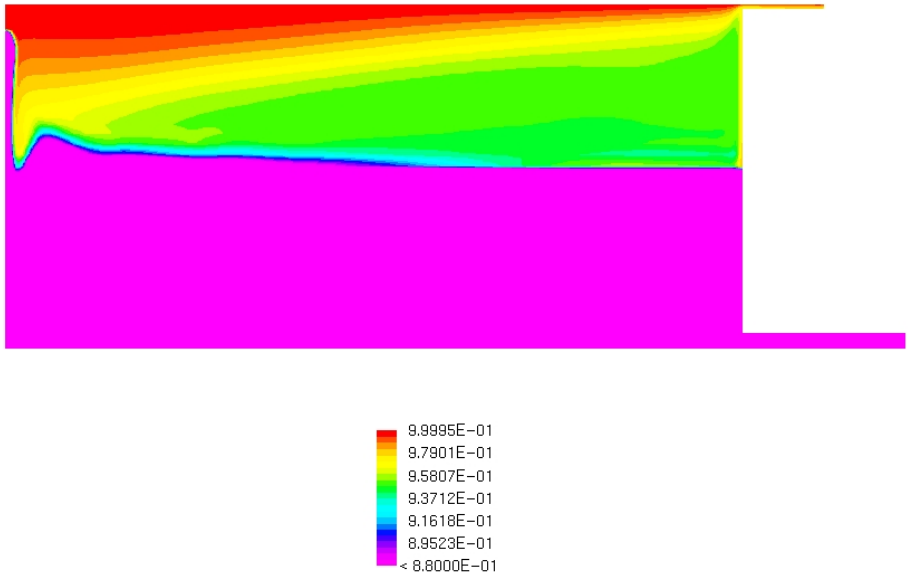

Figure 27. The volume fraction of the organic phase when $f_c = 0.01$.

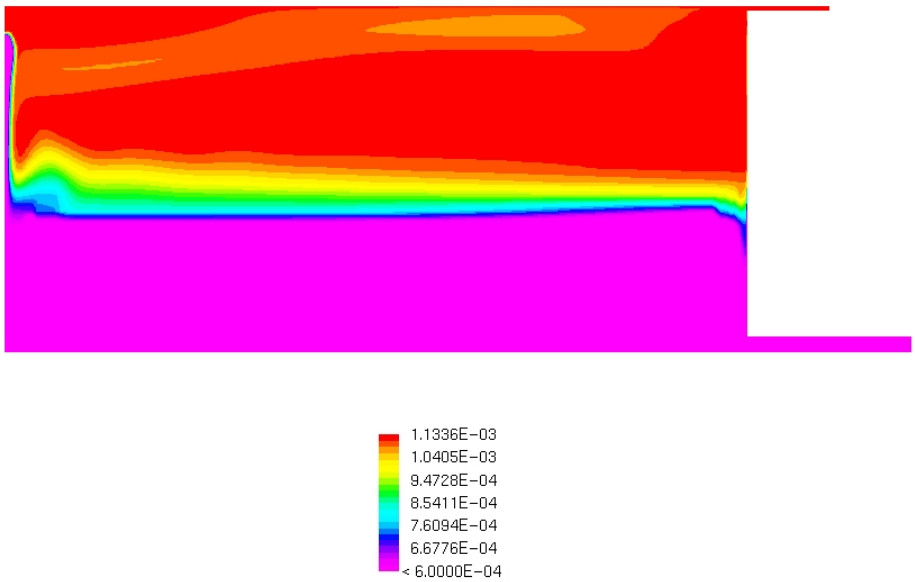

Figure 28. The Sauter mean diameter of the dispersed droplets when $f_c = 0.01$.

It can be noticed from Figures 23, 25 and 27 that the volume fraction distribution of the organic phase is similar in all cases, but the thickness of the dispersion layer is different. On the other hand, the Sauter mean diameter distributions differ quite a lot from each other. In the middle height of the settler, the droplet size distribution is most realistic in the third case. The Sauter mean diameter increases smoothly from the water-organic interface to the free surface of the settler.

After these test calculations, it could be concluded that the thicknesses of the phase layers in the CFD model depend on the selected droplet size range, the density difference of the phases, and the defined Sauter mean diameter used for drag force calculation and for the MUSIG size group distribution. Furthermore, it was decided to use the following boundary conditions for the MUSIG model: The number of the

droplet size groups was 10 and the minimum diameter of the droplet was 100 μm and the maximum diameter was 2000 μm. The mean diameter was 1000 μm. The default value of the calibration coefficient of the break-up process (f_B = 1) was used and the coalescence process was scaled by the calibration coefficient of 0.01.

6.2 Developed six item CFD calculation procedure

The simulation tests were quite complicated to carry out and the converged result was difficult to notice with the new and more realistic boundary conditions. It was thought that the difficulties were due to the similar phase densities, the separated phase layers in which the volume fraction of the other phase was almost zero and the slightly inconsistent mass flow rate of the phases between the inlet and two outlets. These supposed difficulties affected the simulation so that, near the converged point, the absolute value of the variables started to fluctuate, which further caused errors in mass flow rates and finally the mass of the continuous phase started to disappear from the calculation domain. Due to the previous difficulties, which appeared in the settler simulation, the special CFD calculation procedure was developed. Hanumanth et al. (1992) also used calculation "limits", which assisted to obtain the converged and accurate results.

The developed CFD calculation procedure for two-phase simulation was divided into six items, which all had to be obtained before the results could be confirmed as converged; the results were accurate enough.

1. Velocity profiles of the phases can be considered as stable when the fluctuation of the $\underline{u}$-velocities (main velocity component) are less than 5 to 10 %; at least two monitoring points are in a calculation domain.

2. At the outlets, total mass flow rate error of the phases should be less than 1 %.

3. Volume ratio of the phases (O/A) should be between 0.85-1.05 (Ekman, 2004) in the calculation domain.

4. Break point of the height of the continuous phase has to be reached.

5. Scaled residuals should be smaller than 10^{-4}.

6. Difference between two straight mass ratio values should be stable during the iteration (Equation (65)).

$$\Delta\left[\frac{m_{org}}{m_{water}}\right] = \left[\frac{m_{org}}{m_{water}}\right]_i - \left[\frac{m_{org}}{m_{water}}\right]_{i-1} \tag{65}$$

where m_{org} is the mass of the organic phase, m_{water} is the mass of the water phase and i is the iteration number.

CFX-4.4 did not include the option for calculating the difference between two straight mass ratio values during the iteration. Therefore, this calculation procedure was implemented into CFX-4.4 via the user subroutine. During iteration, the mass of both phases in all grid cells was calculated and then these masses were summed up and finally the mass ratio was calculated. Figure 29 shows the difference between two straight mass ratio values versus iterations when the simulation is converging. Respectively, Figure 30 shows the situation when the simulation is diverging. Break point of the continuous phase means the maximum height that the continuous phase can reach before it turns and starts to move downwards or fluctuate. During the simulation, the firsts five convergence items were quite easy to obtain, but the last item needed very careful calculation in order to make the diverging point noticeable. Therefore, simulations had to be carried out in short periods (about 10 000 - 30 000 iterations) and under-relaxation had to be decreased step by step. In general, the total number of iterations was about 100 000 - 300 000.

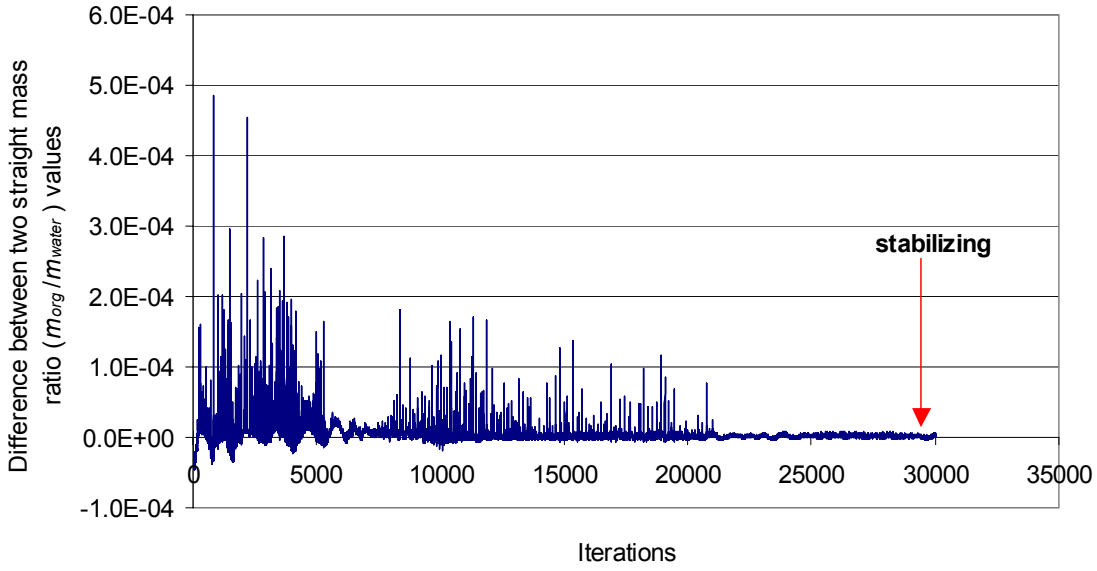

Figure 29. Difference between two straight mass ratio values versus the 30 000 iterations.

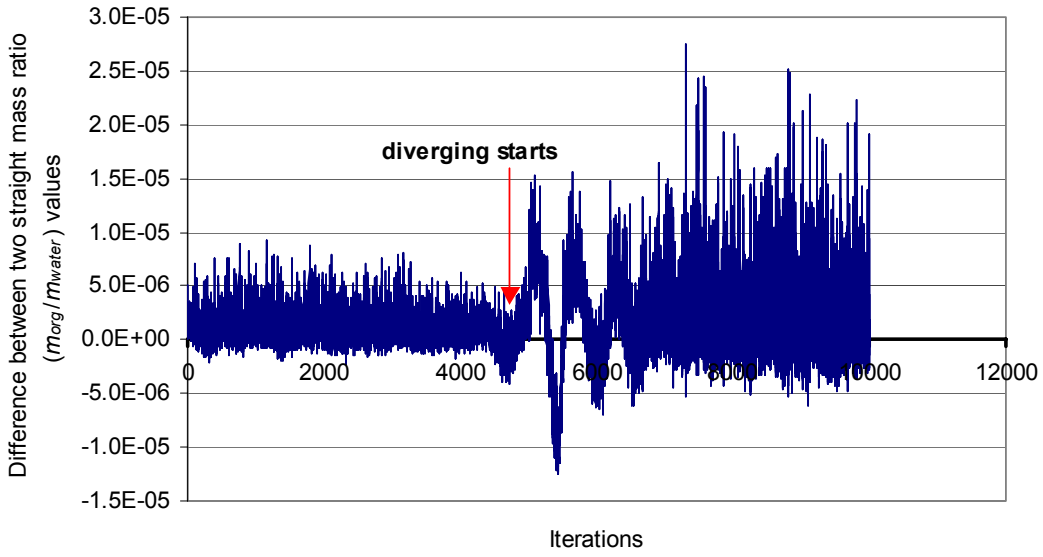

Figure 30. Difference between two straight mass ratio values versus the previous 5 000 iterations (Figure 29) and the next 5 000 iterations.

6.3 HYBRID versus QUICK scheme discretisations

Since all previous simulation cases had been carried out with the first-order (HYBRID) discretisation method, the second/third-order (QUICK) scheme was tested and the results compared with the results of the first-order calculation. The idea was to decrease the fluctuation of the variables near the converging point by increasing the discretisation method. The simulations were carried out with the developed calculation procedure and the boundary conditions were the same as those that had been used in the MUSIG calculations at a temperature of 20 °C and proposed in the end of Chapter 6.1.5. The comparison was carried out in the middle of the settler on the studying line containing 200 data points. Some of figures are shown in Appendix 2.

The velocity components ($\bar{u}$ and $\bar{v}$) agreed quite well. The largest difference between these two discretisation methods occurred in the dispersion layer in the middle height of the settler. The pressure and volume fraction of the phases were similar. The QUICK scheme predicted stronger turbulent kinetic energy for the water phase than the HYBRID method. However, for the organic phase, this was vice versa, and thus the turbulent kinetic energy was lower when the QUICK method was used. The turbulence dissipation energy of the water phase was similar in both methods, but there was a small difference when comparison was made for the organic phase. The largest difference between the QUICK and HYBRID schemes was in the volume fractions of the MUSIG groups and especially in the middle height of the settler. This difference of the MUSIG groups also affected the Sauter mean diameter values. Over all, it could be pointed out that the QUICK scheme predicted more accurate results than the HYBRID scheme, as Versteeg and Malalasekera (1995) have also mentioned, but the difference was not so large. The difference between these two discretisation methods was the largest in the dispersion layer, where the grid was not so dense (Figure 17). It would have been possible to avoid this small difference if the denser grid had been used in that area.

However, in the settler geometry it was more important to make a denser grid in the area of the upper and the lower outlets, because the developed calculation procedure was based on the mass balance controlling. If the denser grid had been also made in the middle height of the settler, the total number of grid cells would have been too large; in that case, the calculation time would have been increased too much.

According to the discretisation scheme comparison, the results and conclusions of the test simulations calculated with the HYBRID scheme were accurate enough. Thus, the developed settler model with the boundary conditions and the calculation procedure were reliable. However, it was decided to use the QUICK scheme to carry out the next simulations of the settler, when the developed CFD procedure was tested for optimization and designing work.

6.4 Temperature-related phase separation correlation coefficient

The phase separation decreases with temperature due to changed values of the physical properties. The main reason for this is that the thin film of the continuous phase between two droplets does not rupture so easily, because it is more viscous. In the MUSIG model, the temperature effect can be taken into account by the calibration coefficients. The break-up process of droplets was not scaled with temperature, but the coalescence coefficient and droplet size range were scaled with correlation Equation (66), which is based on the physical properties of the dispersed and continuous phase at different temperatures.

$$\frac{f_C^{T_1}}{f_C^{T_2}} = \frac{\Delta\rho^{T_1}}{\Delta\rho^{T_2}} \cdot \frac{\mu_d^{T_2}}{\mu_d^{T_1}} \cdot \frac{\mu_c^{T_2}}{\mu_c^{T_1}} \cdot \left(\frac{\sigma^{T_2}}{\sigma^{T_1}} \right)^{1/2} \tag{66}$$

Superscripts T_1 and T_2 indicate temperatures at which the physical properties are set, and T_2 is higher than T_1, $\Delta\rho$ is the density difference between the dispersed and the continuous phase. The correlation was developed by the theory of the coalescence rate of a droplet with its homophase. The coalescence rate decreases when the density difference decreases and the viscosity of the dispersed and the continuous phase increases. This means that the ratios of the density difference and the viscosities have to be smaller than 1 when those are compared with the ratio of the calibration coefficients. The interfacial tension is not so unambiguous because it may decrease or increase the coalescence rate, and thus the ratio is exponentiated by the value 0.5.

6.5 Transient simulation

The fluctuation phenomenon, which appeared nearby the converged solution point, was studied more carefully with the transient calculation. This was started from the converged steady-state solution and was carried out with the previous boundary conditions and, what is more, two picket fences and the QUICK scheme with the improved RHIE-CHOW (Rhie and Chow, 1983) interpolation method were used. The total time period was 41.2 s with time steps: 10^{-5} s, $5 \cdot 10^{-5}$ s, 10^{-4} s, 10^{-3} s, $5 \cdot 10^{-3}$ s, 0.01 s and 0.05 s. Figure 31 shows the $\bar{u}$-velocity of the continuous phase as a function of

time in the middle of the settler and dispersion layer. It can be noticed that the velocity value firstly fluctuates and then decreases. At 2.5 s, the velocity value agrees with the value of the fluctuating steady-state situation, which was obtained after the converged solution (Appendix 3). Although Figures A1-A2 in Appendix 3 show very small differences considering $\bar{u}$-velocity values, other variables also fluctuated to a greater or lesser degree. The overall results of the variables also changed when these were compared with the converged results of steady state. The transient CFD test proves that the dispersion flows are not totally stable in the settler. Miller (2000) has also reported the transient behaviour of the settler. He explained that an unsteady transient behaviour was due to pressure gradients, which induced high velocities. However, this instability seen in the CFD results might be either numerical or physical, but the percentage values of these two possible fluctuation reasons could not be defined by simulation. Physical measurements will be needed for a more thorough study. However, the overall situation of the settler can be considered as stable and thus the settler process can be studied as steady state when the separation time between the phases is not of primary interest.

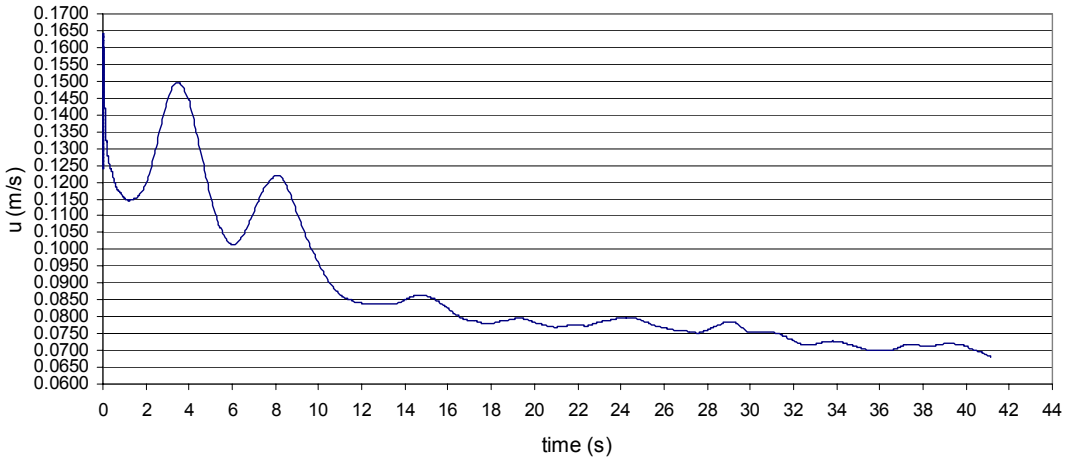

Figure 31. $\bar{u}$-velocity of the continuous phase versus time in the middle of the settler and the dispersion layer.

7 MODELLING OF DESIGN PARAMETERS OF THE SETTLER

The developed CFD calculation procedure was applied to the pilot settler process, which is presented in Figure 7. The previous constant droplet size simulations were extended so that the coalescence and break-up processes with two different temperatures and two specific volume flow rates were taken into account. The settler was simulated without picket fences and with one and two picket fences (Figure 8). The locations of the picket fences are shown in Figure 16. At a temperature of 20 °C, the droplet size range from 100 μm to 2000 μm was divided into 10 size groups, which are shown in Table VI. The mean diameter was 1000 μm and the calibration coefficients of the break-up process (f_B) and the coalescence process (f_C) were 1 and 0.01, respectively.

Table VI. Musig model group discretisations at a temperature of 20 °C, when droplet sizes are equally divided.

Musig group number	Minimum droplet diameter (μm)	Maximum droplet diameter (μm)	Mean droplet diameter (μm)
1	100	290	233
2	290	480	407
3	480	670	590
4	670	860	777
5	860	1050	964
6	1050	1240	1153
7	1240	1430	1342
8	1430	1620	1531
9	1620	1810	1720
10	1810	2000	1910

At a temperature of 10 °C, the droplet size range, the mean droplet diameter and the calibration coefficient of the coalescence process were scaled by the value of 0.6, which was calculated by Equation (66). Thus the mean droplet diameter was 600 μm and f_C was 0.006. The droplet size groups are shown in Table VII.

Table VII. Musig model group discretisations at a temperature of 10 °C, when droplet sizes are equally divided.

Musig group number	Minimum droplet diameter (μm)	Maximum droplet diameter (μm)	Mean droplet diameter (μm)
1	60	174	140
2	174	288	244
3	288	402	354
4	402	516	466
5	516	630	579
6	630	744	692
7	744	858	805
8	858	972	919
9	972	1086	1032
10	1086	1200	1146

At the inlet, the organic-aqueous (O/A) ratio was 1. Other boundary conditions are given in Tables VIII and IX. The calculations were carried out in turbulent, isothermal, incompressible and steady-state situations. The free surface (organic-air interface) was treated as a flat and frictionless wall. The sidewalls of the settler were treated as the symmetry planes. The drag force correlation of Ishii-Zuber (1979) was used and the value of 0.1 was used for the lift force coefficient (Behzadi et al., 2004; Thakre and Joshi, 1999) and for the turbulent dispersion coefficient (Olmos et al., 2001). The QUICK discretisation scheme was used. The default values of the initial (10^{-4} m) and the critical film thicknesses (10^{-8} m) of the continuous phase were used. The droplet size distribution, which was set at the inlet, was quite similar at both temperatures, because, as Ruiz et al. (2001) reported, the droplet size distribution was independent of temperature. They explained that the mixing vessel was in balance between the droplets coalescence and break-up processes. Thus, it was assumed that the mixer in the pilot unit behaved in a similar way.

Table VIII. Boundary conditions at a temperature of 20 °C.

	Water phase	Organic phase	c (mm)
Re-numbers at the inlet (V_{spec} = 12 m^3/m^2h)	9727	5406	17
Normal velocity at the inlet (m/s)	0.108	0.108	
Re-numbers at the inlet (V_{spec} = 6 m^3/m^2h)	4864	2702	10
Normal velocity at the inlet (m/s)	0.054	0.054	
Turbulence intensity at the inlet	5.0 %	5.0 %	
Dissipation length scale (m) at the inlet	0.114	0.114	
Mean droplet sizes (μm) at the inlet		Volume fraction	
233		0.4	
407		0.3	
590		0.2	
777		0.1	

Table IX. Boundary conditions at a temperature of 10 °C.

	Water phase	Organic phase	c (mm)
Re-numbers at the inlet (V_{spec} = 12 m^3/m^2h)	7675	4737	17
Normal velocity at th inlet (m/s)	0.108	0.108	
Re-numbers at the inlet (V_{spec} = 6 m^3/m^2h)	3838	2368	10
Normal velocity (m/s) at the inlet	0.054	0.054	
Turbulence intensity at the inlet	5.0 %	5.0 %	
Dissipation length scale (m) at the inlet	0.114	0.114	
Mean droplet sizes (μm) at the inlet		Volume fraction	
244		0.4	
354		0.3	
466		0.2	
579		0.1	

7.1 Results

CFD results were divided into five different parts, which are all important in designing the settler: thickness of the dispersion layer, pressure drop over the picket fence, droplet size distribution, linear velocity of the organic phase at the top of the settler, hydrodynamic force balances. Results were defined from seven study lines, which are shown in Figure 32. Study lines A, B and C contained 399 points, line D contained 362 and lines E, F and G contained 326.

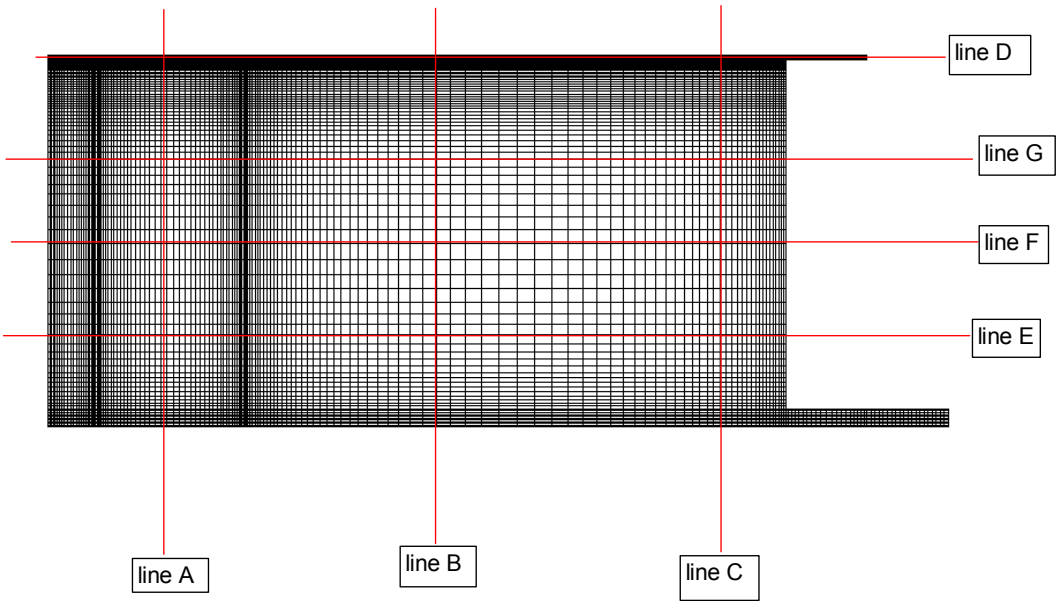

Figure 32. Study lines and their locations. The place of line A is 427.5 mm from the front end of the settler and it locates between two picket fences, line B is 1275.5 mm from the front end of the settler and line C is 2349.5 mm from it. Lines E, F and G locate at the height of 300 mm, 600 mm and 900 mm from the bottom, respectively. Line D locates at the height of 1188 mm, when the specific volume flow rate is 6 m^3/m^2h and at the height of 1195 mm, when the specific volume flow rate is 12 m^3/m^2h. The place of the overflow weir is 2584 mm from the front end of the settler. (Notice that the line locations are not in scale.)

7.1.1 Thickness of the dispersion layer

The thickness of the dispersion layer is not unambiguous, because it depends on the amount of entrainments, which may vary in different locations of the settler due to circulation flows. Furthermore, validation is also quite a difficult, because the experimental measurement values are usually taken only from some places at the top of the settler.

Due to these difficulties, the thickness of the dispersion layer was defined from study lines A, B and C, and allowed entrainment amounts 0.5 vol-% (5 000 ppm), 2.0 vol-% (20 000 ppm) and 5.0 vol-% (50 000 ppm) were used in both phases. This meant that, in the upper part of the settler, the organic phase might contain 5 000 ppm, 20 000 ppm or 50 000 ppm water as an entrainment and, conversely, in the lower part of the settler, the continuous water phase might contain the same amounts of organic as an entrainment. The thickness of the dispersion layer on lines A, B and C as a function of the picket fences (0, 1 and 2), temperatures (10 °C and 20 °C) and the specific volume flow rates (6 m^3/m^2h and 12 m^3/m^2h) are shown in Tables X and XI. The volume fractions of the organic phase with different specific volume flow rates, temperatures and picket fences are presented in Appendix 4.

Table X. Predicted thicknesses of the dispersion layer in millimetres at a temperature of 10 °C.

V_{spec}	entrainment	**No picket fences**			**One picket fence**			**Two picket fences**		
(m^3/m^2 h)	(vol-%)	Line A	Line B	Line C	Line A	Line B	Line C	Line A	Line B	Line C
6	0.5	587	645	626	475	531	599	650	468	544
6	2.0	431	512	543	200	136	131	480	130	152
6	5.0	208	175	120	141	118	109	322	113	121
12	0.5	660	669	675	595	591	637	766	494	150
12	2.0	512	579	594	354	461	526	622	156	129
12	5.0	275	366	412	191	157	122	505	122	115

Table XI. Predicted thicknesses of the dispersion layer in millimetres at a temperature of 20 °C.

V_{spec}	entrainment	**No picket fences**			**One picket fence**			**Two picket fences**		
(m^3/m^2 h)	(vol-%)	Line A	Line B	Line C	Line A	Line B	Line C	Line A	Line B	Line C
6	0.5	515	646	634	210	136	175	536	135	164
6	2.0	193	156	93	167	120	116	291	110	130
6	5.0	153	95	87	128	90	89	140	88	100
12	0.5	579	666	667	222	204	135	633	134	134
12	2.0	247	240	111	191	147	123	427	124	106
12	5.0	196	132	89	146	109	99	276	104	88

7.1.2 Pressure drops over picket fences

The average pressure drop value over the picket fence was defined by a difference of 399 pressure values, which were situated 1.0 mm before and after the picket fence. Because the picket fence restricts the dispersion flow, it dams the organic phase or the dispersion at the front of the fence. This height of the liquid layer was defined with the pressure drop value and the density of the dispersion. The pressure drop values over the total height of the fence and in the middle of the fence are shown in Table XII.

Table XII. The average pressure drop values over the picket fence.

	One PF		Two picket fences				One PF		Two picket fences			
Fence	I		I		II		I		I		II	
V (m^3/m^2h)	6		6		6		12		12		12	
T (°C)	10	20	10	20	10	20	10	20	10	20	10	20
Δp* (Pa)	56	48	52	44	23	21	126	115	115	113	78	76
Δp^* (mm)	6	5	6	5	2	2	14	12	12	12	8	8
Δp^{**} (Pa)	127	103	114	96	36	26	274	236	244	225	111	87
Δp^{**} (mm)	14	11	12	10	4	3	30	26	26	24	12	9

When T = 10 °C, density of the dispersion is 946.3 kg/m^3

When T = 20 °C, density of the dispersion is 941.35 kg/m^3

* Pressure drop over the total height of the picket fence

** Pressure drop in the middle of the picket fence (424-854 mm / 424-856 mm)

7.1.3 Droplet size distributions

Droplet size distributions were defined at five different locations of the settler, which are shown in Figure 33. These locations were selected from the dispersed phase flow path. Figures 34-38 show the droplet size distributions from the inlet to the organic overflow weir, when the specific volume flow rate is 12 m^3/m^2h and the temperature is 20 °C. The other droplet size distributions are similar with the specific volume flow rate 12 m^3/m^2h and 10 °C and with 6 m^3/m^2h at temperatures 10 °C and 20 °C; they are shown in Appendixes 5-7.

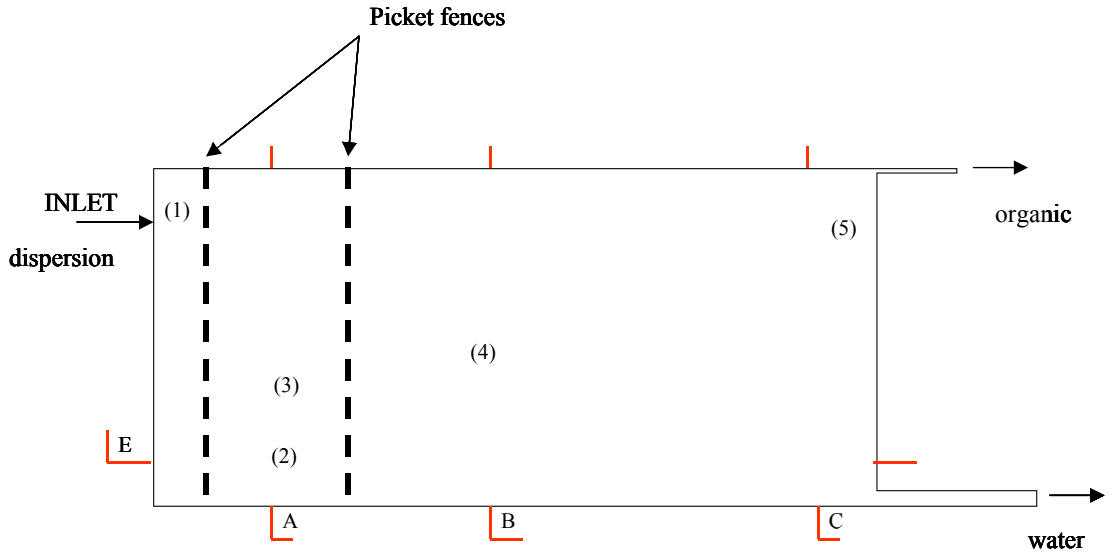

Figure 33. Locations in which the droplet size distributions are defined. The location number (1) is at the inlet, number (2) is at the intersection of lines A and E (Figure 32), number (3) is at the height of 500 mm on line A, number (4) is in the middle of the dispersion layer at the height of 600 mm on line B and number (5) is near the overflow weir.

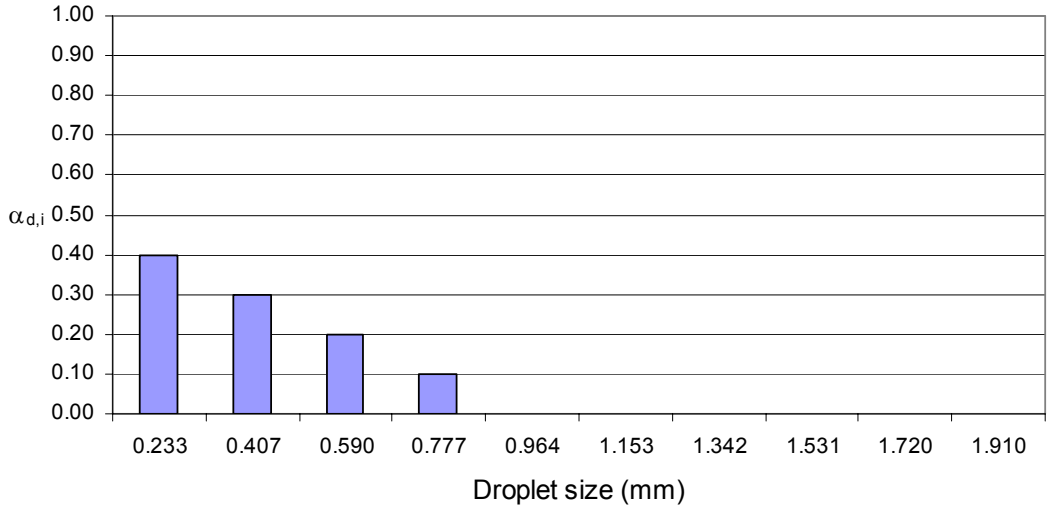

Figure 34. Droplet size distribution at point (1) when the specific volume flow rate is 12 m^3/m^2h and the temperature is 20 °C.

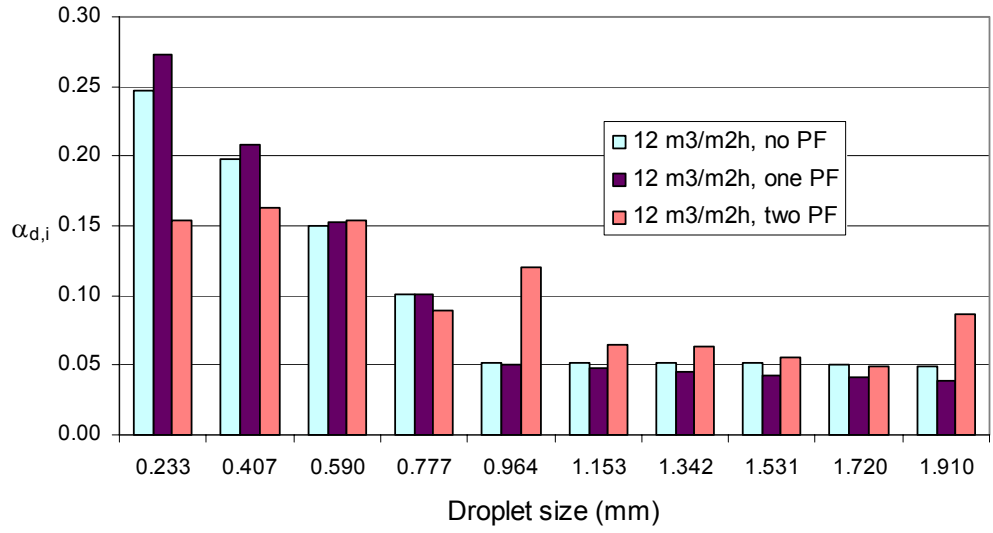

Figure 35. Droplet size distributions at point (2) for different numbers of picket fences (PF), when the specific volume flow rate is 12 m^3/m^2h and the temperature is 20 °C.

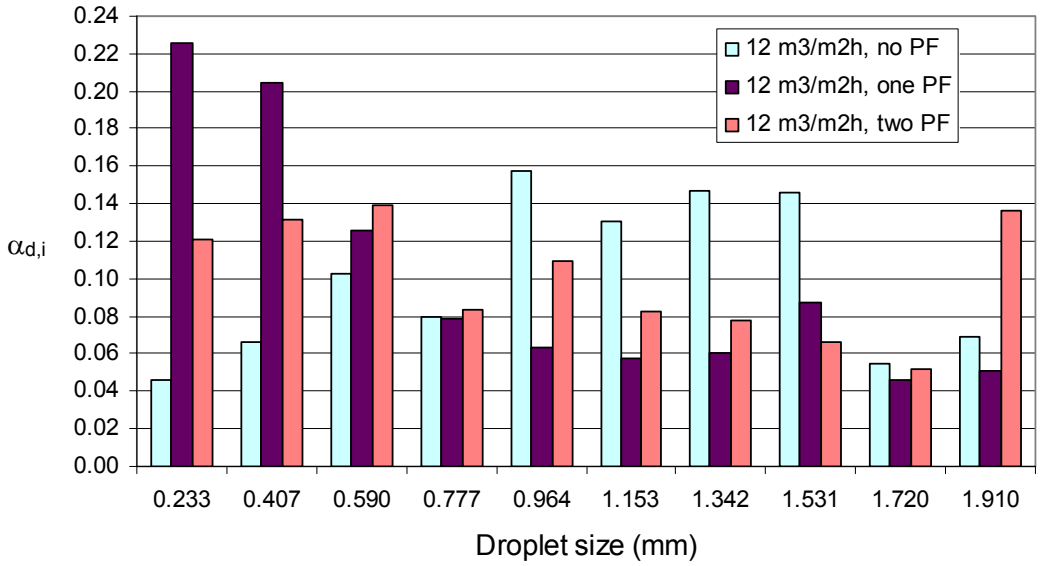

Figure 36. Droplet size distributions at point (3) for different numbers of picket fences (PF), when the specific volume flow rate is 12 m^3/m^2h and the temperature is 20 °C.

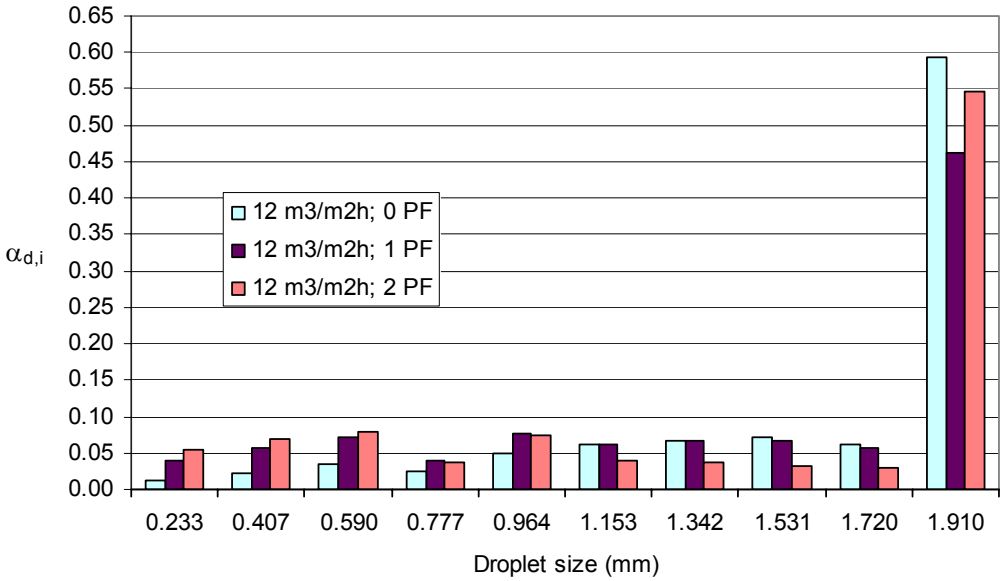

Figure 37. Droplet size distributions at point (4) for different numbers of picket fences (PF), when the specific volume flow rate is 12 m^3/m^2h and the temperature is 20 °C.

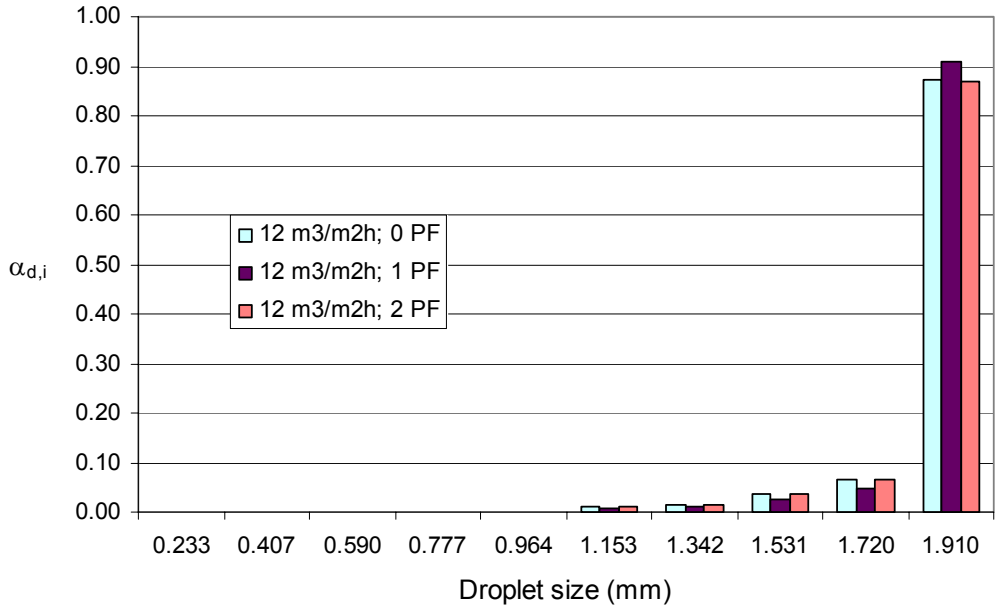

Figure 38. Droplet size distributions at point (5) for different numbers of picket fences (PF), when the specific volume flow rate is 12 m^3/m^2h and the temperature is 20 °C.

7.1.4 Linear velocity of the organic phase

Figures 39-42 show the linear velocity of the organic phase with the temperatures, the specific volume flow rates and the picket fences as a function of the settler length on line D. Y-axis is scaled so that the difference between the picket fences can be seen. The original figures are shown in Appendix 8.

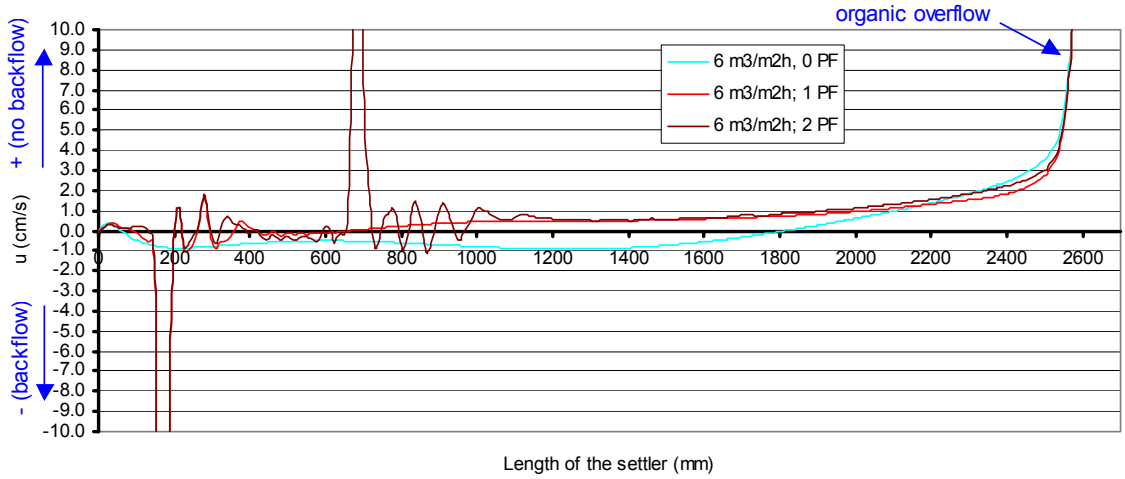

Figure 39. Linear velocity of the organic phase on line D, when the temperature is 10 °C and the specific volume flow rate is 6 m^3/m^2h.

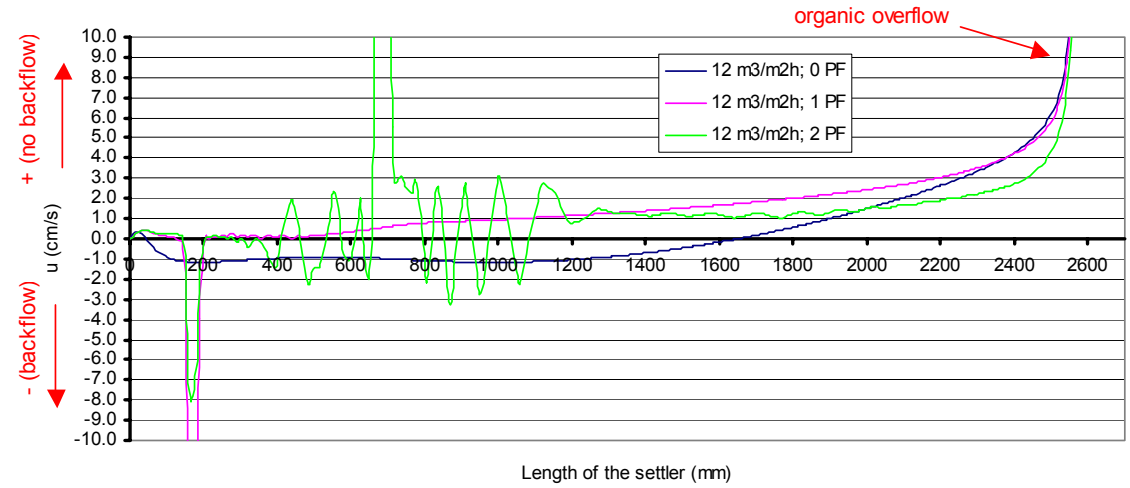

Figure 40. Linear velocity of the organic phase on line D, when the temperature is 10 °C and the specific volume flow rate is 12 m^3/m^2h.

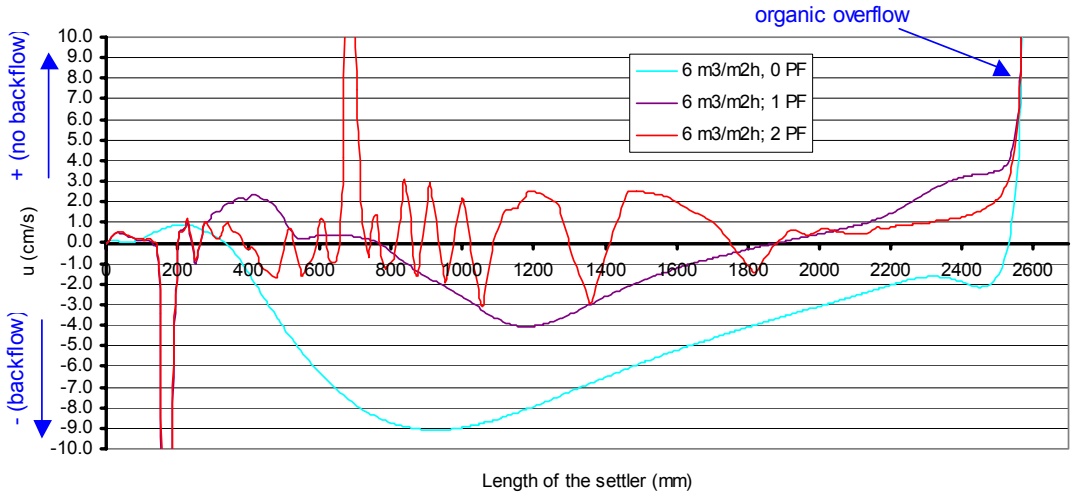

Figure 41. Linear velocity of the organic phase on line D, when the temperature is 20 °C and the specific volume flow rate is 6 m^3/m^2h.

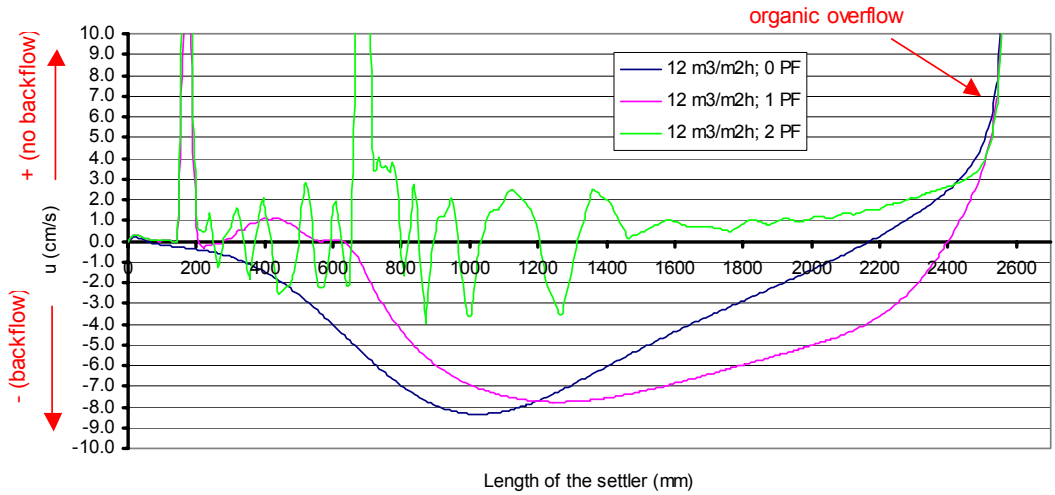

Figure 42. Linear velocity of the organic phase on line D, when the temperature is 20 °C and the specific volume flow rate is 12 m^3/m^2h.

7.1.5 Hydrodynamic force balances

In physical experiments, dimensionless group numbers, such as Reynolds number, are usually defined only for the total process, because the detailed velocity information is unavailable. Now this "problem" can be solved when CFD modelling is used because it gives an opportunity to create a very detailed velocity profile and thus local dimensionless group numbers can be calculated. In this study, Reynolds (Equation (67)), Froude (Equation (68)) and Weber (Equation (69)) numbers were defined on study lines A, B, C, E, F and G. These three dimensionless group numbers represent buoyancy, surface, inertia and viscous forces, which control the separation process as a point of view of hydrodynamics.

The Reynolds number represents the ratio of inertia forces to viscous forces:

$$Re = \frac{\rho V_o L}{\mu} \Leftrightarrow \frac{inertia}{viscous} \tag{67}$$

The Froude number represents the ratio of inertia forces to buoyancy forces:

$$Fr = \frac{V_o^2}{Lg} \Leftrightarrow \frac{inertia}{buoyancy} \tag{68}$$

The Weber number represents the ratio of inertia forces to surface forces:

$$We = \frac{\rho V_o^2 L}{\sigma} \Leftrightarrow \frac{inertia}{surface} \tag{69}$$

Force balances between these forces can be calculated from the ratios of *Re*-, *Fr*- and *We*-numbers, which are given in Equations (70), (71) and (72).

$$\frac{Re}{Fr} = \frac{\rho \cdot g}{\mu} \cdot \frac{L^2}{V_o} \Leftrightarrow \frac{buoyancy}{viscous} \tag{70}$$

$$\frac{Re}{We} = \frac{\sigma}{\mu} \cdot \frac{1}{V_o} \Leftrightarrow \frac{surface}{viscous} \tag{71}$$

$$\frac{Fr}{We} = \frac{\sigma}{g \cdot \rho} \cdot \frac{1}{L^2} \Leftrightarrow \frac{surface}{buoyancy} \tag{72}$$

The relative velocity, Sauter mean diameter of droplets used as a characteristic length (L) and the physical properties of the continuous phase are used in dimensionless group numbers when behaviour and disengagement of the dispersion are of interest. On the other hand, L can be either a liquid depth of the settler or a hydraulic diameter of the settler, but then the dimensionless group numbers represent overall force balances in the settler. In these cases, fluid velocity (V_o) is either the mean vectorial velocity of the continuous phase ($\boldsymbol{U}_c$) or the mean vectorial velocity of the dispersed phase ($\boldsymbol{U}_d$), and thus the physical properties are also selected for the certain phase. In this study, the liquid depth only is used, because it is more typical for the deep and narrow settler unit.

The average values of the dimensionless group numbers and their ratios were calculated on study lines A, B, C, E, F and G. The force balances in proportion to viscous forces for the dispersion are shown in Appendix 9. The detailed profiles of the force balance between the surface and the buoyancy forces as a function of the height of the liquid on lines A, B and C, are shown in Appendix 10. The force balances for the continuous phase and for the dispersed phase are shown in Appendix 11.

8 DISCUSSION

8.1 Simulation with the developed calculation method

The boundary conditions performed well in both specific volume flow rate cases. The grid was dense enough in the outlet areas to ensure that the mass flow rate of the phases could be followed exactly during calculations. The total mass flow rate error was less than 1 % and backflow could be avoided in both outlets. In each case, the calculation proceeded so that, firstly, the thickness of the continuous phase layer became thicker and thicker, while, at the same time, the entrainment levels decreased in both phases. After the continuous phase had reached its maximum height, the thickness of the dispersed phase layer started to increase. The specific volume flow rate and temperature controlled the thickness of the dispersion layer. This phenomenon behaved in a way similar to its behaviour in real water continuous processes. The drop-drop coalescence was prevailing in the feed end of the settler and between the picket fences, and the drop-interface coalescence was prevailing in the rear end of the settler.

The results suggested that the developed calculation procedure was valid and performed well. The most important factor was that the procedure ensured that all cases could be calculated in a similar manner, and thus the results were comparable. Due to the Eulerian-Eulerian two-phase model, together with the MUSIG model and the phase separation phenomenon with two separate outlets, all cases had to be carried out in short periods and under-relaxation had to be decreased step by step. In general, there were about five to ten calculation periods and each of them had about 20 000 to 30 000 iterations. This meant that about 100 000 to 300 000 iterations were needed for the converged result. CPU-times in Table XIII indicate that the calculation cases took a lot of time, although the used computer was quite powerful. It can be seen that total CPU-times increase very much when the number of MUSIG groups are doubled. This points out that, if the calculation times have to be kept reasonably short, the accuracy of the physical phenomena has to be given up to some extent. In future, when computing capacity will increase as Moore's law predicts (Tuomi, 2002), two-phase calculations will be carried out in a much more shorter time. On the other hand, increasing calculation resources usually also allow the use of more accurate physical models and thus the calculation times will remain quite similar to current times.

During the calculations it was noticed that the overall results did not differ so much from the final results when the iterations had been calculated about 70 to 80 % of the fully converged case. Of course the results were not so accurate because the convergence criteria were not totally fulfilled. However, this highlights the fact that calculation times can be decreased when the convergence criteria are slightly eased. This option is useful when, for example, different kinds of geometries of a settler are tested. Results can be achieved in a shorter time and the test cases are anyway comparable, which is important when the final conclusions are drawn.

Although the turbulence model was not the point of our focus, it was noticed that, on the walls, Y^+ -values were quite small for both phases. For the continuous phase, Y^+-values varied between 0.3 and 110 and, for the dispersed phase, between 0.04 and 64. This meant that the used k-ε turbulence model with standard logarithmic wall function

overestimated slightly the velocity values near the walls, because the grid was too dense. According to Versteeg and Malalasekera (1995), Y^+-values should be between 30 and 500 for the standard k-ε model. However, this inaccuracy could not be avoided, because the grid had to be made very dense near the area of the lower and upper outlets due to the boundary conditions. According to that, the height of one cell became very small because the heights of the outlets were already small. Both outlets had ten cells in the vertical direction, which ensured that the mass flow rate balance calculation for both phases was accurate enough. These inaccurate velocity values due to the turbulence model near the walls do not affect the phase separation substantially, but it is possible that they have some influence on developed swirls, which may grow, and thus disturb the true phase separation. On the other hand, nothing can be said about this effect with regard to the results of the simulated cases, and thus more studies are needed from the area of turbulence in multiphase flows. Generally speaking, the k-ε turbulence model was assumed to perform quite well when it was applied to the droplet coalescence and break-up processes of the MUSIG model.

Table XIII. CPU-time as a function of numbers of the MUSIG groups and iterations.

Computer:	Pentium IV, 3.2 GHz, memory 2 Gb			
Number of MUSIG groups	Iterations between MUSIG groups	Average CPU-time (h) / 10 000 iterations	Average number of total iterations for converged result	Approximately total CPU-time (h)
0*	0	1.9	91 000	17
5	50	2.9	84 000	24
5	100	2.8	81 000	23
5	200	2.8	81 000	23
5	400	3.1	81 000	25
10	50	4.3**		
10	100	4.3**		
10	200	4.3	100 000 - 280 000	43 - 120
10	200	5***	100 000 - 280 000	50 - 140
10	400	4.8**		

*Normal two-phase Eulerian-Eulerian calculation.

**Approximated from the simulated results

***Maximum average CPU-time (h), which depends on the numbers of total iteration per calculation step

8.2 Flow pattern of the dispersion

In the front end of the settler, when the dispersion flows out from the inlet, it first turns down and moves towards the bottom of the settler. Half way down the settler height, it turns again and moves towards the settler back wall, where the water phase flows through the lower outlet and the organic phase through the upper outlet. In the lower and upper parts of the settler, there appears a backflow. Lewis (1979) also reported about a similar phenomenon when the settler was operated without baffles. Actually, the backflow causes some kind of circulation flow below and above the dispersion layer. Above the dispersion layer, when the dispersion strikes against the settler back wall, the flow turns up and moves in the opposite direction. In proportion, below the dispersion layer, the flow turns down and moves in the opposite direction. These circulation flows and the dispersion flow are stronger when the specific volume

flow rate and temperature increase (viscosities are lower). The flow pattern of the dispersion for the case of V_{spec} = 12 m^3/m^2h, T = 20 °C and without picket fences is shown in Figure 43 only as an example because a similar flow phenomenon was obtained in all other cases.

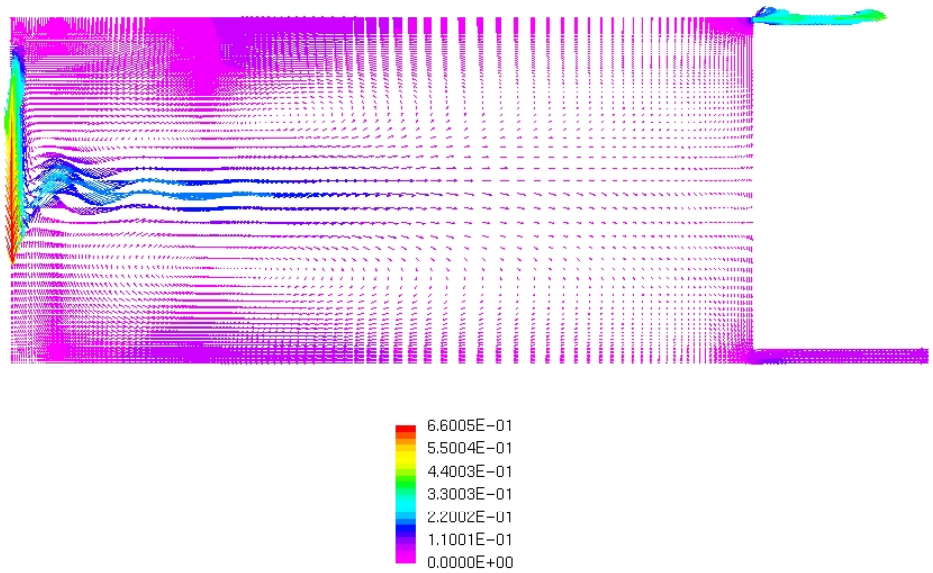

Figure 43. Flow pattern (m/s) of the dispersion without picket fences when V_{spec} = 12 m^3/m^2h and T = 20 °C.

When the droplet size was not large enough, the dispersion down flow did not occur (Figures 44, 45 and 46). This was noticed during the test calculations when the appropriate droplet size range was tested. The down flow effect occurred when the droplet size was larger than about 200 μm.

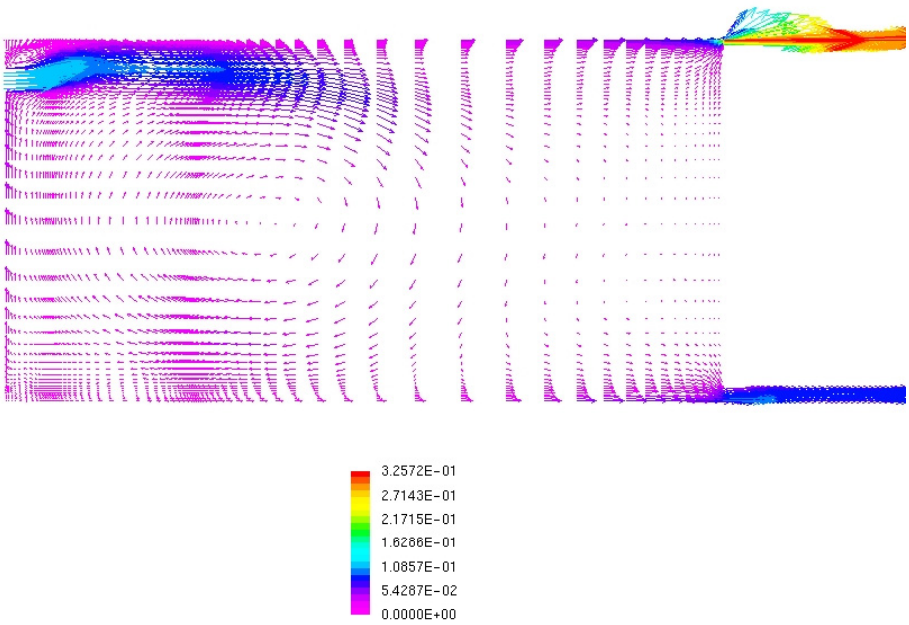

Figure 44. Flow pattern (m/s) of the dispersion when the droplet size is 100 μm and V_{spec} = 12 m^3/m^2h.

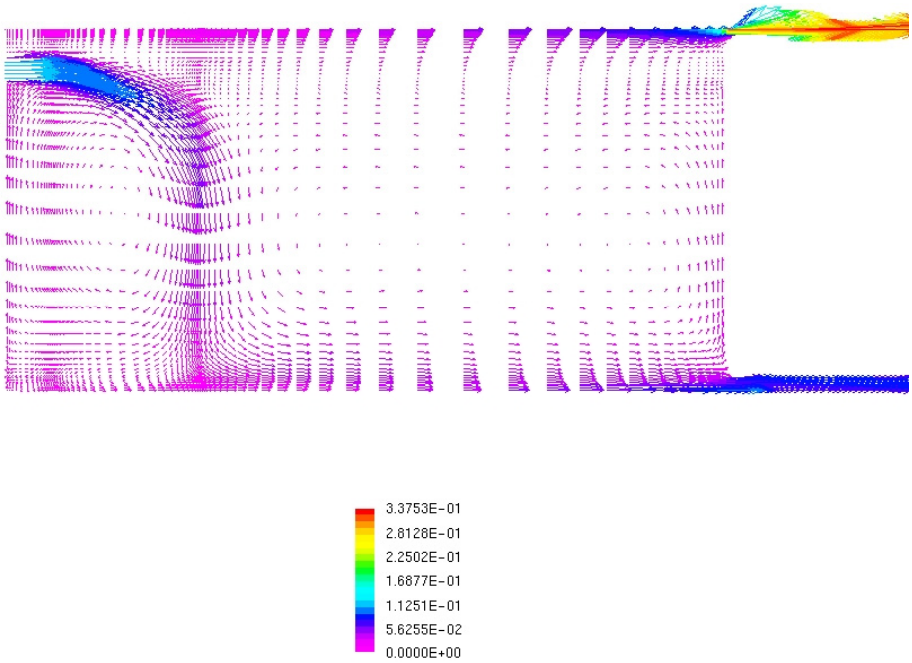

Figure 45. Flow pattern (m/s) of the dispersion when the droplet size is 200 μm and V_{spec} = 12 m^3/m^2h.

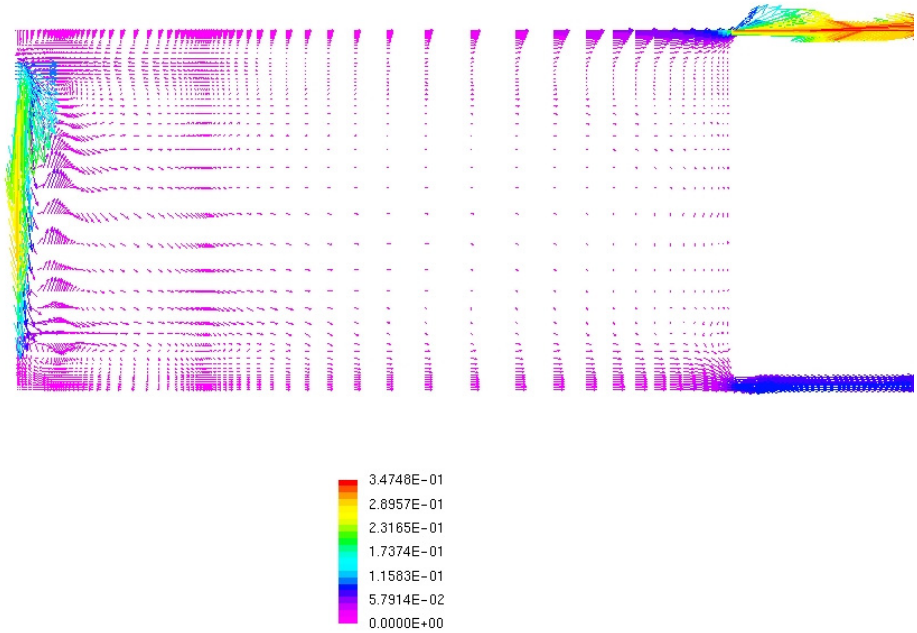

Figure 46. Flow pattern (m/s) of the dispersion when the droplet size is 300 μm and V_{spec} = 12 m^3/m^2h.

The dispersion down flow is a consequence of gravitational force. However, at some point, the buoyancy effect becomes significant and the droplet moves up. Thus, this upwards and downwards flow of the dispersion or droplets depends on the gravitational and buoyancy forces, which control the kinetic energy of the dispersion flow. This

phenomenon can be described as follows: When the phases do not separate from each other (the droplet size is smaller than 200 μm), the incoming dispersion discharges into the dispersion layer, which has the same density. In this case, the gravitational and buoyancy forces do not affect the flow pattern. However, the situation is different when the incoming dispersion discharges into the lighter separated dispersed phase layer. Then the heavier dispersion flow turns downwards due to the density difference and the gravitational force. In the lower part of the settler when the dispersion meets the separated continuous phase (higher density), the dispersion flow turns upwards due to the buoyancy force and the density difference.

In the porous media, which describes the picket fence, the dispersion flow is increased and the fluctuating flow is slightly damped. However, the first picket fence is not effective enough for hindering the dispersion flow. The circulation flow can be damped only when two picket fences are set into the settler. It does not totally disappear, but its length is smaller than without the picket fences or with one picket fence. Since the flow patterns were similar in all cases, only the flow pattern of the dispersion for the case of V_{spec} = 12 m^3/m^2h, T = 20 °C with one and two picket fences are presented in Figures 47 and 48. It can be seen from Figures 49 and 50 that near the overflow weir the circulation pattern at 20 °C is not so strong when two picket fences are used. At a lower temperature, the difference between two picket fences and without picket fences is not so clear. This "un-circulating" phenomenon can be also seen when linear velocity of the organic phase is plotted as a function of the length of the settler (Figures 39-42). It can be noticed that the linear velocity does not fluctuate so much when picket fences are used. In the front end of the settler and between the picket fences, the dispersion flow circulates quite strongly (Figure 51). However, this is good for phase separation, because, in this case, turbulence is strong (Figure 52), and thus droplets break-up and coalescence processes take place effectively. This further means that droplet size distribution is also quite uniform, because larger droplets break up into smaller ones and smaller droplets coalesce into bigger ones.

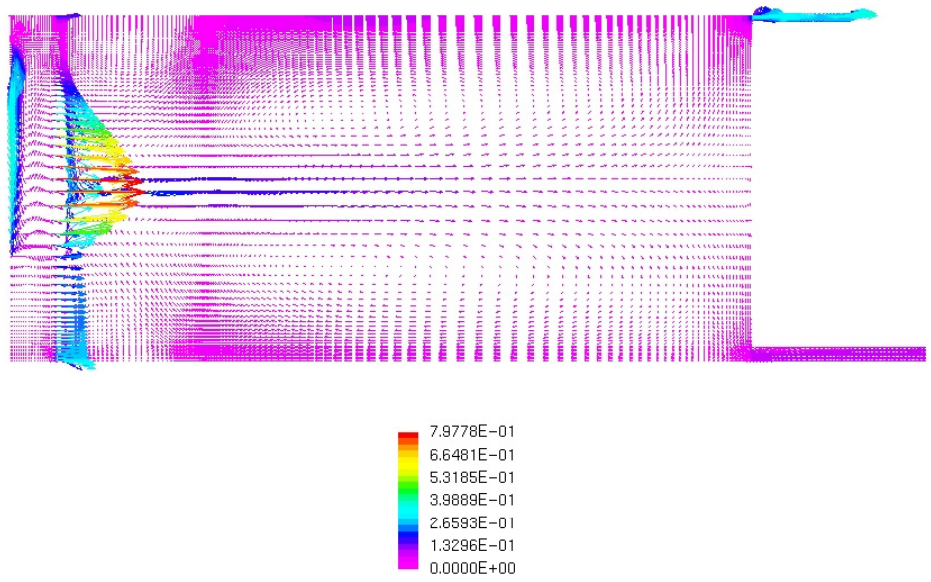

Figure 47. Flow pattern (m/s) of the dispersion when V_{spec} = 12 m^3/m^2h, T = 20 °C and there is one picket fence.

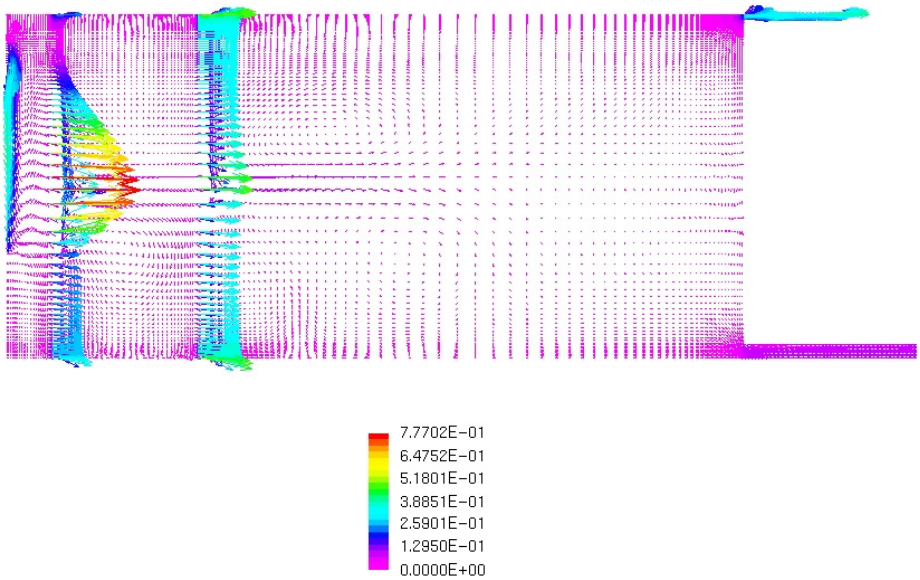

Figure 48. Flow pattern (m/s) of the dispersion when V_{spec} = 12 m^3/m^2h, T = 20 °C and there are two picket fences.

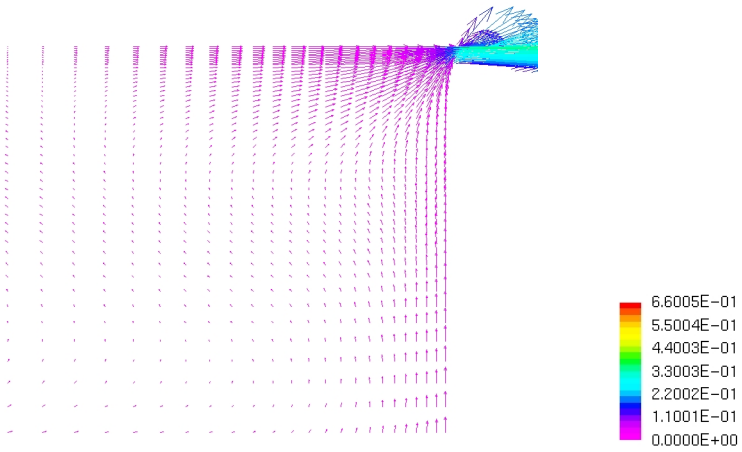

Figure 49. Flow pattern (m/s) of the dispersion near the overflow weir when V_{spec} = 12 m^3/m^2h, T = 20 °C and there are no picket fences.

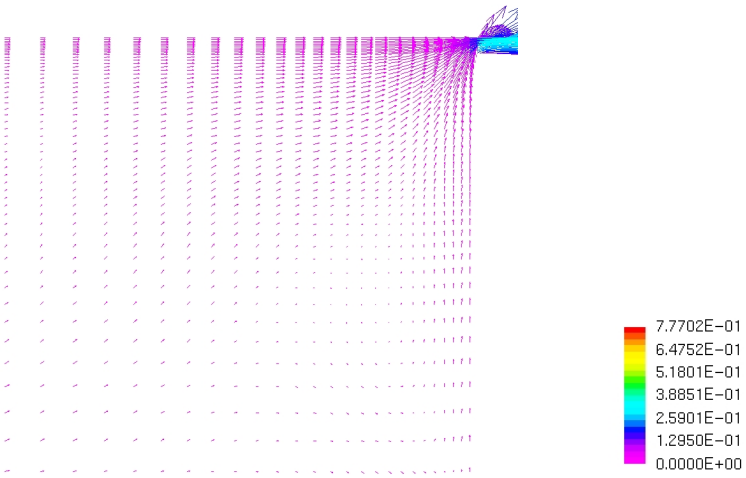

Figure 50. Flow pattern (m/s) of the dispersion near the overflow weir when V_{spec} = 12 m^3/m^2h, T = 20 °C and there are two picket fences.

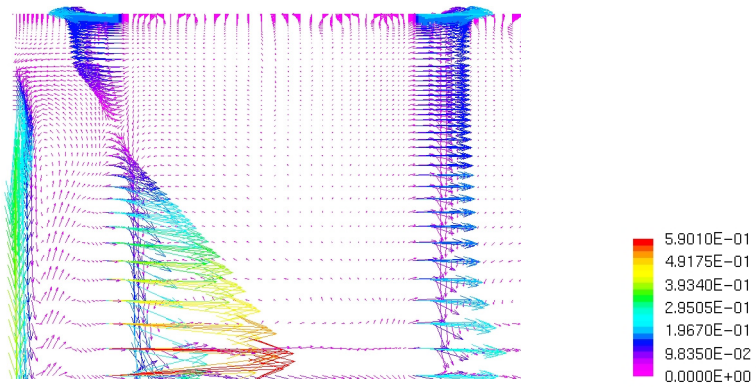

Enlarged view from the inlet area

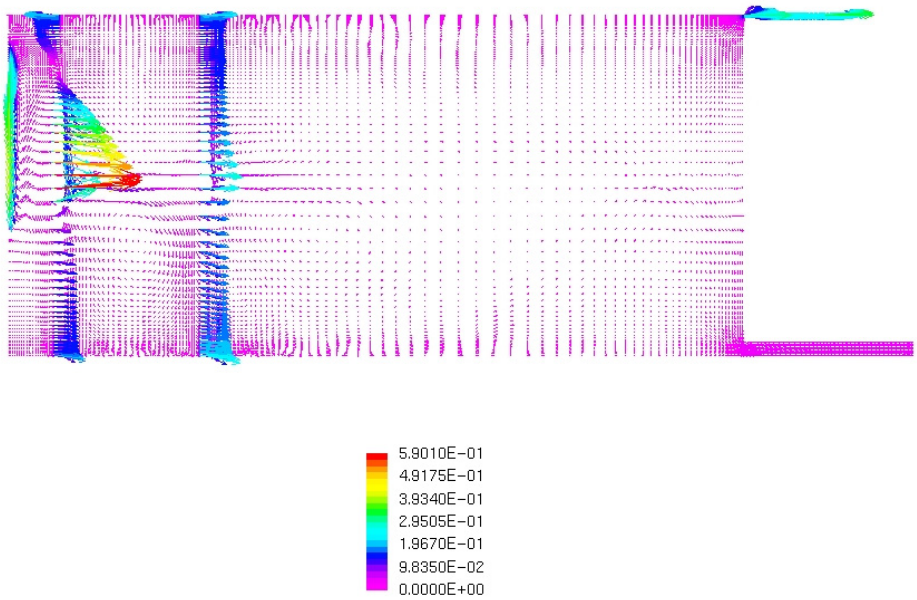

Figure 51. Flow patterns (m/s) of the dispersion when there are two picket fences in the settler. The specific volume flow rate is 6 m^3/m^2h and the temperature is 20 °C.

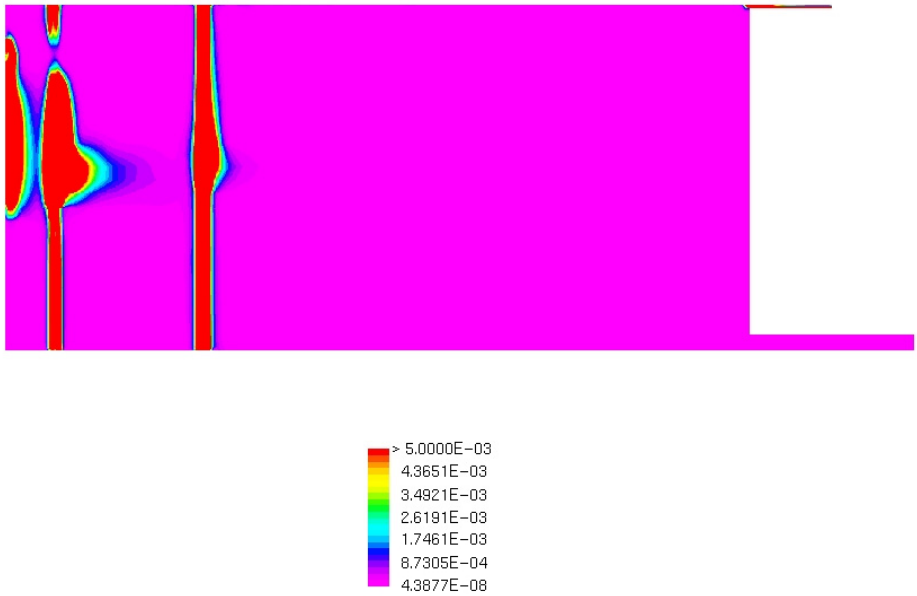

Figure 52. Turbulence dissipation rate (m^2/s^3) of the continuous water phase when there are two picket fences and the specific volume flow rate is 6 m^3/m^2h and the temperature is 20 °C.

Velocity vector profiles for the dispersed organic phase and for the continuous water phase are similar as the flow patterns of the dispersion. Absolute velocity values of the dispersed and continuous phase differ only slightly from each other.

8.2.1 Linear velocity of the organic phase

The linear velocity of the organic phase at 10 °C fluctuates less than at 20 °C. Furthermore, the absolute values at 10 °C are smaller than at 20 °C. These are due to the higher viscosity values at the temperature of 10 °C. The picket fences affect all cases in the same way; strong fluctuation and backflows disappear when two picket fences are set into the settler. The values of the linear velocity are in the right range, especially near the overflow weir. Ekman (1999) has measured linear velocities for organic continuous dispersion at 20 °C. When he had two picket fences in the settler, the thickness of the separated organic phase layer was about 500 mm and the entrainments level of water droplets was about 500-1300 ppm. The measured linear velocities for the specific volume flow rates 6 and 12 m^3/m^2h were about 0.55 cm/s and 1.1 cm/s, respectively. It can be seen from Figures 41 and 42 that the predicted linear velocity values with two picket fences in the rear end of the settler (x = 2 000 mm) are about 0.5 cm/s and about 1.0 cm/s for the specific volume flow rates 6 and 12 m^3/m^2h, respectively. In these cases, the thickness of the separated organic phase layers was about 487 mm and 524 mm for 6 and 12 m^3/m^2h, respectively. It can be noticed that the values agree very well when the measured and simulated values are compared. The only difference is that the entrainment levels in the simulation cases are about five times higher than in the measurements. The difference between the continuous phases does not affect the linear velocities, because the phase layers are separated and it can be assumed that the size of the entrainment droplets are quite similar, and thus the drag force between the phases is also quite similar.

The fluctuation of the linear velocity, which can be seen in Figures 39-42, is due to the porous media describing the picket fences. Part of this fluctuation may be also numerical error, because turbulence values are zero on the free surface (frictionless wall).

8.2.2 Droplet size distribution

Figures 34-38 and Appendixes 5-7 show that, in the front end of the settler, the droplet size distribution changes quite a lot in the vertical direction. One of reasons is that there is the strongest turbulence (Figure 52) that causes droplet break-up and coalescences. The size of the droplets is smallest in the lower part of the settler; this proves that break-up is the controlling process at the bottom of the settler. When the droplets move upwards due to buoyancy, the coalescence process becomes more significant in that near the overflow weir almost all droplets have maximum diameter. On the other hand, it can be seen from Equation (38) that, when the volume fraction of the dispersed phase increases, the collision frequency of eddies decreases, and thus the break-up process is damped and droplet sizes are increased.

The droplet size distribution in the vertical direction agrees well with the relative velocity curve as a function of the liquid height also. For example, Figure 21 shows that the relative velocity (inertia forces) decreases when the droplet moves upwards from the dispersion layer to the upper part of the settler and, at the same time, its Sauter mean diameter and the volume fraction of the dispersed phase increase. The MUSIG model of the CFX-4.4 does not calculate the drag force for each droplet size groups, but uses the Sauter mean diameter. However, it seems that this approximation predicts the results quite well. Of course, the results would be more accurate if the drag force were calculated for each individual droplet size.

8.3 Force balances in the settler

The force balance calculations gave a more detailed view about the settler operation. Although, it is well known that buoyancy or gravity forces are the most important controlling forces in a separation process, the impact actually is very close to surface forces, which hinder the phase separation on the droplet level. These calculations proved that picket fences and their number affect the phase separation via the force balance. It was also noticed that the characteristic length and the fluid velocity have to be selected correctly; otherwise, the calculated force balances will give incorrect results, and conclusions drawn from these may be harmful.

8.3.1 Force balances on the droplet level

The following conclusions can be drawn from Appendix 9 and Figure 32, although there are some discrepancies in the trend. The inertia forces increase on line A, but decrease on lines B and C when picket fences are added. The inertia forces are the strongest on line A when there are two picket fences. The buoyancy and the surface forces do not change in any particular order on lines A and B, although there are picket

fences present. But both of these forces increase on line C when picket fences are added. However, it can be presumed that the buoyancy and the surface forces also increase on lines A and B with the picket fences, although it cannot be distinguished clearly from the simulated results.

In horizontal lines E, F and G, the inertia forces increase when we move up from line E to line F and decrease when we move up from line F to line G. On the other hand, the effect of the picket fences is not so obvious. The strongest inertia force locates on line F without picket fences. The buoyancy and the surface forces increase from line E to line G and when picket fences are added. The forces are the strongest on line G, with and without picket fences.

It can be seen from Appendix 10 that the surface-buoyancy ratio decreases sharply at a liquid height of 400-700 mm. This proves that the buoyancy forces start to control the phase separation in the dispersion layer. Furthermore, the buoyancy controlling is more effective when temperature increases and the picket fences are set into the settler. In the lower and upper parts of the settler at 10 °C, the surface forces are stronger than the buoyancy forces, although there are picket fences. In these cases, the surface forces resist the phase separation and it is more effective when specific volume rate is increased (from 6 to 12 m^3/m^2h), because *Fr*-*We*-ratio is increased in the lower part of the settler. When the temperature is 20 °C, the surface forces are stronger than the buoyancy forces only in the lower part of the settler, but, in the upper part of the settler, the buoyancy forces becomes stronger. Furthermore, the *Fr*-*We*-ratio difference between the specific volume flow rates is much smaller than at 10 °C. This behaviour of the surface-buoyancy ratio agrees well with the results of the thickness of the dispersion layers. The dispersion layer becomes narrower and entrainment levels in separated phases decrease when temperature increases, which means that the phases separate better. The reason for this can be seen from the force balances in which the buoyancy forces become stronger than the surface forces.

At 10 °C, the surface and the buoyancy forces are about 10^4-10^5 times stronger than the inertia and viscous forces on lines A, B and C. Respectively, on lines E, F and G, the surface and the buoyancy forces are about 10^2-10^4 times stronger than the inertia and the viscous forces.

At 20 °C, the surface and the buoyancy forces are about 10^4-10^7 times stronger than the inertia and viscous forces on lines A, B and C. Respectively, on lines E, F and G, the surface and the buoyancy forces are about 10^2-10^4 times stronger than the inertia and the viscous forces.

The buoyancy forces are the strongest in the end of the settler on line C, when there are two picket fences in the settler and the temperature is 20 °C and the specific volume flow rate is 6 m^3/m^2h.

According to the previous conclusions the inertia forces decrease and the buoyancy and the surface forces increase when the dispersion disengages and flows from the front end of the settler towards the overflow weir. In this “flow path”, relative velocity decreases and droplet size increases, which ensure a smooth flow, the effective droplet coalescence and phase separation. This force balance phenomenon, and thus the phase separation, is achieved more effectively when picket fences are used.

8.3.2 Force balances for the continuous and the dispersed phase

The following conclusions can be drawn regarding the continuous and the dispersed phase from Appendix 11 and Figure 32, although there are some discrepancies in the trend. The inertia forces for both phases decrease on lines A, B and C when the picket fences are set. Respectively, the buoyancy and the surface forces increase with the picket fences. In all cases, the inertia forces are the strongest on line A when there are no picket fences. The buoyancy and the surface forces are the strongest on line C with two picket fences at 20 °C. At a temperature of 10 °C, the situation is similar when the specific volume flow rate is 6 m^3/m^2h, but with the specific volume flow rate of 12 m^3/m^2h, the buoyancy and the surface forces are the strongest on line A with two picket fences.

In the horizontal lines, the force balances of the continuous and the dispersed phase differ slightly from each other. The order of magnitude of the forces is similar for both phases, but the locations of the forces differ with temperature, the specific volume flow rate and the picket fences. Therefore, the force balance trend is only deduced for the continuous phase. The inertia forces are the strongest on line F. The forces decrease on lines E, F and G when the picket fences are added. The buoyancy and the surface forces increase with the picket fences and they are the strongest on line G and the weakest on line F.

At both temperatures and both specific volume flow rates, the magnitude order of the forces in proportion to viscous forces for both phases is as follows: the buoyancy forces are about 10^8-10^9 times stronger, the inertia forces are about 10^3-10^5 times stronger and the surface forces are about 10^3 times stronger than the viscous forces.

The buoyancy forces for the continuous phase are the strongest in the end of the settler on lines C and G, when there are two picket fences and the temperature is 20 °C and the specific volume flow rate is 6 m^3/m^2h.

It can be seen that the force balance for the whole settler differs from that of the dispersion on the droplet level. The liquid depth as a characteristic length is a very good parameter when a settler is narrow and high. This gives an opportunity to test, for example, different settler heights and compare their force balances with each other. It is quite likely that there are some limits where the forces do not change remarkably, even when the settler height is increased, but it also depends on the specific volume flow rate. When the whole process is studied, it is better to define the force balance only for the continuous phase. Respectively, when the behaviour of the dispersion is studied, the force balance should be calculated on a droplet level where the relative velocity of the continuous and dispersed phases is taken into account.

8.4 The thickness of the dispersion layer

The simulated results in Tables X and XI show that the thicknesses of the dispersion layer differ quite a lot from each other when different amounts of entrainments are used. However, the following conclusions about the dispersion behaviour in the settler can be deduced when temperature, specific volume flow rate and number of picket fences are changed.

The dispersion layer is quite smooth when picket fences are not used and when the temperature is 10 °C. This tells us that the phases do not separate very well, but when temperature increases, it can be seen from lines B and C that the separation becomes slightly more effective. This cannot be seen so easily when the allowed entrainment level is the lowest (5 000 ppm), but when it is allowed that the phases can contain entrainments 20 000 ppm the difference between temperatures is obvious.

The effect of the picket fences to the phase separation can be seen on all entrainment levels. The dispersion layer thins very quickly on line A when the first picket fence is set. After that, the dispersion layer may become even thicker on lines B and C if the separated phase contains 5 000 ppm entrainments at maximum. One reason is that, in the end of the settler, the overflow weir causes some back-flow swirls, which increase the entrainment level. When the entrainment level is allowed to be higher, it can be noticed that the dispersion layer becomes thinner on lines B and C.

It can be noticed that the thickness of the dispersion layer increases on line A when two picket fences are used. This proves that the aim of the picket fences performs well deep and a dense dispersion layer is achieved. This phenomenon is also noticed in Figures 35 and 36, where the droplet sizes increase when they move up in the middle of the picket fences (location points 2 and 3). On lines B and C, the dispersion layer becomes thinner with two picket fences than with one picket fence. However, there are some situations where the dispersion layer is thicker on line C than on line B due to the back-flow swirls.

The predicted dispersion thicknesses highlight the fact that the organic droplets coalesce better and better and the dispersion layer becomes thinner when the dispersion flows towards the overflow weir and when the picket fences are used. The phase separation becomes more effective when the specific volume flow rate is decreased and the temperature is increased. It can be seen from Figure 53 (the other cases are shown in Appendix 4) that two picket fences very effectively increase the phase separation at 10 °C, but the process becomes even much more effective at 20 °C. The dark red layer, which indicates the totally separated organic phase, becomes thicker. Furthermore, these figures also show that the active surface of the dispersion moves upwards, which was also noticed from the results of the constant droplet size simulations.

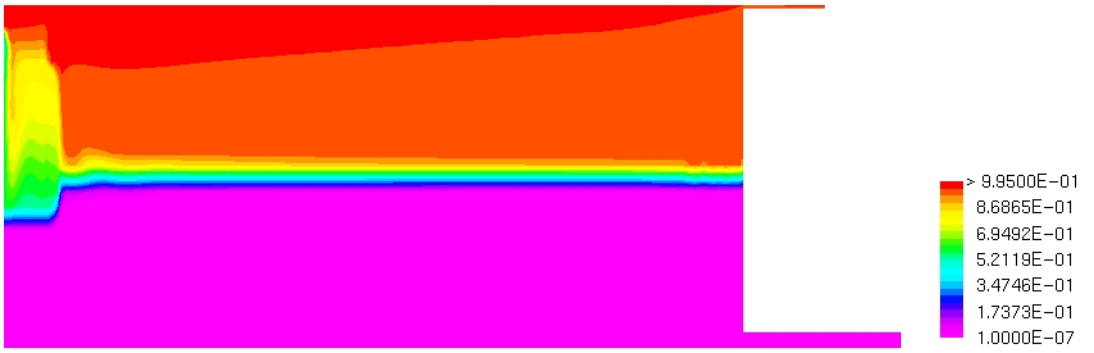

a)

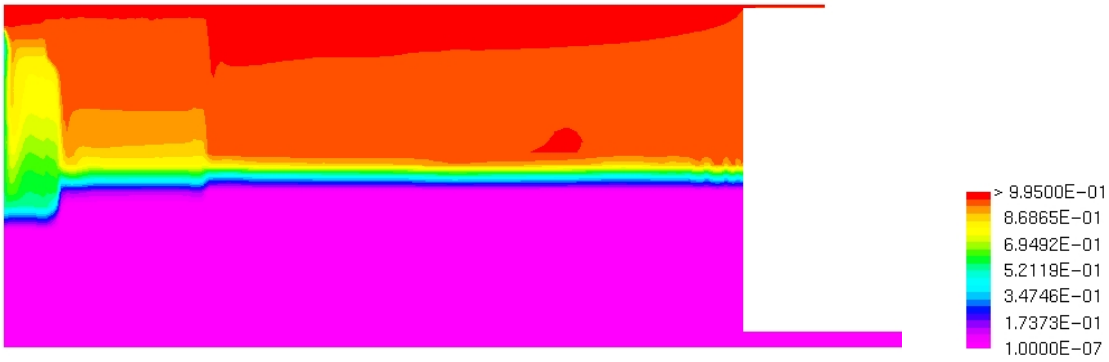

b)

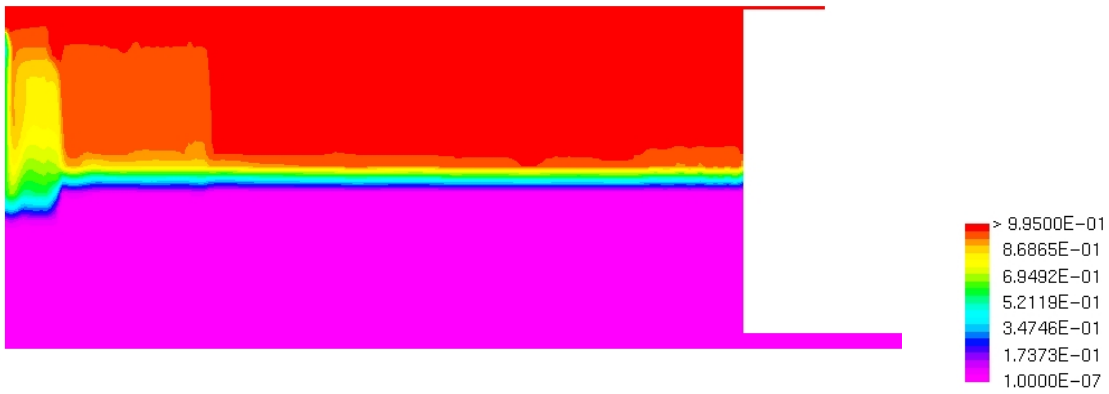

c)

Figure 53. The volume fraction of the organic phase when a) V_{spec} = 6 m^3/m^2h, T = 10 °C and one picket fence, b) V_{spec} = 6 m^3/m^2h, T = 10 °C and two picket fences, c) V_{spec} = 6 m^3/m^2h, T = 20 °C and two picket fences. The permitted entrainment level of the aqueous phase is 5 000 ppm. Dark red indicates the totally separated organic phase, which can contain the aqueous phase under 5 000 ppm. Violet indicates the water phase.

8.4.1 Pressure drop over the picket fence

The used porous media, which describes the picket fences in the settler, performed well, as can be seen from Figure 53. A dense and deep dispersion layer was obtained in the front end of the settler when picket fences were used. Furthermore, the average pressure drop values over the picket fences in Table XII were in the right range. The pressure drop values are similar at two different temperatures, but the values are about two times higher when the specific volume flow rate is doubled. When there are two picket fences, the second fence cannot dam the fluid so much as the first fence. The reason is quite obvious: the inertia forces decrease when the dispersion flows towards the back wall of the settler. The pressure drop is the greatest in the middle height of the fence, because the dispersion main flow takes place in that area, which can be seen from Figure 48.

Although, the validation is very difficult, some values could be approximated from Ekman's (1999) experiments. At 10 °C and with the specific volume flow rate of 6 m^3/m^2h, the picket fence dammed the dispersion or the organic phase about 7 mm in the front of the fence. At 20 °C, and with the specific volume flow rate of 12 m^3/m^2h, the picket fence dammed liquid about 10 mm in the front of the fence. These experimental values agree reasonably well with the simulated ones (Table XII).

8.4.2 Validation of the simulated thicknesses of the dispersion layers

The simulated thicknesses of the dispersion were compared with the physical measurements of Ekman (1999) on lines A, B and C, located in the sections of 186-669 mm, 1162-1389 mm and 2115-2584 mm of the pilot settler (Table II). The simulated results could be validated with one and two picket fences at 10 °C, and without picket fences, and with one picket fence at 20 °C. The thickness of the dispersion layer as a function of the specific volume flow rate with different entrainment amounts, temperatures and number of picket fences is shown in Figures 54-62.

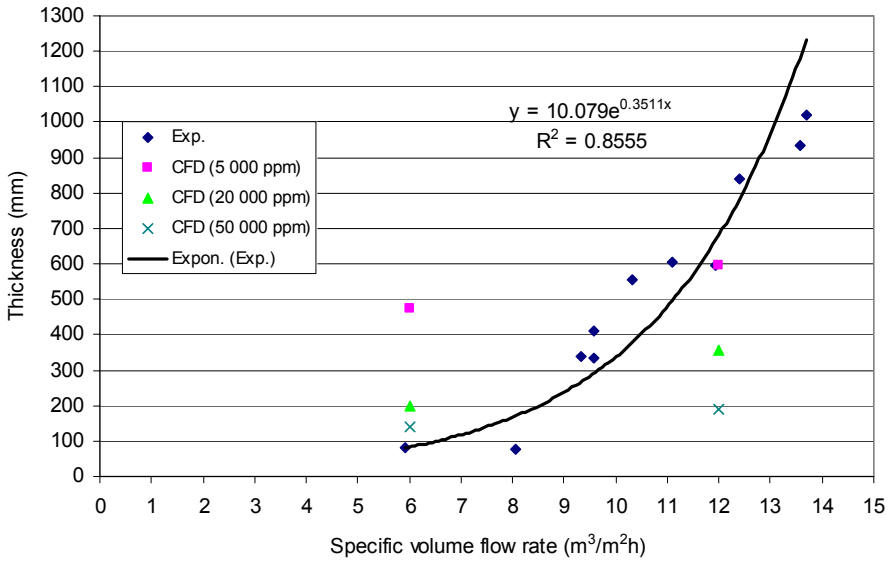

Figure 54. Thickness of the dispersion layer with one picket fence as a function of the specific volume flow rate with different entrainment levels on line A. Temperature is 10 °C.

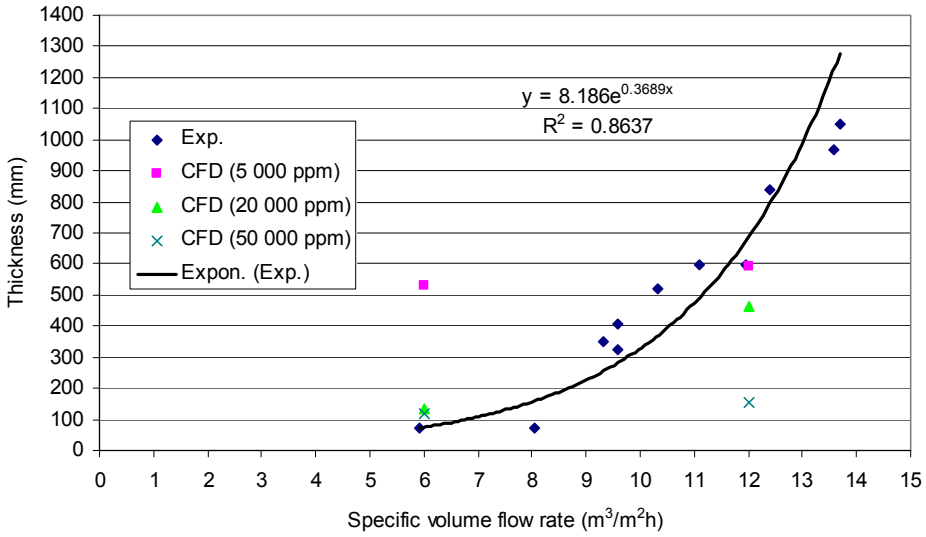

Figure 55. Thickness of the dispersion layer with one picket fence as a function of the specific volume flow rate with different entrainment levels on line B. Temperature is 10 °C.

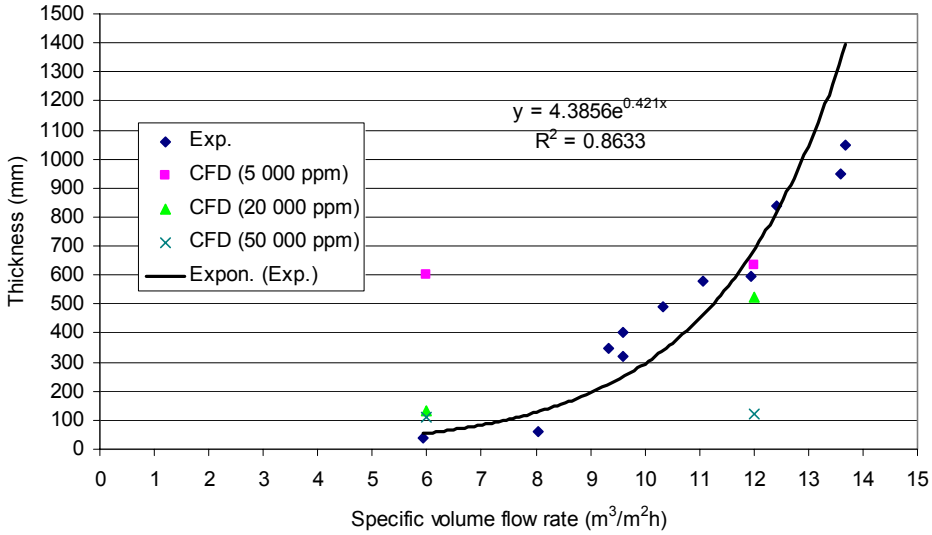

Figure 56. Thickness of the dispersion layer with one picket fence as a function of the specific volume flow rate with different entrainment levels on line C. Temperature is 10 °C.

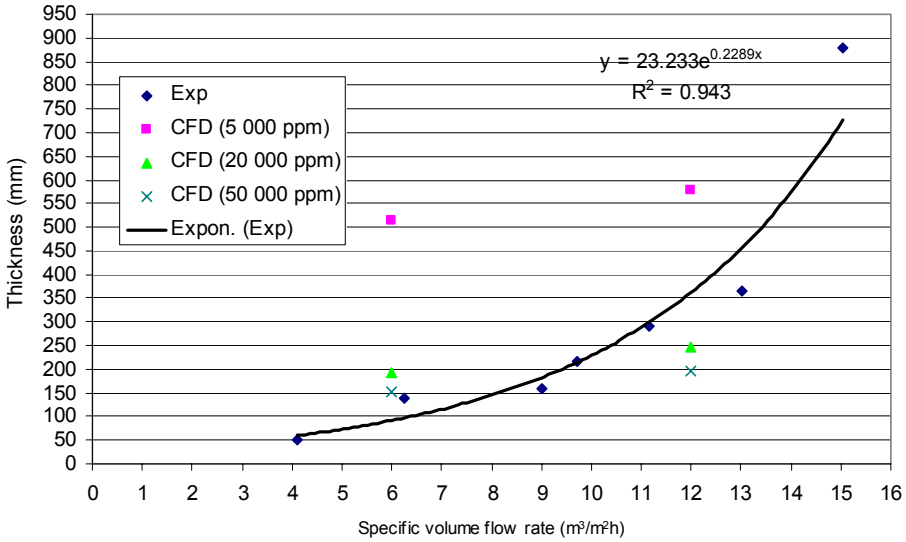

Figure 57. Thickness of the dispersion layer without picket fences as a function of the specific volume flow rate with different entrainment levels on line A. Temperature is 20 °C.

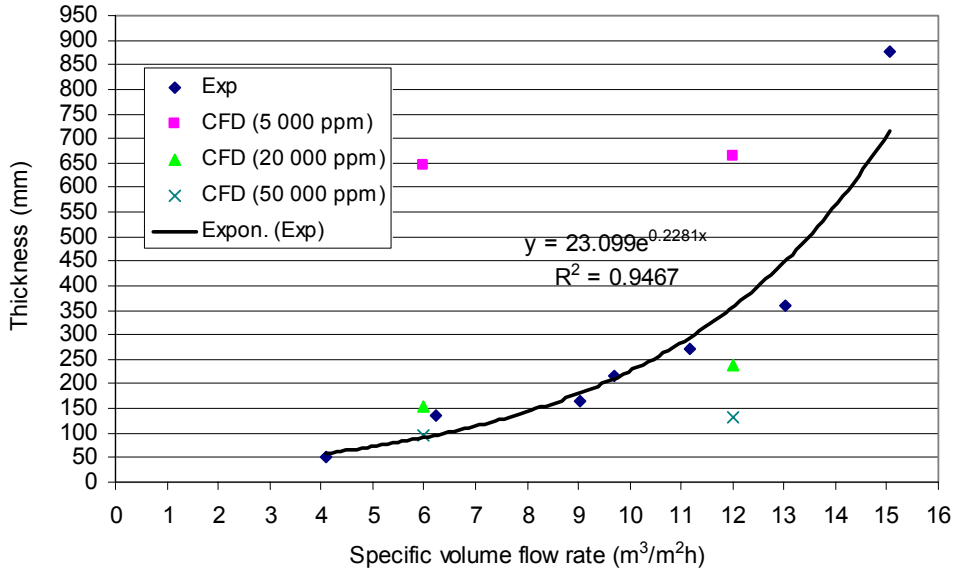

Figure 58. Thickness of the dispersion layer without picket fences as a function of the specific volume flow rate with different entrainment levels on line B. Temperature is 20 °C.

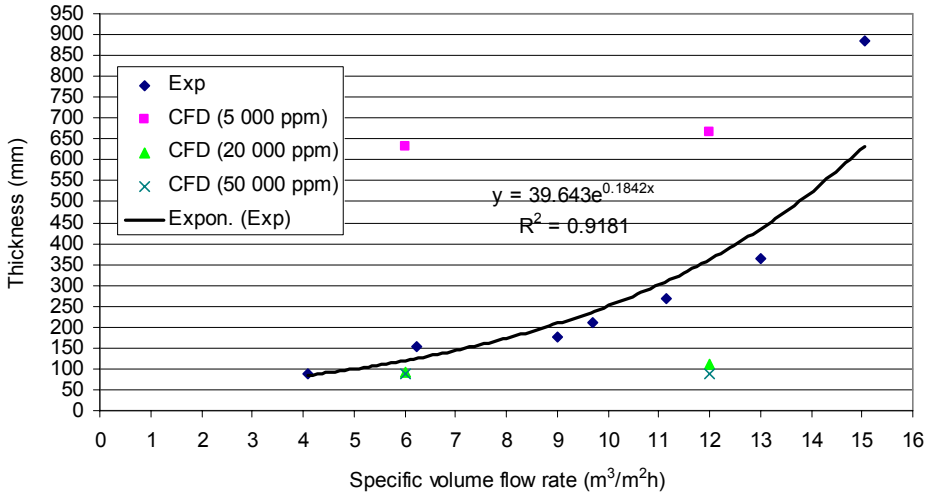

Figure 59. Thickness of the dispersion layer without picket fences as a function of the specific volume flow rate with different entrainment levels on line C. Temperature is 20 °C.

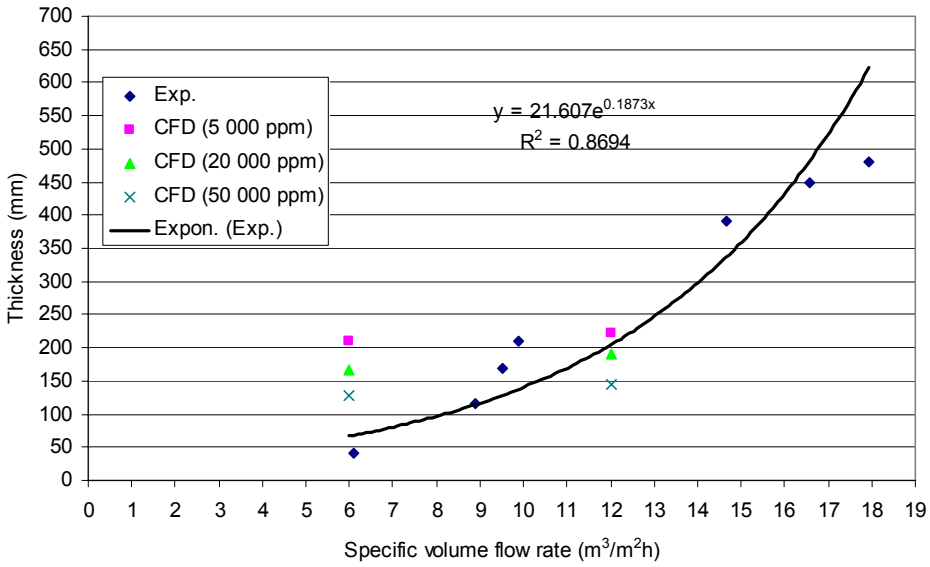

Figure 60. Thickness of the dispersion layer with one picket fence as a function of the specific volume flow rate with different entrainment levels on line A. Temperature is 20 °C.

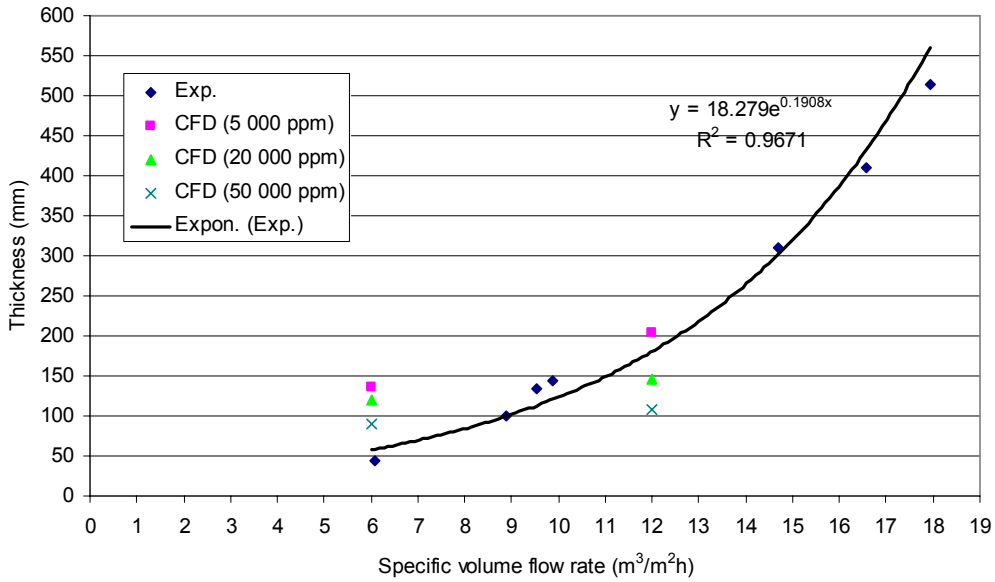

Figure 61. Thickness of the dispersion layer with one picket fence as a function of the specific volume flow rate with different entrainment levels on line B. Temperature is 20 °C.

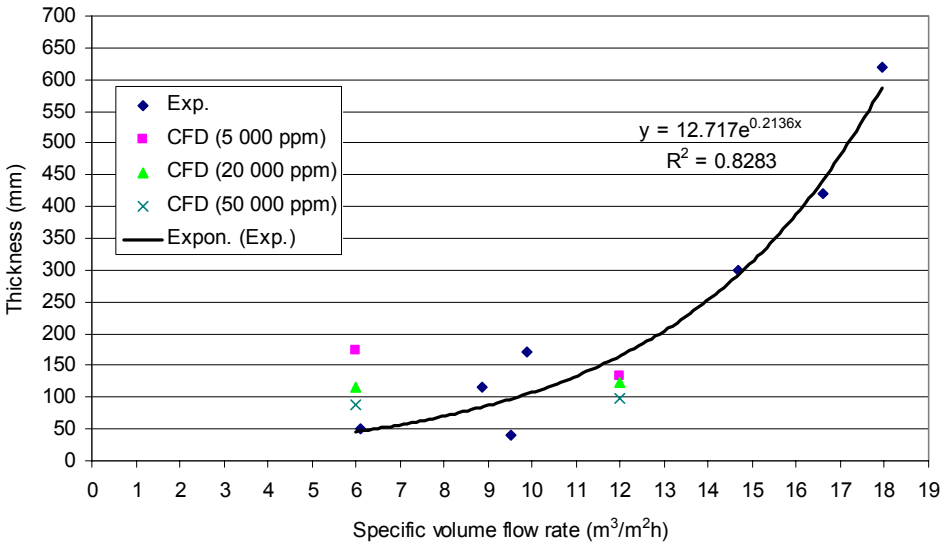

Figure 62. Thickness of the dispersion layer with one picket fence as a function of the specific volume flow rate with different entrainment levels on line C. Temperature is 20 °C.

It can be noticed from Figures 54-62 and Tables II, X and XI that the predicted thicknesses of the dispersion layer are the closest to the measured values when the entrainment level is 2.0 vol-%. However, when the specific volume flow rate is 6 m^3/m^2h, the CFD model predicts on average values about two-times larger than the values predicted by the trend line of the physical measurements. On the other hand, when the specific volume flow rate is 12 m^3/m^2h, the model predicts on average values about two-times smaller than the trend line.

When the entrainment level is 5.0 vol-% and the specific volume flow rate is 6 m^3/m^2h, the CFD model predicts on average values about two-times larger than the trend line. Respectively, when the specific volume flow rate is 12 m^3/m^2h, the model predicts on average values about three-times smaller than the trend line.

When the entrainment level is 0.5 vol-% and the specific volume flow rate is 6 m^3/m^2h, the CFD model predicts on average values about five times larger than the trend line. Respectively, when the specific volume flow rate is 12 m^3/m^2h, the model predicts on average values about two times larger than the trend line.

The simulated thicknesses of the dispersion do not increase exponentially as a function of the specific volume flow rate, as the experimental values do. However, this comparison is difficult, because the simulated results are not so numerous. On the other hand, the experimental values have been taken from large section areas (186-669 mm, 1162-1389 mm and 2115-2584 mm), each of them being hundreds of millimetres wide. In such cross-sections, the thicknesses can be varied quite a lot due to circulation flows. Therefore, the comparison is not so accurate, because the simulated values have been taken from one line of each section. It has also to be remembered that when the

simulated values are compared with the physical experiments, different kinds of error sources of the experiments have to be taken into account, for example, the height measurements of the phases, and small leaks between the fences and the walls of the settler (Kankaanpää et al., 2001).

In spite of some differences between the simulated and the measured values, it can be said that the simulated values are in the right area. These CFD simulations confirm that the CFD method with the developed calculation procedure can be used to study the industrial solvent extraction settler process, when the main target is the enhancement of the phase separation with the aid of picket fences.

9 CONCLUSIONS

A computational fluid dynamics (CFD) has been applied to study the behaviour of an organic - aqueous dispersion in the copper solvent extraction settler. The phase separation in the settler and the factors affecting drop-drop and drop-interface coalescences were discussed. Due to the complicated process and large number of physical phenomena, restrictions of the two-phase modelling, and numerical convergence difficulties, a new CFD calculation procedure was developed. This new calculation procedure fulfilled the following six criteria, which ensured that the results could be confirmed as converged and having sufficient accuracy.

1. Fluctuation of the $\bar{u}$-velocities was typically between about 0-10 % in two monitoring points.
2. Mass flow rate error was less than 1 %.
3. O/A ratio was typically between 0.85-1.05 (Ekman, 2004).
4. Break point of the height of the continuous phase was reached.
5. Scaled residuals were smaller than 10^{-4}.
6. The difference between two straight mass ratio values was stable during the iteration (Equation (65)). In all cases, the stability was ensured by plotting the difference between two straight mass ratio values as a function of total iterations, as Figures 29 and 30 show.

The numerical model takes into account the break-up and coalescence processes of the dispersed droplets via the population balance equation, which had been incorporated in commercial CFD software, CFX-4.4. As a part of the new calculation procedure, temperature-related correlation (66), which takes into account the phase separation when temperature decreases, was also generated. The correlation was used to scale the calibration coefficient of the coalescence model and droplet size range that depend on temperature. The correlation is based on the theory of the coalescence rate of a droplet with its homophase, and the physical properties of the dispersed and continuous phase at different temperatures.

The advantages of the CFD approach can be summarized as follows:

- When the specified boundary conditions are used, the user does not need to know whether the phases can separate from each other with a used droplet size of the dispersed phase.

- A porous media in the settler can replace the complex geometry of the picket fence.

- The six-item calculation procedure ensures that various modelling cases can be simulated in the same way, and thus the obtained results are comparable.

- The procedure improves the level of trust in CFD simulations.

The developed calculation procedure was applied to a pilot settler with the aim of demonstrating the possibilities of the CFD in the settler design and gaining new information about dispersion flows and force balances in the settler. All simulation

cases followed the six-item calculation procedure and illustrated the dispersion disengagement phenomenon correctly. According to the results, the following conclusions can be drawn:

- The dispersion flows are not totally stable in the settler even if the process has achieved a steady-state situation concerning the thickness of the phase layers.

- When the settler is operated without picket fences, the back-flow swirls are formed in the upper and lower parts of the settler.

- When the picket fences are set into the settler, the circulation flows can be dampened, the phase separation becomes more effective, the linear velocities of the organic phase are stabilized, and the entrainment amounts in the separated phases can be decreased.

- The surface and buoyancy forces are about 10^5 times stronger than the inertia and the viscous forces on the droplet level. The phase separation becomes more effective when the buoyancy forces become stronger than the surface forces.

- The inertia forces decrease and the buoyancy and surface forces increase when the dispersion disengages and flows from the front end of the settler towards the settler back wall. Simultaneously, the relative velocity decreases and the droplet size increases that ensure smooth flow and effective droplet coalescence and phase separation.

- With the aid of CFD modelling, precise locations and arrangements of the picket fences, geometry of the picket fence, and length-to-width ratios of the settler can be optimized as a function of the specific volume flow rate, the linear velocity of the organic phase, pressure drop over the picket fence and thicknesses of the dispersion and phase layers. This means that the industrial settlers can be designed easier, cheaper and with a shorter lead-time, and thus some physical experiments in a laboratory or pilot scale are unnecessary.

The following features are suggested for further research:

- Development of coalescence models for dispersed droplets that can be implemented into CFD and that take into account the film thinning of the continuous phase.

- Transient simulation of the dispersion flows and phase separation that can be used for validating the assumption in CFD calculations that the dispersion behaviour is stable in the settler.

REFERENCES

AEA Technology plc, *CFX-4.4 Solver Manual*, England 2001.

Allan, R.S. and Mason, S.G., Effect of electric fields on coalescence in liquid+liquid systems, *Transactions of the Faraday Society*, Vol. **57**, 1961, p. 2027-2040.

Arntzen, R. and Andresen, P.A.K., Three-phase wellstream gravity separation. In the book of *Encyclopedic handbook of emulsion technology*, ed. Sjöblom, J., Marcel Dekker, Inc., U.S.A. 2001, p. 661-678.

Augier, F., Masbernat, O. and Guiraud, P., Slip velocity and drag law in a liquid-liquid homogeneous dispersed flow, *AIChE Journal*, Vol. **49**, No. 9, 2003, p. 2300-2316.

Bailey, C., Patel, M. and Kumar, S., Computational modelling – a key component in materials processing, *Transactions of the Institution of Mining and Metallurgy, Section C, Mineral Processing and Extractive Metallurgy*, Vol. **110**, 2001, p. 25-32.

Bakker, A., Haidari, A.H. and Marshall, E.M., Design reactors via CFD, *Chemical Engineering Progress*, Vol. **97**, No. 12, 2001a, p. 30-39.

Bakker, A., Haidari, A.H. and Oshinowo, L.M., Realize greater benefits from CFD, *Chemical Engineering Progress*, Vol. **97**, No. 3, 2001b, p. 45-53.

Barnea, E. and Mizrahi, J., Separation mechanism of liquid-liquid dispersions in a deep-layer gravity settler: Part I – The structure of the dispersion band, *Trans. Instn. Chem. Engrs.*, Vol. **53**, 1975a, p. 61-69.

Barnea, E. and Mizrahi, J., Separation mechanism of liquid-liquid dispersions in a deep-layer gravity settler: Part II – Flow patterns of the dispersed and continuous phases within the dispersion band, *Trans. Instn. Chem. Engrs.*, Vol. **53**, 1975b, p. 70-74.

Barnea, E. and Mizrahi, J., Separation mechanism of liquid-liquid dispersions in a deep-layer gravity settler: Part III – Hindered settling and drop-to-drop coalescence in the dispersion band, *Trans. Instn. Chem. Engrs.*, Vol. **53**, 1975c, p. 75-82.

Barnea, E. and Mizrahi, J., Separation mechanism of liquid-liquid dispersions in a deep-layer gravity settler: Part IV – Continuous settler characteristics, *Trans. Instn. Chem. Engrs.*, Vol. **53**, 1975d, p. 83-92.

Behzadi, A., Issa, R.I. and Rusche, H., Modelling of dispersed bubble and droplet flow at high phase fractions, *Chemical Engineering Science*, Vol. **59**, 2004, p. 759-770.

Birdi, K.S., Surface tension and interfacial tension of liquids. In the book of *Handbook of surface and colloid chemistry*, ed. Birdi, K.S., CRC Press LLC, USA 1997, p. 71-118.

Biswas, A.K. and Davenport, W.G., *Extractive Metallurgy of Copper*, 3. Edition, BPC Wheatons Ltd, Exeter, England, 1994, p. 383-400.

Burrill, K.A. and Woods, D.R., Film shapes for deformable drops at liquid-liquid interfaces, II. The mechanisms of film drainage, *Journal of Colloid and Interface Science*, Vol. **42**, No. 1, 1973, p. 15-34.

Chapman, T.W., Extraction-Metals processing. In the book of *Handbook of separation technology*, ed. Rousseau, R.W., John Wiley & Sons Inc., U.S.A. 1987, p. 467-499.

Chappelear, D.C., Models of a liquid drop approaching an interface, *Journal of Colloid Science*, Vol. **16**, 1961, p. 186-190.

Charles, G.E. and Mason, S.G., The coalescence of liquid drops with flat liquid/liquid interfaces, *Journal of Colloid Science*, Vol. **15**, 1960a, p. 236-267.

Charles, G.E. and Mason, S.G., The mechanism of partial coalescence of liquid drops at liquid/liquid interfaces, *Journal of Colloid Science*, Vol. **15**, 1960b, p. 105-122.

Chatzi, E. and Lee, M., Analysis of interactions for liquid-liquid dispersions in agitated vessels, *Ind. Eng. Chem. Res*., Vol. **26**, 1987, p. 2263-2267.

Chen, J.D., A model of coalescence between two equal-sized spherical drops or bubbles, *Journal of Colloid and Interface Science*, Vol. **107**, No. 1, 1985, p. 209-220.

Chen, J.D., Effects of London-van der Waals and electric double layer forces on the thinning of a dimpled film between a small drop or bubble and a horizontal solid plane, *Journal of Colloid and Interface Science*, Vol. **98**, No. 2, 1984, p. 329-341.

Chesters, A.K. and Hofman, G., Bubble coalescence in pure liquids, *Applied Scientific Research*, Vol. **38**, 1982, p. 353-361.

Chesters, A.K., The modelling of coalescence processes in fluid-liquid dispersions: A review of current understanding, *Trans IChemE*, Vol. **69**, Part A, 1991, p. 259-270.

Clift, R., Grace, J.R. and Weber, M. E., Bubbles, drops and particles, Academic Press Inc., 1978 USA, 380 p.

Coulaloglou, C.A. and Tavlarides, L.L., Description of interaction processes in agitated liquid-liquid dispersions, *Chemical Engineering Science*, Vol. **32**, 1977, p. 1289-1297.

Cox, M., Liquid-liquid extraction in hydrometallurgy. In the book of *Science and practice of liquid-liquid extraction*, **Vol. 2**, Process chemistry and extraction operations in the hydrometallurgical, nuclear, pharmaceuticals, and food industries, ed. Thornton, J.D., Oxford University Press, Great Britain 1992, p. 1-101.

Dalingaros, W. and Hartland, S., Effect of drop size and physical properties on dispersion height in the separating section of a liquid/liquid extraction column, *The Canadian Journal of Chemical Engineering*, Vol. **64**, 1986, p. 925-930.

Dalingaros, W., Jeelani, S.A.K. and Hartland, S., Prediction of steady-state dispersion height in the disengaging section of an extraction column from batch settling data, *The Canadian Journal of Chemical Engineering*, Vol. **65**, 1987, p. 210-213.

Davenport, W.G., King, M., Schlesinger, M. and Biswas, A.K., *Extractive Metallurgy of Copper*, 4. Edition, Elsevier Science Ltd., Netherlands 2002, 432 p.

Dreher, T.M., Glass, J., O'Connor, A.J. and Stevens, G.W., Effect of rheology on coalescence rates and emulsion stability, *AIChE Journal*, Vol. **45**, No. 6, 1999, p. 1182-1190.

Drew, D.A. and Lahey, R.T. Jr., The virtual mass and lift force on a sphere in rotating and straining inviscid flow, *International Journal of Multiphase Flow*, Vol. **13**, No. 1, 1987, p. 113-121.

Ekman, E., *Private communication*, Outokumpu Research Oy, 8.9.2004.

Ekman, E., *Written notification*, Outokumpu Research Oy, 2003.

Ekman, E., *Written notification*, Outokumpu Research Oy, 1999.

Erbil, H.Y., Interfacial interactions of liquids. In the book of *Handbook of surface and colloid chemistry*, ed. Birdi, K.S., CRC Press LLC, USA 1997, p. 5-69.

Fisher, J.F.C. and Notebaart, C.W., Commercial processes for copper, In the book of *Handbook of solvent extraction*, ed. Lo, T.C., Baird, M.H.I. and Hanson, C., John Wiley & Sons, Inc. U.S.A. 1983, p. 649-671.

Fox, R.W. and McDonald, A.T., *Introduction to fluid mechanics*, third edition, John Wiley & Sons, Inc. 1985, Canada, 741 p.

Friberg, S.E. and Yang, J., Emulsion stability, In the book of *Emulsions and emulsion stability*, ed. Sjöblom, J., Marcel Dekker, Inc., U.S.A. 1996, p. 1-40.

Frising, T., Noïk, C. and Dalmazzone, C., The liquid/liquid sedimentation process: From droplet coalescence to technologically enhanced water/oil emulsion gravity separators: A review, *Journal of Dispersion Science and Technology*, Vol. **27**, No. 7, 2006, p. 1035-1057.

Gigas, B. and Giralico, M.A., Advanced methods for designing today's optimum solvent extraction mixer settler unit, *Proceedings of the International Solvent Extraction Conference*, ISEC 2002, ed. Sole, K.C., Cole, P.M., Preston, J.S. and Robinson, D.J., Johannesburg 2002, p. 1388-1395.

Gillespie, T. and Rideal, E.K., The coalescence of drops at an oil-water interface, *Transactions of the Faraday Society*, Vol. **52**, 1956, p. 173-183.

Giralico, M., Gigas, B. and Preston, M., Optimized mixer settler designs for tomorrows large flow production requirements, *Proceedings of the Copper 2003-Cobre 2003, the 5thInternational conference*, Vol. VI Hydrometallurgy of copper, Book 2: Modeling,

impurity control and solvent extraction, ed. Riveros, P.A., Dixon, D.G., Dreisinger, D.B. and Menacho, J.M., Santiago, November 30 – December 3, 2003, p. 775-794.

Goldberger, W.M., Robbins, L.A., Fiedler, R.A., Jepsen, T.L.B., Knoll, F.S., Maloney, J.O., Mitchell, D.W., Parekh, B.K., Sorenson, T.C., Stavenger, P.L., Thelen, R.L., Treybal, R.E. and Wechsler, I., Solid-solid and liquid-liquid systems, In the book of *Perry's chemical engineers' handbook*, sixth edition, ed. Perry, R.H. and Green, D., McGraw-Hill Inc., Malaysia 1984, p. 21/1-83.

Grace, J.R., Wairegi, T. and Nguyen, T.H., Shapes and velocities of single drops and bubbles moving freely through immiscible liquids, *Transactions of the Institution of Chemical Engineers*, Vol. **54**, No. 3, 1976, p. 167-173.

Greenkorn, R.A., Single-fluid flow through porous media, *Handbook of fluids in motion*, Ed. Cheremisinoff, N. P. and Gupta, R. The Butterworth Group, 1983 England, p. 279-309.

Hanumanth, G.S., Irons, G.A and Lafreniere, S., Particle sedimentation during processing of liquid metal-matrix composites, *Metallurgical Transactions B*, Vol. **23B**, 1992, p. 753-763.

Hartland, S. and Jeelani, S.A.K., Choice of model for predicting the dispersion height in liquid/liquid gravity settlers from batch settling data, *Chemical Engineering Science*, Vol. **42**, No. 8, 1987, p. 1927-1938.

Hartland, S. and Jeelani, S.A.K., Gravity settlers, In the book of *Liquid-liquid extraction equipment*, ed. Godfrey, J.C. and Slater, M.J., John Wiley & Sons, England 1994, p. 411-530.

Hartland, S. and Jeelani, S.A.K., Prediction of sedimentation and coalescence profiles in a decaying batch dispersion, *Chemical Engineering Science*, Vol. **43**, No. 9, 1988, p. 2421-2429.

Henschke, M., Schlieper, L.H. and Pfennig, A., Determination of a coalescence parameter from batch-settling experiments, *Chemical Engineering Journal*, Vol. **85**, 2002, p. 369-378.

Herbst, J.A., Rate processes in multiparticle metallurgical systems, In the book of *Rate processes of extractive metallurgy*, ed. Sohn, H.Y. and Wadsworth, M.E., Plenum Press, New York 1979, p. 53-112.

Hietala, V., Carrying out measurements, In the book of *Technical Handbook*, No. 1, 8. ed., ed. Jotuni, P., K.J. Gummerus Osakeyhtiö, Jyväskylä 1981, p. 319-356. (in Finnish)

Hirsi, T., *Optimization of a settler with the computational fluid dynamics*, Master's Thesis, Helsinki University of Technology, Espoo 2004, 64 p. (in Finnish)

Hopkins, W.R. and Lewis, I.E., Recent innovations in SX/EW plants to reduce capital and operating costs, *Minerals & Metallurgical Processing*, February 1990, p. 1-8.

Ishii, M. and Zuber, N., Drag coefficient and relative velocity in bubbly, droplet or particulate flows, *AIChE Journal*, Vol. **25**, No. 5, 1979, p. 843-855.

Ivanov, I.B. and Dimitrov, D.S., Thin film drainage, In the book of *Thin liquid films*, Fundamental and applications, ed. Ivanov, I.B., Marcel Dekker, Inc., U.S.A., 1988, p. 379-496.

Jakobsen, H.A., Lindborg, H. and Dorao, C.A., Modeling of bubble column reactors: Progress and Limitations, *Ind. Eng. Chem. Res.*, Vol. **44**, 2005, p. 5107-5151.

Jeelani, S.A.K. and Hartland, S., Collision of oscillating liquid drops, *Chemical Engineering Science*, Vol. **46**, No. 7, 1991, p. 1807-1814.

Jeelani, S.A.K. and Hartland, S., Effect of dispersion properties on the separation of batch liquid-liquid dispersions, *Industrial & Engineering Chemistry Research* (*Ind. Eng. Chem. Res.*), Vol. **37**, No. 2, 1998, p. 547-554.

Jeelani, S.A.K. and Hartland, S., Effect of interfacial mobility on thin film drainage, *Journal of Colloid and Interface Science*, Vol. **164**, 1994, p. 296-308.

Jeelani, S.A.K. and Hartland, S., Effect of velocity fields on binary and interfacial coalescence, *Journal of Colloid and Interfacial Science*, Vol. **156**, 1993b, p. 467-477.

Jeelani, S.A.K. and Hartland, S., Prediction of dispersion height in liquid-liquid gravity settlers from batch settling data, *Chemical Engineering Research & Design* (Chem. Eng. Res. Des.), Vol. **64**, 1986, p. 450-460.

Jeelani, S.A.K. and Hartland, S., Prediction of steady state dispersion height from batch settling data, *AIChE Journal*, Vol. **31**, No. 5, 1985, p. 711-720.

Jeelani, S.A.K. and Hartland, S., The continuous separation of liquid/liquid dispersions, *Chemical Engineering Science*, Vol. **48**, No. 2, 1993a, p. 239-254.

Jeelani, S.A.K., Pandit, A. and Hartland, S., Factors affecting the decay of batch liquid-liquid dispersions, *The Canadian Journal of Chemical Engineering*, Vol. **68**, 1990, p. 924-931.

Jeelani, S.A.K., Panoussopoulos, K. and Hartland, S., Effect of turbulence on the separation of liquid-liquid dispersions in batch settlers of different geometries, *Industrial & Engineering Chemistry Research* (*Ind. Eng. Chem. Res.*), Vol. **38**, No. 2, 1999, p. 493-501.

Jeffreys, G.V., Davies, G.A. and Pitt, K., Rate of coalescence of the dispersed phase in a laboratory mixer settler unit: Part I, *AIChE Journal*, Vol. **16**, No. 5, 1970, p. 823-827.

Jeffreys, G.V., Smith, D.V. and Pitt, K., The analysis of coalescence in a laboratory mixer-settler extractor*, I. Chem.E. Symposium Series*, No. 26, 1967, p. 93-98.

Jenkins, J., Davenport, W.G., Kennedy, B. and Robinson, T., Electrolytic copper – leach, solvent extraction and electrowinning world operating data, *Proceedings of the*

Copper 99-Cobre 99, the 4th International conference, Vol. IV (Hydrometallurgy of copper), ed. Young, S.K., Dreisinger, D.B., Hackl, R.P. and Dixon, D.G., The Minerals, Metals & Materials Society, Phoenix, USA, October 10-13, 1999, p. 493-538.

Kankaanpää, T., Defining the pressure drop over a picket fence by using CFX software package, *Helsinki University of Technology Publications in Materials Science and Metallurgy*, **TKK-MK-98**, Espoo 2000, 20 p. (in Finnish)

Kankaanpää, T., Jokilaakso, A. and Pekkala, P., CFD – An effective tool for optimizing picket fence geometries, Proceedings of the International Symposium, Computer Applications in Metals Processing, ed. S.A. Argyropoulos, *40th Annual Conference of Metallurgist of CIM*, Toronto, August 26-29, 2001, p. 241-252.

Kankaanpää, T., *Numerical modelling of water flows in a liquid-liquid extraction settler*, Master's Thesis, Helsinki University of Technology, Espoo 1999, 68 p. (in Finnish)

Kankaanpää, T., Studying solvent extraction settler process by using CFD, *EPD Congress 2005*, ed. Schlesinger, M.E., TMS (The Minerals, Metals & Materials Society), San Francisco, February 13-17, 2005.

Keskinen, K.I., *Tables and figures of chemical engineering*, 7. ed., Otatieto 845, Helsinki 1998, 76 p. (in Finnish)

Kongas, M. and Hughes, D., New on-line analyzer technology for process monitoring and control, *Proceedings of the Copper 2003-Cobre 2003, the 5th International conference*, Vol. VI, Hydrometallurgy of copper, Book 1: Leaching and process development, ed. Riveros, P.A., Dixon, D.G., Dreisinger, D.B. and Menacho, J.M., Santiago, November 30 - December 3, 2003, p. 395-405.

Kralchevsky, P.A., Danov, K.D. and Denkov, N.D., Chemical physics of colloid systems and interfaces. In the book of *Handbook of surface and colloid chemistry*, ed. Birdi, K.S., CRC Press LLC, USA 1997, p. 333-494.

Kumar, A. and Hartland, S., Gravity settling in liquid/liquid dispersions, *The Canadian Journal of Chemical Engineering*, Vol. **63**, 1985, p. 368-376.

Kumar, A., Vohra, D.K. and Hartland, S., Sedimentation of droplet dispersions in counter-current spray columns, *The Canadian Journal of Chemical Engineering*, Vol. **58**, No. 2, 1980, p. 154-159.

Launder, B. E. and Spalding, D. B., The numerical computation of turbulent flows, *Computer Methods in Applied Mechanics and Engineering*, Vol. **3**, No. 2, 1974, p. 269-289.

Leng, D.E. and Calabrese, R.V., Immiscible liquid-liquid systems, In the book of *Handbook of industrial mixing, science and practice*, ed. Paul, E.L., Atiemo-Obeng, V.A. and Kresta, S.M., John Wiley & Sons Inc., U.S.A. 2004, p. 639-753.

Leonard, B. P., A stable and accurate convective modelling procedure based on quadratic upstream interpolation, *Computer Methods in Applied Mechanics and Engineering*, Vol. **19**, No. 1, 1979, p. 59-98.

Levich, V.G., *Physicochemical hydrodynamics*, Prentice Hall Inc., Englewood Cliffs, New Jersey, 1962, 700 p.

Lewis, I.E., Design of mixer-settlers to achieve low entrainment losses and reduce capital costs, ISEC 1977, Toronto, *CIM Special Volume* **21**, 1979, p. 325-332.

Lindell, E., Nyman, B. and Ekman, E., Development and trends in copper solvent extraction, *International conference "Trends in Copper Metallurgy"*, Instytut Metali Niezelaznych, Gliwice, KGHM "Polska Miedz" S. A. Lubin, Poland April 20-22, 1998, p. 135-153.

Liu, S. and Li, D., Drop coalescence in turbulent dispersions, *Chemical Engineering Science*, Vol. **54**, 1999, p. 5667-5675.

Lo, S. M., Application of the MUSIG model to bubbly flows, *AEAT-1096*, AEA Technology, 1996.

Luo, H. and Svendsen H.F., Theoretical model for drop and bubble breakup in turbulent dispersions, *AIChE Journal*, Vol. **42**, No. 5, 1996, p. 1225-1233.

Mackay, G.D.M. and Mason, S.G., The gravity approach and coalescence of fluid drops at liquid interfaces, *The Canadian Journal of Chemical Engineering*, Vol. **411**, No. 5, 1963, p. 203-212.

Magiera, R. and Blass, E., Separation of liquid-liquid dispersions by flow through fibre beds, *Filtration & Separation*, Vol. **34**, No. 4, 1997, p. 369-376.

Menacho, J.M., Gutiérrez, L.E. and Zivkoviz, Y.I., A dynamic model for chloride control in SX plants, *Proceedings of the Copper 2003-Cobre 2003, the 5th International conference*, Vol. VI, Hydrometallurgy of copper, Book 2: Modeling, impurity control and solvent extraction, ed. Riveros, P.A., Dixon, D.G., Dreisinger, D.B. and Menacho, J.M., Santiago, November 30 - December 3, 2003, p. 517-529.

Miller, G., Design tools to control transients in solvent extraction plants, *Minerals & Metallurgical Processing*, Vol. **19**, No. 2, 2002, p. 57-64.

Miller, G., The modelling and control of transients in solvent extraction mixer-settlers, *MINPREX 2000*, International Congress on Mineral Processing and Extractive Metallurgy, September 11-13, 2000, Melbourne, p. 271-280.

Mizrahi, J. and Barnea, E., Compact settler gives efficient separation of liquid/liquid dispersions, *Process engineering*, Vol. **1**, 1973, p. 60-65.

Mukhopadhyay, A., Devulapalli, B., Dutta, A. and Grald, E.W., Computational Fluid Dynamics: A virtual prototyping tool for materials engineering, *JOM*, Vol. **56**, No. 3, 2004, p. 44-48.

Murdoch, P.G. and Leng, D.E., The mathematical formulation of hydrodynamic film thinning and its application to colliding drops suspended in a second liquid-II, *Chemical Engineering Science*, Vol. **26**, 1971, p. 1881-1892.

Nadiv, C. and Semiat, R., Batch settling of liquid-liquid dispersion, *Ind. Eng. Chem. Res.*, Vol. **34**, 1995, p. 2427-2435.

Nienow, A.W., Break-up, coalescence and catastrophic phase inversion in turbulent contactors, *Advances in Colloid and Interface Science*, Vol. **108-109**, 2004, p. 95-103.

Nir, S. and Vassilieff, C.S., Van der Waals interactions in thin films, In the book of *Thin liquid films, fundamentals and applications*, ed. Ivanov, I.B., Marcel Dekker, Inc., U.S.A. 1988, p. 207-274.

Nyman, B., Ekman, E., Kuusisto, R. and Pekkala, P., The OutoCompact SX approach to copper solvent extraction, *JOM*, Vol. **55**, 2003b, Nro. 7, p. 27-30.

Nyman, B., Ekman, E., Kuusisto, R., Pekkala, P. and Lyyra, J., The OutoCompact SX technology – An ideal approach to copper solvent extraction, *Proceedings of the Copper 2003-Cobre 2003, the 5th International conference*, Vol. VI (Hydrometallurgy of copper, Book 2: Modeling, impurity control and solvent extraction, ed. Riveros, P.A., Dixon, D.G., Dreisinger, D.B. and Menacho, J.M.), Santiago, November 30 - December 3, 2003a, p. 761-774.

Nyman, B., Kuusisto, R., Taipale, P. and Lyyra, J., Emphasis on feed end settling in Outokumpu's copper VSF mixer-settler, *ALTA 1996 Copper Hydrometallurgy Forum*, Brisbane, Australia, October 14-15, 1996, 9 p.

Oliveira, P.J. and Issa, R.I., Numerical aspects of an algorithm for the Eulerian simulation of two-phase flows, *International Journal for Numerical Methods in Fluids*, Vol. **43**, No. 10-11, 2003, p. 1177-1198.

Olmos, E., Gentric, C., Vial, Ch., Wild, G. and Midoux, N., Numerical simulation of multiphase flow in bubble column reactors. Influence of bubble coalescence and break-up, *Chemical Engineering Science*, Vol. **56**, 2001, p. 6359-6365.

Orjans, J.R., Notebaart, C.W., Godfrey, J.C., Hanson, C. and Slater, M.J., The design of mixer-settlers for the Zambian copper industry, ISEC 1977, Toronto, *CIM Special Volume* **21**, 1979, p. 340-346.

Padilla, R., Ruiz, M.C. and Trujillo, W., Separation of liquid-liquid dispersions in a deep-layer gravity settler: Part I. Experimental study of the separation process, *Hydrometallurgy*, Vol. **42**, No. 2, 1996, p. 267-279.

Pekkala, P., Kuusisto, R., Lyyra, J., Nyman, B., Lindell, E. and Ekman, E., Solvent extraction – How to get over hard times, *Proceedings of the Copper 99-Cobre 99, the 4th International conference*, Vol. IV (Hydrometallurgy of copper), ed. Young, S.K., Dreisinger, D.B., Hackl, R.P. and Dixon, D.G., The Minerals, Metals & Materials Society, Phoenix, USA, October 10-13, 1999, p. 305-318.

Perez de Ortiz, E.S., Marangoni phenomena, In the book of *Science and practice of liquid-liquid extraction*, **Vol. 1**, ed. Thornton, J.D., Oxford University Press, New York 1992, p. 157-209.

Peuha, E.-L. and Paatero, E., Physical properties of the copper oxime reagents, *Report of the Laboratory of Industrial Chemistry*, Lappeenranta University, Lappeenranta 2004, 12 p. (in Finnish)

Pope, S. B., *Turbulent flows*, Cambridge University Press, United Kingdom 2003, 771 p.

Prince, M.J. and Blanch, H.W., Bubble coalescence and break-up in air sparged bubble columns, *AIChE Journal*, Vol. **36**, No. 10, 1990, p. 1485-1499.

Princen, H.M., Shape of a fluid drop at a liquid-liquid interface, *Journal of Colloid Science*, Vol. **18**, 1963, p. 178-195.

QNET-CFD Network Newsletter, A Thematic Network for Quality and Trust in the Industrial Applications of CFD, Vol. 2, No. 4, 2004, p. 1-48. *The Final QNET-CFD Workshop "Best Practise Advise (BPA) for Industrial CFD"*, Brussels, May 13-14, 2004.

Radoev, B.P., Scheludko, A.D. and Manev, E.D., Critical thickness of thin liquid films: Theory and experiment, *Journal of Colloid and Interface Science*, Vol. **95**, No. 1, 1983, p. 254-265.

Ramkrishna, D. and Mahoney, A.W., Population balance modeling. Promise for the future, *Chemical Engineering Science*, Vol. **57**, 2002, p. 595-606.

Ramkrishna, D., *Population balances, Theory and applications to particulate systems in engineering*, Academic Press, U.S.A. 2000, 355 p.

Rhie, C.M. and Chow, W.L., Numerical study of the turbulent flow past an airfoil with trailing edge separation, *AIAA Journal*, Vol. **21**, 1983, p. 1527-1532.

Ritcey, G.M. and Ashbrook, A.W. *Solvent Extraction, principles and applications to process metallurgy,* **Part I**, Elsevier Science Publishers B.V., Amsterdam, 1984, p. 1-39 and 207-229, total 348 p.

Ritcey, G.M. and Ashbrook, A.W., *Solvent extraction, principles and applications to process metallurgy*, **part II**, Elsevier Scientific Publishing Company, Amsterdam 1979, p. 42-138, total 715 p.

Robbins, L.A., Liquid-liquid extraction, In the book of *Perry's chemical engineers' handbook*, sixth edition, ed. Perry, R.H. and Green, D., McGraw-Hill Inc., Malaysia 1984, p. 15/1-20.

Rother, M.A., Zinchenko, A.Z. and Davis, R.H., Buoyancy-driven coalescence of slightly deformable drops, *J. Fluid Mech.*, Vol. **346**, 1997, p. 117-148.

Ruiz, M.C. and Padilla, R., Separation of liquid-liquid dispersions in a deep-layer gravity settler: Part II. Mathematical modeling of the settler, *Hydrometallurgy*, Vol. **42**, No. 2, 1996, p. 281-291.

Ruiz, M.C., Muller, X. and Padilla, R. Determination of drop size distributions in a continuous mixer, *Proceedings of the Extraction and Processing Division*, ed. Taylor, P.R., TMS Annual Meeting, New Orleans 2001, p. 371-383.

Sawistowski, H., Interfacial phenomena. In the book of *Recent advances in liquid-liquid extraction*, ed. Hanson, C., Pergamon Press Ltd, Hungary 1971, p. 293-366.

Shanley, A., CFD for the real world, *Chemical Engineering*, October 2000, p. 139-143.

Shelley, S., Taking high-shear mixing to the next level, *Chemical Engineering*, Vol. **111**, No. 4, 2004, p. 24-26.

Simmons, M.J.H., Komonibo, E., Azzopardi, B.J. and Dick, D.R., Residence time distributions and flow behaviour within primary crude oil-water separators treating well-head fluids, *Transactions of the Institution of Chemical Engineers, Part A, Chemical Engineering Research and Design*, Vol. **82**, No. A10, 2004, p. 1383-1390.

Simmons, M.J.H., Wilson, J.A. and Azzopardi, B.J., Interpretation of the flow characteristics of a primary oil-water separation from the residence time distribution, *Transactions of the Institution of Chemical Engineers, Part A, Chemical Engineering Research and Design*, Vol. **80**, No. A5, 2002, p. 471-481.

Skelland, A.H.P. and Tedder, D.W., Extraction – Organic chemicals processing, In the book of *Handbook of separation technology*, ed. Rousseau, R.W., John Wiley & Sons Inc., U.S.A. 1987, p. 405-466.

Soo, L.S., *Multiphase fluid dynamics*, Science Press 1990, Hong Kong, 691 p.

Spalding, D.B., Developments in the IPSA procedure for numerical computation of multiphase-flow phenomena with interphase slip, unequal temperature, etc., Proceedings of the second national symposium, *Numerical Properties and Methodologies in Heat Transfer*, ed. Shih, T.M., Hemisphere, Washington, 1983, p. 421-436.

Spalding, D.B., The calculation of free-convection phenomena in gas-liquid mixtures, In the book of *Heat transfer and turbulent buoyant convection*, Vol. III, ed. Spalding, D.B. and Afgan, N., Hemispere Publishing Corporation, U.S.A. 1977, p. 569-586.

Stein, H.N., *The preparation of dispersions in liquids*, Marcel Dekker Inc., New York 1996, 245 p.

Tadros, T.F. and Vincent, B., Emulsion stability. In the book of *Encyclopedia of emulsion technology*, vol. 1, Basic theory, ed. Becher, P., Marcel Dekker, Inc., New York 1983a, p. 129-285.

Tadros, T.F. and Vincent, B., Liquid/liquid interfaces. In the book of *Encyclopedia of emulsion technology*, vol. 1, Basic theory, ed. Becher, P., Marcel Dekker, Inc., New York 1983b, p. 1-56.

Tadros, T.H.F., Steric interactions in thin liquid films, In the book of *Thin liquid films, fundamentals and applications*, ed. Ivanov, I.B., Marcel Dekker, Inc., U.S.A. 1988, p. 331-377.

Tennekes, H. and Lumley, J.L., *A first course in turbulence*, Third printing, The MIT Press, U.S.A, 1974, 300 p.

Thakre, S.S. and Joshi, J.B., CFD simulation of bubble column reactors: importance of drag force formulation, *Chemical Engineering Science*, Vol. **54**, 1999, p. 5055-5060.

Tobin, T. and Ramkrishna, D., Modeling the effect of drop charge on coalescence in turbulent liquid-liquid dispersions, *The Canadian Journal of Chemical Engineering*, Vol. **77**, No. 6, 1999, p. 1090-1104.

Tsekov, R. and Ruckenstein, E., Dimple formation and its effect on the rate of drainage in thin liquid films, *Colloids and Surfaces A: Physicochemical and Engineering Aspects*, Vol. **82**, 1994, p. 255-261.

Tuomi, I., The lives and death of Moore's law, *URL: http://firstmonday.org/issues/issue7_11/tuomi/index.html*, 27.5.2005, (First Monday, Vol. 7, No. 11, November 2002), 34 p.

Van Doormal, J.P. and Raithby, G.D., Enhancements of the SIMPLE method for predicting incompressible fluid flows, *Numerical Heat Transfer*, Vol. **7**, 1984, p. 147-163.

Vancas, M.F., Innovations in SX-EW, *Randol Copper Hydromet Roundtable*, Vancouver, Canada, November 1996.

Vancas, M.F., Solvent extraction settlers – A comparison of various designs, *Proceedings of the Copper 2003-Cobre 2003, the 5th International conference*, Vol. VI (Hydrometallurgy of copper, Book 2: Modeling, impurity control and solvent extraction, ed. Riveros, P.A., Dixon, D.G., Dreisinger, D.B. and Menacho, J.M.), Santiago, November 30 - December 3, 2003, p. 707-717.

Versteeg, H.K. & Malalasekera, W., *An introduction to computational fluid dynamics, The finite volume method*, Longman Group Ltd. 1995, New York, 257 p.

Virnig, M.J., Olafson, S.M., Kordosky, G.A. and Wolfe, G.A., Crud formation: field studies and fundamental studies, *Proceedings of the Copper 99-Cobre 99, the 4th International conference*, Vol. IV (Hydrometallurgy of copper), ed. Young, S.K., Dreisinger, D.B., Hackl, R.P. and Dixon, D.G., The Minerals, Metals & Materials Society, Phoenix, USA, October 10-13, 1999, p. 291-304.

Warwick, G.C.I. and Scuffham, J.B., The design of mixer-settlers for metallurgical duties, *Solvent extraction in metallurgical processes, International symposium*, Antwerp, May 4-5, 1972, p. 40-47.

Warwick, G.C.I., Scuffham, J.B. and Lott, J.B., Solvent extraction – today's exciting process for copper and other metals, Designers of world's largest ever plant describe process economics and the equipment design factors which affect this, *World Mining*, 1970, p. 46-52.

White, F.M., *Viscous fluid flow*, second edition, McGraw-Hill, Inc. 1991, Singapore, 641 p.

Wilkinson, D. and Waldie, B., CFD and experimental studies of fluid and particle flow in horizontal primary separators, *Transactions of the Institution of Chemical Engineers, Part A, Chemical Engineering Research and Design*, Vol. **72**, No. A2, 1994, p. 189-196.

Wilkinson, D., Waldie, B., Nor, M.I.M. and Lee, H.Y., Baffle plate configurations to enhance separation in horizontal primary separators, *Chemical Engineering Journal*, Vol. **77**, 2000, p. 221-226.

Xia, J.L., Ahokainen, T. and Kankaanpää, T., Nickel droplet settling behavior in an electric furnace, *Metallurgical and Materials Transactions B*, **35B**, 2004, p. 839-845.

Xia, J.L., Ahokainen, T., Kankaanpää, T. and Järvi, J., Numerical modelling of copper droplet settling behaviour in the settler of a flash smelting furnace, *European Metallurgical Conf. EMC-2005*, Dresden, Germany, September 18-21, 2005.

Xia, J.L., Smith, B.L., Benim, A.C., Schmidli, J. and Yadigaroglu, G., Effect of inlet and outlet boundary conditions on swirling flows, *Computers & Fluids*, Vol. **26**, No. 8, 1997, p. 811-823.

Appendix 1

Tested boundary conditions at the lower and upper outlets

Table A. Boundary conditions at the lower and upper outlets.

1	**Lower outlet**	pressure boundary	no volume fraction information
	Upper outlet	pressure boundary	no volume fraction information
	Ref. pressure	normal atmospheric pressure at the interface of the free surface, in the last grid cell of the upper outlet	
	Observations	strong back flow in other outlet and water disappeared	
2	**Lower outlet**	mass flow fraction of the water phase, which was calculated from inlet information	no volume fraction information
	Upper outlet	mass flow fraction of the organic phase, which was calculated from inlet information	no volume fraction information
	Ref. pressure	at the interface of the free surface, in the last grid cell of the upper outlet	
	Observations	water disappeared from the calculation domain, but the volume fractions of the phases were correct at the outlets	
3	**Lower outlet**	rising pipe, mass flow fraction of the water phase, which was calculated from the inlet information	no volume fraction information
	Upper outlet	mass flow fraction of the organic phase, which was calculated from the inlet information	no volume fraction information
	Ref. pressure	at the interface of the free surface, in the last grid cell of the upper outlet	
	Observations	water disappeared from the calculation domain, but the volume fractions of the phases were correct at the outlets	
4	**Lower outlet**	rising pipe, pressure boundary	no volume fraction information, or $\alpha_c = 1$ and $\alpha_d = 0$
	Upper outlet	pressure boundary	no volume fraction information, or $\alpha_c = 0$ and $\alpha_d = 1$
	Ref. pressure	normal atmospheric pressure at the interface of the free surface, in the last grid cell of the upper outlet	
	Observations	strong back flow in other outlet and water disappeared	
5	**Lower outlet**	rising pipe, mass flow fraction of the water phase, which was calculated from the inlet information	no volume fraction information
	Upper outlet	negative inlet boundary for the organic phase, velocity was calculated from the inlet information	no volume fraction information
	Ref. pressure	at the top of the rising pipe, normal atmospheric pressure	
	Observations	water disappeared from the calculation domain	

Table A. Boundary conditions at the lower and upper outlets.

6	**Lower outlet**	height of the lower outlet was equal to the height of the upper outlet, no rising pipe, mass flow fractions for both phases were calculated from the inlet information	no volume fraction information
	Upper outlet		no volume fraction information
	Ref. pressure	at the interface of the free surface in the last grid cell of the upper outlet	
	Observations	water disappeared	
7	**Lower outlet**	rising pipe with normal atmospheric pressure boundary	$\alpha_c = 1$ and $\alpha_d = 0$
	Upper outlet	negative inlet boundary for the organic phase, velocity was calculated from the inlet information	$\alpha_c = 0$ and $\alpha_d = 1$
	Ref. pressure	at the interface of the free surface, in the last grid cell of the upper outlet	
	Observations	incorrect pressure distribution, water disappeared	
8	**Lower outlet**	rising pipe with negative inlet boundary for the water phase, velocity was calculated from the inlet information	$\alpha_c = 1$ and $\alpha_d = 0$
	Upper outlet	pressure boundary with normal atmospheric pressure	$\alpha_c = 0$ and $\alpha_d = 1$
	Ref. pressure	at the interface of the free surface, in the last grid cell of the upper outlet	
	Observations	correct pressure distribution, back flow at the upper outlet, water disappeared	
9	**Lower outlet**	rising pipe with mass flow rate of the water phase, which was equal to the inlet value, mass flow rate of the organic phase was zero	no volume fraction information
	Upper outlet	mass flow rate of the organic phase, which was equal to the inlet value, mass flow rate of the water phase was zero modified multiphase treatment was set on (CFX-4.4 Solver Manual), which ensured that correct mass flow rates were obtained for both phases	no volume fraction information
	Ref. pressure	at the interface of the free surface, in the last grid cell of the upper outlet	
	Observations	correct pressure distribution, water did not disappear, but at the top of the rising pipe there was some amount of the organic phase, which did not disappear	

Table A. Boundary conditions at the lower and upper outlets.

10	**Lower outlet**	without rising pipe, mass flow rate of the water phase, which was equal to the inlet value, mass flow rate of the organic phase was zero	no volume fraction information
	Upper outlet	mass flow rate of the organic phase, which was equal to the inlet value, mass flow rate of the water phase was zero	no volume fraction information
		modified multiphase treatment was set on (CFX-4.4 Solver Manual), which ensured that correct mass flow rates were obtained for both phases	
	Ref. pressure	at the interface of the free surface, in the last grid cell of the upper outlet	
	Observations	correct pressure distribution, water did not disappear, but at the upper outlet there was some amount of the water phase and very very small back flow. At the lower outlet there was some amount of the organic phase	
11	**Lower outlet**	without rising pipe, mass flow rate value, which was equal to the water phase at the inlet, the mass flow rate of the organic phase was not set	no volume fraction information
	Upper outlet	mass flow rate value, which was equal to the organic phase at the inlet, the mass flow rate of the water phase was not set	no volume fraction information
		modified multiphase treatment was set on (CFX-4.4 Solver Manual), which ensured that correct mass flow rates were obtained for both phases	
	Ref.pressure	at the interface of the free surface, in the last grid cell of the upper outlet	
	Observations	correct pressure distribution, incorrect mass flow rates at the outlets, water disappeared	
12	**Lower outlet**	without rising pipe, mass flow rate of the water phase was equal to the inlet value, mass flow rate of the organic phase was zero	no volume fraction information
	Upper outlet	mass flow rate of the organic phase was equal to the inlet value, mass flow rate of the water phase was zero	no volume fraction information
		without modified multiphase treatment	
	Ref. pressure	at the interface of the free surface, in the last grid cell of the upper outlet	
	Observations	correct pressure distribution, water disappeared, but there was no volume fraction errors	

Table A. Boundary conditions at the lower and upper outlets.

13	**Lower outlet**	without rising pipe, mass flow rate of the water phase and small amount of the organic phase	$\alpha_c = 0.99$ and $\alpha_d = 0.01$
	Upper outlet	mass flow rate of the organic phase and small amount of the water phase	$\alpha_c = 0.01$ and $\alpha_d = 0.99$
	Ref. pressure	at the interface of the free surface, in the last grid cell of the upper outlet	
	Observations	volume fraction errors at the outlets, water disappeared	
14	**Lower outlet**	negative inlet boundary for the water phase, the velocity was calculated from the inlet information	$\alpha_c = 1$ and $\alpha_d = 0$
	Upper outlet	negative inlet boundary for the organic phase, the velocity was calculated from the inlet information	$\alpha_c = 0$ and $\alpha_d = 1$
	Ref. pressure	at the interface of the free surface, in the last grid cell of the upper outlet	
	Observations	water disappeared	
15	**Lower and upper outlet**	Settler geometry was rebuilt so that the last grid cell did not locate in the upper outlet but it was in the top corner in the front end of the settler.	
	Ref. pressure	at the interface of the free surface, in the last grid cell of the upper outlet	
	Observations	correct pressure distribution, the volume fraction errors at the outlets, water dissapeared. The results proved that the volume fraction errors at the outlets were not caused by a mathematical calculation order error of the solver code	
16	**Lower and upper outlet**	In the beginning of the simulation initial guess was used. It was assumed that in the calculation domain there was half and half the water and the organic phase.	
	Ref. pressure	at the interface of the free surface, in the last grid cell of the upper outlet	
	Observations	Initial guess did not solve the previous problems	

Appendix 2

Comparison of discretisation schemes, HYBRID versus QUICK, in the middle of the settler (x = 1.577 m).

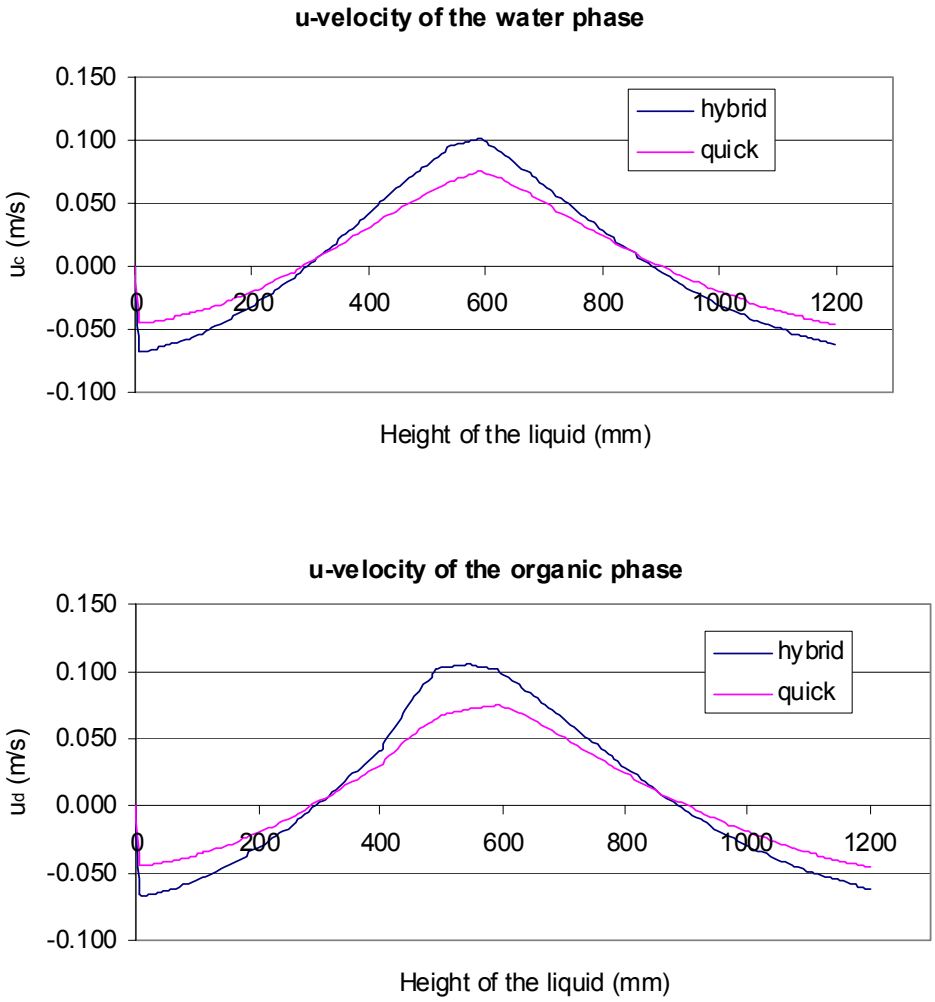

Figure A1. $\bar{u}$-velocities of the water and organic phases, when the hybrid and quick schemes have been used.

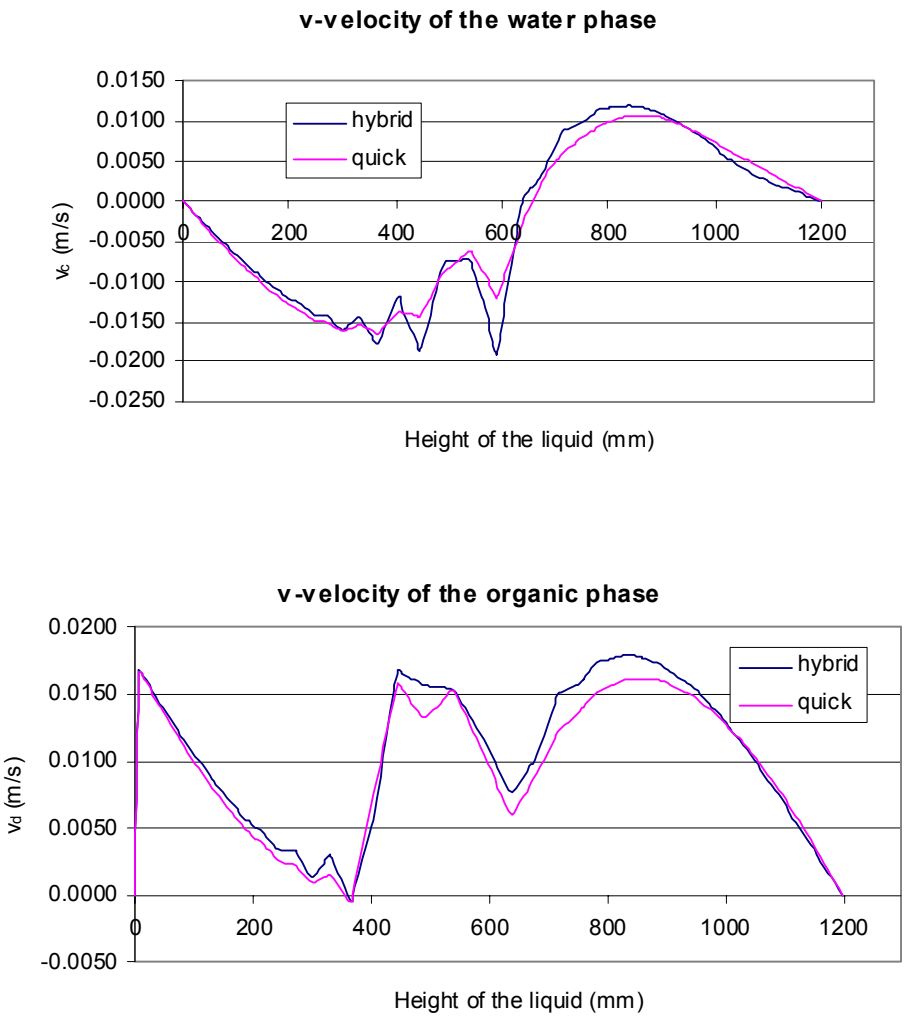

Figure A2. $\bar{v}$-velocities of the water and organic phases, when the hybrid and quick schemes have been used.

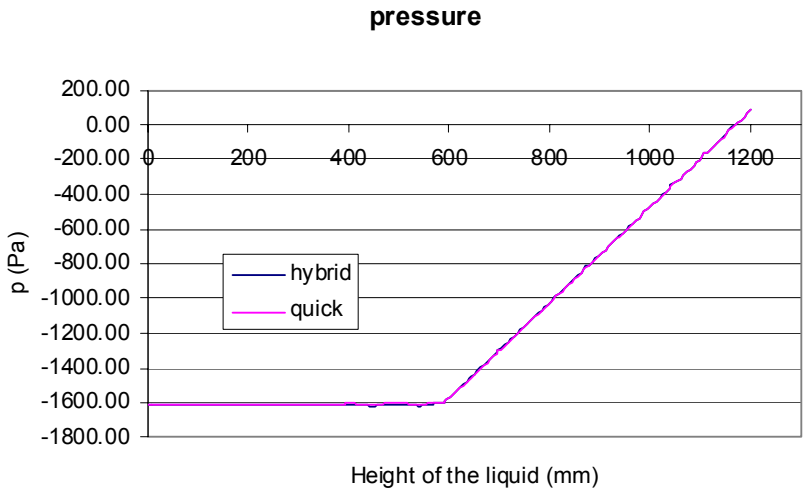

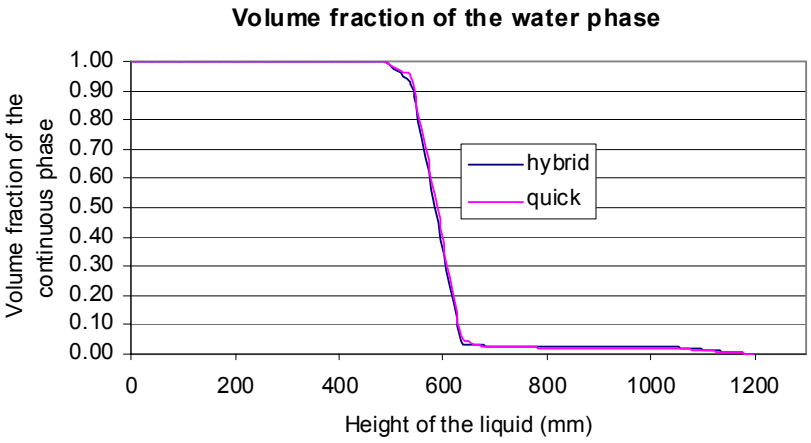

Figure A3. Pressure and volume fraction of the water phase, when the hybrid and quick schemes have been used.

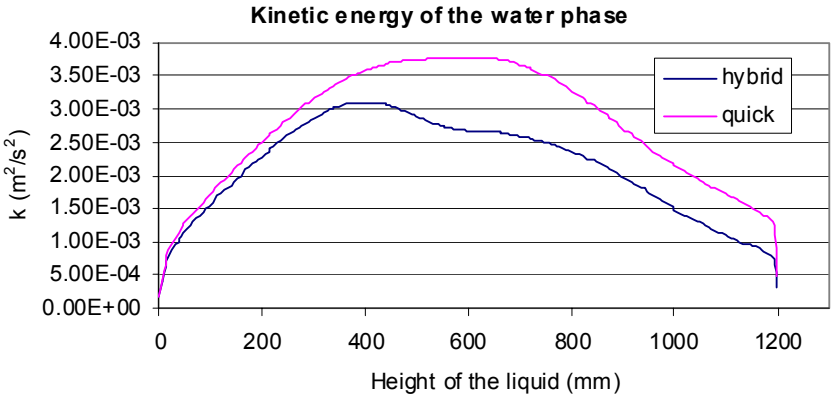

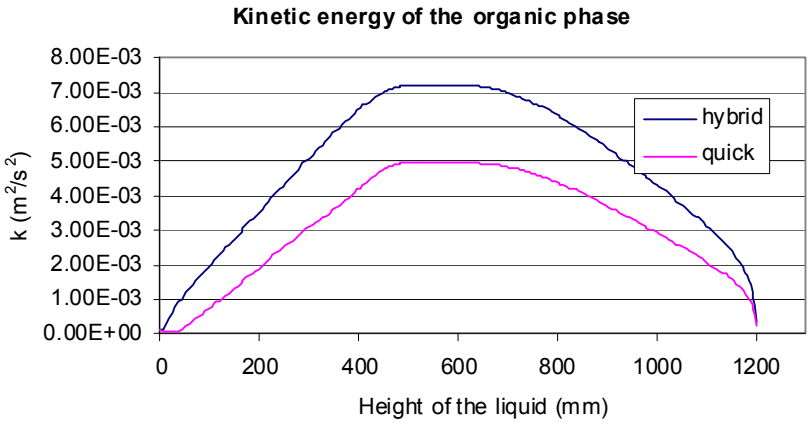

Figure A4. The turbulence kinetic energy of the water and organic phases, when the hybrid and quick schemes have been used.

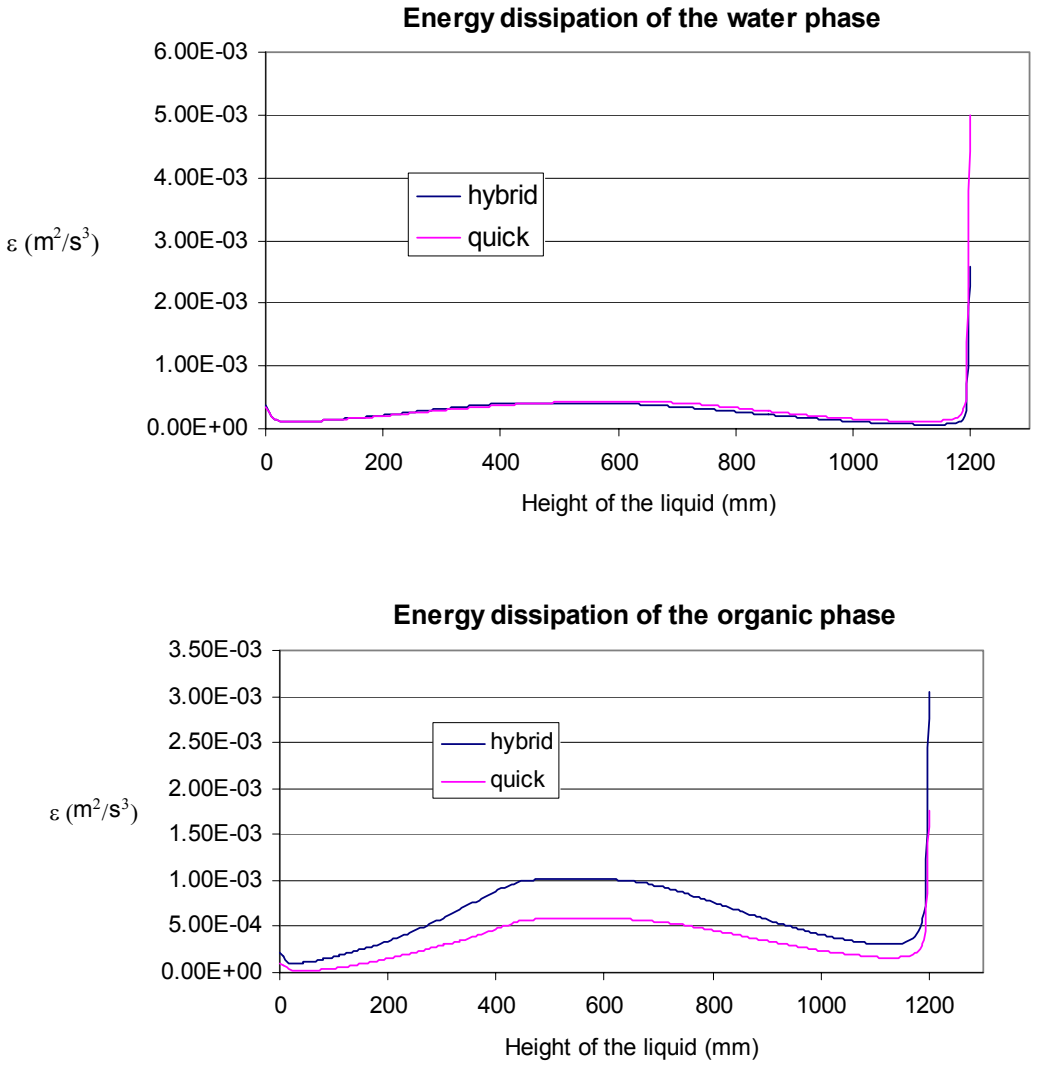

Figure A5. The turbulence dissipation energy of the water and organic phases, when the hybrid and quick schemes have been used.

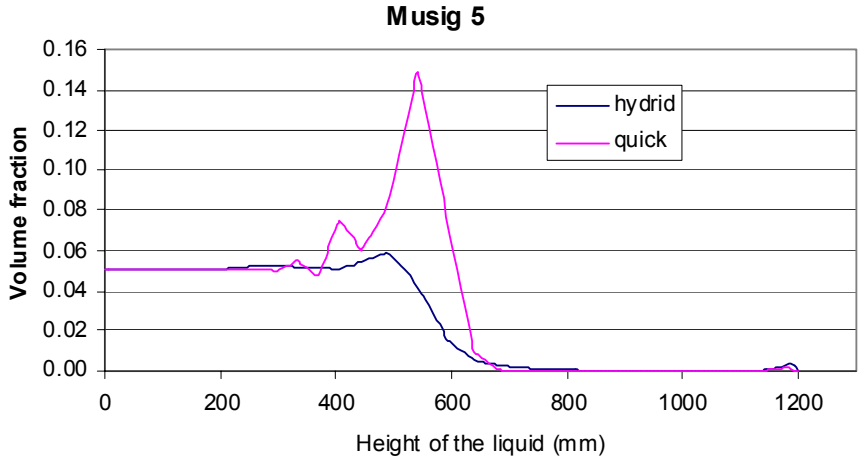

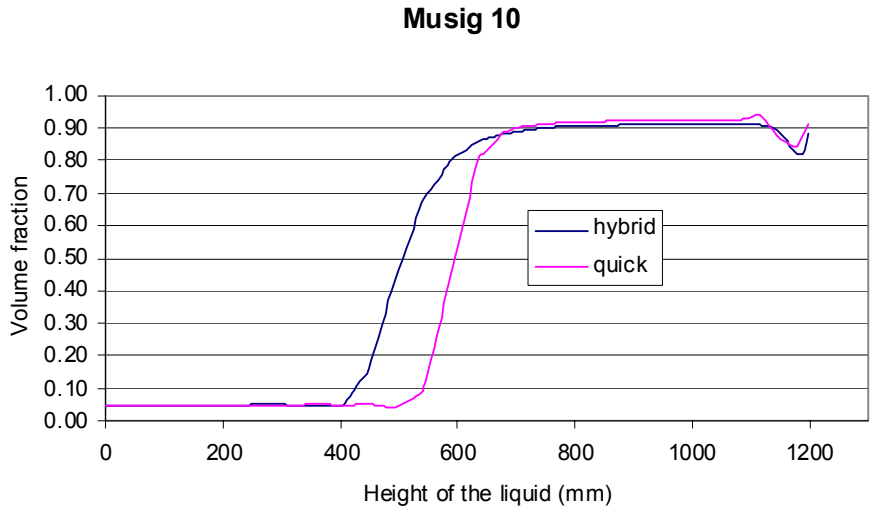

Figure A6. The volume fraction of the Musig-groups 5 and 10, when the hybrid and quick schemes have been used.

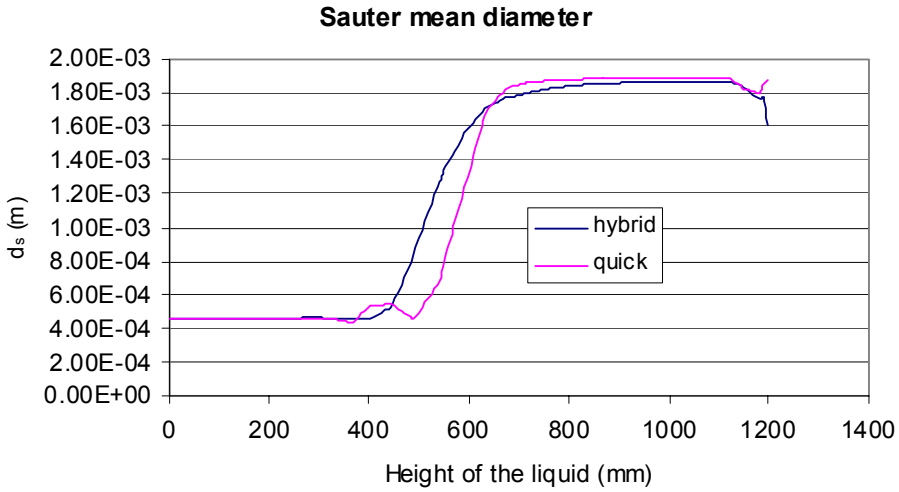

Figure A7. The Sauter mean diameter, when the hybrid and quick schemes have been used.

Appendix 3

Steady-state versus transient situation in the settler

Simulations are carried out with two picket fences. Temperature is 20 °C and specific volume flow rate is 12 m^3/m^2h.

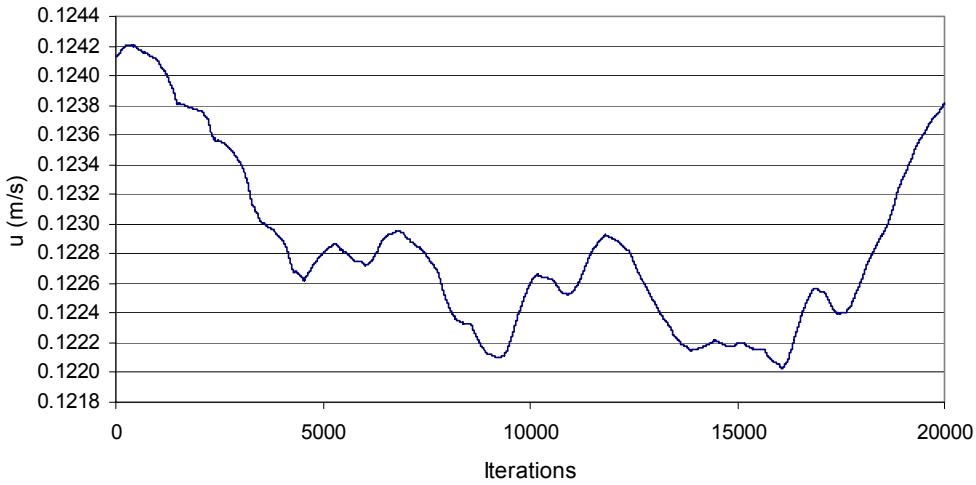

Figure A1. $\bar{u}$-velocity of the continuous phase as a function of iterations in steady-state situation. Solution is converged and it complies with the six-item calculation procedure.

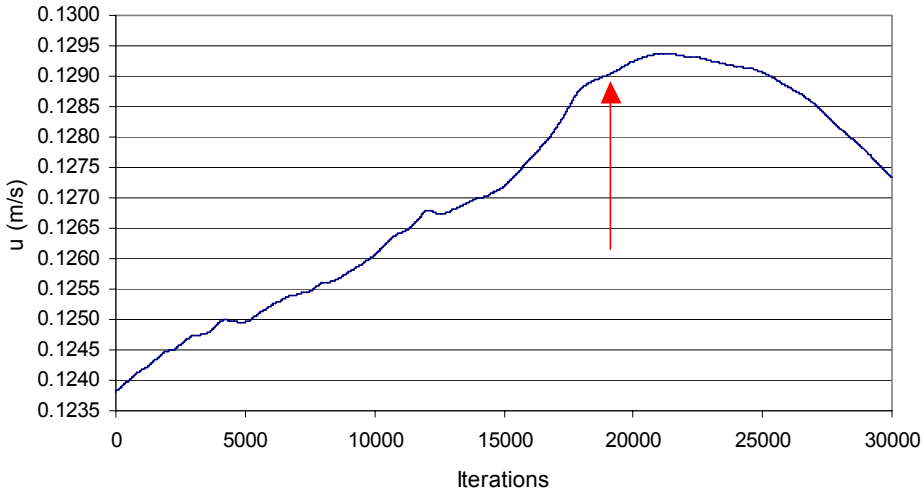

Figure A2. $\bar{u}$-velocity of the continuous phase as a function of iterations in steady state. The solution has been continued from the converged situation (Figure A1), and it does not comply with the six-item calculation procedure.

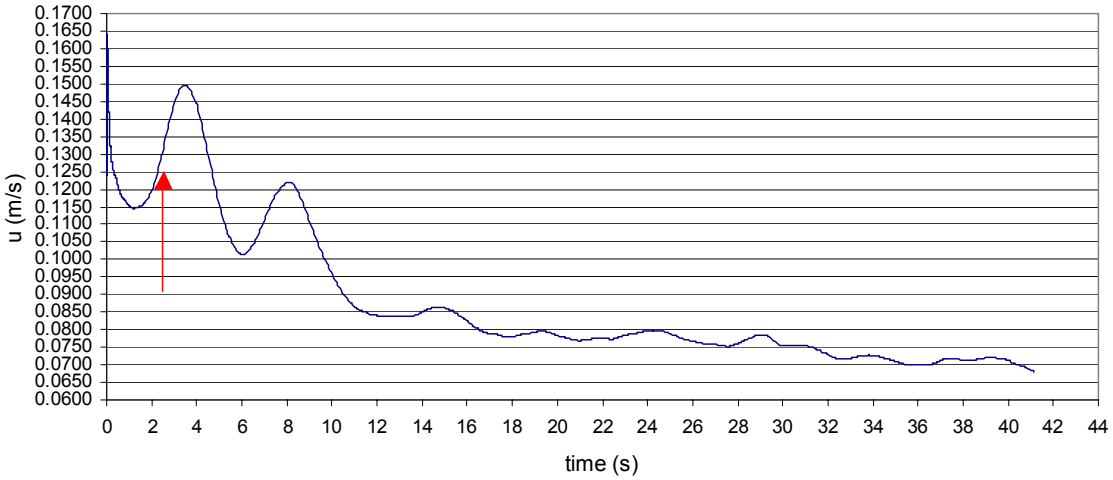

Figure A3. $\bar{u}$-velocity of the continuous phase as a function of time. The solution is continued from the converged situation of steady state (Figure A1).

Appendix 4

The volume fractions of the organic phase with specific volume flow rates, temperatures and picket fences, when an allowed entrainment level of the aqueous phase is 5 000 ppm. Dark red indicates the totally separated organic phase and violet indicates the water phase.

Figure A1. V_{spec} = 6 m^3/m^2h, T = 10 °C and no picket fences.

Figure A2. V_{spec} = 6 m^3/m^2h, T = 10 °C and one picket fence.

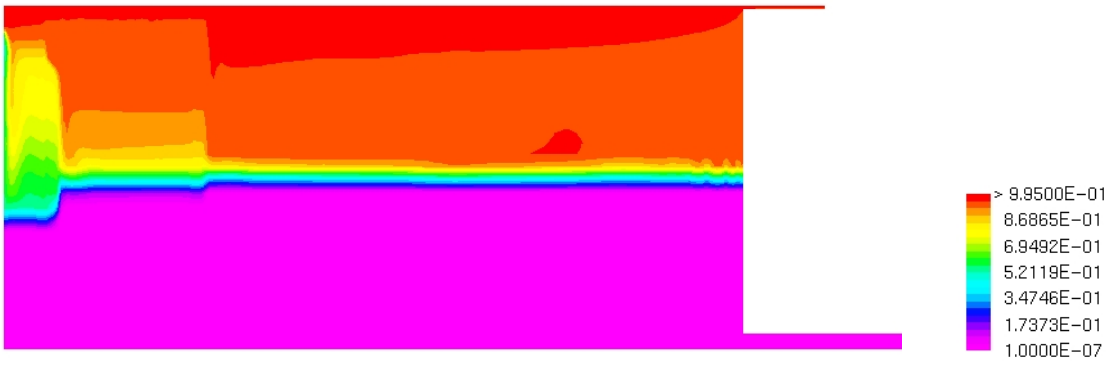

Figure A3. V_{spec} = 6 m^3/m^{2}h, T = 10 °C and two picket fences.

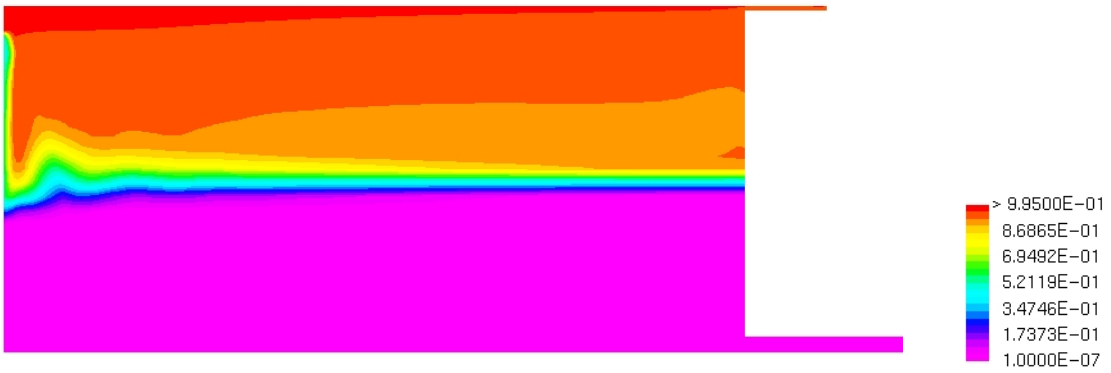

Figure A4. V_{spec} = 12 m^3/m^{2}h, T = 10 °C and no picket fences.

Figure A5. V_{spec} = 12 m^3/m^{2}h, T = 10 °C and one picket fence.

Figure A6. V_{spec} = 12 m^3/m^{2}h, T = 10 °C and two picket fences.

Figure A7. V_{spec} = 6 m^3/m^{2}h, T = 20 °C and no picket fences.

Figure A8. V_{spec} = 6 m^3/m^{2}h, T = 20 °C and one picket fence.

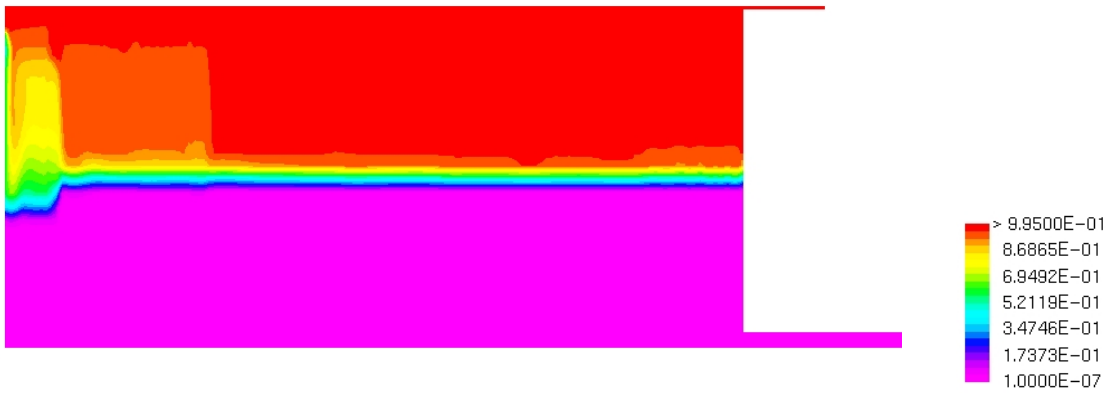

Figure A9. V_{spec} = 6 m^3/m^2h, T = 20 °C and two picket fences.

Figure A10. V_{spec} = 12 m^3/m^2h, T = 20 °C and no picket fences.

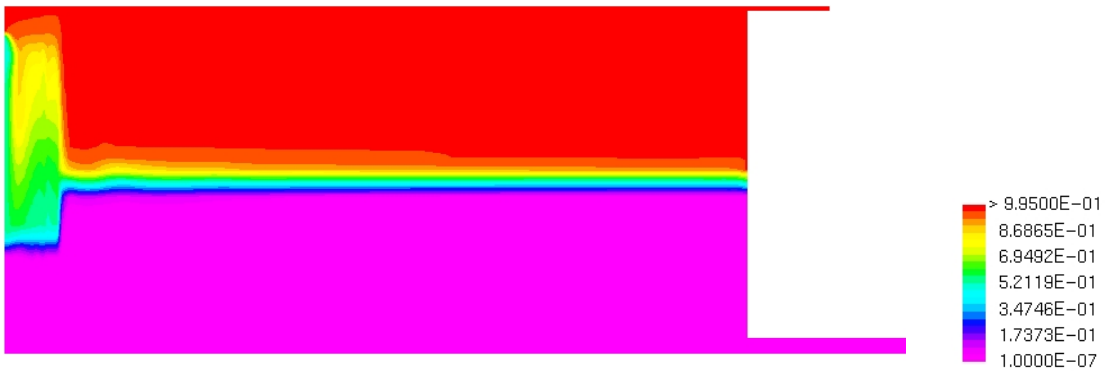

Figure A11. V_{spec} = 12 m^3/m^2h, T = 20 °C and one picket fence.

Figure A12. V_{spec} = 12 m^3/m^2h, T = 20 °C and two picket fences.

Appendix 5

Droplet size distributions at five different locations for different numbers of picket fences (PF), when the specific volume flow rate is 12 m^3/m^2h and the temperature is 10 °C.

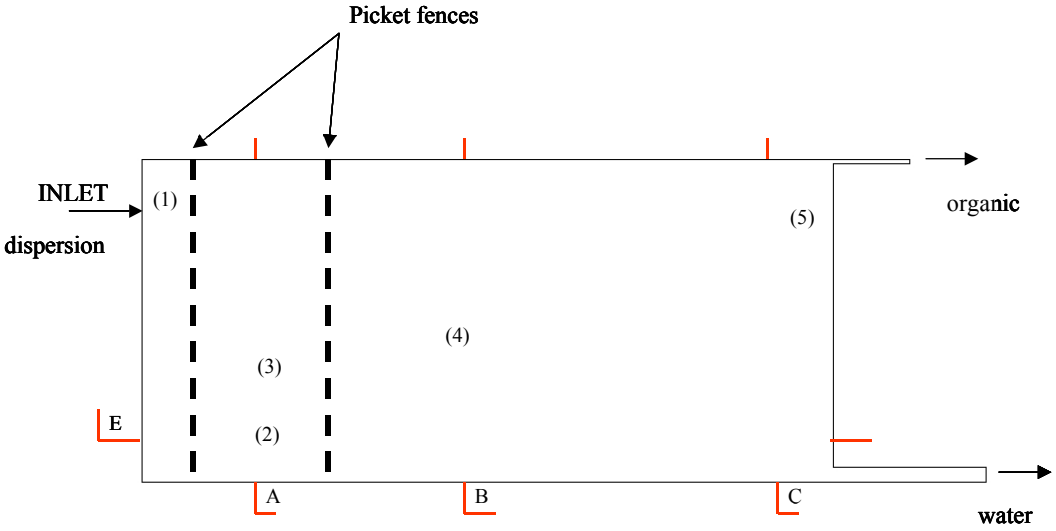

Figure A1. The location number (1) is at the inlet, number (2) is at the intersection of lines A and E, number (3) is at the height of 500 mm on line A, number (4) is in the middle of the dispersion layer at the height of 600 mm on line B and number (5) is near the overflow weir.

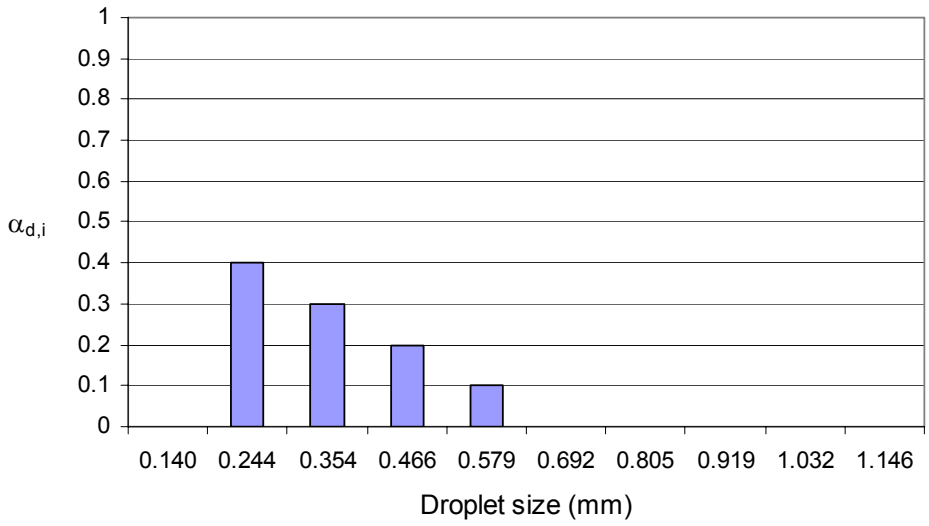

Figure A2. Droplet size distribution at point (1).

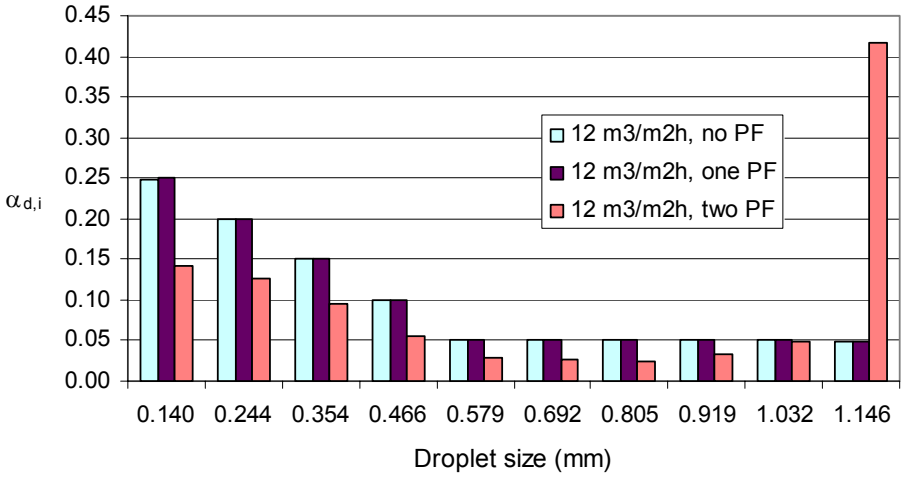

Figure A3. Droplet size distribution at point (2).

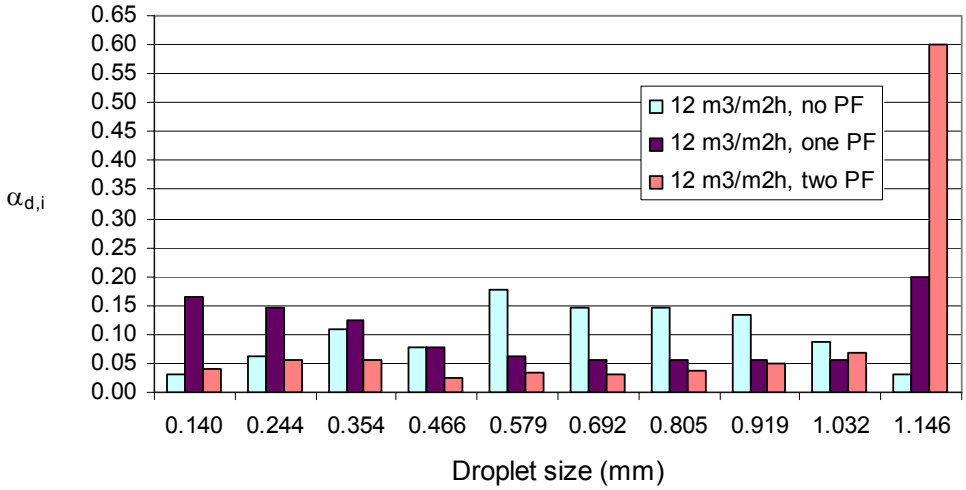

Figure A4. Droplet size distribution at point (3).

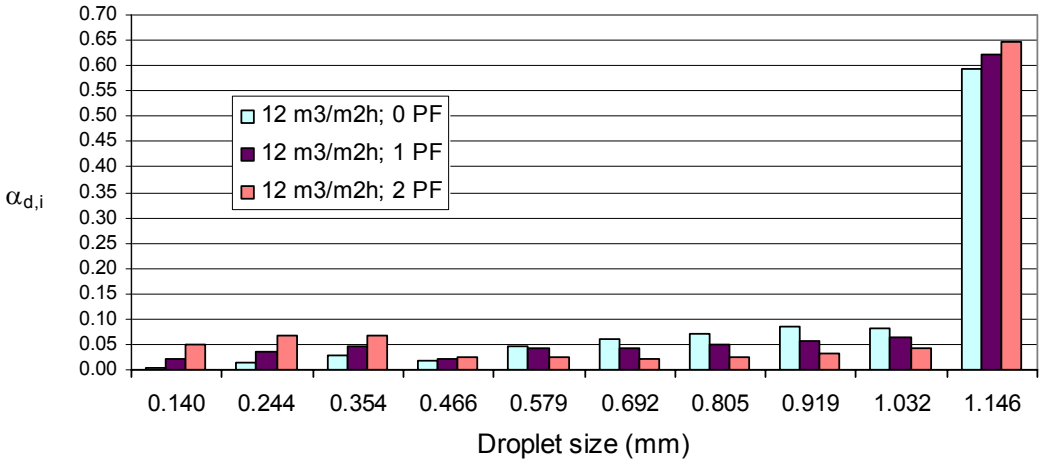

Figure A5. Droplet size distribution at point (4).

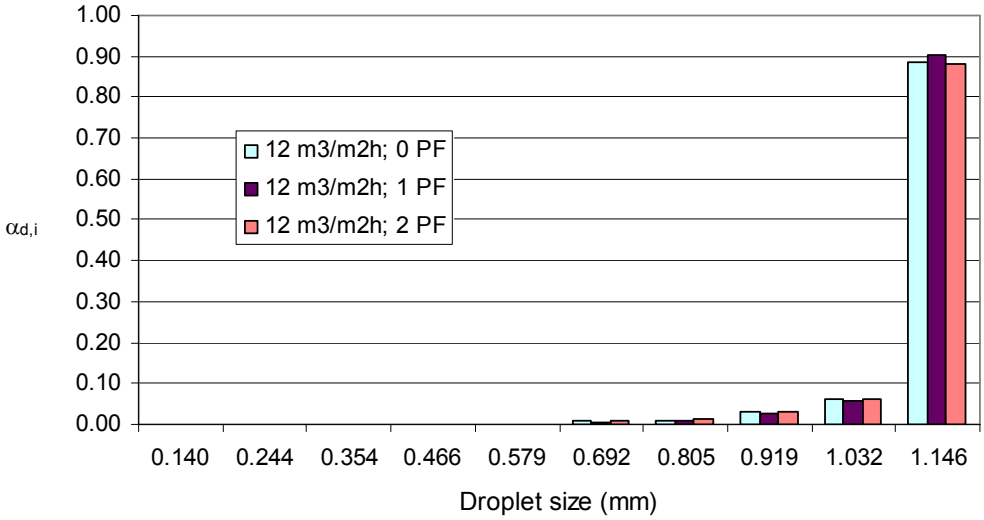

Figure A6. Droplet size distribution at point (5).

Appendix 6

Droplet size distributions at five different locations for different numbers of picket fences (PF), when the specific volume flow rate is 6 m^3/m^2h and the temperature is 10 °C.

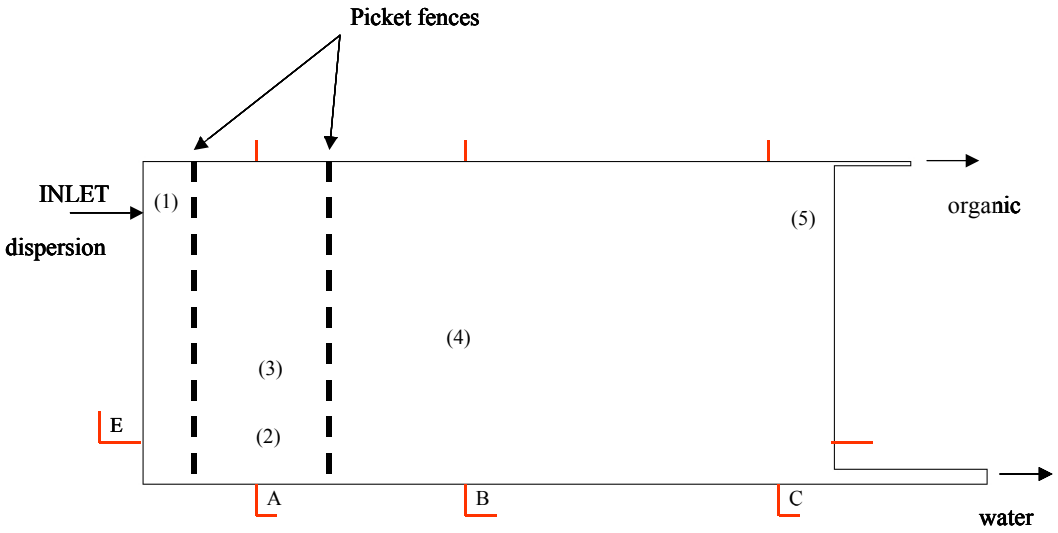

Figure A1. The location number (1) is at the inlet, number (2) is at the intersection of lines A and E, number (3) is at the height of 500 mm on line A, number (4) is in the middle of the dispersion layer at the height of 600 mm on line B and number (5) is near the overflow weir.

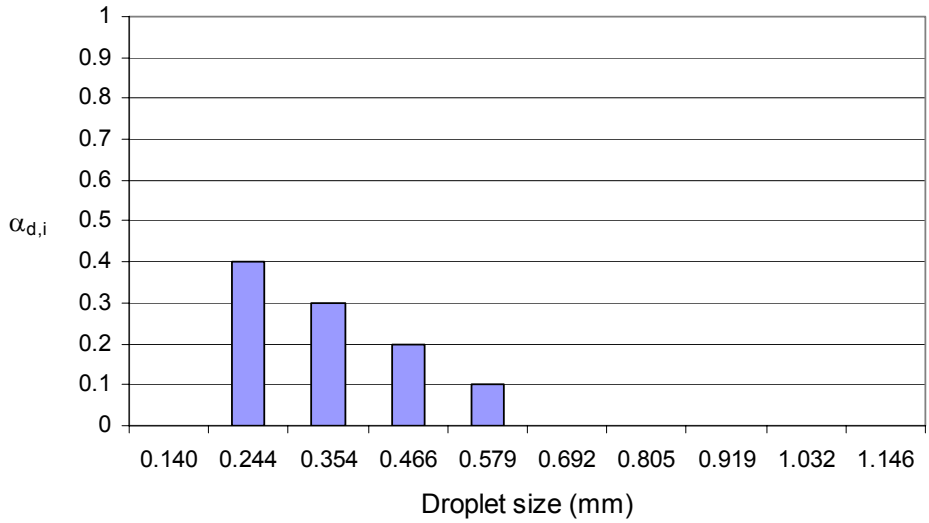

Figure A2. Droplet size distribution at point (1).

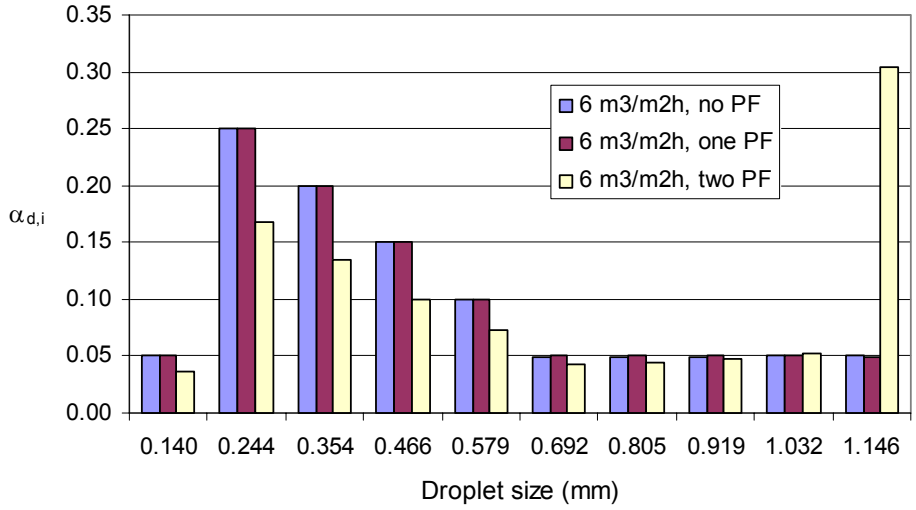

Figure A3. Droplet size distribution at point (2).

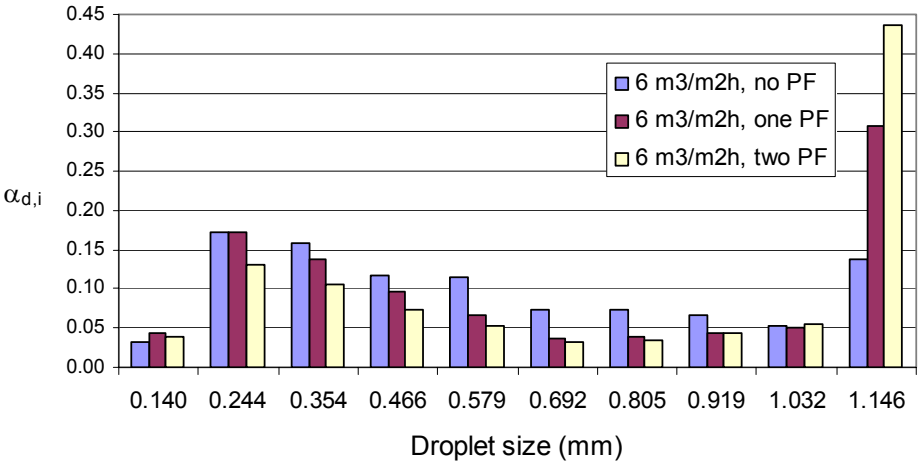

Figure A4. Droplet size distribution at point (3).

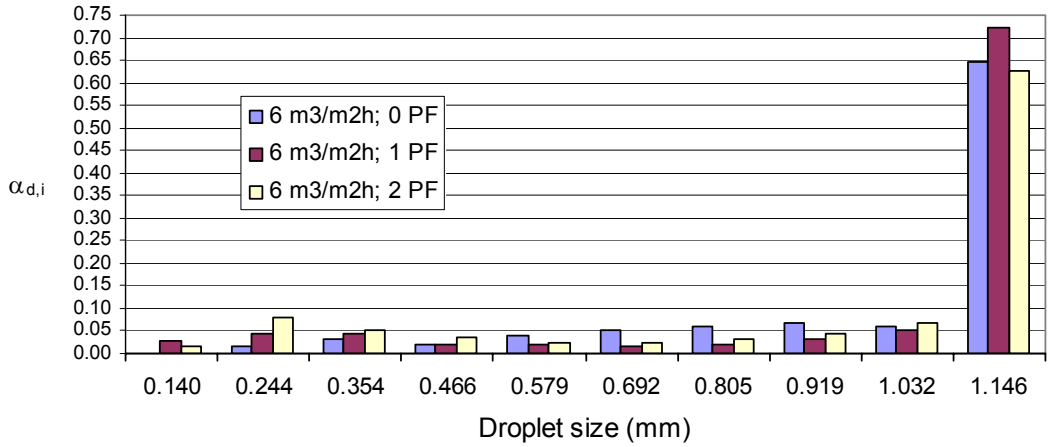

Figure A5. Droplet size distribution at point (4).

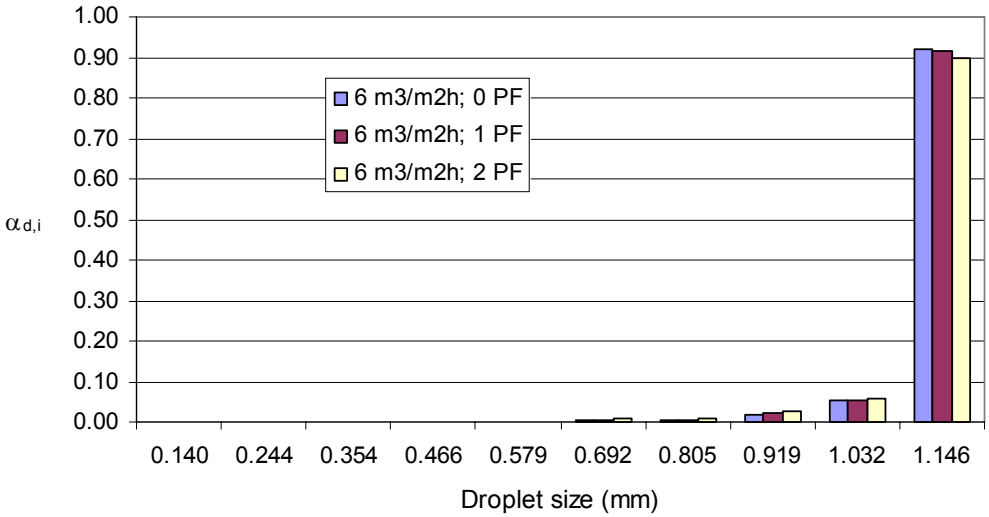

Figure A6. Droplet size distribution at point (5).

Appendix 7

Droplet size distributions at five different locations for different numbers of picket fences (PF), when the specific volume flow rate is 6 m^3/m^2h and the temperature is 20 °C.

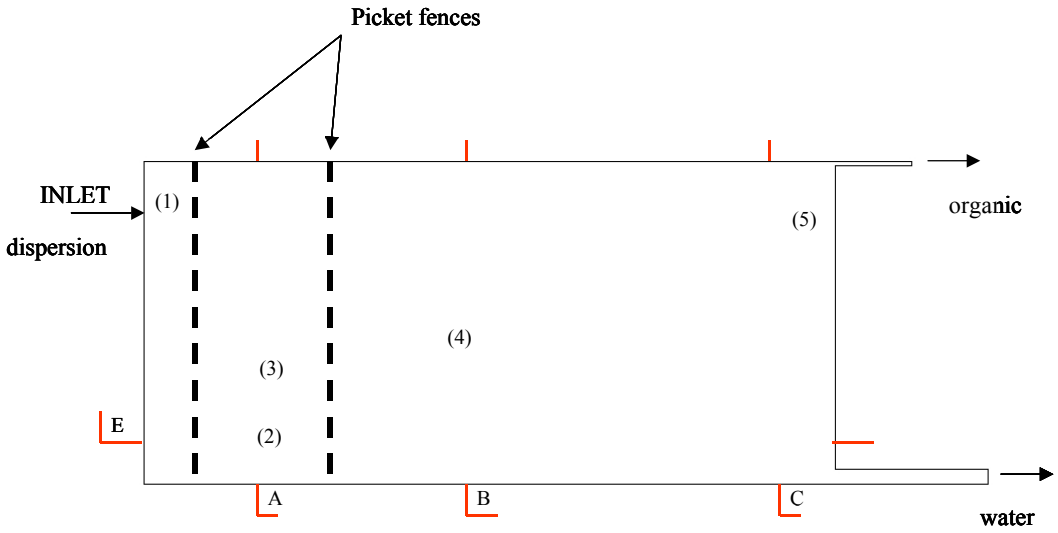

Figure A1. The location number (1) is at the inlet, number (2) is at the intersection of lines A and E, number (3) is at the height of 500 mm on line A, number (4) is in the middle of the dispersion layer at the height of 600 mm on line B and number (5) is near the overflow weir.

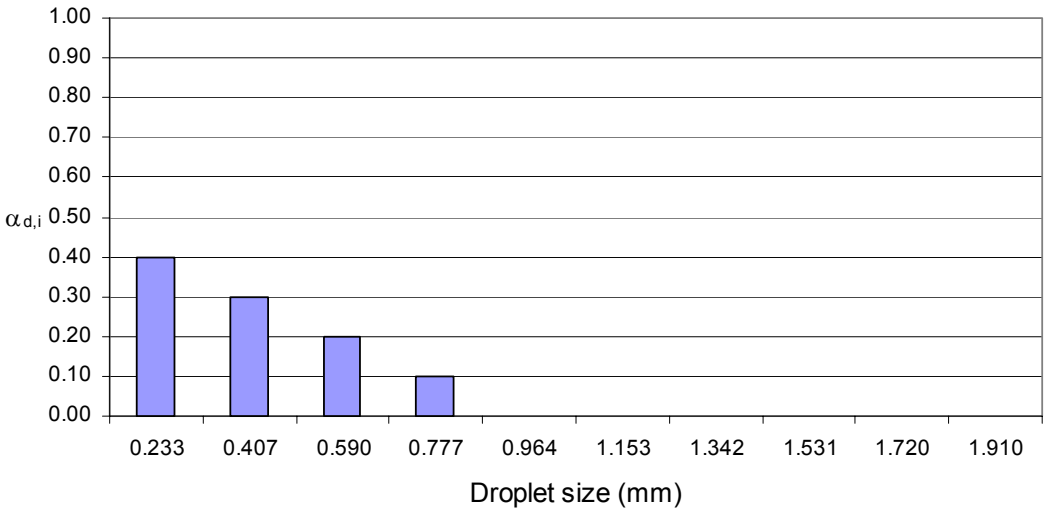

Figure A2. Droplet size distribution at point (1).

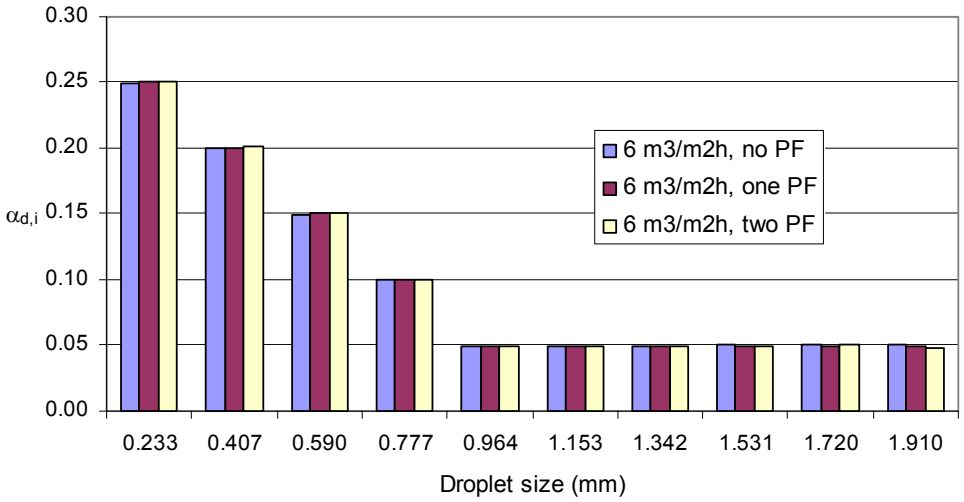

Figure A3. Droplet size distribution at point (2).

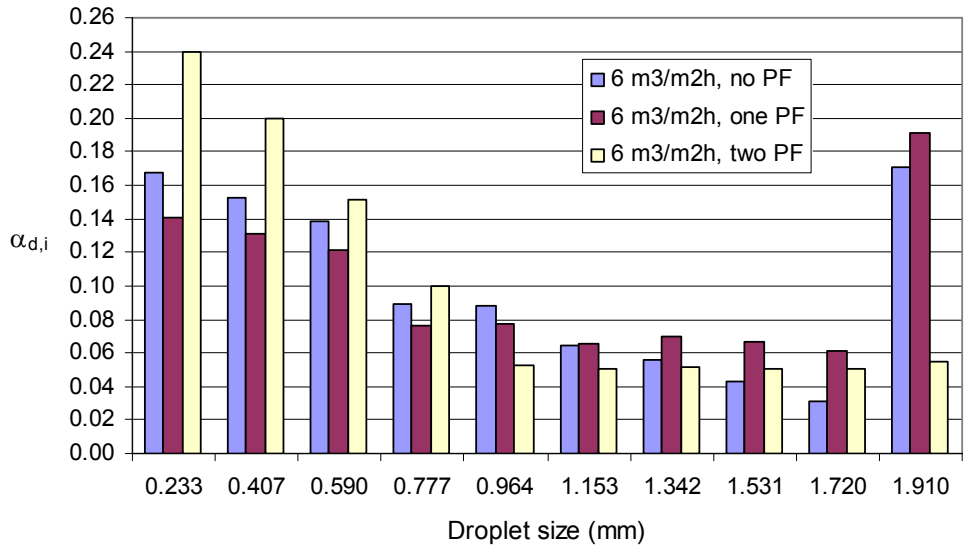

Figure A4. Droplet size distribution at point (3).

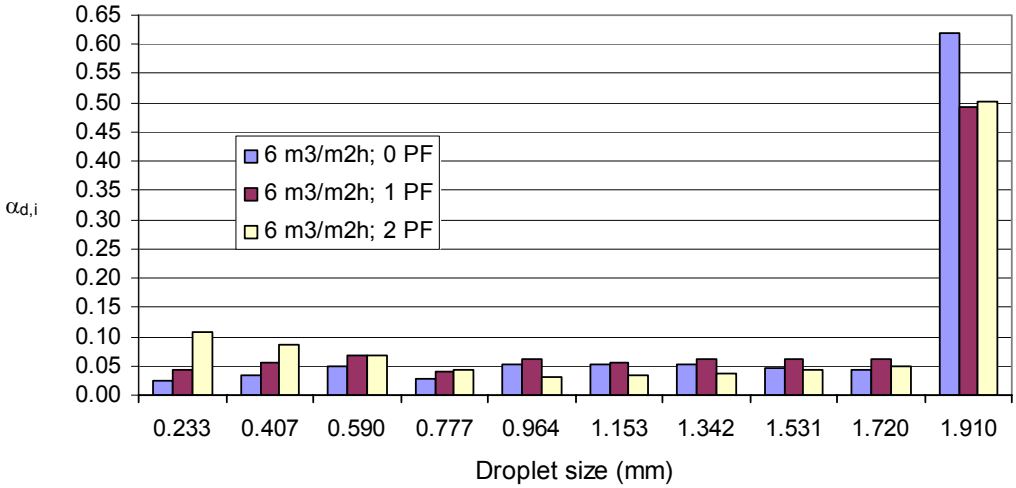

Figure A5. Droplet size distribution at point (4).

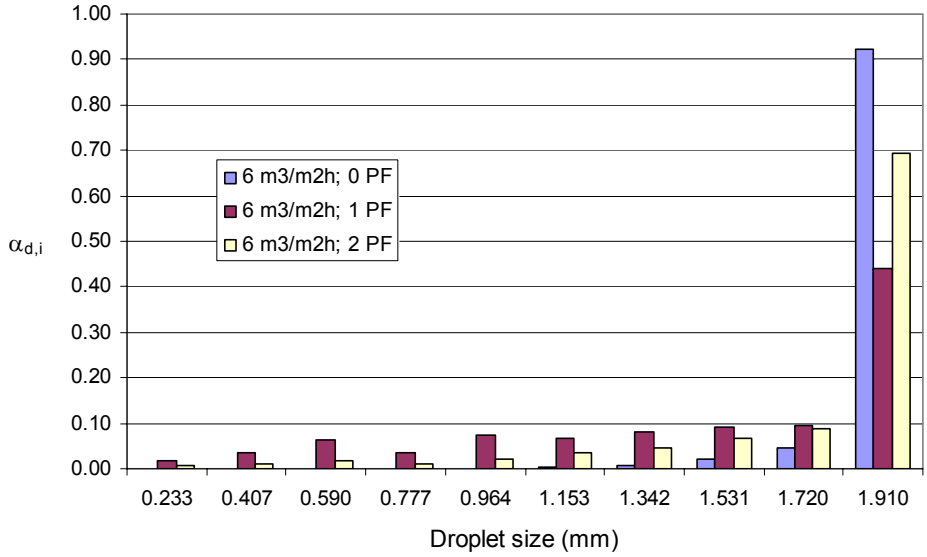

Figure A6. Droplet size distribution at point (5).

Appendix 8

Linear velocity of the organic phase at the top layer (line D) of the settler

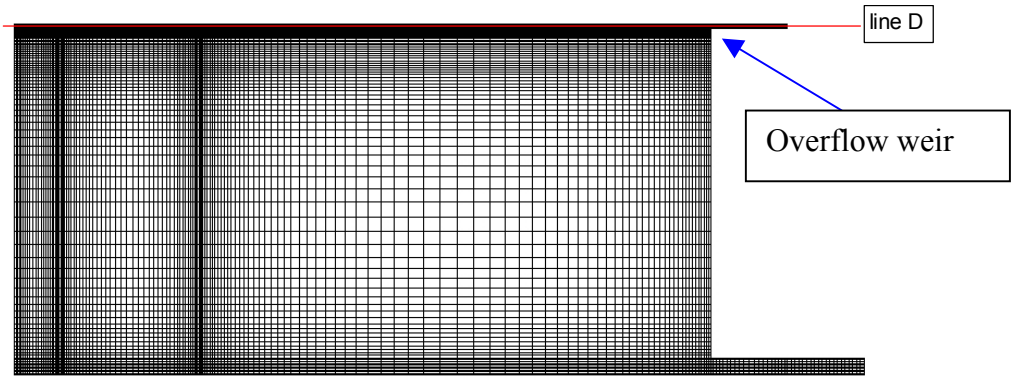

Figure A1. Study line D locates at the height of 1188 mm, when the specific volume flow rate is 6 m^3/m^2h and at the height of 1195 mm, when the specific volume flow rate is 12 m^3/m^2h. The place of the overflow weir is 2584 mm from the front end of the settler.

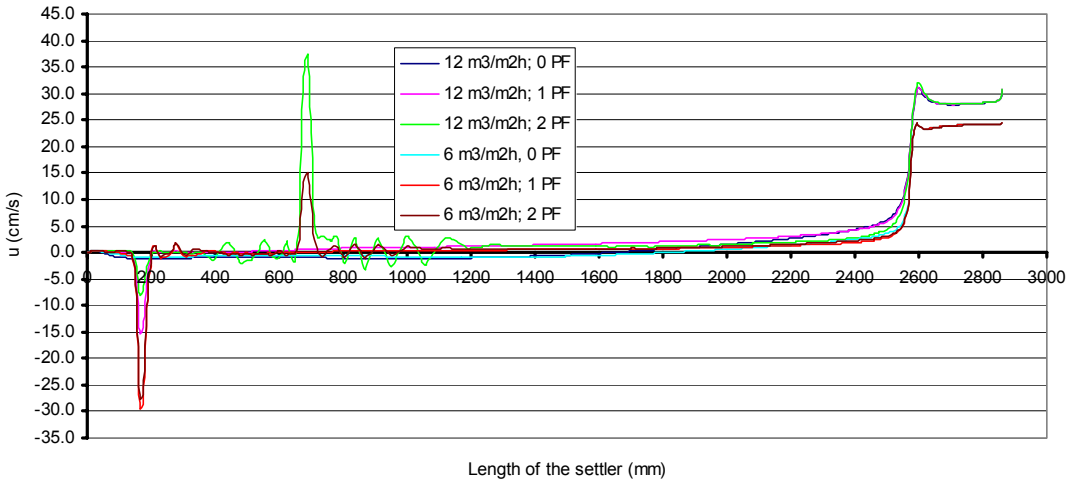

Figure A2. Linear velocity of the organic phase on line D, when the temperature is 10 °C.

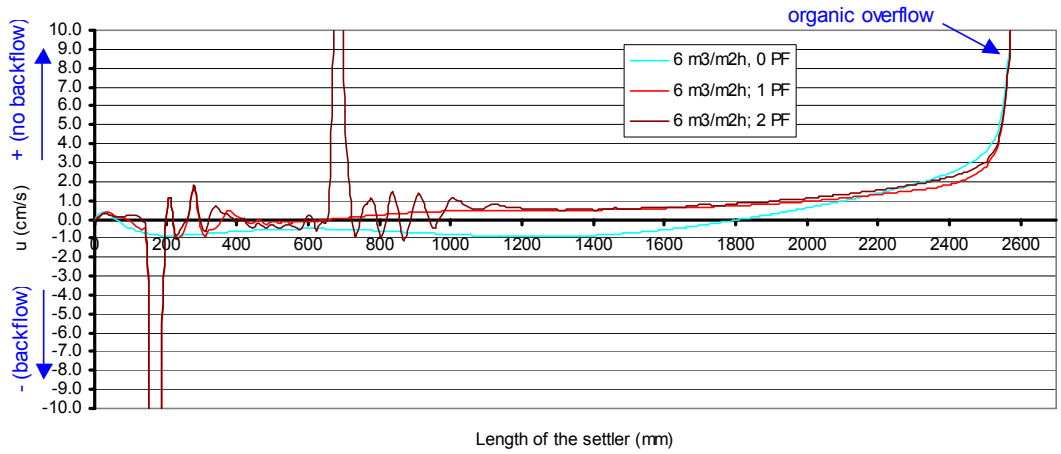

Figure A3. Linear velocity of the organic phase on line D, when the temperature is 10 °C and the specific volume flow rate is 6 m^3/m^2h.

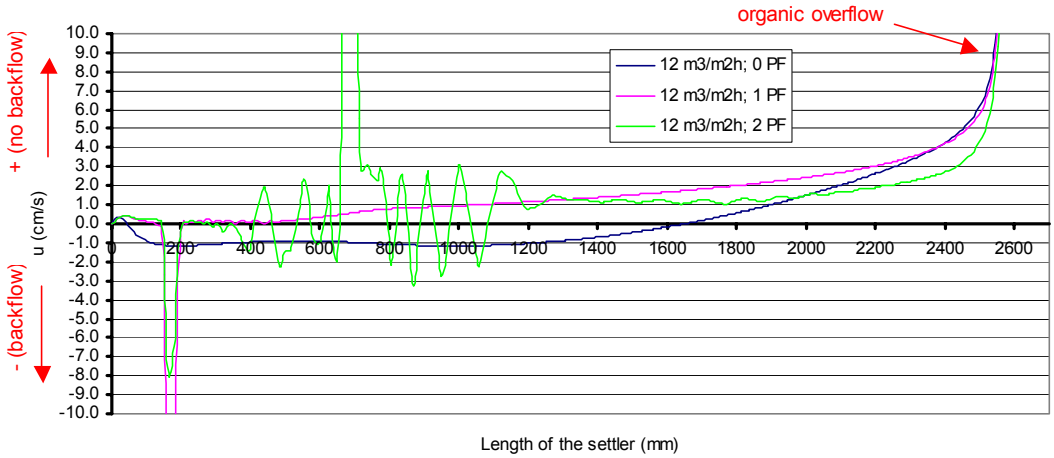

Figure A4. Linear velocity of the organic phase on line D, when the temperature is 10 °C and the specific volume flow rate is 12 m^3/m^2h.

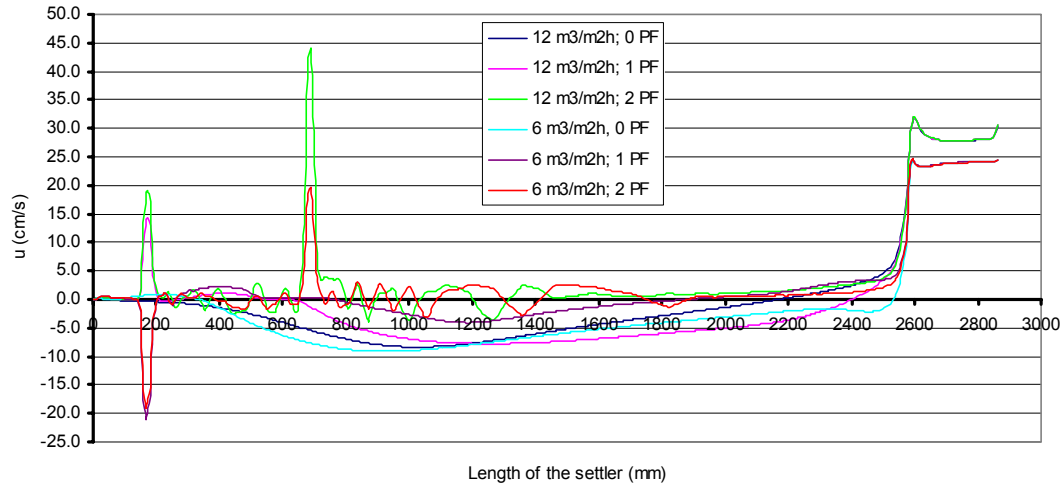

Figure A5. Linear velocity of the organic phase on line D, when the temperature is 20 °C.

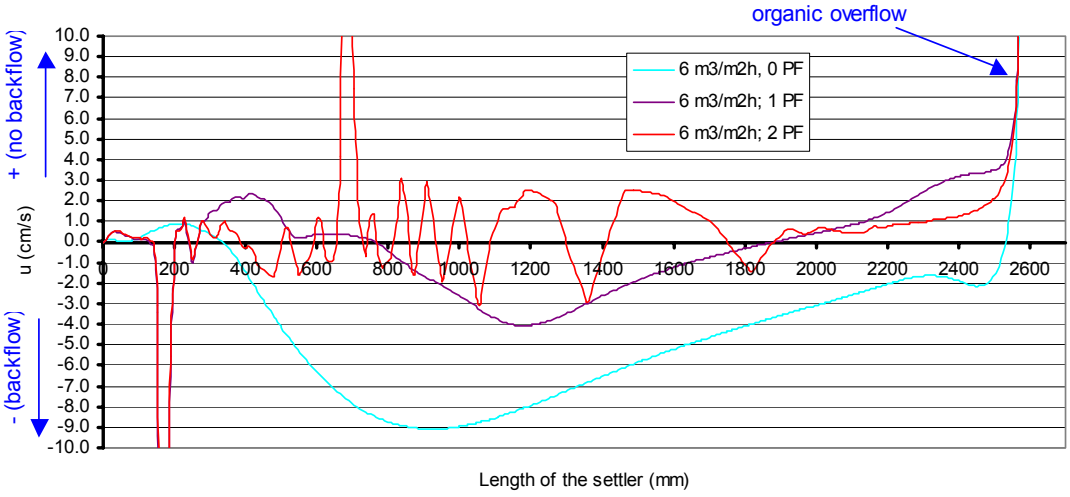

Figure A6. Linear velocity of the organic phase on line D, when the temperature is 20 °C and the specific volume flow rate is 6 m^3/m^2h.

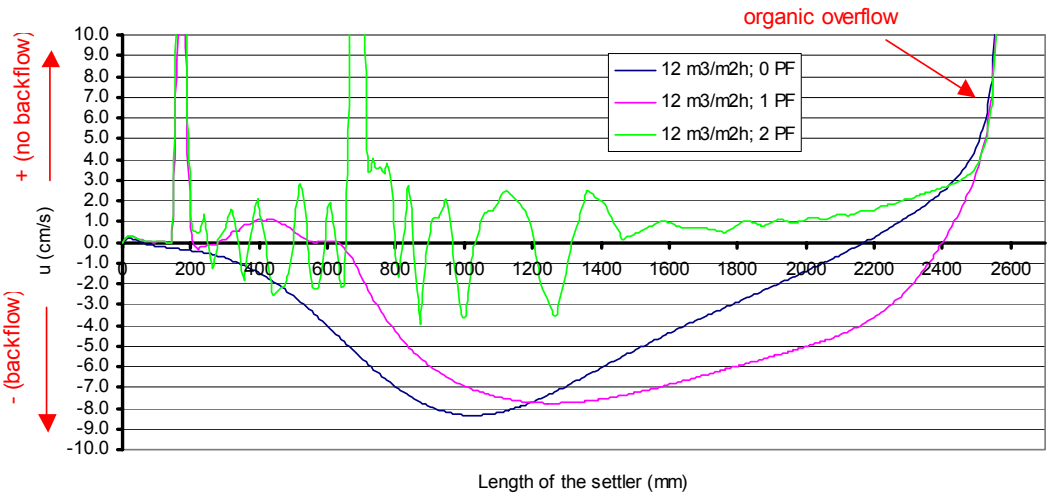

Figure A7. Linear velocity of the organic phase on line D, when the temperature is 20 °C and the specific volume flow rate is 12 m^3/m^2h.

Appendix 9

Force balances in proportion to viscous forces for the dispersion

Table A. Force balances in proportion to viscous forces, when T = 10 °C and V_{spec} = 6 and 12 m^3/m^2h. Dimensionless group numbers are average values from the study lines. The relative velocity of the phases, Sauter mean diameter of droplets as a characteristic length, and the physical properties of the continuous phase are used.

Temperature 10 °C									
Specific volume flow rate 6 m^3/m^2h									
Picket fences	No PF	One PF	Two PF	No PF	One PF	Two PF	No PF	One PF	Two PF
Study line	Line A	Line A	Line A	Line B	Line B	Line B	Line C	Line C	Line C
Viscous forces	1.0E+00	1.0E+00	1.0E+00	1.0E+00	1.0E+00	1.0E+00	1.0E+00	1.0E+00	1.0E+00
Inertia forces	3.1E+00	2.4E+00	3.0E+00	2.8E+00	1.9E+00	1.8E+00	2.3E+00	1.8E+00	2.7E+00
Buoyancy forces	1.3E+04	2.0E+05	5.2E+05	7.5E+03	8.0E+04	3.5E+04	1.5E+04	1.0E+05	2.8E+04
Surface forces	3.5E+04	5.4E+05	1.4E+06	2.1E+04	2.1E+05	9.7E+04	4.1E+04	2.7E+05	7.5E+04
Picket fences	No PF	One PF	Two PF	No PF	One PF	Two PF	No PF	One PF	Two PF
Study line	Line E	Line E	Line E	Line F	Line F	Line F	Line G	Line G	Line G
Viscous forces	1.0E+00	1.0E+00	1.0E+00	1.0E+00	1.0E+00	1.0E+00	1.0E+00	1.0E+00	1.0E+00
Inertia forces	2.3E+00	2.3E+00	3.2E+00	8.1E+00	6.9E+00	7.4E+00	2.1E+00	1.5E+00	1.5E+00
Buoyancy forces	8.2E+01	8.2E+01	8.5E+01	3.2E+02	3.2E+02	3.3E+02	2.7E+03	5.9E+03	7.3E+03
Surface forces	2.0E+03	2.1E+03	2.0E+03	1.4E+03	1.7E+03	1.6E+03	7.2E+03	1.6E+04	2.0E+04
Temperature 10 °C									
Specific volume flow rate 12 m^3/m^2h									
Picket fences	No PF	One PF	Two PF	No PF	One PF	Two PF	No PF	One PF	Two PF
Study line	Line A	Line A	Line A	Line B	Line B	Line B	Line C	Line C	Line C
Viscous forces	1.0E+00	1.0E+00	1.0E+00	1.0E+00	1.0E+00	1.0E+00	1.0E+00	1.0E+00	1.0E+00
Inertia forces	2.8E+00	2.0E+00	3.8E+00	2.8E+00	1.9E+00	1.2E+00	2.2E+00	1.6E+00	1.1E+00
Buoyancy forces	3.9E+04	1.6E+05	6.7E+04	1.4E+05	6.2E+05	3.1E+04	2.4E+04	2.0E+04	4.3E+04
Surface forces	1.0E+05	4.3E+05	1.8E+05	3.8E+05	1.6E+06	8.3E+04	7.1E+04	5.4E+04	1.2E+05
Picket fences	No PF	One PF	Two PF	No PF	One PF	Two PF	No PF	One PF	Two PF
Study line	Line E	Line E	Line E	Line F	Line F	Line F	Line G	Line G	Line G
Viscous forces	1.0E+00	1.0E+00	1.0E+00	1.0E+00	1.0E+00	1.0E+00	1.0E+00	1.0E+00	1.0E+00
Inertia forces	1.1E+00	1.8E+00	2.3E+00	8.2E+00	5.7E+00	5.8E+00	3.0E+00	2.3E+00	2.1E+00
Buoyancy forces	7.6E+01	7.9E+01	8.8E+01	2.9E+02	3.0E+02	2.9E+02	1.8E+03	3.0E+03	5.2E+03
Surface forces	3.4E+03	3.0E+03	2.8E+03	1.4E+03	1.9E+03	1.8E+03	4.9E+03	8.1E+03	1.4E+04

Table B. Force balances in proportion to viscous forces, when T = 20 °C and V_{spec} = 6 and 12 m^3/m^2h. Dimensionless group numbers are average values from the study lines. The relative velocity of the phases, Sauter mean diameter of droplets as a characteristic length, and the physical properties of the continuous phase are used.

Temperature 20 °C									
Specific volume flow rate 6 m^3/m^2h									
Picket fences	No PF	One PF	Two PF	No PF	One PF	Two PF	No PF	One PF	Two PF
Study line	Line A	Line A	Line A	Line B	Line B	Line B	Line C	Line C	Line C
Viscous forces	1.0E+00	1.0E+00	1.0E+00	1.0E+00	1.0E+00	1.0E+00	1.0E+00	1.0E+00	1.0E+00
Inertia forces	7.2E+00	7.0E+00	7.8E+00	6.6E+00	4.7E+00	3.9E+00	4.6E+00	3.9E+00	6.5E+00
Buoyancy forces	2.4E+04	1.7E+05	1.7E+07	5.5E+04	2.3E+05	9.8E+04	5.8E+04	5.7E+04	2.7E+06
Surface forces	2.0E+04	1.7E+05	1.3E+07	5.8E+04	2.9E+05	7.6E+04	5.5E+04	6.6E+04	2.2E+06
Picket fences	No PF	One PF	Two PF	No PF	One PF	Two PF	No PF	One PF	Two PF
Study line	Line E	Line E	Line E	Line F	Line F	Line F	Line G	Line G	Line G
Viscous forces	1.0E+00	1.0E+00	1.0E+00	1.0E+00	1.0E+00	1.0E+00	1.0E+00	1.0E+00	1.0E+00
Inertia forces	6.3E+00	6.3E+00	9.2E+00	2.2E+01	1.7E+01	1.8E+01	4.4E+00	3.2E+00	3.9E+00
Buoyancy forces	9.5E+01	9.5E+01	1.0E+02	6.5E+02	6.5E+02	1.0E+03	9.6E+03	2.4E+04	3.2E+04
Surface forces	1.1E+03	1.1E+03	1.1E+03	9.9E+02	1.2E+03	1.5E+03	7.0E+03	2.6E+04	2.8E+04
Temperature 20 °C									
Specific volume flow rate 12 m^3/m^2h									
Picket fences	No PF	One PF	Two PF	No PF	One PF	Two PF	No PF	One PF	Two PF
Study line	Line A	Line A	Line A	Line B	Line B	Line B	Line C	Line C	Line C
Viscous forces	1.0E+00	1.0E+00	1.0E+00	1.0E+00	1.0E+00	1.0E+00	1.0E+00	1.0E+00	1.0E+00
Inertia forces	1.0E+01	5.2E+00	9.4E+00	8.7E+00	5.1E+00	4.4E+00	6.4E+00	3.7E+00	3.5E+00
Buoyancy forces	2.7E+05	5.5E+05	1.2E+05	6.2E+05	3.5E+05	2.8E+05	9.1E+04	4.7E+04	6.9E+04
Surface forces	2.0E+05	4.0E+05	8.9E+04	4.4E+05	2.5E+05	2.0E+05	6.7E+04	3.5E+04	5.2E+04
Picket fences	No PF	One PF	Two PF	No PF	One PF	Two PF	No PF	One PF	Two PF
Study line	Line E	Line E	Line E	Line F	Line F	Line F	Line G	Line G	Line G
Viscous forces	1.0E+00	1.0E+00	1.0E+00	1.0E+00	1.0E+00	1.0E+00	1.0E+00	1.0E+00	1.0E+00
Inertia forces	6.2E+00	5.9E+00	1.2E+01	2.5E+01	1.6E+01	1.8E+01	7.5E+00	4.3E+00	4.6E+00
Buoyancy forces	9.5E+01	9.4E+01	1.1E+02	6.9E+02	5.9E+02	5.8E+02	5.7E+03	2.0E+04	5.0E+04
Surface forces	1.1E+03	1.2E+03	9.9E+02	9.8E+02	1.2E+03	1.1E+03	4.1E+03	1.5E+04	3.7E+04

Appendix 10

Force balances between surface and buoyancy forces

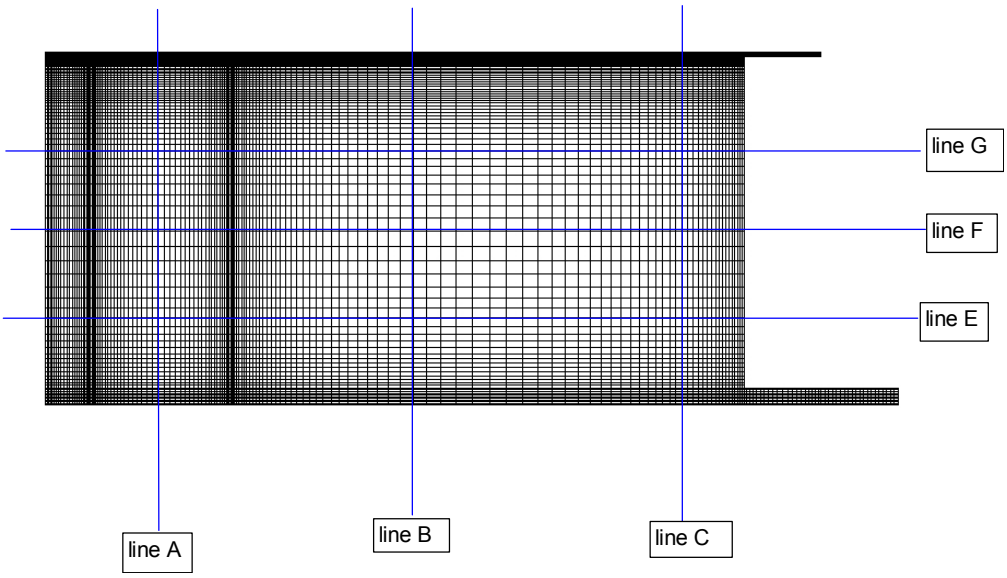

Figure A1. Study lines and their locations. The place of line A is 427.5 mm from the front end of the settler and it locates between two picket fences, line B is 1275.5 mm from the front end of the settler and line C is 2349.5 mm. Line E locates at the height of 300 mm, line F locates at the height of 600 mm and line G at the height of 900 mm. (Notice, the line locations are not in scale.)

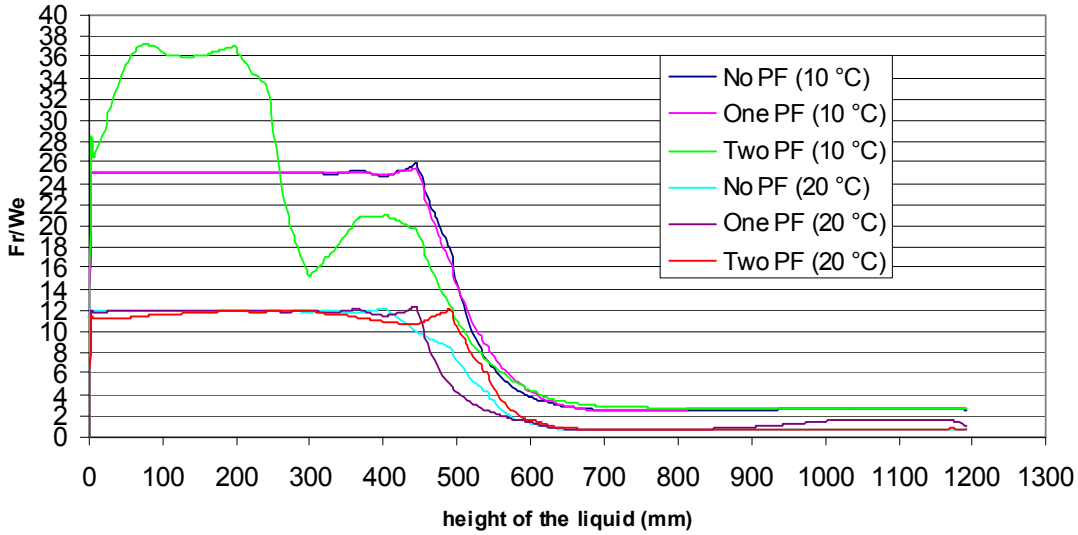

Figure A2. Fr-We ratio on line A as a function of the height of the liquid. Specific volume flow rate is 6 m^3/m^2h**.**

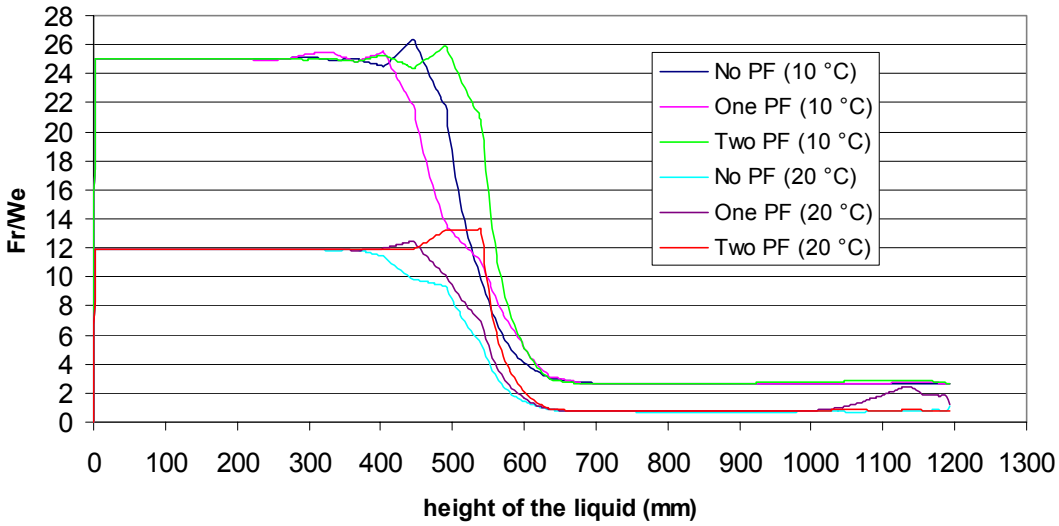

Figure A3. Fr-We ratio on line B as a function of the height of the liquid. Specific volume flow rate is 6 m^3/m^2h**.**

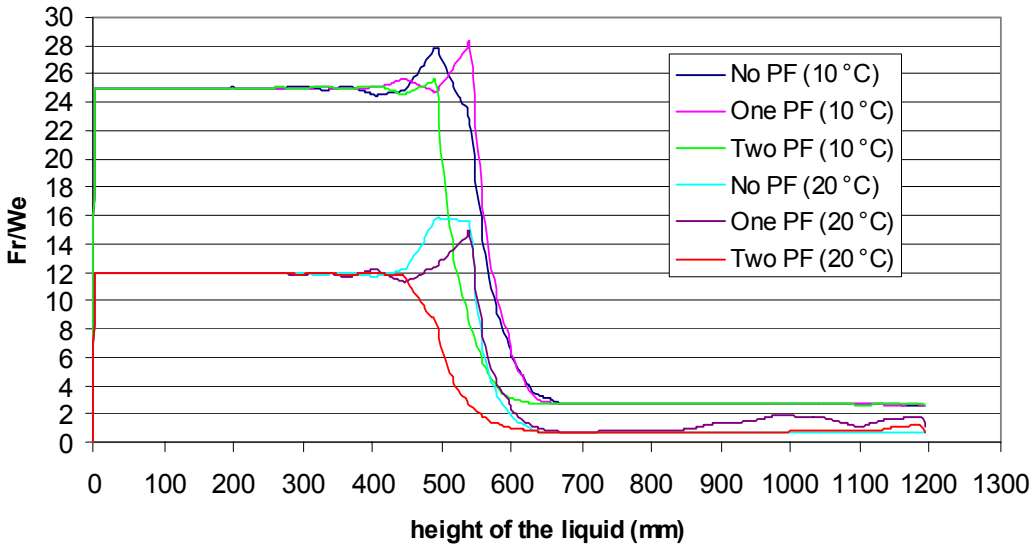

Figure A4. Fr-We ratio on line C as a function of the height of the liquid. Specific volume flow rate is 6 m^3/m^2h**.**

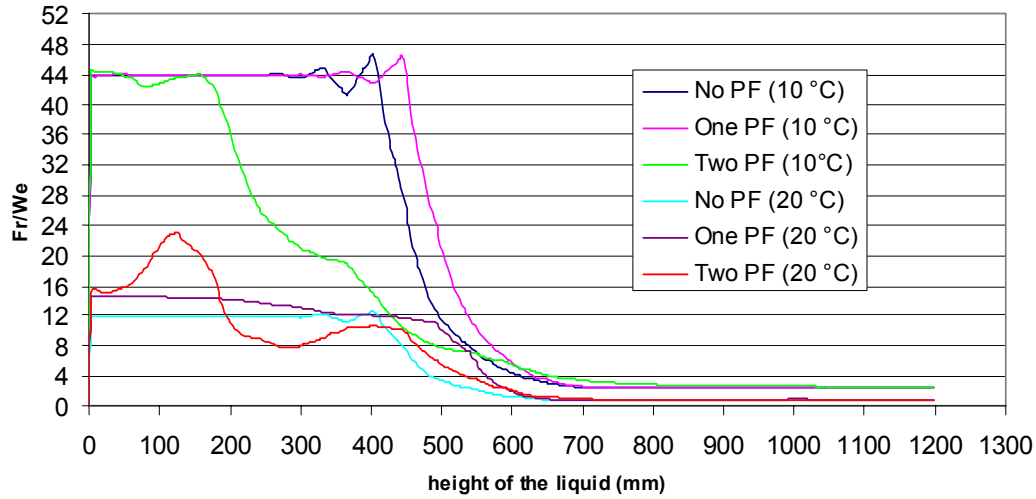

Figure A5. Fr-We ratio on line A as a function of the height of the liquid. Specific volume flow rate is 12 m^3/m^2h**.**

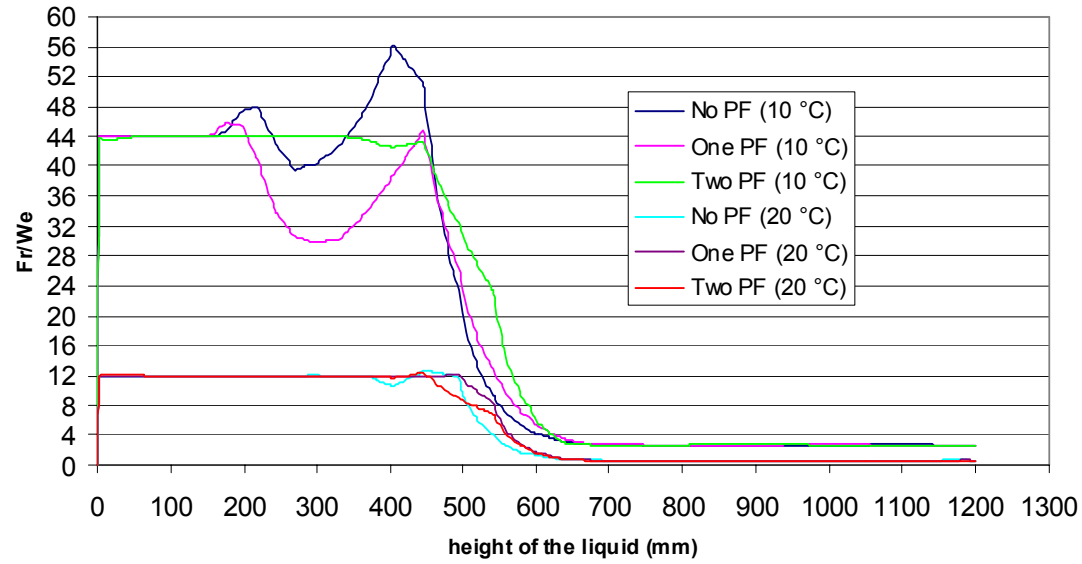

Figure A6. Fr-We ratio on line B as a function of the height of the liquid. Specific volume flow rate is 12 m^3/m^2h**.**

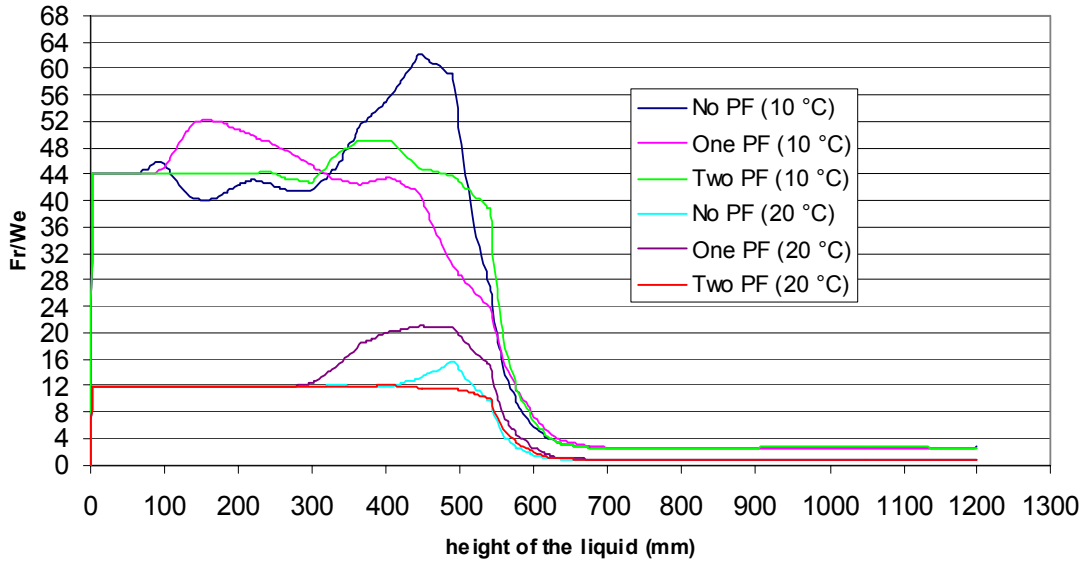

Figure A7. Fr-We ratio on line C as a function of the height of the liquid. Specific volume flow rate is 12 m^3/m^2h**.**

Appendix 11

Force balances in proportion to viscous forces for the continuous and the dispersed phase

Table A. Force balances in proportion to viscous forces, when T = 20 °C and V_{spec} = 6 m^3/m^2h. Dimensionless group numbers are average values from the study lines. Characteristic length is the liquid depth.

Temperature 20 °C									
Specific volume flow rate 6 m^3/m^2h									
Continuous water phase									
Picket fences	No PF	One PF	Two PF	No PF	One PF	Two PF	No PF	One PF	Two PF
Study line	Line A	Line A	Line A	Line B	Line B	Line B	Line C	Line C	Line C
Viscous forces	1.0E+00	1.0E+00	1.0E+00	1.0E+00	1.0E+00	1.0E+00	1.0E+00	1.0E+00	1.0E+00
Inertia forces	5.1E+04	2.1E+04	1.4E+04	4.8E+04	3.5E+04	8.4E+03	9.4E+03	9.4E+03	5.3E+03
Buoyancy forces	2.8E+08	1.0E+09	1.6E+09	2.9E+08	3.9E+08	2.0E+09	1.4E+09	1.5E+09	5.3E+09
Surface forces	4.9E+02	1.9E+03	2.8E+03	5.1E+02	7.0E+02	3.6E+03	2.5E+03	2.7E+03	9.4E+03
Picket fences	No PF	One PF	Two PF	No PF	One PF	Two PF	No PF	One PF	Two PF
Study line	Line E	Line E	Line E	Line F	Line F	Line F	Line G	Line G	Line G
Viscous forces	1.0E+00	1.0E+00	1.0E+00	1.0E+00	1.0E+00	1.0E+00	1.0E+00	1.0E+00	1.0E+00
Inertia forces	1.6E+04	1.3E+04	1.3E+04	9.4E+04	6.3E+04	3.5E+04	2.4E+04	2.1E+04	1.0E+04
Buoyancy forces	7.4E+08	1.1E+09	2.0E+09	3.4E+08	4.9E+08	1.2E+09	8.2E+08	1.2E+09	1.2E+10
Surface forces	1.3E+03	2.0E+03	3.7E+03	6.1E+02	8.8E+02	2.1E+03	1.5E+03	2.2E+03	2.1E+04

Temperature 20 °C									
Specific volume flow rate 6 m^3/m^2h									
Dispersed organic phase									
Picket fences	No PF	One PF	Two PF	No PF	One PF	Two PF	No PF	One PF	Two PF
Study line	Line A	Line A	Line A	Line B	Line B	Line B	Line C	Line C	Line C
Viscous forces	1.0E+00	1.0E+00	1.0E+00	1.0E+00	1.0E+00	1.0E+00	1.0E+00	1.0E+00	1.0E+00
Inertia forces	3.1E+04	1.6E+04	1.1E+04	2.7E+04	2.0E+04	5.6E+03	6.9E+03	7.6E+03	6.4E+03
Buoyancy forces	1.3E+08	2.9E+08	6.7E+08	2.0E+08	2.2E+08	8.2E+08	5.1E+08	4.5E+08	7.9E+08
Surface forces	3.3E+02	7.1E+02	1.6E+03	5.0E+02	5.5E+02	2.0E+03	1.2E+03	1.1E+03	1.9E+03
Picket fences	No PF	One PF	Two PF	No PF	One PF	Two PF	No PF	One PF	Two PF
Study line	Line E	Line E	Line E	Line F	Line F	Line F	Line G	Line G	Line G
Viscous forces	1.0E+00	1.0E+00	1.0E+00	1.0E+00	1.0E+00	1.0E+00	1.0E+00	1.0E+00	1.0E+00
Inertia forces	9.7E+03	9.7E+03	1.2E+04	5.2E+04	3.6E+04	2.0E+04	1.4E+04	1.2E+04	6.2E+03
Buoyancy forces	7.6E+08	6.8E+08	6.3E+08	1.8E+08	2.3E+08	7.6E+08	3.6E+08	5.8E+08	4.5E+09
Surface forces	1.8E+03	1.7E+03	1.5E+03	4.3E+02	5.7E+02	1.8E+03	8.7E+02	1.4E+03	1.1E+04

Table B. Force balances in proportion to viscous forces, when T = 20 °C and V_{spec} = 12 m^3/m^2h. Dimensionless group numbers are average values from the study lines. Characteristic length is the liquid depth.

Temperature 20 °C									
Specific volume flow rate 12 m^3/m^2h									
Continuous water phase									
Picket fences	No PF	One PF	Two PF	No PF	One PF	Two PF	No PF	One PF	Two PF
Study line	Line A	Line A	Line A	Line B	Line B	Line B	Line C	Line C	Line C
Viscous forces	1.0E+00	1.0E+00	1.0E+00	1.0E+00	1.0E+00	1.0E+00	1.0E+00	1.0E+00	1.0E+00
Inertia forces	5.6E+04	3.5E+04	1.8E+04	5.1E+04	5.1E+04	2.2E+04	9.8E+03	2.0E+04	8.3E+03
Buoyancy forces	2.9E+08	9.3E+08	1.7E+09	2.8E+08	5.3E+08	9.0E+08	1.5E+09	5.9E+08	2.3E+09
Surface forces	5.2E+02	1.6E+03	2.9E+03	4.9E+02	9.3E+02	1.6E+03	2.7E+03	1.0E+03	4.1E+03
Picket fences	No PF	One PF	Two PF	No PF	One PF	Two PF	No PF	One PF	Two PF
Study line	Line E	Line E	Line E	Line F	Line F	Line F	Line G	Line G	Line G
Viscous forces	1.0E+00	1.0E+00	1.0E+00	1.0E+00	1.0E+00	1.0E+00	1.0E+00	1.0E+00	1.0E+00
Inertia forces	1.7E+04	1.8E+04	2.0E+04	1.1E+05	1.1E+05	5.9E+04	2.7E+04	2.7E+04	2.3E+04
Buoyancy forces	6.8E+08	8.5E+08	1.4E+09	2.1E+08	2.2E+08	7.5E+08	1.1E+09	6.8E+08	1.4E+09
Surface forces	1.2E+03	1.5E+03	2.5E+03	3.6E+02	3.9E+02	1.3E+03	1.9E+03	1.2E+03	2.5E+03

Temperature 20 °C									
Specific volume flow rate 12 m^3/m^2h									
Dispersed organic phase									
Picket fences	No PF	One PF	Two PF	No PF	One PF	Two PF	No PF	One PF	Two PF
Study line	Line A	Line A	Line A	Line B	Line B	Line B	Line C	Line C	Line C
Viscous forces	1.0E+00	1.0E+00	1.0E+00	1.0E+00	1.0E+00	1.0E+00	1.0E+00	1.0E+00	1.0E+00
Inertia forces	3.4E+04	2.3E+04	1.2E+04	2.9E+04	3.0E+04	1.6E+04	6.3E+03	9.9E+03	6.9E+03
Buoyancy forces	2.0E+08	4.3E+08	5.0E+08	2.5E+08	1.9E+08	4.0E+08	5.5E+08	8.9E+08	8.6E+08
Surface forces	4.8E+02	1.0E+03	1.2E+03	6.0E+02	4.6E+02	9.7E+02	1.3E+03	2.1E+03	2.1E+03
Picket fences	No PF	One PF	Two PF	No PF	One PF	Two PF	No PF	One PF	Two PF
Study line	Line E	Line E	Line E	Line F	Line F	Line F	Line G	Line G	Line G
Viscous forces	1.0E+00	1.0E+00	1.0E+00	1.0E+00	1.0E+00	1.0E+00	1.0E+00	1.0E+00	1.0E+00
Inertia forces	9.5E+03	1.1E+04	1.5E+04	5.9E+04	6.1E+04	3.4E+04	1.6E+04	1.5E+04	1.3E+04
Buoyancy forces	1.0E+09	6.8E+08	5.4E+08	1.4E+08	1.1E+08	3.6E+08	3.4E+08	3.5E+08	6.7E+08
Surface forces	2.4E+03	1.6E+03	1.3E+03	3.5E+02	2.6E+02	8.7E+02	8.2E+02	8.3E+02	1.6E+03

Table C. Force balances in proportion to viscous forces, when T = 10 °C and V_{spec} = 6 m^3/m^2h. Dimensionless group numbers are average values from the study lines. Characteristic length is the liquid depth.

Temperature 10 °C

Specific volume flow rate 6 m^3/m^2h

Continuous water phase

Picket fences	No PF	One PF	Two PF	No PF	One PF	Two PF	No PF	One PF	Two PF
Study line	Line A	Line A	Line A	Line B	Line B	Line B	Line C	Line C	Line C
Viscous forces	1.0E+00	1.0E+00	1.0E+00	1.0E+00	1.0E+00	1.0E+00	1.0E+00	1.0E+00	1.0E+00
Inertia forces	3.1E+04	1.8E+04	7.0E+03	2.4E+04	1.9E+04	7.6E+03	6.3E+03	6.4E+03	3.1E+03
Buoyancy forces	3.8E+08	7.6E+08	2.5E+09	4.4E+08	1.2E+09	2.7E+09	1.3E+09	1.5E+09	4.1E+09
Surface forces	9.1E+02	1.8E+03	6.0E+03	1.0E+03	3.0E+03	6.5E+03	3.1E+03	3.5E+03	9.7E+03

Picket fences	No PF	One PF	Two PF	No PF	One PF	Two PF	No PF	One PF	Two PF
Study line	Line E	Line E	Line E	Line F	Line F	Line F	Line G	Line G	Line G
Viscous forces	1.0E+00	1.0E+00	1.0E+00	1.0E+00	1.0E+00	1.0E+00	1.0E+00	1.0E+00	1.0E+00
Inertia forces	9.1E+03	8.7E+03	7.9E+03	6.0E+04	4.9E+04	2.9E+04	2.0E+04	1.5E+04	9.8E+03
Buoyancy forces	8.2E+08	1.1E+09	1.4E+09	2.7E+08	2.9E+08	1.4E+09	5.7E+08	7.3E+08	4.2E+09
Surface forces	1.9E+03	2.7E+03	3.3E+03	6.4E+02	6.9E+02	3.3E+03	1.3E+03	1.7E+03	1.0E+04

Temperature 10 °C

Specific volume flow rate 6 m^3/m^2h

Dispersed organic phase

Picket fences	No PF	One PF	Two PF	No PF	One PF	Two PF	No PF	One PF	Two PF
Study line	Line A	Line A	Line A	Line B	Line B	Line B	Line C	Line C	Line C
Viscous forces	1.0E+00	1.0E+00	1.0E+00	1.0E+00	1.0E+00	1.0E+00	1.0E+00	1.0E+00	1.0E+00
Inertia forces	2.1E+04	1.3E+04	6.2E+03	1.5E+04	1.2E+04	5.9E+03	4.1E+03	4.4E+03	4.2E+03
Buoyancy forces	1.9E+08	4.0E+08	8.0E+08	3.3E+08	8.4E+08	1.2E+09	7.6E+08	7.1E+08	1.4E+09
Surface forces	6.1E+02	1.3E+03	2.6E+03	1.1E+03	2.7E+03	3.8E+03	2.4E+03	2.3E+03	4.5E+03

Picket fences	No PF	One PF	Two PF	No PF	One PF	Two PF	No PF	One PF	Two PF
Study line	Line E	Line E	Line E	Line F	Line F	Line F	Line G	Line G	Line G
Viscous forces	1.0E+00	1.0E+00	1.0E+00	1.0E+00	1.0E+00	1.0E+00	1.0E+00	1.0E+00	1.0E+00
Inertia forces	5.2E+03	5.5E+03	6.1E+03	3.7E+04	3.1E+04	1.9E+04	1.3E+04	9.6E+03	6.5E+03
Buoyancy forces	2.2E+09	1.2E+09	7.1E+08	1.4E+08	1.7E+08	3.9E+08	3.0E+08	4.2E+08	2.0E+09
Surface forces	7.0E+03	3.9E+03	2.3E+03	4.4E+02	5.6E+02	1.2E+03	9.6E+02	1.3E+03	6.4E+03

Table D. Force balances in proportion to viscous forces, when T = 10 °C and V_{spec} = 12 m^3/m^2h. Dimensionless group numbers are average values from the study lines. Characteristic length is the liquid depth.

Temperature 10 °C

Specific volume flow rate 12 m^3/m^2h

Continuous water phase

Picket fences	No PF	One PF	Two PF	No PF	One PF	Two PF	No PF	One PF	Two PF
Study line	Line A	Line A	Line A	Line B	Line B	Line B	Line C	Line C	Line C
Viscous forces	1.0E+00	1.0E+00	1.0E+00	1.0E+00	1.0E+00	1.0E+00	1.0E+00	1.0E+00	1.0E+00
Inertia forces	3.7E+04	2.7E+04	1.0E+04	2.9E+04	2.6E+04	1.5E+04	9.0E+03	9.5E+03	8.0E+03
Buoyancy forces	3.4E+08	1.0E+09	1.6E+09	3.8E+08	7.5E+08	1.5E+09	1.1E+09	1.0E+09	1.1E+09
Surface forces	7.9E+02	2.4E+03	3.8E+03	9.0E+02	1.8E+03	3.5E+03	2.5E+03	2.5E+03	2.5E+03

Picket fences	No PF	One PF	Two PF	No PF	One PF	Two PF	No PF	One PF	Two PF
Study line	Line E	Line E	Line E	Line F	Line F	Line F	Line G	Line G	Line G
Viscous forces	1.0E+00	1.0E+00	1.0E+00	1.0E+00	1.0E+00	1.0E+00	1.0E+00	1.0E+00	1.0E+00
Inertia forces	1.2E+04	1.3E+04	1.3E+04	7.3E+04	7.3E+04	5.0E+04	2.1E+04	2.1E+04	1.7E+04
Buoyancy forces	6.2E+08	6.1E+08	8.2E+08	1.9E+08	1.9E+08	3.0E+08	6.4E+08	5.7E+08	1.1E+09
Surface forces	1.5E+03	1.4E+03	1.9E+03	4.4E+02	4.6E+02	6.9E+02	1.5E+03	1.3E+03	2.6E+03

Temperature 10 °C

Specific volume flow rate 12 m^3/m^2h

Dispersed organic phase

Picket fences	No PF	One PF	Two PF	No PF	One PF	Two PF	No PF	One PF	Two PF
Study line	Line A	Line A	Line A	Line B	Line B	Line B	Line C	Line C	Line C
Viscous forces	1.0E+00	1.0E+00	1.0E+00	1.0E+00	1.0E+00	1.0E+00	1.0E+00	1.0E+00	1.0E+00
Inertia forces	2.4E+04	1.8E+04	6.5E+03	1.8E+04	1.6E+04	9.9E+03	5.3E+03	5.4E+03	4.5E+03
Buoyancy forces	1.7E+08	7.2E+08	8.8E+08	2.3E+08	4.4E+08	6.7E+08	7.2E+08	7.5E+08	7.1E+08
Surface forces	5.3E+02	2.3E+03	2.8E+03	7.3E+02	1.4E+03	2.1E+03	2.3E+03	2.4E+03	2.2E+03

Picket fences	No PF	One PF	Two PF	No PF	One PF	Two PF	No PF	One PF	Two PF
Study line	Line E	Line E	Line E	Line F	Line F	Line F	Line G	Line G	Line G
Viscous forces	1.0E+00	1.0E+00	1.0E+00	1.0E+00	1.0E+00	1.0E+00	1.0E+00	1.0E+00	1.0E+00
Inertia forces	6.4E+03	7.3E+03	7.5E+03	4.5E+04	4.5E+04	3.1E+04	1.4E+04	1.3E+04	1.1E+04
Buoyancy forces	5.8E+08	6.3E+08	8.6E+08	1.2E+08	1.2E+08	2.0E+08	3.0E+08	3.2E+08	5.8E+08
Surface forces	1.8E+03	2.0E+03	2.7E+03	3.7E+02	3.8E+02	6.5E+02	9.6E+02	1.0E+03	1.8E+03

HELSINKI UNIVERSITY OF TECHNOLOGY DOCTORAL THESES IN MATERIALS AND EARTH SCIENCES

TKK-ME-DT-1 Ranki-Kilpinen, T.,
Sulphation of Cuprous and Cupric Oxide Dusts and Heterogeneous Copper Matte Particles in Simulated Flash Smelting Heat Recovery Boiler Conditions, 2004.

TKK-ME-DT-2 Söderberg, O.,
Novel Ni-Mn-Ga Alloys and their Magnetic Shape Memory Behaviour, 2004.

TKK-ME-DT-3 Kaskiala, T.,
Studies on Gas-Liquid Mass Transfer in Atmospheric Leaching of Sulphidic Zinc Concentrates, 2005.

TKK-ME-DT-4 Grau, R.A.,
An Investigation of the Effect of Physical and Chemical Variables on Bubble Generation and Coalescence in Laboratory Scale Flotation Cells, 2006.

TKK-ME-DT-5 Kivikytö-Reponen, P.,
Correlation of Material Characteristics and Wear of Powder Metallurgical Metal Matrix Composites, 2006.

TKK-ME-DIS-6 Ge, Y.,
The Crystal and Magnetic Microstructure of Ni-Mn-Ga Alloys, 2007.

ISBN 978-951-22-9038-3
ISBN 978-951-22-9039-0 (electronic)
ISSN 1795-0074